DOKTORANDSKÉ DNY 2015

sborník workshopu doktorandů FJFI
oboru Matematické inženýrství

20. a 27. listopadu 2015

P. Ambrož, Z. Masáková (editoři)

Seznam příspěvků

Předmluva

Workshop Doktorandské dny pro doktorandy oboru Matematické inženýrství na FJFI slaví v roce 2015 již desáté výročí. Letošní ročník se koná ve dnech 20. a 27. listopadu 2015 a bude hostit přes 30 příspěvků studentů prezenčního i kombinovaného studia na FJFI. Příspěvky jako obvykle přesahují z oblasti aplikované matematiky i do informatiky a matematické fyziky. Prezentací před svými kolegy-studenty, školiteli, členy oborové rady MI i dalšími zájemci z řad odborné veřejnosti doktorandi získávají neocenitelnou zkušenost pro účast na konferencích v širším měřítku. Sepsání příspěvku do sborníku je pro mnohé z nich první příležitostí k vytvoření samostatné vědecké publikace. Proto považujeme konání této studentské konference za nezbytné pro vytváření vhodných podmínek při doktorském studiu na FJFI. Za finanční podporu workshopu děkujeme Studentské grantové soutěži (grant SVK 30/15/F4). Zájem o toto setkání neutuchá, a tak lze doufat, že v tradici konání konference Doktorandské dny bude i možno nadále pokračovat.

Organizátoři

Suitable Bases for Quantum Walks with Wigner Coins

Iva Bezděková*

4th year of PGS, email: `bezdekova.iva@gmail.com`
Department of Physics
Faculty of Nuclear Sciences and Physical Engineering, CTU in Prague

advisors:

Igor Jex, Department of Physics
Faculty of Nuclear Sciences and Physical Engineering, CTU in Prague

Martin Štefaňák, Department of Physics
Faculty of Nuclear Sciences and Physical Engineering, CTU in Prague

Abstract. The analysis of a physical problem simplifies considerably when one uses a suitable coordinate system. We apply this approach to the discrete-time quantum walk model, where the coins are given by $2j + 1$-dimensional Wigner rotation matrices (Wigner walks). The model was introduced by T. Miyazaki et al. [1] and the limit density with respect to the standard coin basis was analysed. First we show that the number of parameters of the Wigner rotation matrix can be reduced from three to only one parameter which influences the dynamics of the walk. Next we construct an optimal basis of the coin space in which the limit density of the Wigner walk gains much simpler form. Moreover, the optimal basis allow us to identify interesting regimes that are in the standard basis description hidden. The optimal basis description is based on such regimes, where we are cancelling one or more peaks in the probability distribution by a specific choice of the initial state. We provide a tool for construction of the optimal basis in any dimension. Furthermore, the models with integer j (odd-state walks) lead to the interesting trapping effect, which means that the walker is trapped around the origin with high probability (central peak in the probability distribution). Most of the known results regarding the trapping were obtained for the three-state Grover walk on a line [2, 3]. This feature was not analysed for Wigner walks before. We find that the optimal basis is more convenient and interesting even for the trapping probability. For example it shows that the trapping peak can be highly asymmetric and deviates from purely exponential decay. We provide explicit results for both the limit density and the trapping probability up to dimension five. Similar analysis of the limit distribution was done earlier [4] for special deformations of the Grover walk. In that case the optimal basis is different than for the Wigner walks since it is directly given by the eigenvectors of the coin operator [5].

Keywords: quantum walk, Wigner rotation matrix, limit density, trapping effect optimal basis

Abstrakt. Použití správného souřadnicového systému značně zjednoduší popis každého fyzikálního problému. Tuto ideu použijeme na diskrétní model kvantové procházky, kde je naší mincí $2j + 1$-dimenzionální Wignerova rotační matice (Wignerovy procházky). Model Wignerovy procházky byl zaveden a analyzován T. Miyazakim a dalšími [1] z hlediska limitní hustoty a vzhledem k standartní bázi prostoru mince. Nejprve ukážeme, že počet parametrů Wignerovy matice, které jsou fyzikálně relevantní a ovlivnují dynamiku kvantové procházky, se dá redukovat

---

ze tří na pouhý jeden. Dále zkonstruujeme bázi prostoru mince, kterou nazýváme optimální. V této bázi se limitní hustota Wignerovy procházky značně zjednoduší. Volba optimální báze navíc odkryje zajímavé režimy, které jsou v popisu pomocí standartní báze skryty. Ukážeme jak se dá optimální báze jednoduše zkonstruovat pro libovolnou dimenzi. V modelu, kde je parametr j přirozené číslo, můžeme pozorovat efekt záchytu. To znamená, že chodec je s velkou pravděpodobností lokalizován v okolí počátku (centrální pík v pravděpodobnostím rozdělení je navíc). Většina známých výsledků týkajících se záchytu je pro Groverovu procházku na přímce o třech možných stavech [2, 3]. Pro Wignerovy procházky nebyla tato vlastnost dříve analyzována. Ukážeme, že optimální báze je vhodnější a zajímavá také co se týče efektu záchytu v počátku. Jeden z příkladů který ukážeme je, že centrální pík může být díky vhodné volbě počátečního stavu značně asymetrický, navíc je porušen exponenciální pokles. Explicitní výsledky jak pro limitní hustotu, tak pro záchyt v počátku uvádíme až do dimenze pět. Podobná analýza limitního rozdělení byla provedena již dříve pro speciální modifikaci Groverovy procházky [4]. Konstrukce optimální báze byla v tomto případě zcela jiná než u Wignerovy procházky. Optimální báze prostoru mince přímo odpovídala vlastním vektorům mince [5].

Klíčová slova: kvantová procházka, Wignerova rotační matice, limitní hustota, efekt záchytu, optimální báze

The full paper: I. Bezděková, M. Štefaňák and I. Jex, Phys. Rev. A **92** (2015), 022347 or arXiv:1509.00960.

References

[1] T. Miyazaki, M. Katori and N. Konno. *Wigner formula of totation matrices and quantum walks.* Phys. Rev. A **76** (2007), 012332.

[2] N. Inui and N. Konno. *Localiyation of multi-state quantum walk in one dimension.* Physica A, **353** (2005) 133.

[3] N. Inui, N. Konno and E. Segawa. *One-dimensional three-state quantum walk.* Phys. Rev. E, **72** (2005) 056112.

[4] T. Machida. *Limit theorems of a 3-state quantum walk and its application for discrete uniform measures.* ArXiv:1401.1522.

[5] M. Štefaňák, I. Bezděková and I. Jex. *Limit distributions of three-state quantum walks: the role of coin eigenstates.* Phys. Rev. A **90** (2014), 012342.

Box Counting with Bayesian Correction

David Blatský

2nd year of PGS, email: `blatsdav@fjfi.cvut.cz`
Department of Software Engineering
Faculty of Nuclear Sciences and Physical Engineering, CTU in Prague

advisors:

Pavel Sovka, Department of Circuit Theory
Faculty of Electrical Engineering, CTU in Prague

Jaromír Kukal, Department of Software Engineering
Faculty of Nuclear Sciences and Physical Engineering, CTU in Prague

Abstract. Fractal patterns appear in a wide variety of sources across nature. The unusual characteristic of fractals is that they entail non-integer dimension. The Box Counting method is one of the often used approach to estimate the fractal dimension of a signal. Thanks to the relationship between entropy and the fractal dimension, it is possible to employ entropy in estimating the fractal dimension. In this paper, we propose to utilize Bayesian estimate of Hartley entropy of a finite sample in fractal dimension estimation. This method was tested on fractals generated by recursive expansion of appropriate matrices.

Keywords: unbiased estimation, Hartley entropy, Shannon entropy, Box Counting

Abstrakt. Fraktální struktury se vyskytují napříč přírodou. Neobvyklou vlastností fraktálů je, že mají neceločíselnou dimenzi. Metoda box counting je jedním z často využívaných přístupů k odhadu fraktální dimenze signálu. Tu je možné odhadovat díky vztahu entropie a fraktální dimenze. V tomto článku je navržen postup odhadu fraktální dimenze pomocí Bayesovského odhadu Hartleyovy entropie konečného vzorku dat. Tato metoda byla otestována na fraktálech generovaných rekurzivní expanzí vhodných matic.

Klíčová slova: nestranný odhad, Hartleyova entropie, Shannonova entropie, box counting

1 Introduction

A fractal is an object whose so-called fractal dimension exceeds its topological dimension and its Hausdorff dimension is non-integer at the same time. The Box Counting method [6] can be used for estimating the fractal dimension due to the relationship

$$\ln C(a) = A - D_0 \ln a, \tag{1}$$

where $a > 0$ is a box size and $C(a)$ is a number of covering elements. Capacity dimension [1] D_0 is estimated as a slope of the line computed by the least square method. These estimates tend to be biased especially for small values of a. We propose to enhance the Box Counting method by Bayesian estimation of Hartley entropy H_0, which offers better estimate of capacity dimension D_0.

2 Multinomial Distribution and Naive Entropy Estimates

A multinomial distribution [5] model plays the main role in investigating of point set structures. Let $n \in \mathbb{N}$ be a number of distinguished events. Let $p_j > 0$ be a probability of the jth event for $j = 1, ..., n$ satisfying $\sum_{j=1}^{n} p_j = 1$. Then the random variable j has a multinomial distribution $\text{Mul}(p_1, ..., p_n)$. After realization of multinomial distribution sample of size $N \in \mathbb{N}$, we can count the events and obtain $N_j \in \mathbb{N}_0$ as the number of jth event occurrences for $j = 1, ..., n$ satisfying $\sum_{j=1}^{n} N_j = N$. Therefore, we define the number of various events in a sample as $K = \sum_{N_j > 0} 1 \leq \min(n, N)$. Revising Hartley [8] and Shannon [8] entropy definitions

$$H_0 = \ln n, \tag{2}$$

$$H_1 = -\sum_{j=1}^{n} p_j \ln p_j, \tag{3}$$

we can perform a direct but naive estimation of them as

$$\hat{H}_{0,\text{naive}} = \ln K, \tag{4}$$

$$\hat{H}_{1,\text{naive}} = -\sum_{N_j > 0} \frac{N_j}{N} \ln \frac{N_j}{N}. \tag{5}$$

The main disadvantage of the naive estimates is their biasness. The random variable $K \in \{1, ..., n\}$ is capped by n, which causes $\text{E}\hat{H}_{0,\text{naive}} = \text{E} \ln K < \text{E} \ln n = \ln n = H_0$. Hence, the naive estimate of Hartley entropy $\hat{H}_{0,\text{naive}}$ is negatively biased. On the other hand, the traditional Box Counting Technique is based on this estimate. There we plot the logarithm of the covering element number $C(a) \in \mathbb{N}$ against the logarithm of the covering element size $a > 0$ and then estimate their dependency in the linear form $\ln C(a) = A_0 - \hat{D}_{0,\text{naive}} \ln a$. Recognizing equivalence $C(a) = K$ leads to $\ln C(a) = \ln K = \hat{H}_{0,\text{naive}}$ and then $\hat{H}_{0,\text{naive}} = A_0 - \hat{D}_{0,\text{naive}} \ln a$. Defining $\hat{D}_{0,\text{naive}}$ as an estimate of capacity dimension and recognizing the occurrence of $\hat{H}_{0,\text{naive}}$ in the Box Counting procedure [6], we are not surprised to be victims of the bias of Hartley entropy estimate.

A similar situation is the case of Shannon entropy estimation. There are several approaches how to decrease the bias of $\hat{H}_{1,\text{naive}}$ to be closer to a theoretical value of Shannon entropy H_1. Miller [4] modified the naive estimate $\hat{H}_{1,\text{naive}}$ using a first-order Taylor expansion resulting in

$$\hat{H}_{1,\text{M}} = \hat{H}_{1,\text{naive}} + \frac{K - 1}{2N}. \tag{6}$$

Lately, Harris [4] improved the formula to

$$\hat{H}_{1,\text{H}} = \hat{H}_{1,\text{naive}} + \frac{K - 1}{2N} - \frac{1}{12N^2} \left(1 - \sum_{p_j > 0} \frac{1}{p_j} \right). \tag{7}$$

Finally, we can estimate the capacity and information dimensions according to relation

$$\hat{H}_d = A_d - \hat{D}_d \ln a, \tag{8}$$

where $\hat{H}_d$ is any estimate of H_d. Therefore, we can also estimate Hausdorff dimension D_{H} using inequalities $D_1 \leq D_{\mathrm{H}} \leq D_0$ under the assumption that $\hat{D}_1 \leq D_{\mathrm{H}} \leq \hat{D}_0$ for any "good" estimates $\hat{D}_0$, $\hat{D}_1$ of capacity and information dimensions, respectively. The next section is oriented to Bayesian estimation of H_0 and H_1, which are essential for evaluating $\hat{D}_0$ and $\hat{D}_1$.

3   Bayesian Estimation of Hartley Entropy

We suppose Dirichlet distribution [5] of a random vector $\mathbf{p} = (p_1, ..., p_n)$ satisfying $p_j \geq 0$, $\sum_{j=1}^{n} p_j = 1$, with $\alpha_j = \alpha^* > 0$. Using properties of multinomial and its conjugate distribution — the Dirichlet distribution, we can calculate probability estimate $\hat{\mathrm{p}}(K|n, N)$ of the random variable $K \in \mathbb{N}$ for $K \leq \min(n, N)$ as

$$
\begin{aligned}
\hat{\mathrm{p}}(K \mid n, N) &= \mathrm{prob}\left(\sum_{N_j > 0} 1 = K \;\middle|\; n, \sum_{j=1}^{n} N_j = N \right) \\
&= \binom{n}{K} \frac{\Gamma(N+1)\Gamma(n\alpha^*)}{\Gamma(N + n\alpha^*)} \sum_{\vec{N} \in \mathbb{D}_{K,N}} \prod_{j=1}^{K} \frac{\Gamma(N_j + \alpha^*)}{\Gamma(N_j + 1)\Gamma(\alpha^*)}.
\end{aligned}
\tag{9}
$$

Derivation of (9) is included in the Appendix 8.1. When $N \geq K + 2$, we can calculate

$$S_{K,N} = \sum_{n=K}^{\infty} \hat{\mathrm{p}}\left(K \mid n, N \right). \tag{10}$$

When the number of events is constrained as $n \leq n_{\max}$, we apply an alternative formula

$$S_{K,N}^* = \sum_{n=K}^{n_{\max}} \hat{\mathrm{p}}\left(K \mid n, N \right). \tag{11}$$

Convergence of the infinite series (10) is proved in the Appendix 8.2. Having a knowledge of K, N where $N \geq K + 2$, we can calculate a Bayesian density

$$\hat{\mathrm{p}}\left(n \mid K, N \right) = \frac{\hat{\mathrm{p}}\left(K \mid n, N \right)}{S_{K,N}}, n \geq K \tag{12}$$

Thereafter, Bayesian estimate of Hartley entropy comes out as

$$
\begin{aligned}
\hat{H}_{0,\mathrm{Bayes}} = \mathrm{E} H_0 &= \sum_{n=K}^{\infty} \hat{\mathrm{p}}\left(n \mid K, N \right) \ln n = \sum_{n=K}^{\infty} \frac{\hat{\mathrm{p}}\left(K \mid n, N \right) \ln n}{S_{K,N}} \\
&= \frac{\sum_{n=K}^{\infty} \hat{\mathrm{p}}\left(K \mid n, N \right) \ln n}{\sum_{n=K}^{\infty} \hat{\mathrm{p}}\left(K \mid n, N \right)} > \ln K,
\end{aligned}
\tag{13}
$$

which is a convergent sum as well. We gain an equivalent formula by substituting $n = K + j$

$$\hat{H}_{0,\text{Bayes}} = \frac{\sum_{j=0}^{\infty} b_j \ln{(K+j)}}{\sum_{j=0}^{\infty} b_j}, \tag{14}$$

where

$$b_j = \binom{K+j}{j} \frac{\text{B}\left((K+j)\alpha^*, N\right)}{\text{B}\left(K\alpha^*, N\right)}. \tag{15}$$

Convergence of the sums in (13) is proved in Appendix 8.2. Particular coefficients b_j can also be generated recursively

$$
\begin{aligned}
b_0 &= 1 \\
b_j &= \frac{K+j}{j} \frac{\Gamma((K+j)\alpha^*)}{\Gamma((K+j)\alpha^* - \alpha^*)} \frac{\Gamma(N + (K+j)\alpha^* - \alpha^*)}{\Gamma(N + (K+j)\alpha^*)} b_{j-1} \\
b_j &= b_{j-1} \frac{K+j}{j} \prod_{u=0}^{N-1} \left(1 - \frac{\alpha^*}{(K+j)\alpha^* + u}\right).
\end{aligned}
\tag{16}
$$

4   Bayesian Estimation of Shannon Entropy

In the case when the number of events n is known, we perform Bayesian estimation of Shannon entropy for arbitrary $\alpha_j = \alpha^* > 0$ as

$$-\sum_{i=1}^{M} \frac{\Gamma(N+\alpha)}{\Gamma(n_i + \alpha_i)} \frac{\Gamma(n_i + \alpha_i + 1)}{\Gamma(N + \alpha + 1)} \left(\psi^{(0)}(n_i + \alpha_i + 1) - \psi^{(0)}(N + \alpha + 1)\right)$$

$$\hat{H}_{1,\text{n}} = \text{E}H_1(K=n) = -\sum_{j=1}^{n} \left(\frac{N_j + \alpha^*}{N + n\alpha^*} \left(\psi(N_j + \alpha^* + 1) - \psi(N + n\alpha^* + 1)\right)\right), \quad (17)$$

where ψ is digamma function. However, when the number of events n is unknown, we can use K as a lower estimate of n and perform the final Bayesian estimation as

$$\hat{H}_{1,\text{Bayes}} = \sum_{n=K}^{\infty} \text{p}\left(n \mid K, N\right) \hat{H}_{1,\text{n}}, \tag{18}$$

which is also a convergent sum for $N \geq K + 2$.

Substituting $n = K + j$, we obtain an adequate formula

$$\hat{H}_{1,\text{Bayes}} = \frac{\sum_{j=0}^{\infty} b_j \hat{H}_{1,K+j}}{\sum_{j=0}^{\infty} b_j}. \tag{19}$$

Unfortunately, asymptotic expansion of (19) depends on individual frequencies N_j. But $\hat{H}_{1,n} \leq \ln n$, hence $\hat{H}_{1,K+j} \leq \ln K + j$, which implies the convergence of $\sum_{j=0}^{\infty} b_j \hat{H}_{1,K+j}$ based on majority rule and (14).
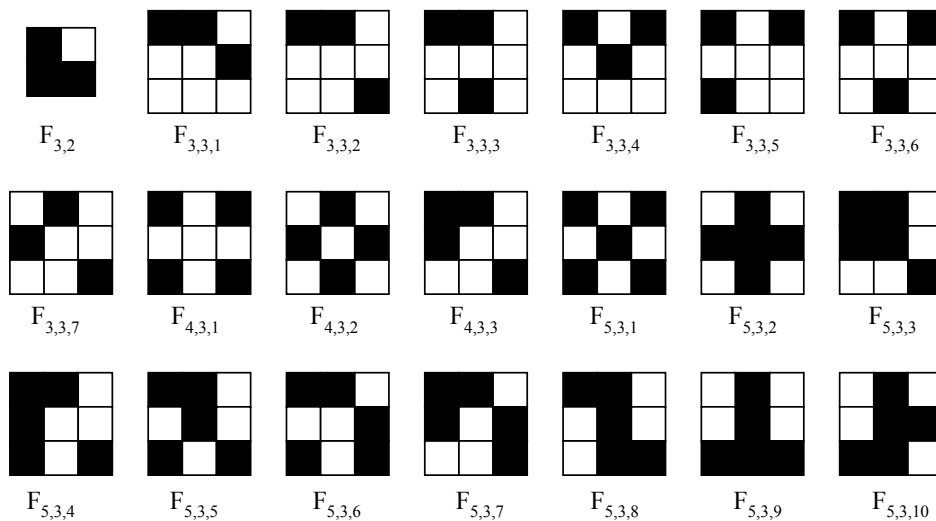
Figure 1: Table of the fractals involved in the research.

5 Revisited Box Counting Method

Let $\mathbb{F} \subset \mathbb{R}^m$ be a set of N points placed into m-dimensional rectangular grid of element size $a > 0$. Let $\hat{H}_{0,\mathrm{Bayes}}$ be an unbiased estimate of Hartley entropy H_0. Fitting the linear model

$$\hat{H}_{0,\mathrm{Bayes}} = A - \hat{D}_0 \ln a \tag{20}$$

via the method of least squares is called Revisited Box Counting.

Revisited Box Counting can be modified by using $\hat{H}_{1,\mathrm{Bayes}}$ instead of $\hat{H}_{0,\mathrm{Bayes}}$ which comes to estimation of information dimension [7] according to

$$\hat{H}_{1,\mathrm{Bayes}} = A - \hat{D}_1 \ln a. \tag{21}$$

6 Experimental Part

The Revisited Box Counting technique will be tested on models of deterministic self-similar 2D fractal sets. They are generated by recursive expansion of binary matrix $\mathbb{G}_{u,v} \in \{0,1\}^{v \times v}$, where u a is the number of non-zero elements (units), $v > 1$ is a matrix dimension, and $v < u < v^2$.

Recursive expansion of $\mathbb{G}_{u,v}$ generates a binary matrix which represents fractal set $\mathbb{F}_{u,v}$ of a similarity dimension $D_S = D_H = D_0 = D_1 = \frac{\log u}{\log v}$. Depth h of recursion depends on v and should be appropriate to computer memory size. The structures involved in the research are depicted in Fig. 1

At first, adequate point sets of given depth h were generated. Then, they were randomly rotated around the origin, and finally they were randomly shifted. Afterwards, a grid of size a was put on the data points and entropy estimates were calculated. Due to physical interpretation of entropy, the estimates were averaged over 20 realizations and mean
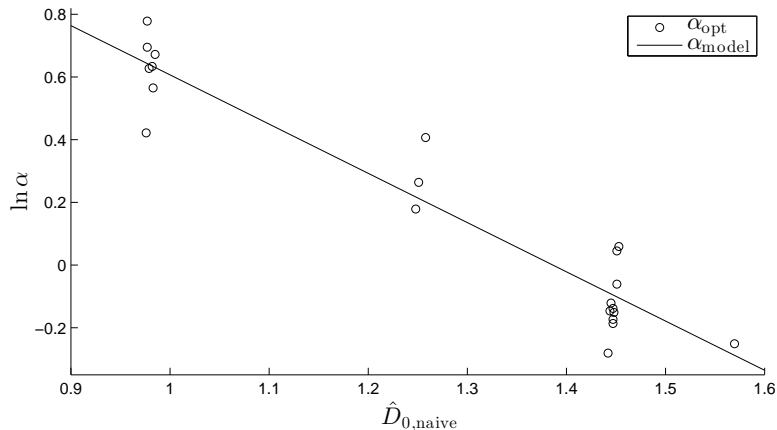
Figure 2: Optimum α values of exponential model and its linear regression.

values of entropy were calculated.

The relationship between $\hat{D}_{\text{naive}}$ and optimum value of α was studied on the aforementioned fractals for the grid of size $a = 12, 16, 20, ..., 480, 500$. The results of optimization are collected in Tab. 1. We suppose, the relationship can be approximated by linear, exponential, or power model respectively as

$$\alpha = A + B\hat{D}_{0,\text{naive}},$$
$$\ln \alpha = A + B\hat{D}_{0,\text{naive}},$$
$$\ln \alpha = A + B \ln \hat{D}_{0,\text{naive}}.$$

(22)

Linear regression was used for the estimation of unknown parameters A and B. The values are included in Tab. 2 together with correlation coefficient r. The exponential model had the best correlation and will be used for corrected estimation. But the differences among models are not statistically significant. Using exponential model, we calculated α_{model} from $\hat{D}_{0,\text{naive}}$, then recalculated $\hat{D}_0$, and tested hypothesis $H_0 : E\hat{D}_0 = D_0$ via two-sided t-test. The resulting values are also collected in Tab. 1 as $\hat{D}_0$ and p_{value}. In this case of multiple hypothesis testing we had to apply False Discovery Rate (FDR) [2] methodology on critical level $p_{crit} = 0.05$. We were not able to reject any hypotheses and therefore the improved $\hat{D}_0$ estimate was not biased in our experiments.

7   Conclusion

In this paper we developed the Bayesian estimator $\hat{H}_{0,\text{Bayes}}$ of Hartley entropy for Dirichlet prior. This estimate enables to estimate $\hat{D}_0$ with suppressed bias in comparison with naive box-counting estimate. The novel methodology is based on the box-counting estimate $\hat{D}_{0,\text{naive}}$ which helps to specify the Dirichlet prior and finally reestimate the capacity dimension. This procedure is recommended for 2D structures with $1 \leq \hat{D}_0 \leq 1.6$ and can be easily extended for information dimension D_1 estimation and higher dimensions.

Table 1: Optimum α values and their exponential model

Fractal	h	D_0	$\hat{D}_{0,\text{naive}}$	α_{opt}	α_{model}	p_{value}
$F_{3,2}$	11	1.585	1.567	0.778	0.749	0.392
$F_{3,3,1}$	7	1	0.982	1.885	1.886	0.995
$F_{3,3,2}$	7	1	0.977	2.178	1.901	0.131
$F_{3,3,3}$	7	1	0.977	2.004	1.901	0.667
$F_{3,3,4}$	7	1	0.985	1.958	1.878	0.743
$F_{3,3,5}$	7	1	0.976	1.525	1.904	0.129
$F_{3,3,6}$	7	1	0.983	1.760	1.883	0.698
$F_{3,3,7}$	7	1	0.979	1.873	1.895	0.929
$F_{4,3,1}$	7	1.262	1.251	1.302	1.236	0.789
$F_{4,3,2}$	7	1.262	1.248	1.196	1.242	0.850
$F_{4,3,3}$	7	1.262	1.258	1.502	1.223	0.283
$F_{5,3,1}$	7	1.465	1.447	0.871	0.908	0.653
$F_{5,3,2}$	7	1.465	1.447	0.830	0.908	0.427
$F_{5,3,3}$	7	1.465	1.451	0.941	0.903	0.544
$F_{5,3,4}$	7	1.465	1.445	0.886	0.911	0.720
$F_{5,3,5}$	7	1.465	1.444	0.864	0.913	0.367
$F_{5,3,6}$	7	1.465	1.451	1.046	0.903	0.185
$F_{5,3,7}$	7	1.465	1.453	1.061	0.900	0.019
$F_{5,3,8}$	7	1.465	1.447	0.841	0.908	0.122
$F_{5,3,9}$	7	1.465	1.442	0.755	0.916	0.009
$F_{5,3,10}$	7	1.465	1.448	0.860	0.907	0.186

Table 2: Comparison of the models fitting the relationship between $\hat{D}_{0,\text{naive}}$ and α

model	A	B	r
linear	3.905	-2.066	-0.9542
exponential	2.178	-1.571	-0.9553
power	0.605	-1.892	-0.9524

References

[1] G. L. Baker and J. B. Gollub. *Chaotic Dynamics: An Introduction, 2nd ed.* Cambridge University Press (1996).

[2] Y. Benjamini and D. Yekutieli. *The control of the false discovery rate in multiple testing under dependency.* The Annals of Statistics (2001), 29(4), 1165–1188.

[3] T. J. Bromwich and T. M. MacRobert. *An Introduction to the Theory of Infinite Series, 3rd ed.* Chelsea (1991).

[4] B. Harris. *The statistical estimation of entropy in the non-parametric case.* MRC Technical Summary Report, 1975.

[5] S. Kotz, N. Balakrishnan, and N. L. Johnson. *Continuous Multivariate Distributions. Volume 1: Models and Applications.* Wiley (2000).

[6] B. B. Mandelbrot. *The Fractal Geometry of Nature.* W.H. Freeman and Company (1982).

[7] E. Ott. *Chaos in Dynamical Systems.* Cambridge University Press (1993).

[8] A. Renyi. *On measures of entropy and information.* In 'Proc. Fourth Berkeley Symp. Math. Stat. Prob., Vol. 1', University of California Press (Berkeley, 1961), 547–561.

[9] J. Wendel. *Note on the gamma function.* In 'Amer. Math. Monthly **55** (1948)', 563–564.

8   Appendix

8.1   Derivation of $\hat{\mathrm{p}}(K|n,N)$ in (9)

Let $\mathbb{Q}_n = \{\vec{q} \in (\mathbb{R}_0^+)^n | \sum_{j=1}^n q_j = 1\}$ be a support set of a Dirichlet-distributed random variable $\vec{p} \in \mathbb{Q}_n$ with parameters α_j, for $j = 1,...,n$. The conditional probability of an integer K satisfying $1 \leq K \leq \min(n,N)$ is

$$\mathrm{p}(K \mid n, N) = \mathrm{prob}\left(\sum_{N_j > 0} 1 = K \,\middle|\, n, \sum_{j=1}^n N_j = N\right). \tag{23}$$

The vector of N_j can be reorganized to begin with positive values:

$$\mathrm{p}(K \mid n, N) = \binom{n}{K}\mathrm{prob}\left(\forall j = 1,...,n : N_j > 0 \Leftrightarrow j \leq K \,\middle|\, n, \sum_{j=1}^K N_j = N\right). \tag{24}$$

Let $\mathbb{D}_{K,N} = \{\vec{x} \in \mathbb{N}^K | \sum_{j=1}^K x_j = N\}$ be the domain of $\vec{N} = (N_1,...,N_K) \in \mathbb{D}_{K,N}$. Using the mean value of a multinomial distribution over $\mathbb{Q}_n$, we obtain an unbiased estimate of

$p(K \mid n, N)$ as

$$
\begin{aligned}
\hat{p}(K \mid n, N) &= \binom{n}{K} E \left(\sum_{\vec{N} \in \mathbb{D}_{K,N}} \binom{N}{N_1, ..., N_K} \prod_{j=1}^{K} p_j^{N_j} \prod_{j=k+1}^{n} p_j^0 \right) \\
&= \binom{n}{K} \sum_{\vec{N} \in \mathbb{D}_{K,N}} \binom{N}{N_1, ..., N_K} E \left(\prod_{j=1}^{K} p_j^{N_j} \right).
\end{aligned}
\tag{25}
$$

Using the generalized Beta function

$$
B(\vec{x}) = \int_{\vec{p} \in \mathbb{Q}_m} \prod_{j=1}^{m} p_j^{x_j - 1} \mathrm{d}\vec{p} = \frac{\prod_{j=1}^{m} \Gamma(x_j)}{\Gamma(\sum_{j=1}^{m} x_j)},
\tag{26}
$$

we can calculate

$$
\begin{aligned}
E \left(\prod_{j=1}^{K} p_j^{N_j} \right) &= \frac{\int_{\vec{p} \in \mathbb{Q}_n} B(\vec{\alpha})^{-1} \prod_{j=1}^{K} p_j^{N_j + \alpha_j - 1} \prod_{j=K+1}^{n} p_j^{\alpha_j - 1} \mathrm{d}\vec{p}}{\int_{\vec{p} \in \mathbb{Q}_n} B(\vec{\alpha})^{-1} \prod_{j=1}^{n} p_j^{\alpha_j - 1} \mathrm{d}\vec{p}} \\
&= \frac{\Gamma(\alpha)}{\Gamma(N + \alpha)} \prod_{j=1}^{K} \frac{\Gamma(N_j + \alpha_j)}{\Gamma(\alpha_j)},
\end{aligned}
\tag{27}
$$

where α is the sum of all α_j. Therefore,

$$
\begin{aligned}
\hat{p}(K \mid n, N) &= \binom{n}{K} \sum_{\vec{N} \in \mathbb{D}_{K,N}} \frac{N!}{\prod_{j=1}^{K} N_j!} \frac{\Gamma(\alpha)}{\Gamma(N + \alpha)} \frac{\prod_{j=1}^{K} \Gamma(N_j + \alpha_j)}{\prod_{j=1}^{K} \Gamma(\alpha_j)} \\
&= \binom{n}{K} \frac{\Gamma(N+1)\Gamma(\alpha)}{\Gamma(N + \alpha)} \sum_{\vec{N} \in \mathbb{D}_{K,N}} \prod_{j=1}^{K} \frac{\Gamma(N_j + \alpha_j)}{\Gamma(N_j + 1)\Gamma(\alpha_j)}
\end{aligned}
\tag{28}
$$

In this particular paper, we assume $\alpha_j = \alpha^*, \forall j = 1, ..., n$ which results in a simpler form of Equation 28

$$
\hat{p}(K \mid n, N) = \binom{n}{K} \frac{\Gamma(N+1)\Gamma(n\alpha^*)}{\Gamma(N + n\alpha^*)} \sum_{\vec{N} \in \mathbb{D}_{K,N}} \prod_{j=1}^{K} \frac{\Gamma(N_j + \alpha^*)}{\Gamma(N_j + 1)\Gamma(\alpha^*)}.
\tag{29}
$$

8.2 Convergence of $\sum_{j=0}^{\infty} b_j \ln(K + j)$ in (14) and $\sum_{j=0}^{\infty} b_j$ in (10)

The ratio of coefficients b_j could be expressed as:

$$
\begin{aligned}
q_j &= \frac{b_j}{b_{j-1}} \frac{\ln(K + j)}{\ln(K + j - 1)} \\
&= \frac{(K + j)}{j} \frac{\ln(K + j)}{\ln(K + j - 1)} \frac{\Gamma((K + j)\alpha^*)}{\Gamma((K + j - 1)\alpha^*)} \frac{\Gamma(N + (K + j - 1)\alpha^*)}{\Gamma(N + (K + j)\alpha^*)}.
\end{aligned}
\tag{30}
$$

Starting with inequality proved by Wendel [9]:

$$\forall d \in [0; 1], \forall x > 0 : \frac{\Gamma(x + d)}{\Gamma(x)} \le x^d; \tag{31}$$

that can be generalized for $\delta = D + d$ where $D \in \mathbb{N}_0, d \in [0; 1)$ as

$$\frac{\Gamma(x + \delta)}{\Gamma(x)} \le x^d \prod_{i=0}^{D-1} (x + i + d). \tag{32}$$

We should see the similarity between $\alpha^* = A + a$, where $A \in \mathbb{N}_0, a \in [0; 1)$, and δ leading to

$$\begin{aligned}
q_j &= \frac{b_j}{b_{j-1}} \frac{\ln(K + j)}{\ln(K + j - 1)} \\
&\le \frac{K + j}{j} \frac{\ln(K + j)}{\ln(K + j - 1)} \left(\frac{(K + j - 1)\alpha^*}{(K + j - 1)\alpha^* + N} \right)^a \cdot \prod_{i=0}^{A-1} \frac{(K + j - 1)\alpha^* + i + a}{(K + j - 1)\alpha^* + i + a + N}
\end{aligned} \tag{33}$$

$$\begin{aligned}
q_j &= \frac{b_j}{b_{j-1}} \frac{\ln(K + j)}{\ln(K + j - 1)} \\
&\le \frac{K + j}{j} \frac{\ln(K + j)}{\ln(K + j - 1)} \left(\frac{(K + j - 1)\alpha^*}{(K + j - 1)\alpha^* + N} \right)^a
\end{aligned} \tag{34}$$

The Raabe criterion [3] will state series of positive members $\sum_{n=0}^{\infty} a_n$ as convergent if exists $L = \lim_{n \to \infty} n \left(\frac{a_n}{a_{n+1}} - 1 \right)$ satisfying $L > 1$. Then we can calculate

$$\begin{aligned}
L &= \lim_{j \to \infty} j \left(\frac{b_{j-1}}{b_j} \frac{\ln(K + j - 1)}{\ln(K + j)} - 1 \right) \\
&\ge \lim_{j \to \infty} j \left(\frac{j}{K + j} \frac{\ln(K + j - 1)}{\ln(K + j)} \left(\frac{(K + j - 1)\alpha^* + N}{(K + j - 1)\alpha^*} \right)^a - 1 \right).
\end{aligned} \tag{35}$$

Substitution $x = K + j$ leads to

$$L = \lim_{x \to \infty} (x - K) \left(\frac{x - K}{x} \frac{\ln(x - 1)}{\ln(x)} \left(\frac{(x - 1)\alpha^* + N}{(x - 1)\alpha^*} \right)^a - 1 \right), \tag{36}$$

and finally

$$L = -K + \lim_{x \to \infty} \left(x \left(1 + \frac{N - \alpha^*}{x\alpha^*} \right)^a - x \left(1 - \frac{1}{x} \right)^a \right). \tag{37}$$

Substituting $h = x^{-1} \to 0^+$ and applying l'Hospital rule, we obtain

$$L = -K + \lim_{h \to 0^+} \frac{\left(1 + \frac{N - \alpha^*}{\alpha^*} h \right)^a - (1 - h)^a}{h} = N - K. \tag{38}$$

Thus the series $\sum_{j=0}^{\infty} b_j \ln(K + j)$ converges absolutely for $K \le N - 2$ because $L = N - K > 1$. According to majority rule, the series $\sum_{j=0}^{\infty} b_j = \sum_{n=K}^{\infty} \hat{\mathrm{p}}(K \mid n, N)$ converges as well.

Discrete Multivariate (Anti)Symmetric Trigonometric Transforms[*]

Brus Adam

2nd year of PGS, email: `brusadam@fjfi.cvut.cz`
Department of Physics
Faculty of Nuclear Sciences and Physical Engineering, CTU in Prague

advisor: Jiří Hrivnák, Department of Physics
Faculty of Nuclear Sciences and Physical Engineering, CTU in Prague

Abstract. The set of discrete trigonometric transforms, which correspond to the antisymmetric and symmetric multivariate trigonometric functions, is extended. The multivariate discrete trigonometric transforms are derived using the standard one-dimensional variants of discrete cosine and sine transforms. The resulting generalized transforms are then used to derive interpolation formulas for interpolation by multivariate trigonometric functions. The obtained interpolation methods are then tested on a given model function.

Keywords: Discrete trigonometric transforms, Multivariate trigonometric functions, Interpolation

Abstrakt. Soubor diskrétních trigonometrických transformací, které odpovídají antisymetrickým a symetrickým trigonometrickým funkcím více proměnných je rozšířen. Diskrétní trigonometrické transformace více proměnných jsou odvozeny za užití jednodimensionálních variant diskrétních kosinových a sinových transformací. Výsledné zobecnění je poté užito k odvození interpolačních formulí pro interpolaci za užití trigonometrických funkcí více proměnných. Získané interpolační metody jsou následně testovány na zvolené modelové funkci.

Klíčová slova: Diskrétní trigonometrické transformace, Trigonometrické funkce více proměnných, Interpolace

1 Introduction

The aim of this paper is to summarize and extend the knowledge of antisymmetric and symmetric generalizations of trigonometric functions of one variable [5]. There exist eight discrete cosine transforms (DCTs) and eight discrete sine transforms (DSTs) based on various boundary conditions [1]. Each of these transforms can be generalized using antisymmetric or symmetric multivariate trigonometric functions [5]. First four DCTs and first DST were generalized in [5], the following four DCTs in [2]. The example of generalization of the remaining DSTs is shown, then the antisymmetric multivariate discrete sine transforms (AMDSTs) and the symmetric multivariate discrete sine transforms (SMDSTs) are used to derive interpolation formulas.

The DCTs and DSTs are naturally obtained as discretized solution of undamped harmonic oscillator equation with certain homogeneous boundary conditions [1]. These

---

13

transforms can be generalized using antisymmetric and symmetric multivariate trigono-
metric functions, which are introduced as determinants and permanents of matrices,
whose entries are trigonometric functions of one variable [1]. The case for dimension
$n = 2$, is investigated in [3], [4]. These functions have some remarkable properties such as
discrete orthogonality, which lead to Fourier-like transforms. This orthogonality is con-
sequence of DCTs, DSTs and their Cartesian product generalizations. There exist eight
different types DCTs and eight different types DSTs, the first four of DCTs and first DST
are generalized into their multivariate variants in [5]. The generalization of DCTs V-VIII
can be found in [2]. The remaining discrete sine transforms have to be generalized into
antisymmetric and symmetric multivariate sine transforms. The full set of 32 transforms
can then be used for applications, i.e. interpolation methods.

Due to the properties of antisymmetric and symmetric trigonometric functions, we
can restrict these functions to their fundamental domains, certain subset of $\mathbb{R}^n$. Using
properties of these functions one can map any point of $\mathbb{R}^n$ to a point inside fundamental
domain with same value of given function. Interpolation of functions defined on funda-
mental domain can be done directly. For functions defined in $\mathbb{R}^n$ the fundamental domain
is mapped into $\mathbb{R}^n$ using extended symmetry group and then interpolated for each block
independently. The resulting coefficients can be further analyzed in multidimensional
analogue of image recognition [8] and reversible data hiding [7] This interpolation method
can be applied to any model function, but more the given function satisfies antisymmetry
resp. symmetry and boundary conditions of discrete trigonometric transforms, the more
suitable is the method.

2   Discrete trigonometric transforms

The one-dimensional Discrete Trigonometric transforms, which have many applica-
tions in various parts of mathematics and physics, arise naturally from dicretized solution
of harmonic oscillator equation with different choices of boundary conditions applied at
grid or mid-grid points [1]. The Neumann boundary condition applied at point $x = 0$
with various conditions applied at grid or mid-grid points will produce eight different
DCTs. By replacing the Neumann boundary condition at $x = 0$ by Dirichlet condition
the DSTs are generated. This again lead to eight DSTs, each with different combination
of boundary conditions applied at grid or mid-grid points.

2.1   Discrete Cosine Transforms

DCTs are obtained using the Neumann condition at $x = 0$, by applying additional
conditions at grid or mid-grid we obtain each DCT. For example by applying Neumann
conditions at points $x = 0$ at $l = \frac{1}{2}$ using mid-grid and $x = \pi$ at $l = N - 1$ using grid
points we obtain DCT-VI in following form.

For $N \in \mathbb{N}$ are cosine functions $\cos{(\pi k s)}, k = 0, 1, \ldots, N - 1$, defined on finite grid

$$s \in \left\{ \frac{2\left(r + \frac{1}{2}\right)}{2N - 1} \mid r = 0, 1, \ldots, N - 1 \right\}, \tag{1}$$

pairwise discretely orthogonal,

$$\sum_{r=0}^{N-1} c_{r-1} \cos\left(\frac{2\pi k\left(r+\frac{1}{2}\right)}{2N-1}\right) \cos\left(\frac{2\pi k'\left(r+\frac{1}{2}\right)}{2N-1}\right) = \frac{2N-1}{4c_k}\delta_{kk'}, \qquad (2)$$

where constant

$$c_r = \begin{cases} \frac{1}{2} & \text{if } r = 0 \text{ or } r = N, \\ 1 & \text{otherwise.} \end{cases} \qquad (3)$$

Therefore any discrete function f given on grid (1) is expressed in terms of cosine functions as

$$f(s) = \sum_{k=0}^{N-1} A_k \cos(\pi k s), \ \ A_k = \frac{4c_k}{2N-1}\sum_{r=0}^{N-1} c_{r-1} f\left(\frac{2\left(r+\frac{1}{2}\right)}{2N-1}\right)\cos\left(\frac{2\pi k\left(r+\frac{1}{2}\right)}{2N-1}\right). \quad (4)$$

2.2 Discrete Sine Transforms

To generate the DSTs we replace the Neumann condition at $x = 0$ with a Dirichlet condition. In exactly same way by applying different boundary conditions applied at grid or mid-grid points we obtain eight different DSTs. For example by applying Dirichlet boundary condition applied at grid and mid-grid points we obtain DST-VI in following form.

For $N \in \mathbb{N}$ are sine functions $\sin(\pi k s)$, $k = 1, 2, \ldots, N-1$, defined on finite grid

$$s \in \left\{ \frac{2\left(r+\frac{1}{2}\right)}{2N-1} \mid r = 0, 1, \ldots, N-2 \right\}, \qquad (5)$$

pairwise discretely orthogonal,

$$\sum_{r=0}^{N-2} \sin\left(\frac{2\pi k\left(r+\frac{1}{2}\right)}{2N-1}\right)\sin\left(\frac{2\pi k'\left(r+\frac{1}{2}\right)}{2N-1}\right) = \frac{2N-1}{4}\delta_{kk'}. \qquad (6)$$

Due to this relation any discrete function f given on grid (5) can be expressed in terms of sine functions as

$$f(s) = \sum_{k=1}^{N-1} A_k \sin(\pi k s), \ \ A_k = \frac{4}{2N-1}\sum_{r=1}^{N-1} f\left(\frac{2\left(r+\frac{1}{2}\right)}{2N-1}\right)\sin\left(\frac{2\pi k\left(r+\frac{1}{2}\right)}{2N-1}\right). \quad (7)$$

The remaining discrete trigonometric transforms are be obtained in similar way.

3 Multivariate trigonometric functions

The symmetric and antisymmetric multivariate generalizations of trigonometric functions are defined and their properties detailed in [5]. The antisymmetric trigonometric

functions $\cos_\lambda^-(x)$, $\sin_\lambda^-(x)$ and symmetric trigonometric functions $\cos_\lambda^+(x)$, $\sin_\lambda^+(x)$ of variable $x = (x_1, \ldots, x_n) \in \mathbb{R}^n$ with parameter $\lambda = (\lambda_1, \ldots, \lambda_n)$ are defined as determinants and permanents of matrices with entries $\cos(\pi\lambda_i x_j)$ resp. $\sin(\pi\lambda_i x_j)$, i.e.

$$
\begin{aligned}
\cos_\lambda^-(x) &= \sum_{\sigma \in S_n} \operatorname{sgn}(\sigma) \cos(\pi\lambda_{\sigma_1} x_1) \cos(\pi\lambda_{\sigma_2} x_2) \cdots \cos(\pi\lambda_{\sigma_n} x_n), \\
\sin_\lambda^-(x) &= \sum_{\sigma \in S_n} \operatorname{sgn}(\sigma) \sin(\pi\lambda_{\sigma_1} x_1) \sin(\pi\lambda_{\sigma_2} x_2) \cdots \sin(\pi\lambda_{\sigma_n} x_n),
\end{aligned}
\tag{8}
$$

for the antisymmetric trigonometric functions and

$$
\begin{aligned}
\cos_\lambda^+(x) &= \sum_{\sigma \in S_n} \cos(\pi\lambda_{\sigma_1} x_1) \cos(\pi\lambda_{\sigma_2} x_2) \cdots \cos(\pi\lambda_{\sigma_n} x_n), \\
\sin_\lambda^+(x) &= \sum_{\sigma \in S_n} \sin(\pi\lambda_{\sigma_1} x_1) \sin(\pi\lambda_{\sigma_2} x_2) \cdots \sin(\pi\lambda_{\sigma_n} x_n),
\end{aligned}
\tag{9}
$$

for the symmetric trigonometric functions.

For further applications we will only consider functions $\cos_k^\pm(x)$ and $\sin_k^\pm(x)$ with integer parameter only, $k \in \mathbb{Z}^n$ and denoting

$$
\rho = \left(\frac{1}{2}, \ldots, \frac{1}{2} \right).
\tag{10}
$$

These functions due to properties of determinant, permanent and trigonometric functions can be considered only on closure of the fundamental domain $F(\widetilde{S}_n^{\mathrm{aff}})$ of the form

$$
F(\widetilde{S}_n^{\mathrm{aff}}) = \left\{ (x_1, x_2, \ldots, x_n) \in \mathbb{R}^n \mid 1 \geq x_1 \geq x_2 \geq \ldots \geq x_n \geq 0 \right\}.
\tag{11}
$$

Due to additional properties we can omit boundaries

- $x_i = x_{i+1}, i \in \{1, \ldots, n-1\}$ for $\cos_k^-(x)$ and $\sin_k^-(x)$,

- $x_i = x_{i+1}, i \in \{1, \ldots, n-1\}$ or $x_1 = 1$ for $\cos_{k+\rho}^-(x)$ and $\sin_{k+\rho}^-(x)$,

- $x_i = 1, i \in \{1, \ldots, n\}$ for $\cos_{k+\rho}^+(x)$ and $\sin_{k+\rho}^+(x)$.

In addition the functions are non-zero in interior of their corresponding fundamental domains.

4   Discrete Multivariate Trigonometric transforms

Discrete multivariate trigonometric transforms can be viewed as generalizations of discrete trigonometric transforms using multivariate trigonometric functions. Each of DCTs resp. and DSTs can be generalized using symmetric or antisymmetric multivariate version of cosine resp. sine functions. Denominated as antisymmetric multivariate discrete cosine transforms (AMDCTs) resp. symmetric multivariate discrete cosine functions (SMDCTs) for antisymmetric resp. symmetric generalization of DCTs, and antisymmetric multivariate discrete sine transforms (AMDSTs) resp. symmetric multivariate discrete sine functions (SMDSTs) for antisymmetric resp. symmetric generalization of DSTs.

4.1 AMDCT VI

Let us now consider antisymmetric generalization of DCT VI. For $N \in \mathbb{N}$ we consider function $\cos_k^-(s)$ with parameter $k \in D_N^-$

$$D_N^- \equiv \{(k_1, \ldots, k_n) \mid N - 1 > k_1 > k_2 > \ldots > k_n > 0\}, \tag{12}$$

restricted to finite set of points

$$F_N^{VI,-} \equiv \left\{ \left(\frac{2\left(r_1 + \frac{1}{2}\right)}{2N - 1}, \ldots, \frac{2\left(r_n + \frac{1}{2}\right)}{2N - 1} \right) \mid (r_1, \ldots, r_n) \in D_N^- \right\}. \tag{13}$$

The antisymmetric cosine functions labeled by parameters $k, k' \in D_N^-$ are pairwise orthogonal on the grid $F_N^{VI,-}$, i.e.,

$$\sum_{s \in F_N^{VI,-}} \widetilde{\varepsilon}_s \cos_k^-(s) \cos_{k'}^-(s) = d_k^{-1} \left(\frac{2N - 1}{4} \right)^n \delta_{kk'}, \tag{14}$$

where

$$\begin{aligned} \widetilde{\varepsilon}_s &= c_{r_1+1} c_{r_2+1} \cdots c_{r_n+1}, \\ d_k &= c_{k_1} c_{k_2} \cdots c_{k_n}. \end{aligned} \tag{15}$$

Due to this relation, any function $f : F_N^{VI,-} \mapsto \mathbb{R}$ can be expanded into terms of antisymmetric multivariate cosine functions as

$$f(s) = \sum_{k \in D_N^-} A_k \cos_k^-(s), \ \ A_k = d_k \left(\frac{4}{2N - 1} \right)^n \sum_{s \in F_N^{VI,-}} \widetilde{\varepsilon}_s f(s) \cos_k^-(s). \tag{16}$$

4.2 SMDCT VI

For symmetric generalization of DCT VI we consider $N \in \mathbb{N}$ and function $\cos_k^+(s)$ with parameter $k \in D_N^+$

$$D_N^+ \equiv \{(k_1, \ldots, k_n) \mid N - 1 \geq k_1 \geq k_2 \geq \ldots \geq k_n \geq 0\}, \tag{17}$$

on fixed set of points

$$F_N^{VI,+} \equiv \left\{ \left(\frac{2\left(r_1 + \frac{1}{2}\right)}{2N - 1}, \ldots, \frac{2\left(r_n + \frac{1}{2}\right)}{2N - 1} \right) \mid (r_1, \ldots, r_n) \in D_N^+ \right\}. \tag{18}$$

The symmetric multivariate sine functions labeled by parameters in $k, k' \in D_N^-$, are pairwise discretely orthogonal

$$\sum_{s \in F_N^{VI,+}} \widetilde{\varepsilon}_s H_s^{-1} \cos_k^-(s) \cos_{k'}^-(s) = \frac{H_k}{d_k} \left(\frac{2N - 1}{4} \right)^n \delta_{kk'}, \tag{19}$$

where H_k is number of permutations, which stabilize point $k \in D_N^+$

$$H_k = \# \{\sigma k = k \mid \sigma \in S_N\}. \tag{20}$$

Therefore we expand any function $f : F_N^{VI,+} \mapsto \mathbb{R}$ into terms of symmetric multivariate cosine functions as follows:

$$f(s) = \sum_{k \in D_N^+} A_k \cos_k^-(s), \ A_k = \frac{d_k}{H_k} \left(\frac{4}{2N-1}\right)^n \sum_{s \in F_N^{VI,+}} \widetilde{\varepsilon}_s H_s^{-1} f(s) \cos_k^-(s). \tag{21}$$

4.3   AMDST VI

For $N \in \mathbb{N}$ we consider the antisymmetric sine function $\sin_k^-(s)$ labeled by index set $k \in \widetilde{D}_N^-$ and restricted to finite grid of points $F_{N-1}^{VI,-}$.

$$\widetilde{D}_N^- \equiv \{(k_1, \ldots, k_n) \mid N - 1 > k_1 > k_2 > \ldots > k_n > 1\}. \tag{22}$$

The antisymmetric multivariate sine functions labeled by parameters $k, k' \in \widetilde{D}_N^-$ are then pairwise orthogonal,

$$\sum_{s \in F_{N-1}^{VI,-}} \sin_k^-(s) \sin_{k'}^-(s) = \left(\frac{2N-1}{4}\right)^n \delta_{kk'}. \tag{23}$$

Therefore any function $f : F_{N-1}^{VI,-} \mapsto \mathbb{R}$ can be expanded into terms of antisymmetric multivariate sine functions as

$$f(s) = \sum_{k \in \widetilde{D}_N^-} A_k \sin_k^-(s), \ A_k = \left(\frac{4}{2N-1}\right)^n \sum_{s \in F_{N-1}^{VI,-}} f(s) \sin_k^-(s). \tag{24}$$

4.4   SMDST VI

For symmetric generalization of DST VI, let us consider $N \in \mathbb{N}$ and $\sin_k^+(s)$ labeled by index set $k \in \widetilde{D}_N^+$, restricted to finite set of points $F_{N-1}^{VI,+}$.

$$\widetilde{D}_N^+ \equiv \{(k_1, \ldots, k_n) \mid N - 1 \geq k_1 \geq k_2 \geq \ldots \geq k_n \geq 1\}. \tag{25}$$

The functions labeled by $k, k' \in D_{N-1}^+$ are pairwise orthogonal,

$$\sum_{s \in F_{N-1}^{VI,+}} H_s^{-1} \sin_k^+(s) \sin_{k'}^+(s) = \left(\frac{2N-1}{4}\right)^n \delta_{kk'}, \tag{26}$$

which lead to transformation formulas, which can be applied to any function $f : F_{N-1}^{VI,+} \mapsto \mathbb{R}$ to expand it in terms of symmetric multivariate sine functions,

$$f(s) = \sum_{k \in \widetilde{D}_N^+} A_k \sin_k^+(s), \ A_k = H_k^{-1} \left(\frac{4}{2N-1}\right)^n \sum_{s \in F_{N-1}^{VI,+}} H_s^{-1} f(s) \sin_k^+(s). \tag{27}$$

The formulas for other AMDCTs, SMDCTs, AMDSTs or SMDSTs can be obtained by similar way from their one-dimensional versions

5 Interpolation by Multivariate Discrete trigonometric functions

Let f be real-valued function given on set $F(\widetilde{S}_\eta^{\text{aff}})$. In previous section we introduced transformations for functions defined on grids $F_N^{VI,-}$ and $F_N^{VI,+}$. We are looking for interpolation polynomial of f in form of corresponding trigonometric functions labeled by parameter k, in such a way that the value of function f is equal to value of interpolation function on corresponding grid. The interpolation formulas for multivariate DCT VI and DST VI with corresponding constants A_k follows.

5.0.1 Interpolation by AMDCT VI

$$\psi_N^{VI,-}(x) = \sum_{k \in D_N^-} A_k \cos_k^-(x), \ \psi_N^{VI,-}(s) = f(s), \ s \in F_N^{VI,-}, \tag{28}$$

5.0.2 Interpolation by SMDCT VI

$$\psi_N^{VI,+}(x) = \sum_{k \in D_N^+} A_k \cos_k^+(x), \ \psi_N^{VI,+}(s) = f(s), \ s \in F_N^{VI,+}, \tag{29}$$

5.0.3 Interpolation by AMDST VI

$$\phi_{N-1}^{VI,-}(x) = \sum_{k \in \widetilde{D}_N^-} A_k \sin_k^-(x), \ \phi_{N-1}^{VI,-}(s) = f(s), \ s \in F_{N-1}^{VI,-}, \tag{30}$$

5.0.4 Interpolation by SMDST VI

$$\phi_{N-1}^{VI,+}(x) = \sum_{k \in \widetilde{D}_N^+} A_k \sin_k^+(x), \ \phi_{N-1}^{VI,+}(s) = f(s), \ s \in F_{N-1}^{VI,+}. \tag{31}$$

5.1 Example of Interpolation

For $n = 3$ let us consider model function

$$
\begin{aligned}
f(x,y,z) = &\exp\left(\frac{(x-0,7)^2 + (y-0,5)^2 + (z-0,15)^2}{0,005} + 3\right) \\
&+ \frac{1}{3}\exp\left(\frac{(x-0,87)^2 + (y-0,7)^2 + (z-0,15)^2}{0,005} + 3\right),
\end{aligned}
\tag{32}
$$

and interpolate it by $\phi_{N-1}^{VI,-}(x,y,z)$ and $\phi_{N-1}^{VI,+}(x,y,z)$.
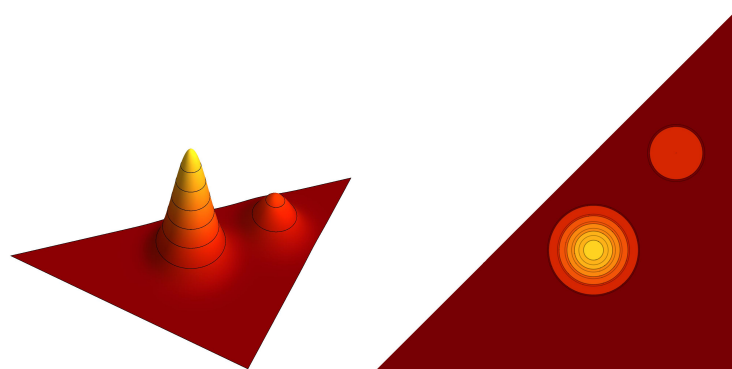
Figure.1. The cut of model function for $z = \frac{1}{4}$.
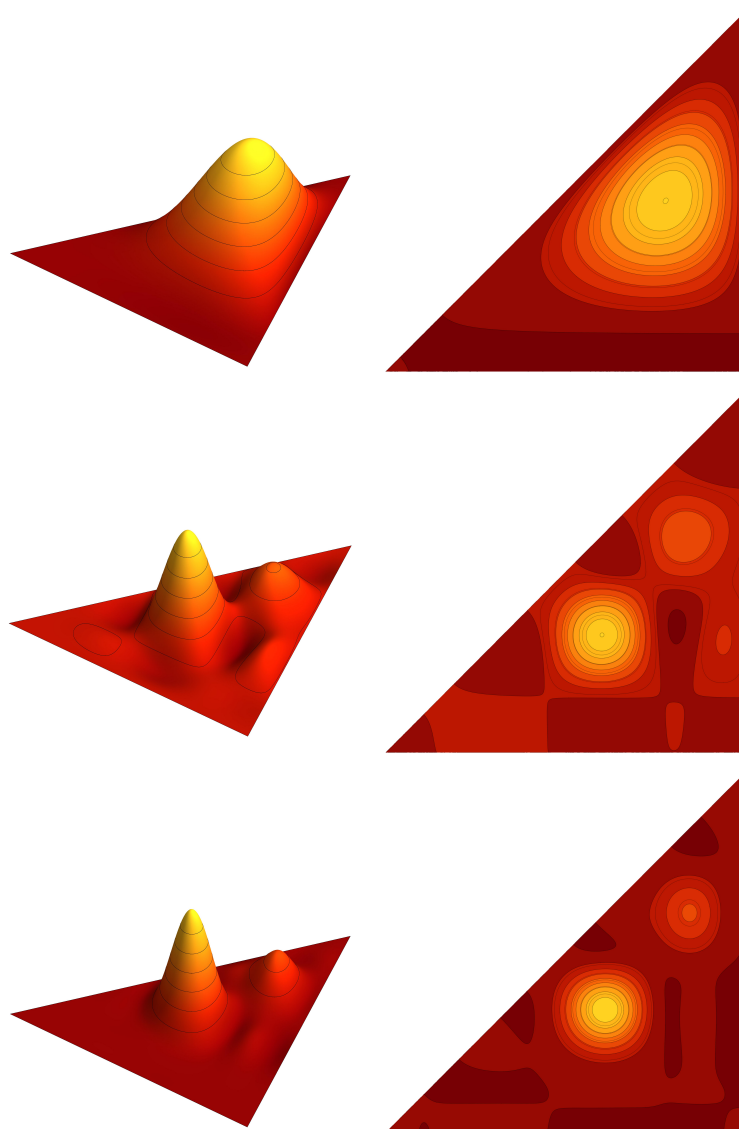
Figure.2. The antisymmetric sine interpolation polynomial $\phi_{N-1}^{VI,-}(x, y, \frac{1}{4})$ for model function with $N = 5, 10, 15$.
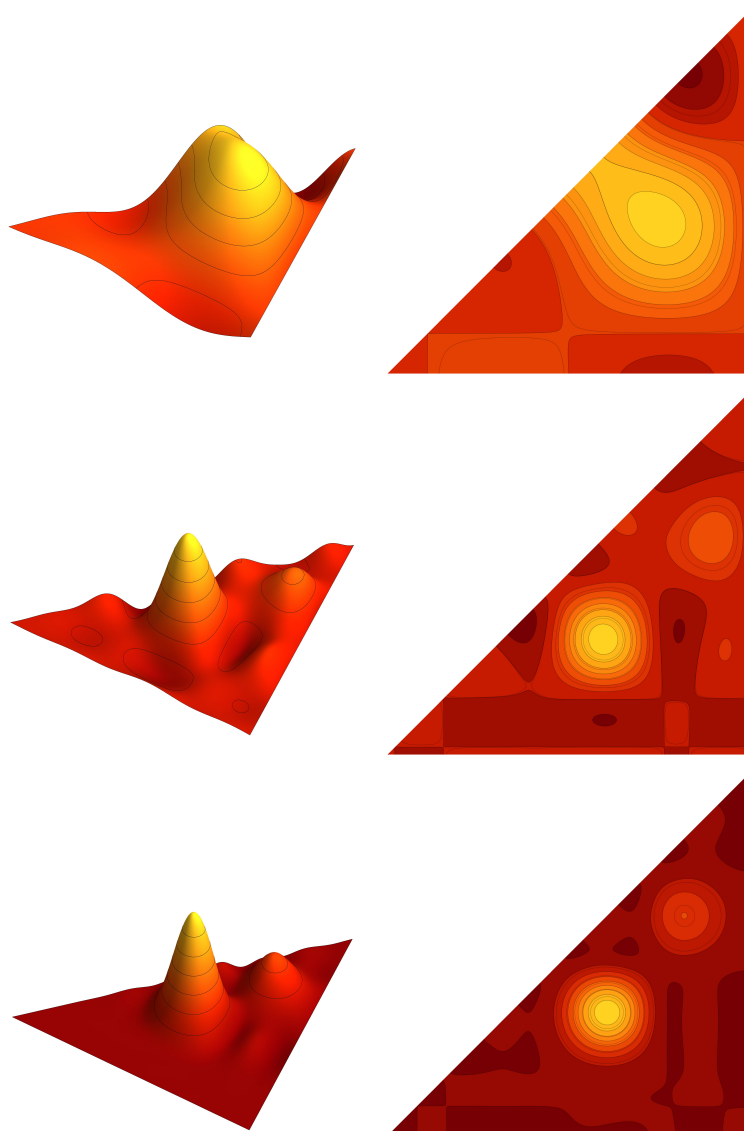
Figure.3. The symmetric sine interpolation polynomial $\phi_{N-1}^{VI,+}(x,y,\frac{1}{4})$ for model function with $N = 5, 10, 15$.

6   Conclusion

The main idea behind generalizations of discrete trigonometric functions was shown. The multivariate antisymmetric and symmetric generalizations of discrete cosine transforms were already defined in [2], [5]. From generalizations of discrete sine functions only DST I was done in [5]. The remaining sine transforms can be generalized in similar way as the DCT VI shown in this paper. Interpolation using these transforms is based on fitting the values for n-dimensional cubic lattice inside n-simplex and then interpolating using multivariate trigonometric functions. The versions differ by small shifts of the lattice points.

Beside the straight-forward application in interpolation the multivariate discrete trans-

forms can also be used as starting step for definition of Chebyshev-like polynomials. The multivariate generalizations of Chebyshev polynomials of first and third kinds was done in [2] using multivariate cosine functions. The possibility of generalization of Chebyshev polynomials of second and fourth type with use of generalizations of sine functions is yet to be investigated, but properties of the multivariate sine transforms suggests the possibility of construction of such multivariate polynomials.

References

[1] V. Britanak, K. Rao, and P. Yip, *Discrete Cosine and Sine Transforms: General Properties, Fast Algorithms and Integer Approximation*, Elsevier/Academic Press, Amsterdam, 2007.

[2] J. Hrivnák and L. Motlochová, *Discrete Transforms and orthogonal polynomials of (anti)symmetric multivariate cosine functions*, SIAM J. Numer. Anal., Vol. 52, No 6, pp. 3021-3055 (2014).

[3] J. Hrivnák, L. Motlochová and J. Patera, *Two dimensional symmetric and antisymmetric generalization of sine functions*, J. Math. Phys., 51 (2010), 073509.

[4] J. Hrivnák and J. Patera, *Two dimensional symmetric and antisymmetric generalization of exponential and cosine functions*, J. Math. Phys., 51 (2010), 023515.

[5] A. Klimyk and J. Patera, *(Anti)symmetric multivariate trigonometric functions and corresponding Fourier transforms*, J. Math. Phys., 48 (2007), 093504.

[6] G. Strang, *The Discrete cosine transforms*, SIAM Rev., 41 (1999), pp. 135-147.

[7] Y.-K. Lin, *High Capacity reversible data hiding scheme based upon discrete cosine transformation*, J. Systems Software, 85 (2012), pp. 2395-2404

[8] K. Manikantan, V. Govindarajan, V. Sasi and S. Ramachandran, *Face recognition using block-based DCT feature extraction*, J. Adv. Comput. Sci. Tehnol., 1 (2012), pp. 266-283.

Heterogeneity in Pedestrian Flow[*]

Marek Bukáček[†]

3rd year of PGS, email: `marek.bukacek@seznam.cz`
Department of Software Engineering
Faculty of Nuclear Sciences and Physical Engineering, CTU in Prague

advisors:

Miroslav Virius, Department of Software Engineering
Faculty of Nuclear Sciences and Physical Engineering, CTU in Prague

Jaromír Kukal, Department of Software Engineering
Faculty of Nuclear Sciences and Physical Engineering, CTU in Prague

Abstract. Systems with socio-physical interactions are characteristic by stochastic nature of both, dynamic aspects and parameters describing single elements. Typical representative of such system may be a group of pedestrians, which rules of motion are too complex for deterministic description [1]. Nevertheless, wide range of models describing various phenomena were developed in last twenty years [2],[3],[4],[5]. The main task of these models is mainly to evaluate the ability of infrastructure to handle extreme events.

Despite significant development of computing technique and monitoring systems, some aspects of pedestrian' behavior have been still underestimated. It is obvious that pedestrians creates quite heterogeneous set from many points of view, but for the purposes of modeling, only different velocity is taken into account. The other qualities as power, aggressiveness or endurance are totally neglected.

Moreover, our recent experiments [7], [8] uncovered rather similar behavior when participants walked freely, but significantly heterogeneous behavior in crowded situations. Quantitative analysis described stepwise linearly increasing trend of travel time with respect to the occupancy. The slope of this trend strongly differs with participants, the least active pedestrians were several times slower than the most energetic ones, under the comparable conditions. More detail study shows that the difference is not caused by difference selection of paths, but only by the ability to push through the crowd. Based on this observation, the quality aggressiveness (α) was defined as the inverse value of this slope:

$$TT_i = \frac{s}{v_0} + Noise + \frac{1}{\alpha_i} \cdot N. \tag{1}$$

To enable the reproduction of this behavior, existing concept of agents' conflicts in the cellular automata family of the models had to be enhanced [6]. The situations, where two or more agents are willing to enter the same cell, were solved by random selection of one agent or by letting this cell empty (simulation of friction). This approach was modify by adding priority to more aggressive agents.

Based on presented study, two conclusions may be highlighted:

1. the concept of aggressiveness extracted from experimental observations may be simulated by the cellular automata models using modify conflict solution method

---

[†]This study has been provided in cooperation with Pavel Hrabák.

2. the free flow velocity may be considered as global constant fro the purposes of simulations, the statistic distribution of observed attributes is reachable due to the stochastic background of the models

Further research on this field should deal with more complex geometry of designed system and confirming our experimental observations with more heterogeneous group of participants.

Keywords: evacuation dynamics, cellular model, heterogeneity

Abstrakt. Systémy se socio-fyzikální interakcí jsou charakteristické stochastickou povahou jak dynamických aspektů, tak parametrů popisujících jednotlivé prvky systému. Typický představitel takového systému může být skupina chodců, jejichž pravidla pohybu jsou tak komplexní, že je není možné deterministicky popsat [1]. Přesto se v posledních dvaceti letech podařilo vyvinout široké spektrum modelů reprodukujících různé pozorované jevy [2],[3],[4],[5]. Cílem těchto modelů je především ověřit schopnosti infrastruktury zvládat extrémní události.

I přes značné pokroky v oblasti výpočetní techniky a monitorovacích systémů se stále zanedbávají některé prvky chování chodců. Je zřejmé, že se jednotliví chodci od sebe značně liší ve spoustě ohledů, přesto se v modelech uvažuje nanejvýš různá rychlost účastníků. Všechny ostatní parametry, jako je síla, agresivita či odolnost jsou zcela zanedbávány.

Naše poslední experimenty přitom odhalily [7], [8], že lidé vykazují velmi podobnou rychlost při pohybu ve volném prostoru, ale v rámci davu se chovají značně odlišně. Kvantitativní analýza ukázala lineárně rostoucí trend závislosti času průchodu místností na její střední obsazenosti. Směrnice tohoto trendu se ale mezi účastníky značně liší, střední čas průchodu nejméně průbojných účastníků byl několikanásobně vyšší než těch nejaktivnějších. Podrobnější studie odhalila, že se jednotlivý účastníci neodlišují volbou trajektorie, ale pouze schopností prosadit se v hustém davu. Na základě tohoto pozorování pak byla definována veličina agresivita (α) jako inverzní hodnota této směrnice:

$$TT_i = \frac{s}{v_0} + Noise + \frac{1}{\alpha_i} \cdot N. \tag{2}$$

Aby bylo možné toto pozorování reprodukovat, bylo nutné upravit stávající koncept řešení konfliktů ve třídě celulárních modelů [6]. Standardně jsou situace, kdy se více agentů snaží vstoupit do jedné buňky, řešeny podle parametru tření buď náhodným výběrem jednoho ze zúčastněných chodců či necháním buňky neobsazené. Tento koncept byl upraven tak, že agresivnější chodci jsou při konfliktech preferovaní.

Na základě provedené studie tak bylo možné udělat následující závěry:

1. koncept agresivity extrahovaný z pozorovaného chování účastníků experimentu je možné simulovat v rámci třídy celulárních modelů pomocí zobecnění řešení konfliktů.

2. rychlost agentů ve volném režimu může být modelovaná jako globální konstanta, statistické rozdělení času průchodu prázdnou místností je dobře simulovatelné stochastickou povahou modelů.

Dalším krokem musí být demonstrace těchto jevů na složitější geometrii systému a potvrzení experimentálních výsledků s komplexnější skupinou účastníků.

Klíčová slova: evakuační dynamika, celulární model, heterogenita

References

[1] A. Schadschneider, D. Chowdhury and K. Nishinari, *Stochastic Transport in Complex Systems*, Elsevier (2010), ISBN: 978-0080560526.

[2] P. Hrabák, M. Bukáček and M. Krbálek, *Cellular Model of Room Evacuation Based on Occupancy and Movement Prediction, Comparison with Experimental Study*, Journal of Cellular Automata **8** (2013), 383–395.

[3] M. Bukáček, P. Hrabák and M. Krbálek, *Cellular Model of Pedestrian Dynamics with Adaptive Time Span*, In PPAM 2013 Proceedings', LNCS **8385** (2014), 669–678.

[4] M. Bukáček and P. Hrabák, *Case Study of Phase Transition in Cellular Models of Pedestrian Flow*, In ACRI 2014 Proceedings', LNCS **8751**, 508–517, 2014.

[5] M. Bukáček and P. Hrabák, *Boundary Induced Phase Transition in Cellular Automata Models of Pedestrian Flow*, Journal of Cellular Automata, to be printed.

[6] M. Bukáček and P. Hrabák, *Conflict Solution According to Aggressiveness of Agents in Floor-Field-Based Model*, In PPAM 2015 Proceedings', to be printed.

[7] M. Bukáček, P. Hrabák and M. Krbálek, *Experimental Analysis of Two-Dimensional Pedestrian Flow in front of the Bottleneck*, Traffic and Granular Flow '13, 93–101, Springer (2014).

[8] M. Bukáček, P. Hrabák and M. Krbálek, *Experimental Study of Phase Transition in Pedestrian Flow*, In PED 2014 Proceedings', in print. [available at http://arxiv.org/abs/1408.6108]

Yangian Symmetric Correlators[*]

Jan Fuksa

4th year of PGS, email: `fuksajan@fjfi.cvut.cz`
Department of Mathematics
Faculty of Nuclear Sciences and Physical Engineering, CTU in Prague

advisors:

Česmír Burdík, Department of Mathematics
Faculty of Nuclear Sciences and Physical Engineering, CTU in Prague

Alexey Petrovich Isaev, Bogoliubov Laboratory of Theoretical Physics
Joint Institute for Nuclear Research Dubna

Abstract. We discuss algebras related to rational R-matrix. We introduce L-operators describing Jordan–Schwinger representations and use them to construct monodromy matrix which generates Yangian algebra. Next, we introduce a notion of Yangian symmetric correlator and give some examples of them. We use the procedure related to similarity transformations of L-operators to generate Yangian symmetric correlators.

Keywords: Yang–Baxter equation, correlator, Yangian, Quantum inverse scattering method

Abstrakt. Diskutujeme algebry vztahující se k racionální R-matici. Zavádíme L-operátory popisující Jordan–Schwingerovy reprezentace a používáme je ke konstrukci matice monodromie, která generuje algebru zvanou Yangián. Dále zavádíme pojem yangovsky symetrického korelátoru a uvádíme některé jeho příklady. Používáme proceduru vztahující se k podobnostním transformacím L-operátorů pro generování nových yangovsky symetrických korelátorů.

Klíčová slova: Yang–Baxterova rovnice, korelátor, Yangián, kvantová inverzní metoda rozptylu

We will use the following notation throughout the text. The vector of coordinates corresponding to the i-th site of the chain is denoted as $\mathbf{x}_i$ with components $x_{i,1}, x_{i,2}, \ldots, x_{i,n}$. Scalar product of vectors $\mathbf{x}_i$ and $\mathbf{x}_j$ is denoted as $(\mathbf{x}_i\mathbf{x}_j) = \sum_{k=1}^{n} x_{i,k}x_{j,k}$. We will also adopt a shorthand notation for it $(ij) = (\mathbf{x}_i\mathbf{x}_j)$. Similarly, we denote vector of derivatives at the i-th site as $\mathbf{p}_i$ with components $p_{i,1}, \ldots, p_{i,n}$ where $p_{i,k} = \frac{\partial}{\partial x_{i,k}}$.

1 L-operators related to $g\ell(n)$ symmetry

There is a R-matrix directly related to $g\ell(n)$ symmetry. It is of the form

$$R_{12}(u) = u \cdot I + P_{12} \tag{1}$$

where $P_{12} = \sum_{i,j} E_{ij} \otimes E_{ji}$ is a permutation operator permuting spaces $\mathbb{C}^n \otimes \mathbb{C}^n$ and E_{ij} are famous matrix units. One can easily prove that it is a solution of Yang-Baxter equation

$$R_{12}(u - v)R_{13}(u)R_{23}(v) = R_{23}(v)R_{13}(u)R_{12}(u - v). \tag{2}$$

We introduce L-operator as operator acting in tensor product of a finite-dimensional (so called auxiliary) space and not necessarily finite-dimensional space (so called quantum space) in the following way

$$L = \sum_{i,j=1}^{n} E_{ij} \otimes t_{ij} \tag{3}$$

where t_{ij} are generators of $g\ell(n)$ satisfying commutation relation

$$[t_{ij}, t_{kl}] = \delta_{kj} t_{il} - \delta_{il} t_{kj}. \tag{4}$$

Introducing parameter dependent L-operator $L(u) = uI + L$ we can equivalently rewrite (4) as

$$R_{12}(u-v)L_1(u)L_2(v) = L_2(v)L_1(u)R_{12}(u-v). \tag{5}$$

We use the advantage of L-operator language throughout the text.

We are basically interested in representations of $g\ell(n)$ on spaces of functions. There is very convenient way how to represent it. It is due to the Heisenberg pair of operators $x_a, p_b = \partial_{x_b}$, well known from quantum mechanics, under commutation relation $[p_a, x_b] = \delta_{ab}$.

There are two fundamental representations of $g\ell(n)$ dual to each other. Accordingly, we define two representations on space of functions of n variables using Heisenberg pair. They are called Jordan-Schwinger representations. To distinguish between them one is denoted with $+$ and second with $-$. We use the advantage of L-operator formulation.

$$L_{ab}^+ = p_a x_b, \qquad L_{ab}^- = -x_a p_b. \tag{6}$$

The representations of $gl(n)$ on space of functions naturally decomposes into invariant subspaces of definite homogeneity $2l$. It is due to the fact that the trace of both L-operators is related to infinitesimal dilatation operator $(\mathbf{xp}) := \sum_{a=1}^{n} x_a p_a$ which commutes with all generators of $g\ell(n)$ and thus decomposes it into $g\ell(n) = s\ell(n) \oplus u(1)$.

The space of homogeneous functions of definite homogeneity is an irreducible lowest weight representation. For $2l \in \mathbb{N}_0$, the moduli space is finite-dimensional.

Let us mention, that there is plenty of algebraic relations satisfied by L-operators (6).

This can be naturally extended to spaces with n bosonic and m fermionic variables. It results then to algebra $g\ell(n|m)$.

2   General R-operators

Beside the fundamental commutation relation (5) with numerical $n \times n$ R-matrix, there is a relation written in a similar way, but the R-operator is now acting in the space of functions of two sets of variables. In general, R-operator acts in product of infinite-dimensional representations of $g\ell(n)$.

The defining relation for R-operator can be written in matrix form as follows

$$R_{12}^{\sigma_1 \sigma_2}(u-v)(L_1^{\sigma_1}(u))_{ab}(L_2^{\sigma_2}(v))_{bc} = (L_1^{\sigma_1}(v))_{ab}(L_2^{\sigma_2}(u))_{bc} R_{12}^{\sigma_1 \sigma_2}(u-v). \tag{7}$$

Let us mention without going into details that this equation is completely different from (5). We should also mention that components of operator L_1 acts now in a space of

functions of variable $\mathbf{x}_1 = (x_{1,1}, x_{1,2}, \ldots, x_{1,n})$ and of L_2 in a space of functions of variables $\mathbf{x}_2 = (x_{2,1}, x_{2,2}, \ldots, x_{2,n})$. Of course, we have also to mention that we have to specify how does the L-operators act on their moduli spaces, if as L^+ or L^-. This is the reason for introducing $\sigma_1, \sigma_2 = \pm$. The R-operator $R_{12}^{\sigma_1 \sigma_2}(u - v)$ acts in the tensor product of these two spaces.

We know two explicit solutions, cf. [2, 8],

$$R_{12}^{+-}(u) = (\mathbf{x}_1 \mathbf{x}_2)^u, \qquad R_{12}^{++}(u) = \int \frac{\mathrm{d}c}{c^{1+u}} e^{-c(\mathbf{x}_1 \mathbf{p}_2)}. \tag{8}$$

If we restrict ourselves to the functions of definite homogeneity $2l_1, 2l_2$ in both sets of variables $\mathbf{x}_1, \mathbf{x}_2$, respectively, we can write additional RLL-relation

$$R_{21}^{\sigma_2 \sigma_1}(u_1^{\sigma_1} - u_2^{\sigma_2})(L_1^{\sigma_1}(u_1))_{ab}(L_2^{\sigma_2}(u_2))_{bc} = (L_1^{\sigma_1}(u_1))_{ab}(L_2^{\sigma_2}(u_2))_{bc} R_{21}^{\sigma_2 \sigma_1}(u_1^{\sigma_1} - u_2^{\sigma_2}) \tag{9}$$

where $u_i^+ = u + 2l_i$, $u_i^- = u - 2l_i - n$.

3   Monodromy matrix and Yangian

Here, we will use the big advantage of Faddeev's Quantum Inverse Scattering Method (QISM) formulation. For a review, see [6, 1].

The mentioned L-operators and $g\ell(n)$ algebra are not all algebraic objects related to rational R-matrix (1). There is one more, much more sophisticated and in the last years studied in many situations appearing in Yang-Mills and super Yang-Mills theory. Its name is Yangian. The Yangian was established as an infinite-dimensional algebra for every simple Lie algebra in works of Drinfeld [4, 5]. In the context of Quantum inverse scattering method was founded by Takhtajan and Faddeev in [10] for Lie algebra $g\ell(n)$. For a review, please, see [9]

The Yangian $Y(g\ell(n))$ is closely related to fundamental RLL-relation (5). Let us introduce $n \times n$ matrix $T(u)$ elements of which are operators. Let this matrix can be expanded in spectral parameter u in the following way

$$(T(u))_{ab} = \delta_{ab} + \sum_{k=1}^{\infty} u^{-k} t_{ab}^{(k)}. \tag{10}$$

Let this matrix satisfy the RTT-relation

$$R_{12}(u - v)T_1(u)T_2(v) = T_2(v)T_1(u)R_{12}(u - v) \tag{11}$$

with rational R-matrix (1). Then this relation defines the commutation relation for the Yangian, explicitly

$$[t_{ab}^{(j+1)}, t_{cd}^{(k)}] - [t_{ab}^{(j)}, t_{cd}^{(k+1)}] = t_{cb}^{(j)} t_{ad}^{(k)} - t_{cb}^{(k)} t_{ad}^{(j)}. \tag{12}$$

It can be seen that at the first level $t_{ab}^{(1)}$ we obtain generators of $g\ell(n)$.

The matrix $T(u)$ is called monodromy matrix and is highly related to L-operators, because it is a product of them. Here, we state the basic procedure of QISM. The L-operator $L_i^{\sigma_i}(u_i)$ is a local object and acts only in the space of function of variable $\mathbf{x}_i$. We scatter from local objects L_i to global object which is the monodromy matrix

$$T(u_1, u_2, \ldots, u_N) = L_1^{\sigma_1}(u_1) L_2^{\sigma_2}(u_2) \cdots L_N^{\sigma_N}(u_N). \tag{13}$$

In the limit $N \to \infty$ and under condition $u_i = u$ for all $i = 1, \ldots, N$ we arrive at the definition of the Yangian above. Nevertheless, for monodromy of finite length we can still speak about Yangian algebra, but it is a special representation where all higher operators $t_{ab}^{(k)}$ are zero for k bigger than the length of the chain N.

4 Yangian symmetric correlators

Yangian symmetric correlators (YSC) were introduced in [2]. N-point Yangian symmetric correlator $\Phi = \Phi(_1, _2, \ldots, _N)$ is a homogeneous eigenfunction of monodromy matrix T, i.e. it is a solution of

$$T_{12...N}^{\sigma}(u_1, u_2, \ldots, u_N)\Phi = E(u)I\Phi. \tag{14}$$

There is plenty of algebraic relations amongst the correlators. Because of lack of the space, we will not mention them, see [2, 8]. We will only mention here their most important property from the point of view of this article. They can be generated by R-operators via RLL-relations (7) and (9) in the sense that if some Φ is a Yangian symmetric correlator, then also $R_{i,i+1}^{\sigma_i \sigma_{i+1}}(u_i - u_{i+1})\Phi$ and $R_{i+1,i}^{\sigma_{i+1}\sigma_i}(u_i^{\sigma_i} - u_{i+1}^{\sigma_{i+1}})\Phi$. Let us remark without going into details that R-operation producing new correlator from the old one changes the arguments of the monodromy matrix as can be seen from RLL-relations.

The basic two YSC's are a constant function 1 and Dirac's distribution $\delta^{(n)}(\mathbf{x})$. The action of L-operators on basic correlators is

$$L^+(u) \cdot 1 = (u+1)I \cdot 1, \qquad\qquad L^+(u) \cdot \delta^{(n)}(\mathbf{x}) = uI \cdot \delta^{(n)}(\mathbf{x}),$$
$$L^-(u) \cdot 1 = uI \cdot 1, \qquad\qquad L^-(u) \cdot \delta^{(n)}(\mathbf{x}) = (u+1)I \cdot \delta^{(n)}(\mathbf{x}). \tag{15}$$

5 Some examples of correlators

In what follows, we use the so called similarity transformation for generating of correlators, i.e our method stays and falls with R-operator R^{+-}. There are another methods of creation of correlators, the most powerfull of them is method using R-operator R^{++} acting on Dirac's delta distributions. Also, a convolution of correlators produces another correlators. But, as we said, we describe here just the method of similarity transformation.

Let us write here some useful relations

$$(ij)^\lambda p_{j,a} = \left(p_{j,a} - \lambda \frac{x_{i,a}}{(ij)}\right)(ij)^\lambda, \qquad\qquad (ij)^\lambda p_{i,a} = \left(p_{i,a} - \lambda \frac{x_{j,a}}{(ij)}\right)(ij)^\lambda. \tag{16}$$

Let us repeat that the infinitesimal dilatation

$$(\mathbf{x}_i \mathbf{p}_i) = \sum_{a=1}^{n} x_{i,a} p_{i,a} \tag{17}$$

measures the homogeneity of functions in the set of variables $\mathbf{x}_i$, e.g.

$$(\mathbf{x}_i \mathbf{p}_i)(ij)^\lambda = \lambda (ij)^\lambda. \tag{18}$$

Let us introduce useful matrix operator

$$(\mathbf{1}_{ij})_{ab} = \frac{x_{i,a} x_{j,b}}{(ij)} \tag{19}$$

satisfying

$$\mathbf{1}_{ij}\mathbf{1}_{ij} = \mathbf{1}_{ij}, \quad \mathbf{1}_{ij}\mathbf{1}_{kj} = \mathbf{1}_{ij}, \quad \mathbf{1}_{ij}\mathbf{1}_{ik} = \mathbf{1}_{ik}, \quad \mathbf{1}_{ij}\mathbf{1}_{jk} = 0, \quad \mathbf{1}_{24}\mathbf{1}_{31} = z\mathbf{1}_{21}, \quad \mathbf{1}_{31}\mathbf{1}_{24} = z\mathbf{1}_{34} \tag{20}$$

where

$$z = \frac{(12)(34)}{(13)(24)} \tag{21}$$

is of zero homogeneity $(\mathbf{x}_i\mathbf{p}_i)z = 0$ for all $i = 1, 2, 3, 4$. Another relations amongst $\mathbf{1}_{ij}$ and z can be written.

5.1   3-site correlators

We will discuss just mostly plus situation. Mostly minus convention is dealt similarly. Situations $+++$ and $---$ are uninteresting because they produce from a constant function a constant function. Correlators for configurations $+-+$ and $++-$ are explained in [2]. Therefore, I will not mention them.

5.1.1   Correlator $-++$

We can use two methods how to calculate the correlator related to a sequence of representations $\sigma = (-, +, +)$.

The first one is the following. First of all, let use RLL relation of the second kind on sites 1 and 2. We can not forget that such a relation holds only when we restrict ourselves to homogeneous functions on both sites. Then we want to apply RLL relation of the second kind on sites 1 and 3. To be able to do that we have to "degenerate" the L-operator on site 2 to a multiple of identity operator. But it is restricted to homogeneous functions. The only functions on which L-operator degenerates to identity operator are its eigenfunctions 1 and Dirac's delta function $\delta^{(n)}(\mathbf{x})$. We choose in this case the function 1.

First of all, let us use the RLL relation of the second kind on sites 1 and 2:

$$L_1^-(u_1)L_2^+(u_2)L_3^+(u_3)(21)^{u_1^- - u_2^+}\varphi(x_1; \lambda) \otimes 1_2 =$$
$$= (21)^{u_1^- - u_2^+}\, L_1^-(u_1)L_2^+(u_2)L_3^+(u_3)\varphi(x_1; \lambda) \otimes 1_2 \tag{22}$$

where $\varphi(x_1; \lambda) \otimes 1_2$ are written to emphasize the fact that this equation is valid only under restriction to functions of definite homogeneity and λ is the homegeneity of function $\varphi(x_1; \lambda)$. We get

$$
\begin{aligned}
L_1^-(u_1)L_2^+(u_2)L_3^+(u_3)(21)^{u_1-n-\lambda-u_2}\varphi(x_1; \lambda) \otimes 1_2 = \\
= (u_2 + 1)(21)^{u_1-n-\lambda-u_2} \, L_1^-(u_1)L_3^+(u_3)\varphi(x_1; \lambda) \otimes 1_2.
\end{aligned}
\tag{23}
$$

We see that on the right hand side can be again used RLL relation of the second kind because we can take $\varphi(x_1; \lambda) = (31)^\lambda$ with $\lambda = u_1 - n - u_3$

$$
\begin{aligned}
L_1^-(u_1)L_3^+(u_3)(31)^{u_1-n-u_3}1_1 \otimes 1_3 = \\
= (31)^{u_1-n-u_3}L_1^-(u_1)L_3^+(u_3)1_1 \otimes 1_3 = u_1(u_3 + 1)(31)^{u_1-n-u_3}1_1 \otimes 1_3.
\end{aligned}
\tag{24}
$$

We get

$$
L_1^-(u_1)L_2^+(u_2)L_3^+(u_3)\Phi = u_1(u_2 + 1)(u_3 + 1)\Phi
\tag{25}
$$

where

$$
\Phi = (21)^{u_3-u_2}(31)^{u_1-u_3-n}.
\tag{26}
$$

On the other hand, we can use methods similar to subsection 5.2 and rewrite the defining relation to

$$
L_2^+(u_2)L_3^+(u_3)\Phi = E'L_1^-(u_1')\Phi
\tag{27}
$$

with $u_1' = -u_1 - 1 + n + \lambda_{12} + \lambda_{13}$ and $E' = E/(u_1 u_1')$. We use the ansatz

$$
\Phi = (12)^{\lambda_{12}}(13)^{\lambda_{13}}.
\tag{28}
$$

Commuting the operator Φ to the left, acting on constant function and cancelling Φ we get the following condition on E', λ_{12} and λ_{13}:

$$
(u_2+1)(u_3+1)\mathbf{1} + \lambda_{12}(u_3+1)\mathbf{1}_{12} + \lambda_{13}(\lambda_{12}+i_2+1)\mathbf{1}_{13} = E'(u_1'\mathbf{1} - \lambda_{12}\mathbf{1}_{12} - \lambda_{13}\mathbf{1}_{13})
\tag{29}
$$

with solution $E' = -(u_3 + 1)$, $\lambda_{12} = u_3 - u_2$ and $\lambda_{13} = u_1 - u_3 - n$.

5.2   4-site correlator $+--+$

Let us try to find a correlator for configuration $+--+$, in other words, let us solve condition

$$
L_1^+(u_1)L_2^-(u_2)L_3^-(u_3)L_4^+(u_4)\Phi = E\Phi.
\tag{30}
$$

Equivalently, we can find

$$
L_3^-(u_3)L_4^+(u_4)\Phi = E'L_2^-(u_2')L_1^+(u_1')\Phi
\tag{31}
$$

where

$$
u_1' = -u_1 - 1 - \lambda_{12} - \lambda_{13}, \qquad u_2' = -u_2 - 1 + n + \lambda_{12} + \lambda_{24}
\tag{32}
$$

and $E' = \frac{E}{u_1 u_2 u_1' u_2'}$. We choose an ansatz of the form

$$
\Phi = (12)^{\lambda_{12}}(13)^{\lambda_{13}}(24)^{\lambda_{24}}(34)^{\lambda_{34}} \sum b_m z^m,
\tag{33}
$$

because without the sum $\sum b_m z^m$ we get very degenerate solution with many $\lambda_{ij} = 0$.

We will need the following commutation relations with z

$$p_{3,b}z^m = z^m \left(p_{3,b} + m\frac{x_{4,b}}{(34)} - m\frac{x_{1,b}}{(13)} \right), \quad p_{4,b}z^m = z^m \left(p_{4,b} + m\frac{x_{3,b}}{(34)} - m\frac{x_{2,b}}{(24)} \right), \quad (34)$$

$$p_{2,b}z^m = z^m \left(p_{2,b} + m\frac{x_{1,b}}{(12)} - m\frac{x_{4,b}}{(24)} \right), \quad p_{1,b}z^m = z^m \left(p_{1,b} + m\frac{x_{2,b}}{(12)} - m\frac{x_{3,b}}{(13)} \right). \quad (35)$$

Commuting Φ in (31) to the left on both sides and cancelling the prefactors $(ij)^{\lambda_{ij}}$, we we arrive to the expressions for the left hand side

$$\sum z^m \Big\{ b_m u_3(u_4 + 1)\mathbf{1} + b_m u_3(\lambda_{24} - m)\mathbf{1}_{24} - b_m(\lambda_{13} - m)(u_4 + 1)\mathbf{1}_{31}$$
$$+ \Big[b_m(\lambda_{34} + m)(u_3 - u_4 - n + m - \lambda_{34} - \lambda_{24} - \lambda_{13})$$
$$- b_{m-1}(\lambda_{13} - m + 1)(\lambda_{24} - m + 1) \Big] \mathbf{1}_{34} \Big\} \quad (36)$$

and for the right hand side

$$\sum z^m \Big\{ b_m u_2'(u_1' + 1)\mathbf{1} + b_m u_2'(\lambda_{13} - m)\mathbf{1}_{31} - b_m(\lambda_{24} - m)(u_1' + 1)\mathbf{1}_{24}$$
$$+ \Big[b_m(\lambda_{12} + m)(u_2' - u_1' - n + m - \lambda_{12} - \lambda_{24} - \lambda_{13})$$
$$- b_{m-1}(\lambda_{24} - m + 1)(\lambda_{13} - m + 1) \Big] \mathbf{1}_{21} \Big\}. \quad (37)$$

Comparing it we get five equations:

$$u_3(u_4 + 1) = E' u_2'(u_1' + 1), \tag{a}$$
$$u_3(\lambda_{24} - m) = -E'(\lambda_{24} - m)(u_1' + 1), \tag{b}$$
$$-(\lambda_{13} - m)(u_4 + 1) = E'(\lambda_{13} - m)u_2', \tag{c}$$
$$b_m(\lambda_{34} + m)(u_3 - u_4 - n + m - \lambda_{34} - \lambda_{24} - \lambda_{13}) = b_{m-1}(\lambda_{13} - m + 1)(\lambda_{24} - m + 1), \tag{d}$$
$$b_m(\lambda_{12} + m)(u_2' - u_1' - n + m - \lambda_{12} - \lambda_{24} - \lambda_{13}) = b_{m-1}(\lambda_{24} - m + 1)(\lambda_{13} - m + 1). \tag{e}$$

To make equations (d) and (e) consistent it has to hold i) $\lambda_{34} = \lambda_{12}$ and $u_3 - u_4 = u_2' - u_1'$ or ii) $\lambda_{12} + \lambda_{34} + \lambda_{13} + \lambda_{24} = u_3 - u_4 - n$ and $u_3 - u_4 = u_2' - u_1'$.

Let us analyse i). We have two constraints

$$\lambda_{34} = \lambda_{12}, \tag{*}$$
$$u_3 - u_4 = u_2' - u_1'. \tag{**}$$

From (b) and (c) we see that

$$\frac{u_3(u_4 + 1)}{u_2'(u_1' + 1)} = (E')^2 \tag{38}$$

and comparing with (a) we get that $E' = 1$. Then from (b) and (c) we get

$$\lambda_{13} = -\lambda_{12} - u_1 + u_3, \qquad \lambda_{24} = -\lambda_{12} - n + u_2 - u_4. \tag{39}$$

And for b_m we get

$$b_m = b_{m-1} \frac{(u_3 - u_1 - \lambda_{12} - m + 1)(u_2 - u_4 - \lambda_{12} - n - m + 1)}{(\lambda_{12} + m)(\lambda_{12} + m + u_1 - u_2)} \tag{40}$$

which gives a solution

$$b_m = \frac{\Gamma(\overbrace{u_3 - u_1 - \lambda_{12}}^{\lambda_{13}} - m + 1)\Gamma(\overbrace{u_2 - u_4 - \lambda_{12} - n}^{\lambda_{24}} - m + 1)}{\Gamma(\lambda_{12} + m)\Gamma(\lambda_{12} + m + u_1 - u_2)} \tag{41}$$

We choose $\lambda_{12} = u_2 - u_1 + 1$ and get a solution where $b_m = 0$ for $m < 0$. Using integral formula for gamma function

$$y^\lambda = \frac{\Gamma(\lambda + 1)}{2\pi i} \int_{\mathcal{C}} \frac{e^{-cy}}{(-c)^{\lambda+1}} dc \tag{42}$$

where $\mathcal{C}$ is a contour encircling clockwise the positive real semi-axis starting at $+\infty - i\epsilon$ and ending at $+\infty + i\epsilon$, we get the solution

$$\Phi = K \cdot \int \prod dc_{ij} e^{-c_{ij}(ij)} (c_{12}c_{34})^{-\lambda_{12}-1}(-c_{13})^{-\lambda_{13}-1}(-c_{24}^{-\lambda_{24}-1}) \times$$
$$\times \sum_{m \geq 0} \frac{\Gamma(1 + \lambda_{12} + m)}{m!} \left(\frac{c_{13}c_{24}}{c_{12}c_{34}} \right)^m \tag{43}$$

with unimportant constant K. Using formula

$$\sum_{m \geq 0} \frac{\Gamma(\lambda + m)}{m!} x^m = \Gamma(\lambda) \frac{1}{(1-x)^\lambda} \tag{44}$$

we get

$$\Phi = \int dc \frac{e^{-c_{ij}(ij)}}{(c_{12}c_{34} - c_{13}c_{24})^{\lambda_{12}+1}(-c_{13})^{\lambda_{13}+1}(-c_{24})^{\lambda_{24}+1}} \tag{45}$$

up to a constant factor, where $\lambda_{12} = u_2 - u_1 + 1$, $\lambda_{13} = u_3 - u_2 - 1$ and $\lambda_{24} = u_1 - u_4 - n - 1$.

In a similar way we can analyse the case ii).

5.3   Correlator $+ \cdots + -$

Let us denote the monodromy matrix $T_{N \ldots 10}^{+ \cdots + -}(u_N, \ldots, u_1, u_0)$. It can be easily shown that the corresponding correlator and eigenfunction is

$$\Phi^{+\cdots+-} = \prod_{i=1}^{N} (i\,0)^{u_{i-1} - u_i}, \qquad E^{+\cdots+-} = u_N \prod_{i=0}^{N-1} (u_i + 1). \tag{46}$$

6 Conclusions and outline

We have introduced some basic features of general R-operators and used their properties to generated Yangian symmetric correlators. YSC's are very important object in modern approach to quantum field theory. It shows up that amplitudes in weekly coupled $\mathcal{N} = 4$ super Yang-Mills theory are composed out of the YSC's. They were also successfully used for calculation of anomalous dimensions of composite operators in other theories.

It seems that YSC's are related also to parton distributions. This is a specific case, because the problem is related to $gl(2)$ symmetry and corresponding Yangian. There is also still partially open question if the same procedure can be done for q-deformed $U_q(s\ell(2))$. On both of these questions we try to give an answer in our paper in preparation [7].

References

[1] Č. Burdík, J. Fuksa, A. P. Isaev, S. O. Krivonos, O. Navrátil, *Remarks on the spectrum of the Heisenberg spin chain type models*, EChAYa, **46**, No.3 (2015).

[2] D. Chicherin, R. Kirschner, *Yangian symmetric correlators*, Nucl. Phys. B, **877**, (2013) 484–505.

[3] S. Derkachov, D. Karakhanyan, R. Kirschner, *Yang-Baxter R-operators and paramater permutations*, Nucl. Phys. B , **785**, (2007), 263–285.

[4] V. G. Drinfeld, *Hopf algebras and the quantum Yang-Baxter equation*, Sov. Math. Dokl., **32**, (1985), 254–258.

[5] V. G. Drinfeld, *A New realization of Yangians and quantized affine algebras*, Sov. Math. Dokl., **36**, (1988), 212–216.

[6] L. D. Faddeev, *How Algebraic Bethe Ansatz works for integrable model*, (1996), `arXiv: hep-th/9605187`.

[7] J. Fuksa, R. Kirschner, *Yangian symmetric correlators related to $g\ell(2)$ and $U_q(s\ell(2))$*, in preparation.

[8] R. Kirschner, *Yangian symmetric correlators, R operators and amplitudes*, J. Phys.: Conf. Ser., **563**, (2014) 012015.

[9] A. Molev, M. Nazarov, G. Olshanski, *Yangians And Classical Lie Algebras*, Russ. Math. Surv., **51**, (1996), 205.

[10] L. A. Takhtadzhan, L. D. Faddeev, *The Quantum Method of the Inverse Problem and the Heisenberg XYZ Model*, Russian Mathematical Surveys, **34**, No. 5, (1979), 11.

Extended Bidirectional Texture Function Moving Average Model

Michal Havlíček*

6th year of PGS, email: `havlimi2@utia.cas.cz`
Department of Mathematics
Faculty of Nuclear Sciences and Physical Engineering, CTU in Prague

advisor: Michal Haindl, Pattern Recognition Department
Institute of Information Theory and Automation, ASCR

Abstract. The bidirectional texture function (BTF) is the recent most advanced representation of visual properties of material surface. It specifies its appearance due to varying spatial, illumination, and viewing conditions. Corresponding enormous BTF measurements require compact mathematical representation for visual fidelity preserving compression. We present a novel BTF model based on a set of underlying three dimensional moving average random field (3D MA RF) models. 3D MA assumes the texture considered as a product of a convolution of an uncorrelated three dimensional random field with a three dimensional filter which completely characterizes the texture. The BTF model combines several spatial factors, subsequently factorized into a set of 3D MA representations, and range map to produce the required BTF texture. This enables high BTF space compression ratio, unrestricted texture enlargement, and reconstruction of unmeasured parts of the BTF space. We also compare proposed model with its simpler two dimensional variant in terms of colour distribution fidelity.

Keywords: Bidirectional texture function, texture analysis, texture synthesis, data compression, virtual reality, moving average random field model

Abstrakt. Obousměrná funkce textur (BTF) je v současné době nejpokročilejší reprezentace vizuálních vlastností povrchu materiálu. Její vzhled se mění s měnícími se podmínkami osvětlení a s úhlem pohledu. Odpovídající naměřená data vyžadují kompaktní matematickou reprezentaci umožňující kompresi zachovávající vizuální věrnost. V tomto článku představujeme nový BTF model založený na sadě trojrozměrných modelů klouzavého průměru náhodného pole (3D MA RF). 3D MA předpokládá, že texturu lze považovat za produkt konvoluce s nekorelovaného trojrozměrného náhodného pole s trojrozměrným filtrem, který zcela charakterizuje texturu. BTF model kombinuje několik prostorově omezených faktorů reprezentovaných 3D MA a hloubkovou mapu k získání požadované BTF textury. Toto umožňuje kompresi BTF prostoru s vysokým kompresním poměrem, neomezené rozšíření textur a rekonstrukci nenaměřených částí BTF prostoru. Rovněž porovnáváme navržený model s jeho jednodušší dvourozměrnou variantou a to z hlediska věrnosti reprodukce barevného podání.

Klíčová slova: Obousměrná funkce textur, analýza textur, syntéza textur, komprese dat, virtuální realita, model pohyblivých průměrů náhodného pole

---

*Pattern Recognition Department, Institute of Information Theory and Automation, ASCR.

1   Introduction

Realistic virtual reality scenes require objects covered with synthetic textures visually as close as possible to real surface materials appearance they emulate under any required viewing and lighting conditions. Recent most advanced visual representation of such surfaces is Bidirectional Texture Function (BTF) [2] which is a seven dimensional function describing surface appearance variations due to varying spatial position and illumination and viewing angles. Such a function is typically measured as thousands of images per material sample, each taken for a specific combination of the illumination and viewing condition. Textures can be either represented by digitized measured ones or synthetic ones represented by an appropriate mathematical model. Using digitized textures directly suffers among others with evidently extreme memory requirements.

Several so called intelligent sampling methods ([5] among others) were proposed to solve this problem. All of them are based on some sort of original small texture sampling. However, they still require to store thousands images for every combination of viewing and illumination angle of the original target texture sample and additionally they often produce images with undesirable visual artifacts. Moreover some of them are very computationally demanding.

Contrary to the sampling approaches, the synthetic textures generated from mathematical models are more flexible and extremely compressed, because only tens of parameters have to be stored instead of the original inconvenient visual measurements. They may be evaluated directly in a procedural form and can be used to fill virtually infinite texture space without visible discontinuities. On the other hand, mathematical models can only approximate original data, which might result in visual quality compromise. A BTF texture representation requires, in general, seven dimensional mathematical models, but it is possible to approximate the BTF with a set of much simpler three or two dimensional factorial models. Such a compromise obviously leads to some information loss.

We present a novel BTF model based on a set of underlying three dimensional moving average random field (3D MA RF) models. 3D MA model assumes the texture considered as a product of a convolution of an uncorrelated three dimensional random field with a three dimensional filter which completely characterizes the texture. As the proposed underlaying MA model suffers from inability to represent low frequencies present in natural textures we use multi scale extension of the model so that modelled texture is decomposed by means of Gaussian Laplacian (G-L) pyramid and each band limited component is modelled independently. The BTF model combines several spatial factors, subsequently factorized into a set of 3D MA representations, and range map to produce the required BTF texture.

BTF 3D MA model represents a novel method for efficient rough texture modelling which combines an estimated range map with synthetic smooth texture generated by the set of multiscale 3D MA models. The texture visual appearance during changes of viewing and illumination conditions are simulated using either the bump mapping [1] or displacement mapping [8] technique. The obvious advantage of this solution is the possibility to exploit direct support for both bump and displacement mapping techniques in the contemporary graphics hardware.

2 Three Dimensional Moving Average BTF Model

The BTF model combines the estimated and enlarged material range map with the synthetic smooth texture. The range map specifies overall roughness of the textured surface which significantly influences the BTF texture appearance. The BTF model range map estimate can benefit from tens of ideally mutually registered BTF measurements using the method called over determined photometric stereo [9] making such estimate much more accurate. The estimated range map is enlarged into required size using the roller [5], currently the most efficient texture synthesis algorithm.

Analyzed texture is decomposed into a multi resolution grid and each resolution data are independently modelled by their dedicated model. Each one generates a single spatial frequency band of the texture. Decomposition is performed using Laplacian pyramid and the intermediary Gaussian pyramid which is a sequence of images in which each one is a low pass down sampled version of its predecessor. The Laplacian pyramid contains band pass components and provides a good approximation to the Laplacian of the Gaussian kernel. It can be constructed by differencing single Gaussian pyramid layers. The hierarchy of different resolutions of an input image provides a transition between pixel level features and region or global features and hence such a representation simplify modelling a large variety of possible textures. Each band limited component is modeled independently.

A stochastic texture can be considered as a sample from a three dimensional RF defined on an infinite three dimensional lattice. Let us denote the input factor represented by the 3D MA RF model Y, then $Y_{(i,j,k)}$ is the intensity value of a pixel at (i,j) in k-th spectral plane of this factor. The model assumes that each factor is the stochastic texture and therefore the output of an underlying system which completely characterizes it in response to a 3D uncorrelated random input. This system can be represented by the impulse response of a linear 3D filter. The vectors of intensity values of the spectral planes of the most significant pixels together with their neighbours (defined by relative shifts $N(i,j) \in \mathcal{N}$, $i \in \{0, \ldots, |\mathcal{N}| - 1\}$, $j \in \{0; 1\}$) are collected and averaged and the resultant 3D kernel is used as an estimate B of the impulse response of the underlying system. A synthetic factor $Y^{\dagger}$ can be generated by convolving an uncorrelated 3D RF E with this estimate:

$$Y^{\dagger}_{(i,j,k)} = \sum_{n=0}^{|\mathcal{N}|-1} \sum_{k'=0}^{c-1} B_{(n,k,k')} E_{(i+N(n,0),j+N(n,1),k')} \,, \tag{1}$$

where c is the number of the spectral planes of the modelled texture.

2.1 Parameter Estimation

The parameters of B have to be estimated to fit the model equation (1) to certain image Y performing extended method used for two dimensional MA (2D MA) BTF model [4]. The procedure begins by selecting thresholds y_k, $k \in \{0, \ldots, c-1\}$, usually chosen as some percentage $(\frac{0.5}{c})$ of the standard deviation of the intensities of the spectral plane k. The analysis itself starts from the top left corner of the image and proceeds to the

bottom right corner identifying pixels at which the intensities in individual spectral planes cross the thresholds i.e. $(Y_{(i,j,k)} \geq y_k)$ and $((Y_{(i-1,j,k')} < y_{k'})$ or $(Y_{(i+1,j,k')} < y_{k'}))$ and $((Y_{(i,j-1,k')} < y_{k'})$ or $(Y_{(i,j+1,k')} < y_{k'}))$ holds. When such threshold crossing occurs the intensity values of all spectral planes of the support region defined by $\mathcal{N}$ around the crossing point are saved. The same procedure is followed at the next threshold crossing point and these intensity values are added to the previously saved. The summed up values are divided by the total number of contributions for the corresponding parameter estimates, i.e. averaged.

2.2 Synthesis

The underlying 3D MA model is able to generate synthetic images, i.e. stochastic smooth textures, $Y^\dagger$ directly from the parameters saved in B. The synthetic factor can be generated simply by convolving an uncorrelated 3D RF E with the estimate of B according to (1). All generated factors form new G-L pyramid. Fine resolution synthetic smooth texture is obtained by the collapse of the G-L pyramid i.e. an inverse procedure of that one creating the pyramid. Visual appearance of the resulting BTF texture is enhanced by including information from the estimated and enlarged range map using either the bump mapping or displacement mapping technique.

3 Results

We tested the model on BTF textures from the University of Bonn BTF database [7] which consists of several materials such as aluminium foil, corduroy, graved granite stone, leather, upholstery, wood. Each BTF material sample included in the database was measured in 81 illumination and 81 viewing angles and the resulting images have a resolution 800×800 pixels. Several achieved results can be observed in Fig.1 showing BTF texture of lacquered wood applied on nontrivial geometrical body. The presented scene was rendered with several different light conditions to demonstrate the effect and meaning of BTF texture use. We used used BTF texture plug in for Blender (a free and open source 3D animation suite) [6].

Comparison of the presented model with existing alternatives is hardly feasible as there is still a need for a reliable criterion for such validation. Many already developed approaches are limited to monospectral images that is clearly major disadvantage as colour is arguably the most significant visual feature. Currently, psychophysical experiments, i.e. quality assessments performed by humans, represent the only reliable option. Methods of this type require time demanding experiment setup design, strictly controlled laboratory conditions and representative set of human testing subjects. So that such experiments are extremely impractical, expensive, generally demanding. We simply render several common three dimensional textures modelled both by 3D MA model and its simpler two dimensional variant (2D MA). Several examples, which can be seen in Fig.2, clearly shows the information loss and therefore visual quality of the result caused by spectral decorrelation and thus definite advantage of the extended model.

Figure 1: **Several achieved results.** BTF texture of lacquered wood applied on non-trivial geometrical body rendered with several different light conditions. Comparison of 3D MA BTF model (odd rows) with 2D MA BTF model (even rows).
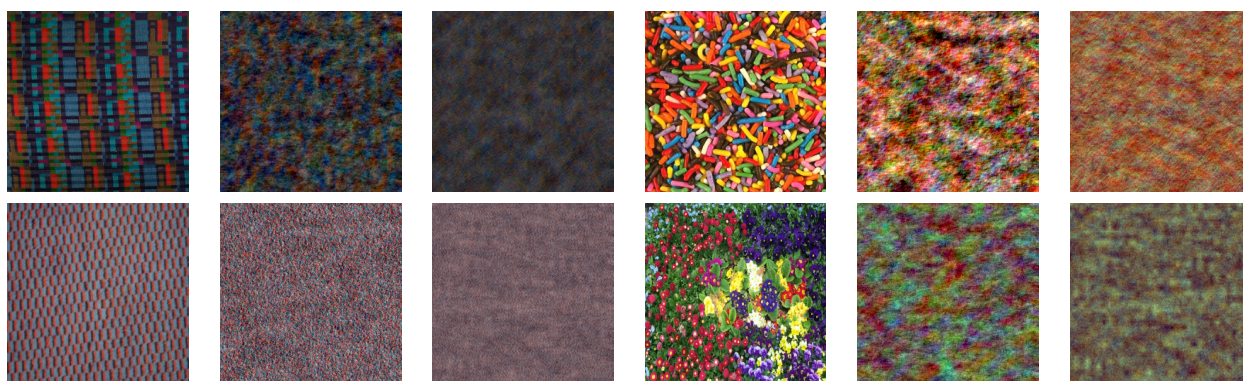

Figure 2: **Demonstration of the advantage of the extended model.** Comparison of original common three dimensional texture (the first image in each triplet) with 3D MA synthesis (the second image in each triplet) and with 2D MA synthesis (the third image in each triplet).

3.1 Future Work

Presented MA 3D model can be used as well as the core of compound texture model similarly to three dimensional causal autoregressive random field model in [3].

4   Conclusion

The presented BTF 3D MA model offers the possibility to compactly represent and theoretically unlimited enlarge BTF textures playing role as a simple alternative to the existing RF based BTF models. It is based on the extension of two dimensional BTF MA model.

   The algorithm has very low computation complexity and does not require any in general time consuming numerical optimization such as the usually employed Markov chain Monte Carlo method or some of their deterministic approximations. Since this model is three dimensional and therefore outfitted for the treatment of multispectral data no spectral decorrelation is needed. Such decorrelation, necessary in case of two dimensional models, increases computing demands and is a cause of certain infomation loss leading to colour quality degradation of synthesized images. On the other hand, the inevitable spatial factorization increases overall time, memory, and computing demands.

   BTF 3D MA model may be also used to reconstruct BTF space i.e. for the synthesis of missing BTF measurement. Due to its simplicity this method can be also potentially implemented taking advantage of new graphics cards to increase overall speed of both analysis and synthesis.

   The results of the experiments on the BTF data are promising although they are only approximation of the original measurements. The presented method enables extremely fast and seamless enlargement of the BTF texture to arbitrary size and also very high BTF texture compression ratio which cannot be achieved by any alternative sampling BTF texture method. This is applicable for transmission, storing or modelling visual surface data.

References

[1] Blinn, J.: Simulation of Wrinkled Surfaces, SIGGRAPH 1978 12(3), (1978), 286–292.

[2] Dana, K.J., Nayar, S.K., van Ginneken, B., Koenderink, J.J.: Reflectance and Texture of Real-World Surfaces, CVPR, IEEE Computer Society, (1997), 151–157.

[3] Haindl, M., Havlíček V.: A Compound MRF Texture Model, Pattern Recognition (ICPR), IEEE, (2010), 1792–1795.

[4] Havlíček, M., Haindl, M.: A Moving Average Bidirectional Texture Function Model, Computer Analysis of Images and Patterns, Lecture Notes in Computer Science, 8048, Springer Berlin Heidelberg, (2013), 338–345.

[5] Haindl, M., Hatka, M.: BTF Roller, Proceedings of the 4th International Workshop on Texture Analysis, Texture 2005, IEEE, (2005), 89–94.

[6] Hatka, M., Haindl M.: Advanced Material Rendering in Blender, The International Journal of Virtual Reality, 11(2), (2012), 15–23.

[7] Müller, G., Meseth, J., Sattler, M., Sarlette, R., Klein, R.: Acquisition, Synthesis and Rendering of Bidirectional Texture Functions, Eurographics 2004, STAR - State of The Art Report, Eurographics Association, (2004), 69–94.

[8] Wang, L., Wang, X., Tong, X., Lin, S., Hu, S., Guo, B., Shum, H.: View-Dependent Displacement Mapping, ACM Transactions on Graphics 22(3), (2003), 334–339.

[9] Woodham, R.: Photometric Method for Determining Surface Orientation from Multiple Images, Optical engineering 19(1), (1980), 139–144.

Multiple Tilings Associated to d-Bonacci Beta-expansions*

Tomáš Hejda

4th year of PGS, email: `tohecz@gmail.com`
Department of Mathematics
Faculty of Nuclear Sciences and Physical Engineering, CTU in Prague

advisors:

Edita Pelantová, Department of Mathematics
Faculty of Nuclear Sciences and Physical Engineering, CTU in Prague

Wolfgang Steiner, LIAFA CNRS UMR 8079
Uniersité Paris Diderot, France

Abstract. It is a well-known fact that when $\beta > 1$ is a d-Bonacci number, i.e., $\beta^d = \beta^{d-1} + \beta^{d-2} + \cdots + \beta + 1$ for some $d \geq 2$, then the Rauzy fractals arising in the greedy β-expansions tile the space $\mathbb{R}^{d-1}$. However, it was recently shown that the Rauzy fractals arising in the symmetric Tribonacci expansions form a multiple tiling with covering degree 2, i.e., almost every point of $\mathbb{R}^2$ lies in exactly 2 tiles. We show that the covering degree for symmetric d-Bonacci expansions is equal to $d - 1$ for any d. We moreover characterize which tiles lie in the same layer of the multiple tiling.

Keywords: beta-expansions, Rauzy fractal, tiling, multiple tiling

Abstrakt. Je známo, že je-li $\beta > 1$ tzv. d-Bonacciho číslo, tedy platí-li $\beta^d = \beta^{d-1} + \beta^{d-2} + \cdots + \beta + 1$ pro nějaké $d \geq 2$, pak Rauzho fraktály pro hladové β-rozvoje dláždí prostor $\mathbb{R}^{d-1}$. Nicméně nedávno se ukázalo, že Rauzyho fraktály pro symetrické Tribonacciho rozhove tvoří 2násobné dláždění, jinými slovy, skoro každý bod $\mathbb{R}^2$ leží právě ve 2 dlaždicích. Ukazujeme, že násobnost tohoto dláždění je $d - 1$ pro každé d-Bonacciho číslo β. Také ukazujeme, které dlaždice tvoří jednotlivé vrstvy násobného dláždění.

Klíčová slova: beta-rozvoje, Rauzyho fraktály, dráždění, násobná dláždění

References

[1] Tomáš Hejda. *Multiple tilings associated to d-Bonacci beta-expansions.* In 'Numeration 2015 (Nancy, 2015)'. `http://numeration2015.sciencesconf.org/` [2015-09-28].

[2] Tomáš Hejda. *Multiple tilings associated to d-Bonacci beta-expansions.* Submitted, 2015, 11 pp. `http://arxiv.org/abs/1503.07744` [2015-09-28].

Selective Dynamical Decoupling for Quantum State Transfer[*]

Antonín Hoskovec

4th year of PGS, email: `hoskoant@fjfi.cvut.cz`
Department of Physics
Faculty of Nuclear Sciences and Physical Engineering, CTU in Prague

advisor: Igor Jex, Department of Physics
Faculty of Nuclear Sciences and Physical Engineering, CTU in Prague

Abstract. State transfer across discrete quantum networks is one of the elementary tasks of quantum information processing. Its aim is the faithful placement of information into a specific position in the network. However, all physical systems suffer from imperfections, which can severely limit the transfer fidelity. We present selective dynamical decoupling schemes which are capable of stabilizing imperfect quantum state transfer protocols on the model of a bent linear qubit chain. The efficiency of the schemes is tested and verified in numerical simulations on a number of realistic cases. The simulations demonstrate that these selective dynamical decoupling schemes are capable of suppressing unwanted errors in quantum state transfer protocols efficiently.

Keywords: quantum state transfer, dynamical decoupling, quantum information

Abstrakt. Přenos stavu po diskrétních kvantových sítích je jedním ze základních stavebních kamenů zpracování kvantové informace. Cílem přenosu stavu je umístění kvantového stavu na danou pozici v síti. Nicméně, všechny fyzikální systémy trpí nedokonalostmi, ty v tomto případě mohou zásadně snížit spolehlivost přenosu stavu. Vypracovali jsme schémata pro dynamical decoupling, která jsou schopna stabilizovat přenos stavu na modelech ohnutých lineárních řetízků qubitů. Efektivnost nalezených schémat jsme ověřili pomocí numerických simulací fyzikálních systémů s reálnými parametry. Simulace ukázaly, že tato schémata jsou schopná efektivního potlačení nežádoucích efektů.

Klíčová slova: přenos kvantového stavu, dynamical decoupling, kvantová informace

Numerical Simulation of High-Frequency Ultrasound Scattering on Articular Cartilage Cellular Structure*

Jana Hradilová

4th year of PGS, email: `hradilovajana@gmail.com`
Department of Mathematics
Faculty of Nuclear Sciences and Physical Engineering, CTU in Prague

advisors:

Zdeněk Převorovský, Impact and Waves in Solids Department
Institute of Thermomechanics, CAS

Kay Raum, Berlin-Brandenburg Center for Regenerative Therapies
Charité – Universitätsmedizin Berlin

Abstract. This study investigates numerically the potential of high-frequency ultrasound to detect changes in inner organized structure of articular cartilage. Specifically, we examined the effects of increasing distances between horizontally oriented layers of cells on the spectral backscatter characteristics.

Several studies have examined the interaction of ultrasound backscattered waves with superficial zone of the cartilage [5], where the backscattered signals were analyzed using amplitude, spectral and envelope statistical parameters and were related to degenerative changes of the cellular matrix given by the Mankin score. In [3], authors suggested that variations in apparent integrated backscatter coefficient reflect changes in shape, size and/or density of scatterers in the cartilage matrix and could also be related to constitutional and strucutral changes in the extracellular cartilage matrix.

It is known that the cartilage has a well organised structure [4]. Based on the data from the literature [8], we determined the shape and size of the cartilage cells and we modeled the cartilage matrix as isotropic and linearly elastic.

In order to investigate the effect of periodic cell structure in the superficial cartilage layer on the ultrasound backscattered signals, two-dimensional numerical models were developed. We designed several 2-dimensional cross-sectional geometries, mimicking the cellular alignment of cartilage in a cross-sectional view. Material parameters, i.e. elastic coefficients and density, were obtained from [6] and [2]. The computational solution of the 2-dimensional wave propagation problem is based on an Finite-Difference Time-Domain code (SimSonic, LIP, Paris, France; www.simsonic.fr [1]).

The configuration of the numerical model consists of the cartilage layer attached to the bone and immersed in water. The cartilage model contains cell-mimicking scatterers of elliptical shape. The values of the major (horizontally oriented) and minor axes of scatterers were 20 μm and 10 μm [9], respectively. Scatterers were randomly arranged, according to the uniform distribution, along the horizontal axis in parallel lines. A virtual linear array was positioned in the middle

---

of the horizontal axis. The array consists of 50 unfocused transducer elements for transmission and reception of signals at the same position with the angle of incidence perpendicular to the cartilage surface, i.e. similar to pulse-echo experiments. Perfectly matched layers with 80 dB attenuation were added as a boundary condition. Grid step of the geometry is $\Delta x = 0.002$ mm (i.e. 1 pixel corresponds to 2 μm). The stability of the model is provided by the CFL stability condition (Courant, Friedrichs and Lévy). A broadband Gauss pulse with a central frequency 25 MHz and a -6 dB bandwidth of 80% was used to excite the emitters of the array to generate a plane wave.

Regarding spectral analysis, the backscattered signals were gated using a Tukey window with a window that covers the time range between the front-side reflection and the second back-side reflection, coming from the cartilage/bone interface. From the logarithmic power spectrum, the logarithmic power spectrum of the reference signal (calculated from the geometry without scatterers) was subtracted, and the result is called a difference spectrum.

Difference spectra show a distinct highly-reflective frequency band centered at the certain frequency, whereby the center of the band depends reciprocally on the spacing of the regular arrangement and obeys excellentlly the Brag's law. This feature was observed for all evaluated geometries with periodical structure. Moreover, for larger spacing a second band at higher frequencies was observed. For reference geometry with randomly distributed cells within the whole cartilage layer, no high-reflective frequency bands in difference spectrum were observed. The observed phenomena can be explained by the constructive interference of waves reflected from multiple interfaces in the periodic structure of the studied geometry.

It was shown that the frequency dependence of the cartilage backscattered signals is closely related to the distances between cells, chondrocytes. The presented results are promising for the development of a new non-invasive method for the quantitative assessment of cellular features that may be related to the degree of the cartilage tissue degeneration.

In the outlook, we want to compare the presented model with experimental measurements. In order to obtain the desired effect, we can estimate the optimal frequency range of the transducer based on the simulation results. Histological data from human donors are being assessed to determine characteristic parameters (e.g. size, shape and spacing of the cartilage cells or Young modulus of the cartilage) of the model. A 3D numerical model is currently under development.

Keywords: articular cartilage, scattering, high-frequency ultrasound, numerical simulations

Abstrakt. Tato studie zkoumá numericky potenciál vysokofrekvenčního ultrazvuku pro detekci změn ve vnitřní organizované struktuře kloubní chrupavky. Konkrétně je zkoumán vliv uspořádání horizontálně orientovaných vrstev buněk na spektrální charakteristiky zpětného rozptylu.

Několik studií se zabývalo interakcí ultrazvukových vln s vrchní vrstvou chrupavky [5], kde byly analyzovány zpět odražené signály pomocí amplitudových, spektrálních a obálkových statistických parametrů a byly dány do souvislosti s degenerativními změnami v buněčné matrici danými Mankinovou škálou. V [3] autoři uvádějí, že rozdíly v AIBC (apparent integrated backscatter coefficient) odrážejí změny ve tvaru, velikosti a/nebo hustotě chondrocytů (chrupavkových buněk) v matrici chrupavky a mohly by také úzce souvisloset se změnami ve skladbě a struktuře extracelulární matrice chrupavky.

Je známo, že chrupavka má dobře organizovanou strukturu [4]. Na základě dat z literatury [8], jsem stanovila tvar a velikost buněk chrupavky ve vrchní vrstvě a chrupavkovou matrici jsem modelovala jako izotropní a lineárně elastickou.

Za účelem zkoumání vlivu pravidelné buněčné struktury ve vrchní vrstvě chrupavky na rozptyl ultrazvukových signálů, byly vyvinuty 2D numerické modely. Navrhla jsem několik 2-

dimenzionálních průřezů geometrií chrupavky, simulujících buněčné uspořádání v řezu. Materiálové parametry, tj. elastické koeficienty a hustota, byly získány z [6] a [2]. Řešení je získáno metodou konečných diferencí využitím programu SimSonic (SimSonic, LIP, Paříž, Francie; www.simsonic.fr [1]).

Konfigurace numerického modelu sestává z vrchní vrstvy chrupavky připojené ke kosti a ponořené do vody. Model chrupavky obsahuje inkluze napodobující buňky eliptického tvaru. Hodnoty hlavní (horizontálně orientované) a vedlejší osy inkluzí jsou 20 μm a 10 μm [9], respektive. Inkluze jsou náhodně uspořádány, podle uniformního rozdělení, podél vodorovné osy v rovnoběžných liniích. Virtuální ultrazvukový snímač typu lineární array je umístěn ve středu vodorovné osy. Snímač se skládá z padesáti nefokusovaných elementů pro vyslání a příjem signálů ve stejné poloze s úhlem dopadu kolmo na povrch chrupavky, tedy podobně jako u puls-echo experimentů. Okrajové podmínky tvoří PML (perfectly matched layers) s útlumem 80 dB. Prostorový krok geometrie je $\Delta x = $ 0,002 mm (tedy 1 pixel odpovídá 2μm). Stabilita modelu je zajištěna CFL podmínkou stability (Courant, Friedrichs a Lévy). K excitaci snímače a ke generování rovinné vlny byl použit širokopásmový Gaussovský puls s centrální frekvencí 25 MHz a -6 dB šířkou pásma 80 %.

Pro spektrální analýzu modelových signálů jsem použila okno typu Tukey, které zahrnuje časový rozsah mezi předním odrazem od povrchu chrupavky a zadním odrazem, který pochází z rozhraní chrupavky a kosti. Odečtením „power spektra" referenčních signálů (získaných z geometrie bez inkluzí) a modelových signálů získáme tzv. diferenční spektrum.

Diferenční spektra vykazují výrazné vysoce reflexní frekvenční pásma se středy na určitých frekvencích, přičemž středy pásem závisí recipročně na rozteči pravidelného uspořádání a řídí se Braggovým zákonem. Tato vlastnost byla pozorována u všech zkoumaných geometrií s periodickou strukturou. Navíc, pro větší rozestupy vrstev inkluzí byl pozorován druhý pás při vyšších frekvencích. Pro referenční geometrii s náhodně rozmístěnými buňkami v celé vrstvě chrupavky nebyla v diferenčním spektru pozorována žádná vysoce reflexní frekvenční pásma. Pozorované jevy lze vysvětlit konstruktivní interferencí vln odražených od různých rozhraní v periodické struktuře studované geometrie.

Bylo ukázáno, že frekvenční závislost modelových signálů úzce souvisí se vzdáleností mezi buňkami, chondrocyty. Uvedené výsledky jsou slibné pro vývoj nové neinvazivní metody pro kvantitativní hodnocení buněčné struktury, která může být v souvislosti se stupni degenerace chrupavkové tkáně.

Dále bychom chtěli porovnat předložený model s experimentálními měřeními. Na základě výsledků simulace můžeme pro dosážení požadovaného efektu odhadnout optimální frekvenční rozsah ultrazvukového snímače. Pro další přiblížení jsou na základě histologických dat z lidských dárců vyhodnocovány charakteristické parametry (například velikost, tvar a rozmístění buněk chrupavky nebo modulu pružnosti chrupavky) modelu a je vyvíjen 3D numerický model.

Klíčová slova: kloubní chrupavka, rozptyl, vysokofrekvenční ultrazvuk, numerické simulace

References

[1] E. Bossy, Q. Grimal. *Numerical methods for ultrasonic bone characterization.* Bone Quantitative ultrasound. P. Laugier and G. Haiat, Eds., New Your, NY: Springer. (2010), 181–228.

[2] A. Bourgnon. *Identification of large basic multicellular units in cortical bone by spectral analysis of ultrasound backscatter.* Master project in Bioengineering (2014).

[3] E. Cherin, A. Saider, P. Laugier, P. Netter, G. Berger. *Evaluation of acoustical parameter sensitivity to age-related and osteoarthritic changes in articular cartilage using 50-MHz ultrasound.* Ultrasound in Med & Biol. **24** (1998) 341–354.

[4] R. Fujioka, T. Aoyama, T. Takakuwa. *The layered structure of the articular cartilage.* Osteoarthritis and Cartilage. **21** (2013), 1092–1098.

[5] N. Männicke, M. Schöne, M. Gottwald, F. Göbel, M.L. Oelze, K. Raum. *3-D high-frequency ultrasound backscatter analysis of human articular cartilage.* Ultrasound in Med. & Biol. (2013).

[6] S.G. Patil, Y.P. Zheng, J.Y. Wu, J. Shi. *Measurement of depth-dependence and anisotropy of ultrasound speed of bovine articular cartilage in-vitro.* Ultrasound Med. Biol. **30(7)** (2004), 953–963.

[7] M. Schöne, N. Männicke, M. Gottwald, F. Göbel, K. Raum. *3-D high-frequency ultrasound improves the estimation of surface properties in degenerated cartilage.* Ultrasound Med Biol. **39(5)** (2013), 834–844.

[8] R.A. Stockwell. *The interrelationship of cell density and cartilage thickness in mammalian articular cartilage.* J. Anat. **109** (1971), 411–421.

[9] R.A. Stockwell. *Biology of Cartilage Cells.* Cambridge University Press 1979.

[10] Y.P. Zheng, J. Shi, L. Qin, S.G. Patil, V.C. Mow, K.Y. Zhou. *Dynamic depth–dependent osmotic swelling and solute diffusion in articular cartilage monitored using real–time ultrasound.* Ultrasound Med Biol. **30(6)** (2004), 841–849.

On Absence of Bound States for Weakly Attractive δ'-interactions Supported on Non-closed Curves in $\mathbb{R}^2$ [*]

Michal Jex

4th year of PGS, email: `jexmicha@fjfi.cvut.cz`
Department of Physics
Faculty of Nuclear Sciences and Physical Engineering, CTU in Prague

advisor: Pavel Exner, Department of Theoretical Physics
Nuclear Physics Institute, AS CR

Abstract. Let $\Lambda \subset \mathbb{R}^2$ be a non-closed piecewise-C^1 curve, which is either bounded with two free endpoints or unbounded with one free endpoint. Let $u_\pm|_\Lambda \in L^2(\Lambda)$ be the traces of a function u in the Sobolev space $H^1(\mathbb{R}^2 \setminus \Lambda)$ onto two faces of Λ. We prove that for a wide class of shapes of Λ the Schrödinger operator $\mathsf{H}_\omega^\Lambda$ with δ'-interaction supported on Λ of strength $\omega \in L^\infty(\Lambda; \mathbb{R})$ associated with the quadratic form

$$H^1(\mathbb{R}^2 \setminus \Lambda) \ni u \mapsto \int_{\mathbb{R}^2} \left|\nabla u\right|^2 dx - \int_\Lambda \omega \left|u_+|_\Lambda - u_-|_\Lambda\right|^2 ds$$

has no negative spectrum provided that ω is pointwise majorized by a strictly positive function explicitly expressed in terms of Λ. If, additionally, the domain $\mathbb{R}^2 \setminus \Lambda$ is quasi-conical, we show that $\sigma(\mathsf{H}_\omega^\Lambda) = [0, +\infty)$. For a bounded curve Λ in our class and non-varying interaction strength $\omega \in \mathbb{R}$ we derive existence of a constant $\omega* > 0$ such that $\sigma(\mathsf{H}_\omega^\Lambda) = [0, +\infty)$ for all $\omega \in (-\infty, \omega*]$; informally speaking, bound states are absent in the weak coupling regime.

Keywords: Schrödinger-type operators, δ'-interactions, non-closed curves, negative spectrum, min-max principle, linear fractional transformations

Abstrakt. Nechť $\Lambda \subset \mathbb{R}^2$ je neuzavřená po částech-C^1 spojitá křivka, konečná s dvěma volnými konci či polonekonečná s jedním volným koncem. Nechť $u_\pm|_\Lambda \in L^2(\Lambda)$ jsou stopy funkce u v sobolevově prostoru $H^1(\mathbb{R}^2 \setminus \Lambda)$ na obou stranách křivky Λ. Pro velkou třídu tvarů křivek Λ ukážeme, že Schrödingerův operátor $\mathsf{H}_\omega^\Lambda$ popisující δ'-interakci lokalizovanou na křivce Λ se silou $\omega \in L^\infty(\Lambda; \mathbb{R})$ asociovaný s kvadratickou formou

$$H^1(\mathbb{R}^2 \setminus \Lambda) \ni u \mapsto \int_{\mathbb{R}^2} \left|\nabla u\right|^2 dx - \int_\Lambda \omega \left|u_+|_\Lambda - u_-|_\Lambda\right|^2 ds$$

nemá žádné záporné vlastní hodnoty pro ω, které je shora omezené striktně positivní funkcí lokalizovanou na křivce Λ. Pokud je množina $\mathbb{R}^2 \setminus \Lambda$ quasikonická, tak ukážeme, že $\sigma(\mathsf{H}_\omega^\Lambda) = [0, +\infty)$. Pro omezené křivky Λ z naší třídy s konstantní silou $\omega \in \mathbb{R}$ odvodíme existenci konstanty $\omega* > 0$ takové, že $\sigma(\mathsf{H}_\omega^\Lambda) = [0, +\infty)$ pro $\omega \in (-\infty, \omega*]$; tzn. pro slabou interakci neexistují vázané stavy.

Klíčová slova: Schrödingerovy operátory, δ'-interakce, neuzavřené křivky, záporné spektrum, princip mini-maxu, lineárně lomená transformace souřadnic

This paper was submitted to Annales Henri Poincaré and it was presented at the conference XVIII International Congress on Mathematical Physics in Santiago de Chile from July 27th to August 1st, 2015.

References

[1] M. Jex, V. Lotoreichik: *On absence of bound states for weakly attractive δ'-interactions supported on non-closed curves in $\mathbb{R}^2$*. arXiv: 1508.04577.

Convolution and Cross-correlation Generalized to Weyl Group Orbits

Ondřej Kajínek

3rd year of PGS, email: `kajinond@fjfi.cvut.cz`
Department of Software Engineering
Faculty of Nuclear Sciences and Physical Engineering, CTU in Prague

advisors:

Goce Chadzitaskos, Department of Physics
Faculty of Nuclear Sciences and Physical Engineering, CTU in Prague

Jiří Hrivnák, Department of Physics
Faculty of Nuclear Sciences and Physical Engineering, CTU in Prague

Abstract. The current boom of orbit functions and orbit transforms based on Weyl groups became an impulse for exploring properties of certain operations on Weyl groups. There are several families of orbit functions that differ by so called sign homomorphism – function describing how the orbit function behave under operations of Weyl group. Two operations, orbit convolution and orbit cross-correlation are described using the sign homomorphisms available for Weyl groups of rank 2. Their properties are described in the later part of this article.

Keywords: convolution, cross-correlation, Weyl groups, orbit transforms

Abstrakt. Současný rozvoj funkcí a transformací na orbitách, založených na Weylových grupách, se stal podnětem ke zkoumání vlastností dalších operací na Weylových grupách. Existuje několik rodin funkcí na orbitách, které se liší tzv. znaménkovým homomorfismem – funkcí popisující vlastnosti funkce na orbitách při působení operací Weylovy grupy. Dvě operace, konvoluce a křížová korelace na orbitách jsou popsány pomocí znaménkových homomorfismů dostupných pro Weylovy grupy ranku 2, včetně jejich vlastností.

Klíčová slova: konvoluce, křížová korelace, Weylovy grupy, transformace na orbitách

1 Introduction

Many types of orbit functions and related transforms were introduced in a series of recent articles, e.g. [1]–[7]. Related Weyl groups which are utilized by these functions and transforms provide a solid framework for defining families of operation for systems with non-orthogonal basis. In this article we deal with two orbit operations, in particular orbit convolution and cross-correlation. These two operations can be defined using Weyl groups in a natural way which leads to operations with properties that are close to properties of common convolution and cross-correlation. Moreover, common convolution and cross-correlation are special cases of orbit operations described in this paper.

2   Weyl groups

2.1   Definition and fundamental domains

Let us have a root system with simple roots $\Delta = \{\alpha_1, \alpha_2\}$ spanning space $\mathbb{R}^2$. Reflections r_i are defined with respect to hyperplanes orthogonal to simple roots and intersecting at the origin. Weyl group W is generated by reflections r_1, r_2.

For definition of orbit functions and transform we use the following set of lattices:

- Root lattice $Q = \mathbb{Z}\alpha_1 + \mathbb{Z}\alpha_2$,

- Dual root lattice $Q^\vee = \mathbb{Z}\alpha_1^\vee + \mathbb{Z}\alpha_2^\vee$, where $\alpha_i^\vee = \frac{2\alpha_i}{\langle \alpha_i, \alpha_i \rangle}$,

- Weight lattice $P = \mathbb{Z}\omega_1 + \mathbb{Z}\omega_2$, where $\langle \omega_i, \alpha_j^\vee \rangle = \delta_{ij}$,

- Dual weight lattice $P^\vee = \mathbb{Z}\omega_1^\vee + \mathbb{Z}\omega_2^\vee$, where $\langle \omega_i^\vee, \alpha_j \rangle = \delta_{ij}$

Longest root in α-basis is expressed as $\alpha_0 = \xi = m_1\alpha_1 + m_2\alpha_2$. The coefficients m_i are called marks. We define another reflection hyperplane orthogonal to the highest root and containing points $\frac{\omega_1^\vee}{m_1}$ and $\frac{\omega_2^\vee}{m_2}$.

Affine Weyl group W^{aff} can be defined in two ways. The first way defines affine Weyl group as a semi-direct product of Weyl group W and translation group defined by lattice $Q^\vee$, i.e. $W^{\text{aff}} = W \rtimes Q^\vee$. Equivalently we can define W^{aff} to be generated by a set of reflections $\{r_0, r_1, r_2\}$.

Fundamental region of W^{aff} is a triangle with vertices $\left\{0, \frac{\omega_1^\vee}{m_1}, \frac{\omega_2^\vee}{m_2}\right\}$, i.e.

$$F = \left\{x_1\omega_1^\vee + x_2\omega_2^\vee \mid x_0, x_1, x_2 \geq 0 \wedge x_0 + m_1 x_1 + m_2 x_2 = 1\right\}.$$

For arbitrary $M \in \mathbb{N}$ we define discrete fundamental domain F_M of affine Weyl group W^{aff} as an intersection of fundamental domain F and a finite lattice $\frac{1}{M}P^\vee/Q^\vee$. The explicit form of the discrete fundamental domain is as follows

$$F_M = \left\{\frac{s_1}{M}\omega_1^\vee + \frac{s_2}{M}\omega_2^\vee \mid s_0, s_1, s_2 \in \mathbb{Z}^{\geq 0} \wedge s_0 + m_1 s_1 + m_2 s_2 = M\right\}$$

2.2   Sign homomorphism

Weyl group can also be defined by set of conditions laid upon the reflections r_i:

$$r_i^2 = 1, \qquad\qquad (r_i r_j)^{m_{ij}} = 1, \quad i, j = 1, 2 \qquad\qquad (1)$$

Coefficients m_{ij} are entries of Coxeter matrix related to reflections r_i.

Sign homomorphism $\sigma : W \to \{\pm 1\}$ has to fulfil the conditions (1):

$$\sigma(r_i)^2 = 1, \qquad\qquad (\sigma(r_i)\sigma(r_j))^{m_{ij}} = 1, \quad i, j = 1, 2 \qquad\qquad (2)$$

Two homomorphisms satisfying (2) are available for all Weyl groups:

$$\mathbb{1}(w) = 1 \qquad\qquad\qquad \sigma^e(w) = \det(w)$$

For groups with short and long roots we denote the reflection with respect to hyperplane orthogonal to long root as r_l and call it "long reflection", the term "short reflection", denoted as r_s, refers to the reflection by a mirror orthogonal to short root. Let's define

$$\sigma^s(r_s) = 1 \qquad\qquad \sigma^s(r_l) = -1$$
$$\sigma^l(r_s) = -1 \qquad\qquad \sigma^l(r_l) = 1$$

Each group operation w can be decomposed into product of reflections $r_{i1}, \ldots, r_{ik}$, where $r_{ij} \in \{r_s, r_l\}$. For groups with long and short roots there are two more sign homomorphisms satisfying (2):

$$\sigma^s(w) = \prod_{j=1}^{k} \sigma^s(r_{ij}), \quad \sigma^l(w) = \prod_{j=1}^{k} \sigma^l(r_{ij})$$

3   Orbit functions and transforms

In this section we define orbit functions, introduce their properties useful for further definition of scalar product and transforms.

3.1   Orbit functions

For any sign homomorphism $\sigma : W \to \{\pm 1\}$, $x \in \mathbb{R}^2$ and $\lambda \in P$ we can define orbit function

$$\phi_\lambda^\sigma(x) := \sum_{w \in W} \sigma(w)\, \mathrm{e}^{\imath 2\pi \langle w\lambda, x\rangle}$$

The choice of homomorphism leads to different orbit functions:

σ	function
$\mathbb{1}$	$C-$function
σ^e	$S-$function
σ^s	S^s-function
σ^l	S^l-function

These orbit functions are either invariant or anti-invariant to actions of $w \in W$

$$\phi_{w\lambda}^\sigma(x) = \sigma(w)\phi_\lambda^\sigma(x) \tag{3}$$
$$\phi_\lambda^\sigma(wx) = \sigma(w)\phi_\lambda^\sigma(x) \tag{4}$$

and are also invariant to shift $q \in Q^\vee$

$$\phi_\lambda^\sigma(x + q) = \phi_\lambda^\sigma(x) \tag{5}$$

Due to the invariance (3), (4) and (5) we can restrict parameter x and label λ to the following lattices and regions

σ	x	λ
$\mathbf{1}$	F	P^+
σ^e	$\text{int } F$	P^{++}
σ^s	$F \setminus H^s$	$P^+ \setminus (H^s \cap P^+)$
σ^l	$F \setminus H^l$	$P^+ \setminus (H^l \cap P^+)$

where $H^s = \{x \in F \mid \langle x, \alpha_s \rangle = 0\}$ and $H^l = \{x \in F \mid \langle x, \alpha_l \rangle = 0 \vee \langle x, \alpha_0 \rangle = 1\}$. Orbit functions with non-trivial sign homomorphism are anti-invariant on some edges of fundamental domain. These functions vanish to zero on the edges due to the invariance, thus we remove the edges from the set of parameters and labels.
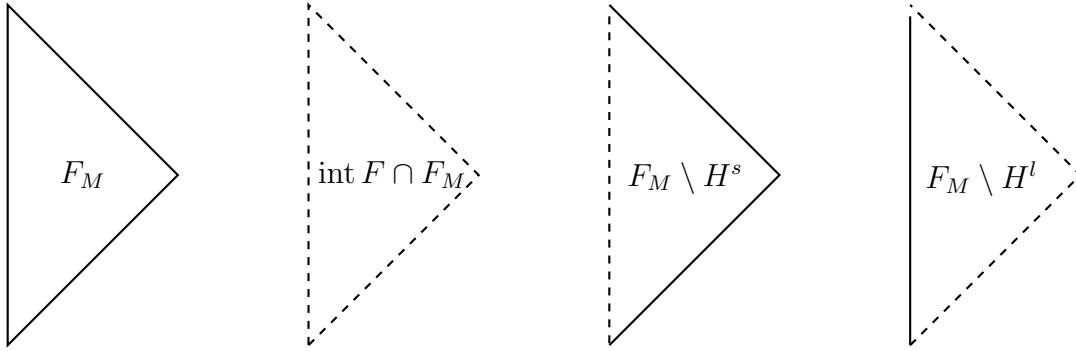
Figure 1: Fundamental region for Weyl group C_2 for different sign homomorphisms σ. From left to right: $\mathbf{1}$, σ^e, σ^s, σ^l.

3.2   Orbit transforms

Scalar product over a discrete fundamental domain is defined as

$$\langle f, g \rangle_{F_M} := \sum_{x \in F_M} \varepsilon(x) f(x) \overline{g(x)}$$

The coefficient $\varepsilon(x)$ is called weight of point x and is computed as $\varepsilon(x) = \frac{|W|}{|\text{stab}_W(x)|}$, where $\text{stab}_W(x) = \{w \in W \mid wx = x\}$. Since orbit functions for $\sigma \neq \mathbf{1}$ are zero-valued on certain parts of boundaries of F_M, the summation range is sometimes shrunken, e.g.

$$\left\langle \phi_\lambda^{\sigma^e}, \phi_\lambda^{\sigma^e} \right\rangle_{\widetilde{F}_M} = \sum_{x \in \widetilde{F}_M} \varepsilon(x) \phi_\lambda^{\sigma^e}(x) \overline{\phi_\lambda^{\sigma^e}(x)} \qquad \text{for } \phi_\lambda^{\sigma^e}$$

where $\widetilde{F}_M = \text{int } F \cap F_M$.

We define discrete set of labels Λ_M as

$$\Lambda_M = P/MQ \cap MF^\vee$$

where $F^\vee$ is dual fundamental domain, simplex with vertices $\left\{ 0, \frac{\omega_1}{m_1^\vee}, \frac{\omega_2}{m_2^\vee} \right\}$, coefficients $m_i^\vee$ are called dual marks and are the coordinates of dual long root ξ in $\alpha^\vee$ basis. The set Λ_M is

restricted in a similar way as fundamental domain F_M with respect to sign homomorphism σ, we use Λ_M for $C-$function, $\widetilde{\Lambda}_M$ for $S-$ function, $\Lambda_M \setminus H^s$ for S^s-function and $\Lambda_M \setminus H^l$ for S^l-function.

For $\lambda, \lambda' \in \Lambda_M$ orbit functions hold orthogonality relation

$$\langle \phi_\lambda^\sigma, \phi_{\lambda'}^\sigma \rangle_{F_M} = cM^2 |W| |\mathrm{stab}_W(\lambda)| \, \delta_{\lambda\lambda'}$$

Constant c denotes determinant of Cartan matrix $C = (c_{ij})_{i,j=1}^2$, $c_{ij} = \langle \alpha_i, \alpha_j \rangle$.

The expansion of function f is the following

$$f(x) = \sum_{\lambda \in \Lambda_M} F_\lambda^{(\sigma)} \phi_\lambda^\sigma(x) \tag{6}$$

$$F_\lambda^{(\sigma)} = \frac{\langle f, \phi_\lambda^\sigma \rangle_{F_M}}{\langle \phi_\lambda^\sigma, \phi_\lambda^\sigma \rangle_{F_M}} \tag{7}$$

4 Orbit convolutions and cross-correlations

In this section we introduce the orbit convolution and orbit cross-correlation and discuss their properties. There are several types of orbit convolutions and cross-correlations, each related to one type of orbit functions. The way how they are defined allows us to use orbit transforms in a similar way the Fourier transform is used with common convolution and cross-correlation, i.e. change the operation into spectra multiplication in frequency domain. Some details about two types of orbit convolutions are to be published in [2].

4.1 Orbit convolution and cross-correlation

Let W be a Weyl group, F_M its discrete fundamental domain. Let functions f and g be defined on F_M and $x \in F_M$ be an arbitrary point in F_M. For sign homomorphism σ we define orbit convolution as:

$$(f *^\sigma g)(x) := \sum_{y \in F_M} \varepsilon(y) f(y) \sum_{w \in W} \sigma(w) g(x - wy)$$

Orbit cross-correlation is defined as follows:

$$(f \star^\sigma g)(x) := \sum_{y \in F_M} \varepsilon(y) \overline{f(y)} \sum_{w \in W} \sigma(w) g(x + wy) \tag{8}$$

For $\sigma \neq \mathbf{1}$ we might need to remove appropriate edges from F_M, otherwise we need to define both functions on the whole fundamental region F_M.

We will use the term "orbit operations" for both orbit convolution and orbit cross-correlation in the following text.

There can be up to four types of orbit operations on Weyl group or rank 2. However, A_2 group has all roots of the same length, thus providing only two types, with sign homomorphisms $\mathbf{1}$ and σ^e.

4.2 Orbit convolution properties

In this subsection we describe properties of orbit convolution. Its properties coincide with properties of common convolution.

commutativity $f *^\sigma g = g *^\sigma f$

associativity $f *^\sigma \left(g *^{\sigma'} h \right) = g *^{\sigma'} \left(f *_\sigma h \right)$

distributivity $f *^\sigma \left(g + h \right) = f *^\sigma g + f *^\sigma h$

scalar multiplication associativity $a \left(f *^\sigma g \right) = (af) *^\sigma g$

One of the ways to prove the commutativity of orbit convolutions uses orbit convolution theorem. Orbit convolution (8) is commutative for all four homomorphisms $\mathbf{1}$, σ^e, σ^s and σ^l.

When both convolutions $f *^\sigma g$ and $f *^{\sigma'} g$ are commutative, the associativity property can be written as $f *^\sigma \left(g *^{\sigma'} h \right) = (f *^\sigma g) *^{\sigma'} h$. The commutativity is held for orbit convolution regardless the sign homomorphism σ.

4.3 Orbit convolution and cross-correlation theorem

Similar to common convolution and cross-correlation, orbit operations are changed to spectra multiplication in frequency domain. There are three transforms involved in the process – one type of transform is used for obtaining spectrum of each function involved, one inverse transform is used for bringing the result from frequency to spatial domain. Generally, these transform are not of the same basic function $\phi_\lambda^\sigma(x)$. Types of transforms involved are bound be certain rules which will become obvious from the formulas of theorems.

For orbit operation theorems we need the formulas for orbit function multiplication. The proof of the following property can be achieved by direct computation.

$$\phi_\lambda^\sigma(x)\phi_\lambda^{\sigma'}(y) = \sum_{w \in W} \sigma'(w)\phi_\lambda^{\sigma\sigma'}(x + wy)$$

Complex conjugation of any factors on the left side changes the sign of the related argument on the right side of the equation.

Let's have two functions f and g and sign homomorphisms σ and σ'. The $\sigma-$orbit operations can be expressed as

$$(f *^\sigma g)(x) = \sum_{\lambda \in \Lambda_M} \langle \phi_\lambda^\sigma, \phi_\lambda^\sigma \rangle_{F_M} F_\lambda^{(\sigma)} G_\lambda^{(\sigma'\sigma)} \phi_\lambda^{\sigma'}(x)$$

$$(f \star^\sigma g)(x) = \sum_{\lambda \in \Lambda_M} \langle \phi_\lambda^\sigma, \phi_\lambda^\sigma \rangle_{F_M} \overline{F_\lambda^{(\sigma)}} G_\lambda^{(\sigma'\sigma)} \phi_\lambda^{\sigma'}(x)$$

For $\sigma \neq \mathbf{1}$ we should use set Λ_M without edges on which $\phi_\lambda^\sigma(x) \equiv 0$, as noted in section 3. For λ laying on the mentioned edge, we can define F_λ^σ to be equal to zero to help us solving this problem and thus obtaining the generic formulas above.

The orbit convolution theorem can be used for a proof of commutativity of orbit convolution. Let's fix the homomorphism $\sigma' = \mathbb{1}$. Since $\mathbb{1}\sigma = \sigma$, we can easily see that both $(f *^\sigma g)(x)$ and $(g *^\sigma f)(x)$ are equal to $\sum_{\lambda \in \Lambda_M} \langle \phi_\lambda^\sigma, \phi_\lambda^\sigma \rangle_{F_M} F_\lambda^{(\sigma)} G_\lambda^{(\sigma)} \phi_\lambda^1(x)$.

The main advantage of orbit operation theorem is the speed at which we could compute the operation, as long as we can do fast computation of orbit transform. We know fast orbit transform algorithms for Weyl group A_1 or semi-simple groups $A_1 \times \ldots \times A_1$, i.e. family of $n-$dimensional Fourier transforms. We still can't provide any way leading to fast orbit transform algorithm for Weyl group of rank above 1.

4.4 Mixed orbit operations

It is also possible to define mixed orbit operations, i.e. convolution and cross-correlation, based on subgroups $W^\sigma = \{w \in W \mid \sigma(w) = 1\}$. These mixed operations will have different fundamental domains and domains of labels for pairwise orthogonal mixed orbit functions. Details about this subgroups and mixed functions can be found in [1]. Subgroups W^σ would provide up to six types of orbit operations for groups with short and long roots, or only one type for group with single-length roots (A_2).

Mixed orbit operations will most likely hold both convolution and cross-correlation theorems, we suppose they are going to be associative, scalar multiplication associative and distributive, however, the commutativity might not be held for mixed orbit convolutions.

4.5 Kernel (anti-)symmetry

All orbit operations introduce some sort of kernel symmetry. The sign homomorphism σ determines which group operations produce symmetric reflections and which reflections are anti-symmetric. The required symmetry of kernel is somehow limiting in applications of orbit operations.

5 Concluding remarks

The topic of orbit functions and related Weyl groups provide strong opportunities for further research. There are several problems to be explored, e.g. fast orbit transform algorithm, mixed orbit operations, application of orbit operations. Orbit convolutions and orbit cross-correlation described in this article are defined to generalization of common convolution and cross-correlation. All types of orbit convolution share several properties known from common convolution.

References

[1] L. Háková, J. Hrivnák, J. Patera, *Six types of E-functions of the Lie groups O(5) and G(2)*, J. Phys. A: Math. Theor. **45** (2012).

[2] L. Háková, O. Kajínek, *Applications of Weyl group orbit functions and related discrete transforms in image processing*, to be published.
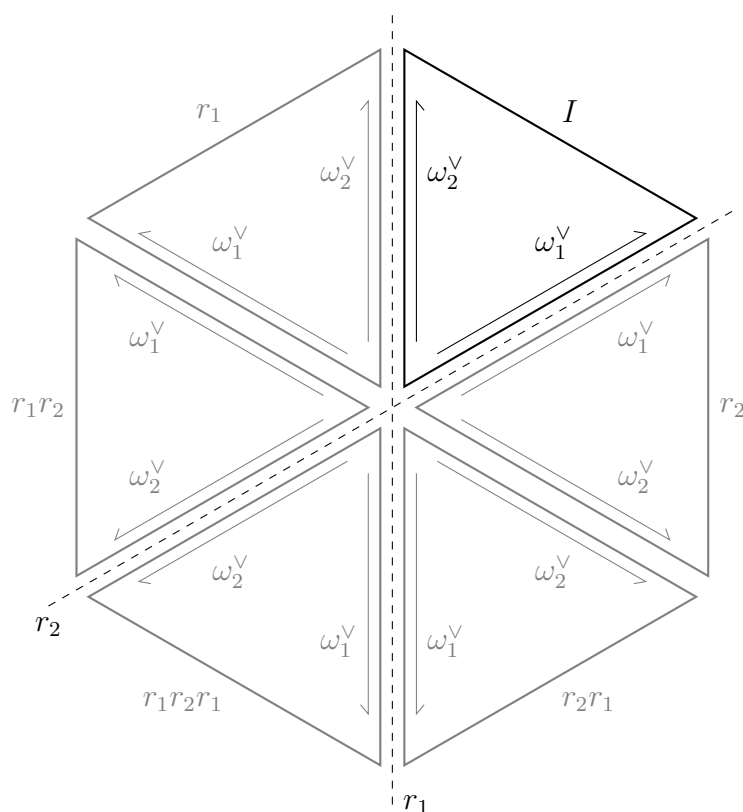
Figure 2: Demonstration of kernel (anti-)symmetry for group A_2. The kernel is reflected by all operations of Weyl group W, the sign is changed with respect to sign homomorphism σ used for orbit operation.

[3] J. Hrivnák, L. Motlochová, J. Patera, *On discretization of tori of compact simple Lie groups II*, J. Phys. A: Math. Theor. **45** (2012).

[4] J. Hrivnák, J. Patera, *On discretization of tori of compact simple Lie groups*, J. Phys. A: Math. Theor. **42** (2009).

[5] A. Klimyk, J. Patera, *Orbit functions*, SIGMA (Symmetry, Integrability and Geometry Methods and Applications) **2** (2006).

[6] R. V. Moody, J. Patera, *Orthogonality within the families of C-, S-, and E-functions of any compact semisimple Lie group*, SIGMA (Symmetry, Integrability and Geometry Methods and Applications) **2** (2006).

[7] M. Szajewska, *Four types of special functions of G2 and their discretization*, Integral Transforms and Special Functions **6** (2012).

Multigrid Method for Linear Complementarity Problem and its Implementation on GPU

Vladimír Klement

4th year of PGS, email: `wlada@post.cz`
Department of Mathematics
Faculty of Nuclear Sciences and Physical Engineering, CTU in Prague

advisor: Tomáš Oberhuber, Department of Mathematics
Faculty of Nuclear Sciences and Physical Engineering, CTU in Prague

Abstract. We present the CUDA implementation of the parallel multigrid solver for the linear complementarity problem (LCP). The linear complementarity problem is considered in the following form

$$\mathbb{A}\mathbf{x} \geq \mathbf{b}, \tag{1}$$

$$\mathbf{x} \geq \mathbf{c}, \tag{2}$$

$$(\mathbb{A}\mathbf{x} - \mathbf{b})^T (\mathbf{x} - \mathbf{c}) = \mathbf{0}, \tag{3}$$

where $\mathbb{A}$ is symmetric positive definite matrix and $\mathbf{c}$ is a given vector (constraint). This kind of problems arises for example in computational mechanics [2], financial mathematics [4] or image processing [3].

To solve such problems the Projected SOR (PSOR) method introduced in [5] can be used. If the problem arises from the discretization of a PDE with a constraint, the geometric multigrid method [1] with the PSOR method used as a smoother can be applied [4, 6]. We present a parallelization of this approach which is applicable even to problems with sparse matrix $\mathbb{A}$. The parallel solver is implemented in CUDA to run on the GPU.

The efficiency of the final algorithm is demonstrated on the constrained level-set method used for image segmentation. For this task, the speed-up up to 3 was achieved on Nvidia GeForce GTX 480 compared to the more expensive 12 core AMD Opteron.

Keywords: LCP, geometric multigrid, projected SOR, GPU.

Abstrakt. Tento článek představuje CUDA implementaci multigridního řešiče pro lineární systém s podmínkami. Za lineární systém s podmínkami je považován systém v následující formě

$$\mathbb{A}\mathbf{x} \geq \mathbf{b}, \tag{4}$$

$$\mathbf{x} \geq \mathbf{c}, \tag{5}$$

$$(\mathbb{A}\mathbf{x} - \mathbf{b})^T (\mathbf{x} - \mathbf{c}) = \mathbf{0}, \tag{6}$$

kde $\mathbb{A}$ je symetrická pozitivně definitní matice a $\mathbf{c}$ je daný vektor podmínek. Tento typ problémů vzniká například při simulaci elastických jevů [2], ve finanční matematice [4] nebo ve zpracování obrazu [3].

Pokud daný problém vznikl diskretizací diferenciálních rovnic s omezeními (a tudíž je výsledná matice $\mathbb{A}$ řídká), je možno ho velmi efektivně řešit pomocí geometrického multigridu [1], který

bude jako zhlazovač využívat projekční SOR (PSOR) metodu [4, 6]). Naše implementace představuje právě tuto možnost, která je navíc plně paralelizována pomocí technologie CUDA a může tak k řešení využívat výkon grafické karty.

Účinnost výsledného algoritmu je demonstrována na úloze segmentace obrazu pomocí constrained level-set metody. Řešení tohoto problému bylo v GPU verzi běžící na GeForce GTX 480 třikrát rychlejší než v CPU verzi používající dražší dvanácti jádrový procesor AMD Opteron.

Klíčová slova: LCP, geometrický multigrid, projekční SOR metoda, GPU.

The article was published in International Journal of Applied Mathematics 45.3 (2015).

References

[1] W. L. Briggs, V. E. Henson and S.F. McCormick, "A Multigrid Tutorial", Society for Industrial and Applied Mathematics, 2000.

[2] Y. Hailing, Z. Depei, "Solving Elastic Contact Problems with Friction as Linear Complementarity Problems Based on Incremental Variational Principles", in *Computational Mechanics' 95*, Springer Berlin Heidelberg, pp. 1504-1509, 1995.

[3] V. Klement, T. Oberhuber, and D. Ševčovič, "On a constrained level-set method with application in image segmentation", submitted for publication, arXiv:1105.1429v1.

[4] C. W. Oosterlee, "On multigrid for linear complementarity problems with application to American-style options", *Electronic Transactions on Numerical Analysis*, voL. 15, no. 1, pp. 165-185, 2003.

[5] O. L. Mangasarian, "Solution of symmetric linear complementarity problems by iterative methods", *Journal of Optimization Theory and Applications*, voL. 22, no. 4, pp. 465-485, 1977.

[6] I. Yavneh, "On Red-Black SOR Smoothing in Multigrid", *SIAM Journal on Scientific Computing*, voL. 17, no. 1, pp. 180-192, 1996.

Evolving Dislocations under Total Strain Control Regime[*]

Miroslav Kolář

4th year of PGS, email: `kolarmir@fjfi.cvut.cz`
Department of Mathematics
Faculty of Nuclear Sciences and Physical Engineering, CTU in Prague

advisor: Michal Beneš, Department of Mathematics
Faculty of Nuclear Sciences and Physical Engineering, CTU in Prague

Abstract. We study the evolution and mutual force interaction of two distinct dislocations in the channel of the persistent slip band, and under the total strain controlled loading condition. In our investigation, we focus on estimation of the endurance limit, i.e., on the value of the applied stress needed for dislocations to escape each other. Our description of the model is based on the parametric method, and for the numerical solution, the semi-implicit flowing finite volume method is used.

Keywords: mean curvature flow, dislocation dynamics, parametric method

Abstrakt. Tento příspěvek se zabývá studiem vývoje a silové interakce dvou dislokaví v PSB kanále. Pohyb dislokací je řízen v tzv. total strain controlled režimu, který je diskutován v článku. Naším cílem je odhadnout hodnotu aplikovaného napětí, při kterém dojde k odtržení silově interagujících dislokací. Matematický popis problému je založen na parametrické metodě a k numerickému řešení je použita metoda plovoucích konečných objemů.

Klíčová slova: pohyb křivek řízený střední křivostí, dislokační dynamika, parametrizace

1 Introduction

Crystalline structure of real materials contains imperfections, i.e., the defects and irregularities in the regular arrangement of atoms. These irregularities occur in nanoscale. In microscale, they have the volume, the surface, or most typically, the line character, and their presence significantly influences the macroscale mechanical properties of crystalline solids. Thus, these imperfections are considered as the key elements to understanding the phenomenon of crystal plasticity [1, 2]. In this contribution, we are concerned with imperfections of the line character, also called dislocations – they act in such a way that the crystallographic arrangement of atoms is disturbed along a so called dislocation line.

Where dislocations are exposed to external forces, they tend to glide in so called slip planes, i.e., the crystallographic planes with high density of atoms. The forces acting on the dislocation originate, e.g., in loading of the crystal by some applied stress, in mutual interactions of multiple dislocations, or in the response of the actual structure the dislocations are gliding in.

Throughout the last century, the comprehensive theoretical framework concerning the dynamics of dislocations was developed, and many modelling techniques were proposed and estabilished. Among them, we recall the standard discrete dislocation dynamics (DDD), which acts on microscale and tries to predict the material properties further usable on higher spatial scales. See, e.g., [3, 4].

In standard DDD, it is typically assumed that the stress applied on the crystal is uniform (see [7, 8]). Thus, we call this a stress controlled regime and discuss it in [9]. Unlike this approach, we evaluate the same DDD problem, assuming different loading condition. In our case, we consider the sum of elastic and plastic strain to be uniform in the crystal, and call this a total strain controlled regime [5, 6]. We have studied the effect of different loading conditions in [9, 15], and our interpretation is that the total strain control regime provides the lower estimate of the endurance limit of the crystal.

Our model problem is the following. We consider the two initially straight dislocations $\Gamma^{(1)}$ and $\Gamma^{(2)}$ of the opposite signs with the Burgers vector $\mathbf{b} = (b, 0, 0)$, defining the distorsion of the crystal lattice. The dislocations are positioned to be parallel with the x-axis of the standard x, y and z coordinate system, and both evolve in distinct slip planes, both of them parallel to the xz-plane and in mutual distance h. The motion of dislocations is also restricted to the channel of the persistent slip band (for details about the PSB structure, see [9]) of the width d_c.

As the dislocations evolve and draw near, their mutual force interaction is to be taken into the account. The nearer they are, the stronger their attractive interaction is, which speeds up their motion. When dislocations overlap, the force interaction becomes repulsive, which slows down their movement, and eventually stops it, forming a dipole configuration. The objective of our investigation is to determine the value of the applied stress needed for the dislocations to pass each other (i.e., the endurance limit) under the total strain control loading condition (compare with [15]).

2 Mathematical model

Our modelling approach is based on the mathematical theory of moving curves [7, 8, 10, 11]. Considering an evolving planar curve, or generally an interface, its motion can be captured by the mean curvature flow, which schematically reads as

$$\text{normal velocity} = (\text{mean}) \text{ curvature} + \text{force}. \tag{1}$$

Now let us consider a dislocation curve Γ_t gliding in its slip plane. Within the context of dislocation dynamics presented in this contribution, we employ the following form of the motion law

$$B v_\Gamma = -T \kappa_\Gamma + F. \tag{2}$$

Here v_Γ is the velocity in the outer normal direction, κ_Γ is the curvature of the Γ_t, and F is the sum of external forces acting on Γ_t in the normal direction. Also, B denotes the drag coefficient and T is the line tension and depends on the tangential angle ξ. In accordance with [1], line tension is aproximated as $T \approx E^{(e)}(1 - 2\nu + 3\nu \cos^2 \xi)$, where $E^{(e)}$ is the dislocation edge energy and ν is the Poisson ratio. All parameters of the model are tabulated in Table 1.

Our aim is to find a family $\{\Gamma_t : t \in [0, T]\}$ of open planar nonselfintersecting curves with fixed endpoints evolving from given initial curve γ_{ini} and satisfying (2). We treat equation (2) in such a way that the curve Γ_t is parametrized by the following vectorial function

$$\mathbf{X} = \mathbf{X}(t, u) = (X_1(t, u), X_2(t, u)) \tag{3}$$

for the dimensionless parameter $u \in [0, 1]$. At $u = 0$ and $u = 1$, the fixed ends boundary conditions are prescribed, i.e., $\mathbf{X}|_{u=0} = \mathbf{X}_0$ and $\mathbf{X}|_{u=1} = \mathbf{X}_1$. The parametrization of $\mathbf{X}$ and the outer unit normal vector $\mathbf{n}_\Gamma$ are oriented in such a way that $\det(\mathbf{n}_\Gamma, \mathbf{t}_\Gamma) = 1$ holds for the unit tangential vector $\mathbf{t}_\Gamma$.

The geometrical quantities of our interest are derived from parametrization $\mathbf{X}$. The unit tangent and normal vectors are given as

$$\mathbf{t}_\Gamma = \frac{\partial_u \mathbf{X}}{|\partial_u \mathbf{X}|}, \quad \mathbf{n}_\Gamma = \frac{\partial_u \mathbf{X}^\perp}{|\partial_u \mathbf{X}|},$$

and the curvature is expressed from Frenet formulae as

$$\kappa_\Gamma = -\frac{1}{|\partial_u \mathbf{X}|} \partial_u \left(\frac{\partial_u \mathbf{X}}{|\partial_u \mathbf{X}|} \right) \cdot \mathbf{n}_\Gamma.$$

Here, $\mathbf{X}^\perp = (X_2, -X_1)$. Also notice that the curvature of the unit circle is $\kappa_\Gamma = 1$. The normal velocity is

$$v_\Gamma = \partial_t \mathbf{X} \cdot \mathbf{n}_\Gamma.$$

Finally, the evolution of dislocation curve Γ_t is driven by the motion law (2) provided the parametric mapping $\mathbf{X}$ satisfies the following system of degenerate parabolic equations

$$\partial_t \mathbf{X} = \frac{1}{|\partial_u \mathbf{X}|} \partial_u \left(\frac{\partial_u \mathbf{X}}{|\partial_u \mathbf{X}|} \right) + F \frac{\partial_u \mathbf{X}^\perp}{|\partial_u \mathbf{X}|},$$
$$\mathbf{X}|_{t=0} = \mathbf{X}_{ini}, \tag{4}$$

for $t \in [0, T]$ and $u \in [0, 1]$.

3   Force term analysis

Here we recall the main idea of modelling of external forces acting on the dislocation curve Γ_t. In our model, we consider the three following force term contributions

- The applied force $F_{app} = b\tau_{app}$. This force is caused by the resolved shear stress aplied on the crystal sample.

- The wall force $F_{wall} = b\tau_{wall}$. This force is generated by the walls of the chammel of the persistent slip band.

- The interaction force $F_{int} = b\tau_{int}$. This force is caused by interaction of multiple dislocation curves.

3.1   The applied force

The stress applied on the crystal is the only external component of our model. In this article, we investigate the so called "total strain controlled regime", which can be basically interpreted as a lower estimate of the reality used in discrete dislocation dynamics techniques (see [5, 15]).

Here, we consider a uniform total shear strain $\varepsilon_{tot}(t)$ in the whole PSB channel. In our computations, we use a simplified linear model in time with the constant total shear strain rate $\dot{\varepsilon}$, i.e.,

$$\varepsilon_{tot}(t) = \dot{\varepsilon}t.$$

Then, we use the decomposition of total shear strain into the elastic part τ_{app}/μ and the plastic part $\varrho b \int_0^t v_\Gamma(u, \tau) d\tau$, i.e.,

$$\varepsilon_{tot}(t) = \dot{\varepsilon}t = \frac{\tau_{app}}{\mu} + \varrho b \int_0^t v_\Gamma(u, \tau) d\tau.$$

Here, τ_{app} is the actual applied stress, μ is the shear modulus, ϱ is the density of the dislocations, and v_Γ is the normal velocity as in (2). The geometrical interpretation of the relaxation term $\int_0^t v_\Gamma(u, \tau) d\tau$ is the area slipped by the dislocation Γ_t. In our computations, the slipped area is approximated by areas of parallelograms constructed as in [5, 6].

Finally, the applied force acting on the crystal reads as

$$F_{app} = b\tau_{app}.$$

3.2   The wall force

The glide of a dislocation is considered within the PSB (persistent slip band) channel [1, 2]. Generally, it is a structure consisting of areas with high density of dislocations (channel walls) and low density of dislocations (channel itself). This pattern typically arises from a cyclic loading of a crystal. Dislocation gliding in the channel interacts with the dipolar loops (another closed dislocation curves inside the crystal). Many clustered dipolar loops create the walls of the channel. This force interaction is usually simulated as elastic fields of infinite edge dipoles in the channel walls, which act like a potential wells generated by the dipoles.

For detailed analysis, we refer the reader to, e.g., [9]. In this article, we restrict ourselves to schematic description, where the stress generated by the PSB channel is approximated as a higher order polynomial

$$\tau_{wall} = \frac{\mu b}{2\pi} \frac{1}{1-\nu} \left(\frac{x_1(x_1^2 - y_1^2)}{(x_1^2 + y_1^2)^2} - \frac{x_2(x_2^2 - y_2^2)}{(x_2^2 + y_2^2)^2} + \frac{x_3(x_3^2 - y_3^2)}{(x_3^2 + y_3^2)^2} - \frac{x_4(x_4^2 - y_4^2)}{(x_4^2 + y_4^2)^2} \right),$$

where $x_{1,2,3,4}$ and $y_{1,2,3,4}$ are coordinates in the psb channel centered to the two pair of dislocation dipolar loops forming a dipoles on both sides of the channel. Then, the wall force reads as

$$F_{wall} = b\tau_{wall}.$$

From the construction, it follows that the channel wall force $F_{wall} = F_{wall}(\mathbf{X}) = F_{wall}(X_1)$ and acts in the x-axis of the channel. The graph is in Figure 1.
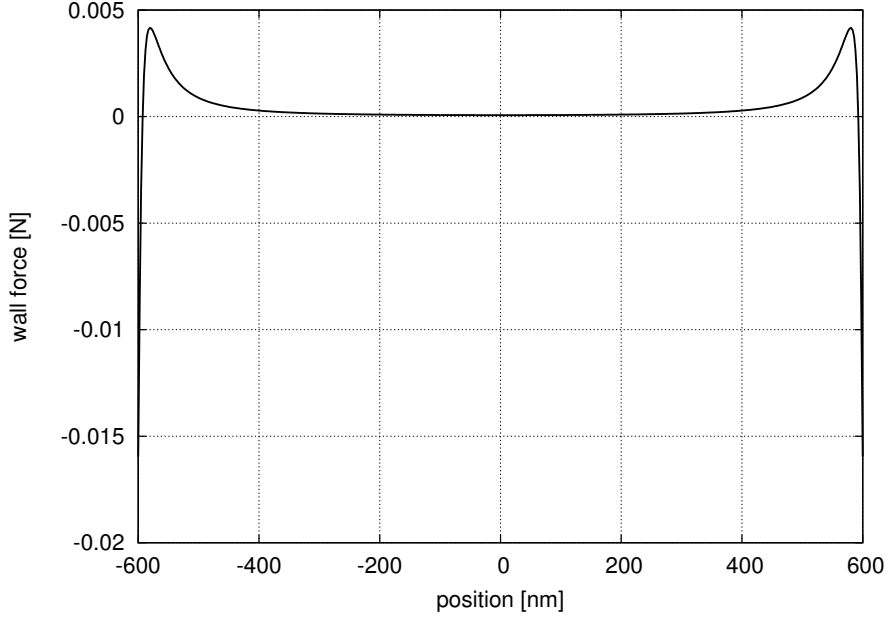
Figure 1: Wall force function, the x-axis is in nanometers, the y-axis is in Newtons.

3.3 The interaction force

As the dislocations glide, they are also influenced by their mutual interaction. Since we approximate the dislocations as polygonal curves, all force interactions are sums of contributions of straight dislocation segments.

To solve this problem, one needs to determine the stress tensor field $\tau_{int} = (\tau_{int}(\mathbf{X}))_{i,j}$ at a position $\mathbf{X}$ from a straight segment AB of a dislocation. This issue is discussed in paper by Devincre [13], where a general formula providing the 3D stress tensor field $\tau^A(\mathbf{X}) = (\tau^A)(\mathbf{X})_{ij}$ at a position $\mathbf{X}$ generated by the dislocation half line from the point $\mathbf{A}$ to infinity is derived.

The stress tensor generated at the point $\mathbf{X}$ by a straight dislocation segment, let us say AB, is given as the difference of the tensors τ^A and τ^B

$$(\tau_{int}(\mathbf{X}))_{ij}^{AB} = \tau(\mathbf{X})_{ij}^A - \tau(\mathbf{X})_{ij}^B.$$

Then the total interaction stress is calculated as the sum of all stress contributions from all the segments of the particular considered dislocation

$$(\tau_{int})_{ij} = \sum_k (\tau_{int})_{ij}^k,$$

where k goes over all segments of the considered dislocation.

The force acting on the dislocation exposed to the stress field τ_{int} is given by Peach-Koehler formula [14], which reads as

$$\vec{F}_{int} = (\tau_{int}\mathbf{b}) \times \mathbf{t}_\Gamma. \tag{5}$$

The normal component of the interaction force is

$$F_{int} = \vec{F}_{int} \cdot \mathbf{n}_\Gamma.$$

Because of the geometry of the model we use, and the particular direction of the Burgers vector described in the Introduction, after some calculations (for more details, check [9, 15]) we see that only τ_{12} component of the interaction tensor τ_{ij} is required, and the interaction force reads as

$$F_{int} = b(\tau_{int})_{12}.$$

4 Numerical approximation scheme

We deal with motion law (4) by means of the semi-implicit method as in [7, 8, 12, 16]. For spatial discretization, the flowing finite volumes method is used. Along the curve Γ_t, we place the discrete nodes $\mathbf{X}_i = \mathbf{X}(t, u_i)$ for $i = 0, 1, \ldots M$, and denote

$$d_j = |\mathbf{X}_j - \mathbf{X}_{j-1}|,$$

for $j = 1, 2, \ldots M$, where $\mathbf{X}_0$ and $\mathbf{X}_M$ are the fixed ends boundary conditions. Discretization in time is provided by the forward differences as

$$\frac{\partial \mathbf{X}_i}{\partial t} \approx \frac{\mathbf{X}_i^{k+1} - \mathbf{X}_i^k}{\Delta t}.$$

The superscript k is the k-th time level for $t_k = k\Delta t$. The time step Δt was chosen as $\Delta t = 1/h^2$, where $h = 1/M$. The discretized forcing term is denoted as $F_i^k = F(\mathbf{X}_i^k)$ The resulting scheme reads as follows

$$\frac{\mathbf{X}_i^{k+1} - \mathbf{X}_i^k}{\Delta t} \frac{d_{i+1}^k + d_i^k}{2} = \frac{T}{B} \left(\frac{\mathbf{X}_{i+1}^{k+1} - \mathbf{X}_i^{k+1}}{d_{i+1}^k} - \frac{\mathbf{X}_i^{k+1} - \mathbf{X}_{i-1}^{k+1}}{d_i^k} \right) + \frac{F_i^k}{B} \frac{\mathbf{X}_{i+1}^{\perp,k} - \mathbf{X}_{i-1}^{\perp,k}}{2}, \quad (6)$$

$$\mathbf{X}_i^0 = \mathbf{X}_{\text{ini}}(u_i). \tag{7}$$

For more detailed discussion on the numerical scheme, we refer the reader to, e.g., [9], where we also discuss the effect of tangential terms and redistribution of the discretization points based on previous work of Ševčovič and Yazaki [12].

5 Computational studies

We show the results of our numerical experiment of two initially straight dislocations of the opposite sign, approaching each other in their slip planes and constrained in the PSB channel. The parameters of the model are tabulated in Table 1. The dynamics of the evolution is depicted in Figure 2.

The objective of our studies is to determine the lower estimate of the value of the passing stress, i.e., the stress when the dislocations break the dipole steady state and escape each other. For this task, we employ the method originally proposed by Mughrabi
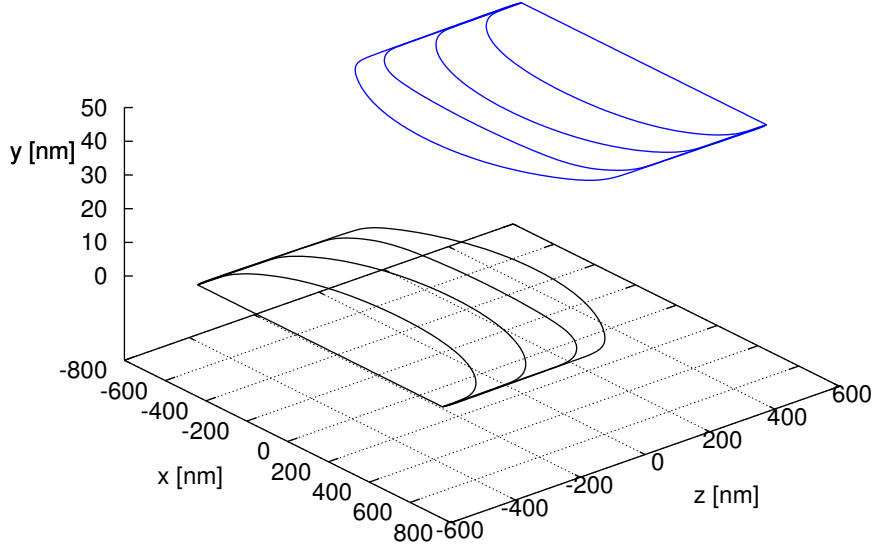
Figure 2: Time evolution of two dislocations (black – lower and blue – upper). When the dislocations draw near, they slows down and tend to straighten, while the applied stress still increases. When overlap, they continue to glide and bow out again.

and Pschenitzka in [17]. According to their approach, to obtain the passing stress, one wants to maximize the following quantity called the overall stress

$$\tau(u,t) = Bv(u,t) - \tau_{app}(u,t),$$

where $u \in [0,1]$. To neglect the nonintended effect of the channel walls, we measure this quantity in the middle of the channel, i.e., in $u = 0.5$. The graph of the passing stress is in Figure 3. Here we can see that the passing stress for our configuration as about $\tau_{pass} \approx 23.8$ MPa.

Burgers vector magnitude	$b = 0.256$ nm
Dislocation edge energy	$E^{(e)} = 2.35$ nN
Drag coefficient	$B = 1.0 \times 10^{-5}$ Pa$\cdot$s
Plane distance	$h = 50$ nm
Channel width	$d_c = 1200$ nm
Shear modulus	$\mu = 42.1$ GPa
Poisson ratio	$\nu = 0.43$
Density of glide dislocations	$\varrho = 1 \times 2 \cdot 10^{-5}$ nm^{-2}
Total strain time rate	$\dot{\varepsilon} = 1.9 \times 10^{-3}$ s^{-1}

Table 1: Parameters of the numerical experiment
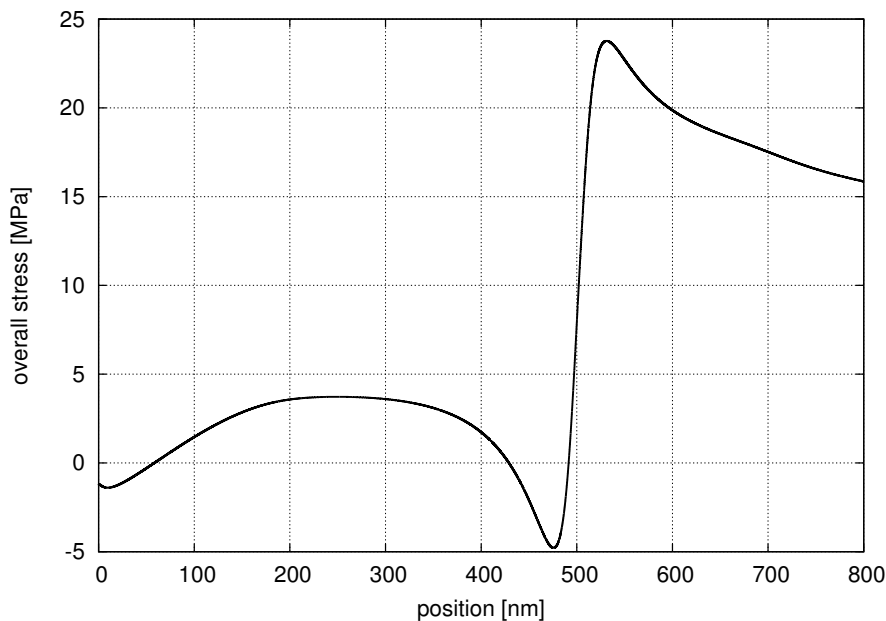
Figure 3: Overall stress reaching its maximum of 23.8 MPa (measured in the middle of the channel).

6 Conclusion

We presented geometrical evolution equation describing the motion of planar curve representing a dislocation. We discussed the parametric description of the problem and analyzed the character of driving forces including the loading condition under the total strain controlled regime. For the numerical solution of the problem, we employ the semi-implicit method with spatial discretization based on the flowing finite volume method. We also presented one of our results of numerical experiments concerning the estimation of the passing stress (i.e., the endurance limit), which is in a good agreement with our previous modelling and also with literature [17].

References

[1] D. Hull and D. Bacon, *Introduction to dislocations*, Fifth ed., Butterworth-Heinemann, 2011.

[2] T. Mura, *Micromechanics of Defects in Solids*, Kluwer Academic Publishers Group, Netherlands, 1987.

[3] V. V. Bulatov and w. Cai, *Computer Simulations of Dislocations*, Oxford University Press, 2006.

[4] A. Vattré, B. Devincre, F. Feyel, R. Gatti, S. Groh, O. Jamond and A. Roos, *Modelling crystal plasticity by 3d dislocation dynamics and the finite element method: The*

discrete-continuous model revisited, Journal of the Mechanics and Physics of Solids, 63 (2014), pp. 491–505.

[5] J. Křišťan, J. Kratochvíl, V. Minárik, M. Beneš *Numerical simulation of interacting dislocations glide in a channel of a persistent slip band*, Modelling and Simulation in Materials Science and Engineering, 17 045009 (2009).

[6] M. Beneš, J. Kratochvíl, J. Křišťan, V. Minárik and P. Pauš, *A parametric simulation method for discrete dislocation dynamics*, European Physical Journal ST, 177 (2009), 177–192.

[7] P. Pauš and M. Beneš, *Direct Approach to Mean-Curvature Flow with Topological Changes*, Kybernetika, 45 (2009), pp. 591–604.

[8] P. Pauš, J. Kratochvíl and M. Beneš, *A dislocation dynamics analysis of the critical cross-slip annihilation distance and the cyclic saturation stress in fcc single crystals at different temperatures*, Acta Materialia, Vol. 61 (2013), Issue 20, pp. 7917-7923.

[9] M. Kolář, M. Beneš, D. Ševčovič and J. Kratochvíl, *Mathematical Model and Computational Studies of Discrete Dislocation Dynamics*, IAENG International Journal of Applied Mathematics, 45 (2015), no. 3, pp. 198–207.

[10] K. Deckelnick, *Parametric mean curvature evolution with a dirichlet boundary condition*, Journal für die reine und angewandte Mathematik, 459 (1995), 37–60.

[11] G. Dziuk, K. Deckelnick and C. M. Elliott, *Computation of geometric partial differential equations and mean curvature flow*, Acta Numerica, 14 (2005), 139–232.

[12] D. Ševčovič and S. Yazaki, *Evolution of plane curves with a curvature adjusted tangential velocity*, Japan Journal of Industrial and Applied Mathematics, 28 (2011), 413–442.

[13] B. Devincre, *Three dimensional stress field expression for straight dislocation segment*, JSolid State Communications, 93 (1995), p. 875

[14] M. Peach and J. S. Koehler, *The forces exerted on dislocations and the stress fields produced by them*, Physical Review, (1950).

[15] M. Kolář, M. Beneš, J. Kratochvíl and P. Pauš, *Numerical Simulations of Glide Dislocations in Persistent Slip Band*, Acta Physica Polonica A, to appear (2015).

[16] K. Mikula and D. Ševčovič, *Computational and qualitative aspects of evolution of curves driven by curvature and external force*, Computing and Visualization in Science, 6 (2004), 211–225.

[17] H. Mughrabi and F. Pschenitzka, *Constrained glide and interaction of bowed-out screw dislocations in confined channels*, Philosophical Magazine 85 (2005), 3029.

Massive Neutrinos and Invisible Axion Minimally Connected

Helena Kolešová*

5th year of PGS, email: `helena.kolesova@fjfi.cvut.cz`
Department of Physics
Faculty of Nuclear Sciences and Physical Engineering, CTU in Prague

advisor: Michal Malinský, Institute of Particle and Nuclear Physics, FMP CU

Abstract. Recent developments in particle physics have established the "standard model" of particle interactions which is in great agreement with the collider experiments, the discovery of the Higgs boson being the last missing part. However, going beyond this standard model is motivated by several hints such as the non-zero mass of the neutrinos, the observation of the dark matter or the matter-antimatter asymmetry.

In this paper, we survey a few minimal extensions of the standard electroweak model by scalar particles that provide a simple setup for massive neutrinos in connection with a dark matter candidate, so called "axion". The presence of a chiral $U(1)$ symmetry drives the pattern of Majorana neutrino masses while providing a dynamical solution to another problem of the standard model, the strong CP problem, similarly as in the original work of Peccei and Quinn [3].

We paradigmatically apply such a renormalizable framework to type-II seesaw [4] and to two viable models for neutrino oscillations where the neutrino masses arise at one and two loops, respectively [2, 5, 1]. We comment on the naturalness of the effective setups as well as on their implications for vacuum stability and electroweak baryogenesis.

Keywords: axion, neutrino mass, type-II seesaw

Abstrakt. Díky současným pokrokům v částicové fyzice byl ustaven tzv. standardní model částicových interakcí, který je v dobrém souladu s experimenty na urychlovačích, završením této shody byl objev Higgsova bosonu. Avšak existují jevy, které tento standardní model vysvětlit nedokáže, jako například nenulová hmota neutrin, pozorování temné hmoty či nerovnováha mezi hmotou a antihmotou ve vesmíru.

V tomto článku se zabýváme několika rozšířeními standardního modelu elektroslabých interakcí o skalární částice tak, aby výsledný model obsahoval hmotná neutrina a zároveň tzv. axion, který může být kandidátem na temnou hmotu. Přítomnost chirální U(1) symetrie udává jednak strukturu Majoranovských hmot neutrin, ale hlavně pomáhá vyřešit další problém standardního modelu, narušení CP invariance silnými interakcemi, podobně jako v originální práci Peccei a Quinnové [3].

Tuto myšlenku aplikujeme na tři již existující modely hmot neutrin: tzv. seesaw mechanismus II. druhu [4] a dva modely, kde je hmota neutrin generovaná jedno- resp. dvousmyčkovým diagramem [2, 5, 1]. Diskutujeme též otázky stability elektroslabého vakua či možnosti elektroslabé baryogeneze pro tyto modely.

Klíčová slova: axion, hmota neutrin, seesaw mechanismus II. druhu

The full paper was published as S. Bertolini, L. Di Luzio, H. Kolešová, and M. Malinský. *Massive neutrinos and invisible axion minimally connected*. Phys.Rev. **D91** (2015), 055014.

References

[1] K. Babu. *Model of 'Calculable' Majorana Neutrino Masses*. Phys.Lett. **B203** (1988), 132.

[2] K. Babu and J. Julio. *Predictive Model of Radiative Neutrino Masses*. Phys.Rev. **D89** (2014), 053004.

[3] R. Peccei and H. R. Quinn. *CP Conservation in the Presence of Instantons*. Phys.Rev.Lett. **38** (1977), 1440–1443.

[4] J. Schechter and J. Valle. *Neutrino Masses in SU(2) x U(1) Theories*. Phys.Rev. **D22** (1980), 2227.

[5] A. Zee. *Quantum Numbers of Majorana Neutrino Masses*. Nucl.Phys. **B264** (1986), 99.

Option Pricing Beyond Black-Scholes Based on Double-Fractional Diffusion

Jan Korbel

3rd year of PGS, email: `korbeja2@fjfi.cvut.cz`
Department of Physics
Faculty of Nuclear Sciences and Physical Engineering, CTU in Prague

advisor: Petr Jizba, Department of Physics
Faculty of Nuclear Sciences and Physical Engineering, CTU in Prague

Abstract. We show how the prices of options can be determined with the help of double-fractional differential equation in such a way that their admixture to a portfolio of stocks provides a more reliable hedge against dramatic price drops than the use of options whose prices were fixed by the Black-Scholes formula. We focus on the application of several definitions of fractional derivatives to obtain several classes of temporally-spatially fractional diffusion equations. We test the fit of the model to the real option prices of index S&P 500 traded in November 2008.

Keywords: Double-fractional diffusion, Lévy option pricing, Risk redistribution.

Abstrakt. Naším cílem je ukázat, jak můžeme s pomocí frakční rovnice v prostoru i čase modelovat ceny opcí tak, že jejich portfolio poskytuje relevantější zajištění proti dramatickým propadům než v případě Black-Scholesova modelu. Zaměříme se také na aplikaci několika možných definic frakční derivace, abychom dostali několik tříd frakční difuzní rovnice. Tento model pak otestujeme na reálných cenách opcí indexu S&P 500 obchodovaných v listopadu 2008.

Klíčová slova: Frakční difuze, Lévyho modely cen opcí, Redistribuce rizika

This article has been submitted to Physica A and is available online at `http://arxiv.org/abs/1503.05655`.

Parabolic Strip Telescope and Control Software[*]

Vladislav Kosejk

2nd year of PGS, email: `kosejvla@fjfi.cvut.cz.cz`
Department of Mathematics
Faculty of Nuclear Sciences and Physical Engineering, CTU in Prague

advisors:

Goce Chadzitaskos, Department of Physics
Faculty of Nuclear Sciences and Physical Engineering, CTU in Prague

Jaromír Kukal, Department of Software Engineering
Faculty of Nuclear Sciences and Physical Engineering, CTU in Prague

Abstract. This contribution is focused on the development of special astronomical telescope, and especially its image processing. The physical model, designed for tests of functions and algorithms for an image reconstruction uses a reflective strip with a length of 30 cm. When comparing the rotational and Newtonian telescope, the main advantage of the rotating telescope is simple design of optical element and the allowance to produce high-resolution with the same objective area. Disadvantage in relation to other its need of one more rotational moving and subsequent image reconstruction. The rotational telescope is a promising technology. It has a potential to supplement the existing types of telescopes used to observe the Universe. Although rotational telescopes are more complex in terms of their assembly and the processing of a final image, but contrary to standard reflectors, the mirror of this type of a telescope is much lighter and cheaper. This enables to construct telescopes with the primary optical element of a size of tens of meters, while the construction remains to be simple and production costs low. The ideal deployment of the telescope will be on an orbit where the size of mirrors could run to hundreds of meters and their resolving abilities will be sufficient for direct tracking of extra solar objects.

Keywords: Rotational Telescope, angular resolution, image processing, astronomy.

Abstrakt. Tento článek se zaměřuje na popis vývoje speciálního astronomického dalekohledu a na zpracování obrazu z tohoto přístroje. Fyzický model dalekohledu vytvořený pro testování technologie a rekonstrukčních algoritmů využívá odrazový pás v délce 30 cm. Pokud srovnáme rotační teleskop a klasický Newtonův teleskopický systém, je hlavní výhodou rotačního teleskopu jednodušší design optického elementu při srovnatelném rozlišení dalekohledu. Nevýhodou tohoto systému v porovnání s ostatními typy dalekohledů je nutnost dalšího pohybu primárního obrazového elementu a následné zpracování obrazu. Rotační dalekohled je slibná technologie, která má potenciál, nahradit stávající dalekohledy pro pozorování vesmíru. I přes nutnost zpracování obrazu a složitější konstrukci je proti klasickému řešení, rotační teleskop levnější. To umožňuje stavět dalekohledy s optickým elementem v délce desítek metrů. Ideální umístění tohoto dalekohledu bude na oběžné dráze Země, kde velikost odrazové plochy může dosáhnout až stovek metrů a tím umožnit přímé sledování objektů mimo naši sluneční soustavu.

Klíčová slova: Rotační teleskop, úhlové rozlišení, zpracování obrazu, astronomie.

---

[*]Obrana a bezpečnost CZ.1.05/3.1.00/14.0304...

References

[1] Chadzitaskos G. 2013, Parabolic strip telescope, arXiv: astro-ph/1304.6530

[2] King H. C. 2003, The History of the Telescope, Dover Publication, New York

[3] Chadzitaskos G., Tolar J. 2007, CZ Patent 298313

[4] ESO 2012, The Very Large Telescope, `https://www.eso.org/public/teles-instr/vlt.html`

[5] Beylkin G. 1987, IEEE Transaction on Acoustics, Speech, and Signal

Monitoring and Modeling Emissions of Soil Radon*

Zuzana Kosejková

2nd year of PGS, email: `knoflice@gmail.cz`
Department of Mathematics
Faculty of Nuclear Sciences and Physical Engineering, CTU in Prague

advisor: Vojtěch Merunka, Department of Software Engineering
Faculty of Nuclear Sciences and Physical Engineering, CTU in Prague

Abstract. This paper was focused on analyse the data of soil radon and the temperatures measured at a height of 2m, ground temperature at a height 5 cm and the temperature below ground at a depth of 80 cm. Data was provided by Czech hydrometeorological institute (CHMI). Data are in weekly frequences in the period from 7.10.2002 to 15.6.2011. To analyse data series was used autoregression model AR(p), which is generally decsribed by the equation: $X_t = c + \sum_{i=1}^{p} \phi_i X_{t-i} + u_t$. According to the graphical representation it shows inverse relationship between temperature and concentration of soil radon. Indicator of correlation was the highest between time series radon concentration and temperature at a height of 2 m. When the appropriate model was selected, the residues was investigated and the exact period, which leads to higher deviations, was detected. In the context of exact period is used database of earthquakes in a world with magnitude higher than 7.0.

Keywords: Soil Radon, temperature, Data analysis, Time series, Autoregressive model.

Abstrakt. Tento článek se zabývá analýzou dat půdního radonu a naměřených teplot ve výšce 2m, přízemní teploty 5cm a teploty pod zemí v hloubce 80cm, které poskytl český hydrometeorologický ústav (ČHMÚ). Data mají týdenní frekvenci v období od 7.10.2002 do 15.6.2011. K analýze časových řad se využívá autoregresní model AR(p), obecně popsán rovnicí: $X_t = c + \sum_{i=1}^{p} \phi_i X_{t-i} + u_t$. Dle grafického znázornění je vidět nepřímá úměra mezi teplotou a koncentrací radonu. Ukazatel korelace byl nejvyšší mezi časovou řadou koncentrace radonu a teploty ve výšce 2m. Po zvolení vhodného modelu jsou dále zkoumána rezidua a zjišťují se přesná období, kdy dochází k vyšším odchylkám. V souvislosti s těmito daty je pak využitá databáze zemětřesení ve světě s magnitudou vyšší jak 7.0.

Klíčová slova: půdní radon, teplota, analýza dat, časové řady, autoregresní model.

Full version of this paper was accepted for publication in Bezpečnost jaderné energie `https://www.sujb.cz/dokumenty-a-publikace/casopis-bje/`.

References

[1] ZVÁRA, Karel a Josef ŠTĚPÁN. Pravděpodobnost a matematická statistika. 5. vyd. Praha: Matfyzpress, 2012, 230 s. ISBN 978-80-7378-218-4.

---

*Obrana a bezpečnost CZ.1.05/3.1.00/14.0304...

[2] CIPRA, Tomáš. Finanční ekonometrie. 1. vyd. Praha: Ekopress, 2008, 538 s. ISBN 978-80-86929-43-9.

[3] USGS: Earthquake "Top 10" Lists amp; Maps. U.S. GEOLOGICAL SURVEY. <i>USGS</i> [online]. 2015, August 03, 2015 15:36:42 UTC [cit. 2015-09-30]. Dostupné z: `http://earthquake.usgs.gov/earthquakes/eqarchives/`

[4] CONRADY, Jurgen, Andreas GUHL a Karel TUREK. Messungen der Radonkonzentration in der Bodenluft. Messungen der Radonkonzentration in der Bodenluft. 2011.

Mathematical Models of Tennis Matches Applied on Real Life Odds

Tomáš Kouřim

2nd year of PGS, email: `kourim@outlook.com`
Department of Mathematics
Faculty of Nuclear Sciences and Physical Engineering, CTU in Prague

advisor: Petr Volf, Department of Stochastic Informatics
Institute of Information Theory and Automation, CAS

Abstract. The demand for proper sport match prediction tools is constantly increasing together with the amount of money put into sports betting. A previously developed model based on Markov chains was further examined and tested against real life bookmaker odds in this paper. The results are based on the 2008-2014 ATP seasons.

Keywords: discrete Markov chain, tennis, in-play modeling

Abstrakt. Celosvětově vzrůstající množství prostředků vložených do sportovních sázek stupňuje poptávku po kvalitních nástrojích k predikci sportovních výsledků. V tomto článku je testován dříve představený model tenisových utkání založený na diskrétních Markovských řetězcích, a to proti skutečným kurzům vypsaných bookmakery. Závěry jsou postaveny na výsledcích světové tenisové série ATP z let 2008 až 2014.

Klíčová slova: diskrétní Markovovy řetězce, tenis, modelování herních situací

1 Introduction

Tennis is one of the oldest and most traditional sports, which is pursued worldwide and on all possible levels. It is an industry that operats with billions of dollars every year. It is therefore no wonder that even in such a traditional sport as tennis there are always new methods and technologies introduced. Computer imaging is used in the hawk-eye technology helping to determine whether a ball was out, material science allows to manufacture better and better rackets and other equipment, medicine science develops new methods of effective training etc. Mathematics is becoming a very important part of tennis as well as it can produce models simulating game situations and predicting their probabilities. This can be useful for the trainers who can use such models to better prepare their players for their matches, but most of all it is used for sports betting. The market of sports betting is despite strict regulations continuously growing both in revenues as in profits not only in the Czech Republic, but worldwide. It is therefore no wonder that the demand for accurate sport models is tremendous.

This paper is organized as follows. In the next section the odds provided by bookmakers and their relation to probability are discussed. Next follows basic application of Central Limit Theorem to the problem of tennis match prediction. Sections 4 and 5 describe the data and the experiments conducted on that data. Section 6 concludes the paper.

2   Odds

Suppose there are M possible outcomes $j = 1 \dots M$ of a random variable X representing a sporting event.[1] Let $p = (p_1, \dots p_M)$ be the probabilities of the respective outcomes j and $a = (a_1, \dots, a_M)$ bookmaker's odds, i.e. the bookmaker pays a_j units if one bets 1 unit[2] on event j and j is the actual outcome of the observation of random variable X and nothing otherwise[4].

Odds in general are some representations of the underlying probabilities, i.e. $a_j = f(p_j)$. More specifically, it holds that $a_j \cong \frac{1}{p_j}$. In order to make profit, bookmakers alter their odds such that $a_j < \frac{1}{p_j}$. Let us define

$$S(a) = 1 - \sum_{i=1}^{M} \frac{1}{a_i}$$

and further define *payout* as $P(a) = \frac{1}{1-S(a)}$ and *margin* as $M(a) = 1 - P(a)$. Payout and margin represent the amount of money lost by the bettor and won by the bookmaker, respectively, in case the bettor bets on all possible outcomes of the random variable the amount of money corresponding to the bookmaker's odds.

We say that the set a is sub fair odds if $S(a) < 0$, fair odds if $S(a) = 0$ and super fair odds if $S(a) > 0$. The special situation where $a_j = \frac{1}{p_j}$, $\forall j \in \hat{M}$ implies a is fair, however a fair does not necessarily imply the equation. In real life, the majority of odds is sub fair, as the bookmakers want to make profit. However as the competition between bookmakers sharpens, there sometimes occurs a situation, when it is possible to find super fair odds as a combination of odds provided by two (or more) different bookmakers.

Odds provided by a single bookmaker are always sub fair (unless there occurs an error in which case the situation is ignored). They also provide the bookmaker's estimate of the actual probabilities p_j of the respective outcomes. In order to obtain those probabilities, a normalizing function $a' = f(a)$ has to be introduced such that $S(a') = 0$ and $p_j = \frac{1}{a'_j}$. The obvious approach is to use the standard normalization procedure, that is

$$f_j(a_j) = a_j \cdot (1 - S(a)).$$

However, this approach does not correspond well with the reality. It consist of lowering the odd-corresponding probabilities to obtain actual probabilities by the formula

$$p_j = \frac{1}{a_j} + \frac{1}{a_j} \cdot S(a).$$

That is, the margin related "extra probability" $-S(a)$ is subtracted from the possible outcomes accordingly to their weights. As a consequence, the outcome with the highest probability is affected most, i.e. the probability of such outcome is lowered significantly more than that of the unlikely outcome. Empirical observation suggest that the most extreme pair of odds describing a tennis match is $a = (1.01, 20)$. This would suggest that the biggest favorite would only have about 95 % probability of winning which is almost

---

[1]Or any other event such as the result of a roulette wheel spin, loterry draw etc.

[2]For example \$1, 1 CZK or 5 % of total assets.

certainly not true. Also, if the bookmaker would like to keep a fixed margin (for example $10\,\%$)[3], then the inverse function of f would very often produce odds such that there would be $a_j < 1$ for some $j \in \hat{M}$. This is certainly an unwanted situation from a business point of view.

Empirical observation suggests that an opposite approach should be used, that is the more probable an outcome is the less is the odds-related probability lowered. For that, new normalization function g is introduced.

$$g_j(a_j) = \frac{a_j \cdot (M-1)}{(M-1) + a_j \cdot (1 - \frac{1}{f_j(a_j)}) \cdot S(a)}.$$

That is, the respective probabilities are obtained using

$$p_j = \frac{1}{a_j} + \frac{1 - \frac{1}{f_j(a_j)}}{M-1} \cdot S(a).$$

Finally, by introducing a parameter t a linear interpolation of the two approaches $F(a,t)$ can be obtained. Theoretically, $t \in \mathbb{R}$, however it only makes sense for $t \in [0,1]$. In practice it is however easier to use $t \in [0,2]$, that is $F(a,2) = f(a)$ and $F(a,0) = g(a)$.

3 Tennis match as a random variable

The result of a tennis match is an observation of a random variable X distributed by a Bernoulli distribution with unknown parameter $p \in (0,\ 1)$. When modeling a tennis match we thus focus on point estimate $\hat{p}$ of the actual parameter p. The biggest issue in this estimation is the fact that there is always only one observation of the random variable. Even if the conditions are as identical as possible, there still would be some differences in two tennis matches. The subject of examination is an interaction between two human beings and such an encounter is always unique.

Let say we want to examine the likeliness of the event that the favorite wins a game. If we consider N games, i.e. N random variables X_i which are all distributed by Bernoulli distributions with parameters $p = (p_1, \ldots, p_N)$, $p_i \in [0.5,\ 1)$[4], then the random variable

$$\dot{Y}_N = \sum_{i=1}^{N} X_i$$

can be by Lyapunov Central Limit Theorem[1] approximated by a normally distributed random variable $U \sim N(\sum_{i=1}^{N} E(X_i),\ \sum_{i=1}^{N} D(X_i))$. This allows us to test the null hypothesis that the actual parameters p are equal to the estimated parameters $\hat{p} = (\hat{p}_1, \ldots, \hat{p}_N)$. Moreover, this hold also for every large enough subset $N' \subseteq N$, which is further used for model testing in Section 5.

In case of odds this can be viewed from a slightly different point of view. Instead of observing the random variable $\dot{Y}_N$, we can take into account variable $\tilde{Y}_N$ representing the

---

[3]$10\,\%$ is still the most common margin on a pair of odds.
[4]p is at least 0.5 as we consider the win of the favorite.

total profit after N bets. First let us assume we bet 1 unit on each match, say we bet always on the favorite. The expected value is then $E(\tilde{Y}_N) = \sum_{i=1}^{N} E(\tilde{X}_i)$, where

$$E(\tilde{X}_i) = p_i \cdot (a_i - 1) + (1 - p_i) \cdot (-1) = p_i a_i - 1$$

and standard deviation

$$D(\tilde{X}_i) = p_i \cdot (a_i - 1 - (p_i a_i - 1))^2 + (1 - p_i) \cdot (-1 - (p_i a_i - 1))^2 = p_i \cdot (1 - p_i) \cdot a_i^2.$$

For the special case of fair odds where $a_i = \frac{1}{p_i}$ this yields $E(\tilde{Y}_N) = 0$ and $D(\tilde{Y}_N) = \sum_{i=1}^{N} \frac{1-p_i}{p_i}$.

Let us now define a random variable $Y_N(s, b)$ which represents the total profit after placing N bets with a betting strategy s and bet type $b \in \{F, O\}$ for betting on either favorite or outsider. The above mentioned function $\tilde{Y}_N = Y_N(1, F)$. Now assuming the fair odds with $a_i = \frac{1}{p_i}$ we get $E(Y_N(1, F)) = E(Y_N(1, O)) = 0$, but we get different values for the standard deviations. This can have some negative effects towards odds quality testing. For example, a good property would be if $Y_N(s, F) = -Y_N(s, O)$, $\forall N$. This does not hold for the strategy $s = 1$. It can even happen that the results for favorite and outsider are both positive or negative for a given set of matches. However, if we choose $s = \frac{1}{a}$ (and still assume $a_i = \frac{1}{p_i}$), then we get

$$E(Y_N(\frac{1}{a}, F)) = E(Y_N(\frac{1}{a}, O)) = \sum_{i=1}^{N} p_i(1 - p_i) + (1 - p_i) \cdot (-p_i) = 0$$

and

$$D(Y_N(\frac{1}{a}, F)) = D(Y_N(\frac{1}{a}, O)) = \sum_{i=1}^{N} p_i(1 - p_i)^2 + (1 - p_i) \cdot (-p_i)^2 = p_i(1 - p_i)$$

and finally

$$Y_N(\frac{1}{a}, F) = -Y(\frac{1}{a}, O), \ \forall N.$$

4   Data description

In order to test all possible models a database was created using information publicly available from www.livesport.com. The database contains information about men tennis games for 2008 thru 2014 ATP seasons. It has data about the game itself, such as who played, when, where, the final score, surface etc. and also about bookmakers' odds. It contains both game winning odds and first set winning odds from 9 bookmakers (two Czech bookmakers Tipsport and Fortuna and seven international bookmakers bet365, bwin, bet-at-home, Interwetten, Sportingbet, Unibet and William Hill). Additionally the maximum and average values for each match were computed and further considered as two different bookmakers.

The experiment considered in this paper only handles matches where there is necessary to win two sets in order to win a match, therefore the best-of-five matches (i.e. Grand
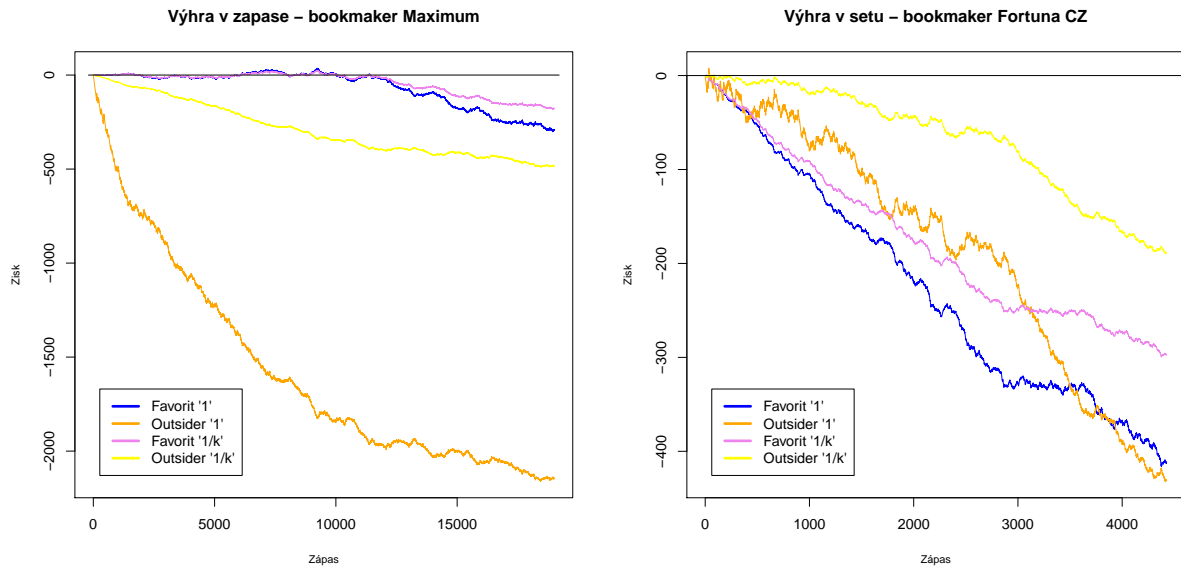
Figure 1: Development of the random variable $Y_N(s, b)$ for different s and b and actual maximal odds for a win in a match and odds by Fortuna for win in the first set.

Slam tournaments, Davis cup and The Olympic Games) were omitted from the database. Also, only ATP tournaments were considered, as these are much more prestigious than Challenger or ITF tournaments and thus the data as well as the bookmakers' odds should be more accurate. Altogether there were about 20 000 matches in the database. There was some information missing for most of them (such as the odds from a certain bookmaker), this however did not affect the usability of such database. If there was certain piece of information missing that was important for a given experiment, the match was simply omitted. In all modes of the experiment there were still enough matches remaining (usually well above one thousand).

5 Experiments

5.1 Bookmaker odds quality

To test bookmakers' odds the betting strategies $s_1 = 1$ and $s_2 = \frac{1}{a}$ defined in Sec. 3 were used. Figure 1 shows some examples of the development of the total profit when employing the two basic betting strategies on the actual odds provided by different bookmakers both on winning the match and winning the first set of a match. The outcome is very similar for all bookmakers as the odds are sub fair. When taken the maximum value there were 1 333 cases when the odds were super fair which opens the opportunity for winning without a risk. The matches in the graphics are ordered by the favorite odds a_i, lowest first. The shape of the curves confirms the suggestion mention in Sec 2, that is the odds of the biggest favorites are very close to those corresponding with the true winning probabilities. No further testing was done as the situation is obvious. The odds are sub fair and do reflect the reality is some way.

5.2 Model derivation

Tracking all the individual variables that might influence the outcome of a tennis match (and the probabilities of an outcome) several years backwards is a difficult task. Some parts of it, such as the past results, past player's rankings or even point by point match development can be done with the help of computers. On the other hand, there are some variables that certainly influence a tennis game which are very difficult to track in real time and virtually impossible to track backwards. Those are especially some life events of individual players, such as a small illness or injury, change of a personal physiotherapist or even a baggage lost during a flight. Such variables can (but not necessarily have to) influence match outcomes and without their knowledge, computing probabilities from past results can introduce some kind of bias. However, professional bookmakers keep (and have always kept) track of all those individual variables and already incorporated those into their match odds. The odds provided by the bookmakers thus serve as a good starting point in deriving any model.

As a first step the simple odds-based models were derived from the odds by different bookmakers. That is, the pair of odds for the win of a match (sub fair odds) were normalized using the normalization function $F(a, t)$ introduced in Section 2 and 9 different parameter values. There were also together 99 odds-based models for the match probabilities.

In [3] a Markov chain based model is introduced. It computes the set winning probabilities using the game winning probabilities provided by bookmakers under the hypothesis that all sets played in a match are independent identically distributed random variables, that is

$$p_{match} = p_{set}^2 + 2 \cdot p_{set}^2 \cdot (1 - p_{set}). \tag{1}$$

The results of [3] suggest that this independence assumption is false in general, but quite accurate for the first set of a match.

The *iid* model is derived by applying Equation 1 to the odds-based model from a certain bookmaker. This cubic equation can be numerically solved for example using the Newton-Raphson algorithm [2], allowing us to obtain a set of first set winning probabilities $p_{set} = (p_{set_1}, \ldots, p_{set_N})$.

5.3 Model testing

To test the quality of the models, new fair odds were derived from the model ($a_i = \frac{1}{p_i}$) and three betting strategies were applied on each model and the corresponding values of random variables $Y_N(1, F)$, $Y_N(1, O)$ and $Y_N(\frac{1}{a}, F)$ (as defined in Sec 3) for all N. For each such strategy the maximum absolute value and the average value (for all possible $n \leq N$) were computed as a quality parameters.

For each[5] $n \leq N$, a null hypothesis H_0 can be stated as the matches is a series of Bernoulli distributions with parameters $p = (p_1, \ldots, p_N)$, i.e. $Y_n \sim N(0, \sum D(X_i))$. To test the hypothesis the critical value of the 95 % confidence interval was computed for each point. Then, the ratio of Y_n and the critical value was observed. Again, the maximal and average values were computed (here, the maximal value greater than 1 indicates that

---

[5]n has to be big enough to satisfy CLT, usually at least 30.

at some point the data were sufficient to decline the null hypothesis on a 95 % level). Finally, the standard log-likelihood was computed for each model.

These 13 criteria were computed for all 99 odds-based models to determine which one should be used as a base for the *iid* model. As these criteria are hardly comparable with each other, the models that "scored" best in one of the criteria were taken into account for further examination. This procedure indicated 4 odds-based models for match winning probabilities. The models and their scores in the testing criteria can be seen in Table 1.

Criterion	bet365, 0.75	Tipsport, 0.25	Fortuna CZ, 0	Fortuna, 0.25
Log-likelihood	-0.563	-0.576	-0.574	-0.576
$max_{n \leq N}\|Y_n(1,F)\|$	162.974	30.567	39.685	59.9
$max_{n \leq N}\|Y_n(1,O)\|$	217.591	124.105	104.188	167.459
$max_{n \leq N}\|Y_n(\frac{1}{a},F)\|$	96.605	23.302	21.714	39.749
$\frac{1}{N}\sum_{i=1}^{N} Y_i(1,F)$	39.177	10.189	7.04	16.379
$\frac{1}{N}\sum_{i=1}^{N} Y_i(1,O)$	74.034	63.765	14.191	87.289
$\frac{1}{N}\sum_{i=1}^{N} Y_i(\frac{1}{a},F)$	25.146	7.864	4.579	11.755
$max_{n \leq N}(\frac{\|Y_n(1,F)\|}{N(0,D(Y_n))})$	1.049	0.641	1.58	0.827
$max_{n \leq N}(\frac{\|Y_n(1,O)\|}{N(0,D(Y_n))})$	0.783	0.57	1.446	0.539
$max_{n \leq N}(\frac{\|Y_n(\frac{1}{a},F)\|}{N(0,D(Y_n))})$	0.964	0.621	1.578	0.82
$\frac{1}{N}\sum_{i=1}^{N}\frac{Y_i(1,F)}{N(0,D(Y_n))}$	0.363	0.212	0.145	0.258
$\frac{1}{N}\sum_{i=1}^{N}\frac{Y_i(1,O)}{N(0,D(Y_n))}$	0.163	0.24	0.069	0.299
$\frac{1}{N}\sum_{i=1}^{N}\frac{Y_i(\frac{1}{a},F)}{N(0,D(Y_n))}$	0.333	0.212	0.138	0.259

Table 1: Best odds-based models for match win. The first line suggest the original bookmaker and the parameter value that was used to transform the sub fair odds into fair odds.

Then the *iid* based probabilities were derived from these top odds-models. Again the model quality was tested using the 13 test criteria, the results are in Table 2.

5.4 Comparison with actual betting

Finally, the quality of the 4 *iid* based first set models was tested against actual odds.[6] The two betting strategies ($s = 1$ and $s = \frac{1}{a}$) were used, but this time one would bet only when the bookmaker's odd was higher than the odd corresponding to the probability given by the model. Bets were done on both favorite and outsider and were ordered as the matches were actually played thorough the time. The results are in Table 3. The results do not show any significant profit and some models even show loss. To improve this result, the betting strategy was slightly altered in the way that the bets were placed only on the odds that are at least 10 % higher than the probability related odds. The results from this upgraded strategy are shown in Table 4. These results are much more

---

[6]Odds that were publicly available for betting.

Criterion	bet365, 0.75	Tipsport, 0.25	Fortuna CZ, 0	Fortuna, 0.25
Log-likelihood	-0.617	-0.631	-0.627	-0.631
$max_{n \leq N}\|Y_n(1,F)\|$	216.761	91.193	117.122	58.169
$max_{n \leq N}\|Y_n(1,O)\|$	627.829	125.874	165.810	92.646
$max_{n \leq N}\|Y_n(\frac{1}{a},F)\|$	151.54	52.221	67.745	29.061
$\frac{1}{N}\sum_{i=1}^{N} Y_i(1,F)$	100.22	28.577	35.976	14.579
$\frac{1}{N}\sum_{i=1}^{N} Y_i(1,O)$	412.731	50.073	64.761	36.522
$\frac{1}{N}\sum_{i=1}^{N} Y_i(\frac{1}{a},F)$	76.689	18.043	22.954	8.66
$max_{n \leq N}(\frac{\|Y_n(1,F)\|}{N(0,D(Y_n))})$	1.936	0.747	1.145	0.91
$max_{n \leq N}(\frac{\|Y_n(1,O)\|}{N(0,D(Y_n))})$	1.936	0.659	0.987	0.678
$max_{n \leq N}(\frac{\|Y_n(\frac{1}{a},F)\|}{N(0,D(Y_n))})$	1.912	0.699	1.082	0.895
$\frac{1}{N}\sum_{i=1}^{N}\frac{Y_i(1,F)}{N(0,D(Y_n))}$	0.982	0.339	0.482	0.232
$\frac{1}{N}\sum_{i=1}^{N}\frac{Y_i(1,O)}{N(0,D(Y_n))}$	1.351	0.253	0.365	0.223
$\frac{1}{N}\sum_{i=1}^{N}\frac{Y_i(\frac{1}{a},F)}{N(0,D(Y_n))}$	1.056	0.325	0.471	0.215

Table 2: Best *iid*-based models for first set win. The names suggest the original bookmaker and the parameter value that was used to derive the *iid* odds.

interesting. It can be seen that the best model was able to generate profit over 20 %, which is a significant gain.

Criterion	Fortuna, 0	Fortuna, 0.25	Tipsport, 0.25	bet365, 0.75
$Y_N(1)$	61.4	45.06	-10.28	-38.24
$Y_N(\frac{1}{a})$	4.59	-2.26	-11.54	2.5
$min_{n \leq N} Y_n(1)$	-30.46	-44.85	-23.11	-129.76
$min_{n \leq N} Y_n(\frac{1}{a})$	-15.51	-20.59	-13.9	-15.72
$\frac{Y_N(1)}{N}$	0.0232	0.0153	-0.0045	-0.0075
$\frac{Y_N(\frac{1}{a})}{N}$	0.0017	-0.0008	-0.0051	0.0005
$\frac{Y_N(\frac{1}{a})}{\sum \frac{1}{a_i}}$	0.0051	-0.0024	-0.0153	0.0015
Bets on favorite	335	221	230	1088
Bets on outsider	2644	2715	2033	4040

Table 3: Results when betting on odd higher than those obtained by the *iid* derived model. The first line indicates which original odds where used as a baseline to derive the *iid* odds.

6   Conclusion and future work

This paper discusses the possible ways of predicting the result of a tennis match and especially the first set. It uses a simple *iid* assumption to derive first set winning probabilities

Criterion	Fortuna, 0	Fortuna, 0.25	Tipsport, 0.25	bet365, 0.75
$Y_N(1)$	14.82	89.01	35.24	65.47
$Y_N(\frac{1}{a})$	-0.23	14.35	8.79	18.59
$min_{n\leq N}Y_n(1)$	-27.46	-28.71	0	-26.54
$min_{n\leq N}Y_n(\frac{1}{a})$	-7.16	-7.65	0.16	-3.02
$\frac{Y_N(1)}{N}$	0.0284	0.12	0.0794	0.1104
$\frac{Y_N(\frac{1}{a})}{N}$	-0.0004	0.0193	0.0198	0.0314
$\frac{Y_N(\frac{1}{a})}{\sum \frac{1}{a_i}}$	-0.0022	0.0934	0.0974	0.2177
Bets on favorite	2	2	1	5
Bets on outsider	520	740	443	588

Table 4: Results when betting on odd at least $10\,\%$ higher than those obtained by the *iid* derived model. The first line indicates which original odds where used as a baseline to derive the *iid* odds.

from the match winning probabilities provided by normalized bookmaker odds. These probabilities were then tested on real data and the results suggest that the predictions are more accurate than the bookmakers' odds as there are possible winning strategies available. The next step is to update the models in a way they could predict the result of set two and possibly set three and also some other aspects of the game.

References

[1] J. Anděl. Základy matematické statistiky. 2., praha: Matfyzpress. Technical report, ISBN 80-86732-40-1, (2005).

[2] C. T. Kelley. *Solving nonlinear equations with Newton's method*, volume 1. Siam, (2003).

[3] T. Kouřim. *Markov chain testing with application in tennis match outcomes*. Doktorandské dny FJFI (2014).

[4] I. Vajda. Information-theoretic methods in statistics. Technical report, Academy of Sciences of the Czech Republic, (1995).

Pattern Formation in Turing Reaction-Diffusion Models with Spatially Dependent Coefficient[*]

Michal Kozák

3rd year of PGS, email: `michal.kozak@fjfi.cvut.cz`
Department of Mathematics
Faculty of Nuclear Sciences and Physical Engineering, CTU in Prague

advisor: Václav Klika, Department of Mathematics
Faculty of Nuclear Sciences and Physical Engineering, CTU in Prague

Abstract. The pattern formation due to the chemical instability is one of the most important phenomenon in many non-equilibrium systems, ranging from a developmental biology to gas-discharge systems, a crystal growth in solidifying alloys, plasma or semiconductors. The recognised fundamental symmetry breaking mechanism is a diffusion-driven instability (Turing instability [2]) in a reaction-diffusion system (RD-system). Turing showed that a small perturbation of a well-mixed homogeneous system of autocatalic and inhibitory diffusing species could cause an instability, which leads to an emergence of the spatial patterns.

The resulting patterns of the model are strongly periodic, which is not sufficient to describe the situations when patterns depend on space; for example a distribution of mouse or cat whiskers [3], alternating thin and thick stripes of Lionfish [6] and an emergence of fingers [4]. The dissimilarities from the symmetric patterns in this cases cannot be elucidated by model simplicity only by the idealization of the model – the non-symetry can be crucial. Hence, we will assume a spatial dependence of coefficients of the RD-system and we will analyze the behavior.

The problem was analyzed numerically, see [6]. The analytic analysis of the solusion stability of the system with spatial dependent coefficients is in general difficult since the stationary solution depends on space. Afterall, some progress has been established; an analysis of so called spikes for Gierer-Meinhardt model [5] or the stability in special cases of spatial dependence: only in the absolute term of the kinetics using ε-series [8] and [9] or if the same term is of the form of a step function [7]. This article deals with the system with the spatial dependent coefficient at the linear term of the activator kinetics.

Let us consider a RD-system in the interval $(0, L)$ and similarly as in [7] we investigate the simplest form of the dependence – a step function at ξ. In the case of linear kinetics the stationary solution can be expressed analytically; in the case of non-linear kinetics it can be obtained, based on the previous case, that the emergence of the non-homogenous pattern can be predicted from the stability of the constant stationary solutions of the systems considered separately on the intervals $(0, \xi)$ and (ξ, L). Therefore, the conditions to the pattern formation are obtained. The results are ilustrated by numerical experiments of RD-model with Schnackenberg's kinetics.

The contribution of the article lies in the interpretation of obtained results. As it is expected, the system behavior is continuous with respect to the size and the position of the step – except when the system parameters do not lie near the border of the Turing's space. In this critical case, a step-driven instability can be said to occur. More importantly, as the stationary state depends nonlinearly on the jump magnitude due to the kinetics, the resulting pattern can show significant changes of wavelength in the considered domain even for small jump values. This is

---

relevant in the biological examples mentioned above as a motivation. Moreover, the procedure is promising to be used to analyze models with more complicated spatial dependence of the coefficients, which is the direction of the future work.

Abstrakt. Vznik prostorových struktur je jedním z nejdůležitějších jevů v mnoha nerovnovážných systémech, počínaje vývojovou biologií přes růst krystalů v tuhnoucích slitinách, konče plasmou nebo polovodiči. Základním mechanismem k narušení symetrie je nestabilita způsobená difuzí (diffusion driven instability; Turingova nestabilita [2]) reakčně-difuzních systémů (RD-systém). Turing ukázal, že malá perturbace homogenního systému autokatalyticky a inhibičně difundujících druhů mohou způsobit nestabilitu, která vede ke vzniku prostorových struktur.

Výsledkem tohoto modelu jsou silně periodické vzorky, což nepokrývá případy obrazců měnících se s prostorem, například rozložení myších fousků [3], měnící se šířka pruhů u perutýnů [6] nebo růst prstů na končetinách [4]. Odlišnosti od symetrických obrazců už v těchto příkladech nelze odůvodnit pouze idealizací matematického modelu, jejich nesymetrie bývá životně důležité pro dané organismy. Pro získání takových obrazců uvažujme prostorovou závislost koeficientů RD-systému a zkoumejme jeho chování.

Tento problém se již zkoumal numericky, viz [6]. Vyšetřovat analyticky stabilitu řešení systému s koeficienty závislými na prostoru je ale obecně obtížné, jelikož již stacionární řešení na prostoru silně závisí. V literatuře se můžeme setkat s vyšetřováním stability tzv. spikes pro Gierer-Meinhardtův systém [5], nebo stability ve speciálních případech závislosti koeficientů: v absolutním členu kinetiky pomocí ε-rozvoje [8] a [9] nebo koeficientu absolutního členu ve formě skokové funkce [7]. Tento článek se zabývá systémem s prostorově závislým koeficientem u lineárního členu aktivátoru.

Uvažujeme RD-systém nad intervalem $(0, L)$ a podobně jako v [7] zkoumáme nejjednodušší případ závislosti ve formě skokové funkce v bodě ξ. V případě lineárníc kinetik jsme schopni nalézt stacionární řešení analyticky, v případě nelineárních kinetik pak na tomto základě dostaneme, že vznik prostorového vzoru jsme schopni predikovat ze stability konstantního stacionárního řešení systému zvlášť nad intervalem $(0, \xi)$ a nad (ξ, L). Odsud pak dostáváme podmínky pro vznik prostorových vzorů. Tyto výsledky jsou pak ilustrovány numerickými výpočty RD-modelu se Schnackenbergovými kinetikami.

Přínos tohoto článku je v interpretaci těchto výsledků. Jak se dalo očekávat, chovaní systému je spojité ve velikosti i poloze skoku skokové funkce – pokud ovšem nejsou parametry systému blízko hranice Turingova prostoru. To pak dochází, přeneseně řečeno, k nestabilitě způsobené skokem. Podstatnější ale je, že jelikož na skoku závisí i stacionární stav, a to nelineárně kvůli kinetikám, můžeme i pro malé skoky dosáhnout vzoru s výraznými odlišnostmi na levé a pravé straně, což je relevatní zvláště vzhledem k aplikacím na popis obrazců v přírodě zmíněné výše. Navíc je tento postup slibný pro analýzu modelů se složitější prostorovou závislostí, což je dílem dalšího zkoumání.

Klíčová slova: reakčně-difuzní systém, nehomogenní Turingův model, pattern formation.

References

[1] Kozák, M. and Klika, V. and Gaffney, E. A., *Pattern formation in Turing reaction-diffusion models with spatially dependent coefficient.* will be submitted in Physical Review E.

[2] Turing, A., *The chemical basis of morphogenesis.* Phil. Trans. R. Soc. Lond. B, **237** (1952), 37–72.

[3] Painter, K. J. and Hunt, G. S. and Wells, K. L. and Johansson, J. A. and Headon, D. J., *Towards an integrated experimetal–theoretical approach for assesing the mechanistic basis of hair and feather morphogenesis.* Interface Focus **2** (2012), 433–450.

[4] Economou, A. D. and Green, J. BA., *Thick and thin fingers point out Turing waves.* Genome Biology **14:101** (2013).

[5] Wei, J. and Winter, M., *Mathematical Aspects of Pattern Formation in Biological Systems.* Volume 189 of Applied Mathematical Sciences (London, 2014), *Dev. Math.*, Springer London (2014), 149–174.

[6] Page, K. M. and Maini, P. K. and Monk, N. A.M., *Complex pattern formation in reaction-diffusion systems with spatially varying parameters.* Physica D **202** (2005), 95–115.

[7] Page, K. M. and Maini, P. K. and Monk, N. A.M., *Pattern formation in spatially heterogeneous Turing reaction-diffusion models.* Physica D **181** (2002), 80–101.

[8] Glim, T. and Zhang, J and Shen Y, *Interaction of Turing patterns with an external linear morphogen gradient.* Nonlinearity **22(10)** (2009), 2541–2560.

[9] Glim, T. and Zhang, J and Shen Y and Newmann S. A., *Reaction-Diffusion Systems and External Morphogen Gradients: The Two-Dimensional Case, with an Application to Skeletal Pattern Formation.* Bull Math Biol **74** (2012), 666–687.

Quantum Walks with Restricted Percolation

Jan Mareš

2nd year of PGS, email: `maresj23@fjfi.cvut.cz`
Department of Mathematics
Faculty of Nuclear Sciences and Physical Engineering, CTU in Prague

advisors:

Igor Jex, Department of Physics
Faculty of Nuclear Sciences and Physical Engineering, CTU in Prague

Jaroslav Novotný, Department of Physics
Faculty of Nuclear Sciences and Physical Engineering, CTU in Prague

Abstract. In this contribution we deal with coined quantum walks defined on graphs undergoing dynamical percolation. This disruption of the walk leads to an asymptotic regime of the time evolution that can be easily predicted once we have solved for so called attractors of the walk. We are in particular interested in the scenario where not all configurations of the percolation graph are allowed and we ask, in which cases this restricted percolation gives rise to the same asymptotic state of the walk. We first present a general definition of a quantum walk able to incorporate many studied special cases and present a canonical way how to define a percolated version of a given quantum walk. The main result is a sufficient condition for the asymptotic equivalence of restricted and fully percolated quantum walk. This contribution also brings generalisation for walks with additional phase-shifts and walk with multiple walkers.

Keywords: quantum walk, percolation, asymptotic state

Abstrakt. Tento příspěvek se zabývá diskrétními kvantovými procházkami definovanými na grafech, které prochází procesem dynamické perkolace. Toto narušení procházky vede k asymptotickému časovému vývoji, který je možné snadno předpovídat, známe-li takzvané atraktory této kvantové procházky. Zde se konkrétně zabýváme situací, kdy nejsou možné všechny konfigurace perkolovaného grafu a ptáme se, v jakých případech tato omezená perkolace vede ke stejnému asymptotickému chování. Nejprve předkládáme obecnou definici kvantové procházky schopnou pojmout mnohé konkrétní studované případy a uváníme kanonický způsob jak definovat perkolovanou vrzi těchto procházek. Hlavním výsledkem je postačující podmínka pro asymptotickou ekvivalenci omezené a plné perkolace kvantové procházky. Tento příspěvek dále přináší zobecnění pro kvantové procházky z dodatečnými fázovými posuny a procházky s více chodci.

Klíčová slova: kvantová procházka, perkolace, asymptotický stav

1 Hadamard Walk on a Line

Despite the fact that the aim of this contribution is to present very general results, let us start with a brief description of a particular coined quantum walk - Hadamrd walk on a finite line. Coined quantum walks are defined on graphs. In this case the graph $G(V, E)$ will consist of N vertices aligned in a line and $N - 1$ edges connecting neighbouring vertices. On this graph we define so called position Hilbert space $\mathcal{H}_p = \mathrm{span}(\{|v\rangle\}_{v \in V})$.

We further define so called coin Hilbert space $\mathcal{H}_c = \text{span}(\{|L\rangle, |R\rangle\})$ corresponding to directions left/right.

The whole quantum walk is defined on the Hilbert space $\mathcal{H} = \mathcal{H}_p \otimes \mathcal{H}_c$. The unitary time evolution proceeds in discrete steps realised by an evolution operator $U = SC$. Here the step operator S is just a permutation matrix given by mapping: $S|v_i, R\rangle = |v_{i+1}, R\rangle$ and $S|v_j, L\rangle = |v_{j-1}, L\rangle$. The only exceptions are at the borders of the graph where the walker is just reflected: $S|v_1, L\rangle = |v_1, R\rangle$ and $S|v_N, R\rangle = |v_N, L\rangle$. The coin operator in every vertex is chosen as the 2-dimensional Hadamard matrix and on the whole $\mathcal{H}$ it is:

$$C = I_p \otimes \frac{1}{\sqrt{2}} \begin{pmatrix} 1 & 1 \\ 1 & -1 \end{pmatrix}, \tag{1}$$

where I_p is the identity operator on $\mathcal{H}_p$. The coin operation therefore mixes the states in particular vertices.

If the walk stars in a pure state $|\psi(0)\rangle$ or a mixed state $\rho(0)$, than at the time-step t the state will be $|\psi(t)\rangle = U^t|\psi(0)\rangle$ or $\rho(t) = U^t\rho(0)(U^\dagger)^t$ respectively. In analogy to the classical random walk, in every step the walker "tosses a coin" and makes a step in direction dependent on the result of the coin toss. The difference is that in quantum walk superpositions are possible.

2 General Definition of a Quantum Walk

2.1 Basic Quantum Walk

We will understand quantum walks as discrete-time quantum processes defined on finite undirected graphs in the following way: Let us have a finite undirected graph $G(V, E)$, where V is the set of vertices and E is the set of edges. (No requirements are posed on the structure of the graph.) With G we associate new directed graph $G^{(d)}(V, E^{(d)})$ with the same set of vertices V. The set of directed edges $E^{(d)}$ consists of two subsets. For every edge $e \in E$ we have two edges $e_1, e_2 \in E^{(d)}$ going in opposite directions and connecting the same two vertices as e. Further we may add some loops (edges beginning and ending in the same vertex).

Now we associate a Hilbert space $\mathcal{H}$ with our graph $G^{(d)}(V, E^{(d)})$. Simply every directed edge corresponds to one base state, so $\mathcal{H} = \text{span}(\{|e^{(d)}\rangle\}_{e^{(d)} \in E^{(d)}})$. From now on we will be using the term directed edge and state from $\mathcal{H}$ interchangeably and also sometimes denote base states just $|x_j\rangle$ ($j \in \{1, \ldots, |E^{(d)}|\}$) without reference to particular directed edges. The loops that we have introduced in $G^{(d)}(V, E^{(d)})$ allow us define directed graphs where every vertex has the same structure - the same number of states associated with it.

The time evolution proceeds in discrete steps governed by a unitary operator U. If the state of the walk in the time step t is given by a density matrix $\rho(t)$, the state at the following step will be

$$\rho(t+1) = U\rho(t)U^\dagger. \tag{2}$$

The evolution operator U has a special structure - it consists of subsequent applications of two unitary operators: so called coin operator C and step operator S:

$$U = SC. \tag{3}$$

The coin operator C does not mix states from different vertices. More precisely stated, every subspace $\mathcal{H}_v$ of $\mathcal{H}$ generated by states in particular vertex $v \in V$ is an invariant subspace of the map C.

The step operator has two important properties. The first is that we only allow "almost permutation" matrices. By this we mean that it just maps every state to some other state without creating superpositions, but some phase can be added to the resulting state:

$$S \left| x_j \right\rangle = e^{i\varphi_j} \left| x_{s(j)} \right\rangle, \tag{4}$$

where s is some permutation map and $\varphi_j \in \mathbb{R}$.

The second property is it's association with the graph $G^{(d)}(V, E^{(d)})$. Simply put, it must follow the direction of edges. Explicitly we may write

$$S \left| v, c \right\rangle = \left| v \oplus c, \tilde{c} \right\rangle, \tag{5}$$

where we now denote states by a vertex v and an edge in this vertex c, $v \oplus c$ denotes the other end-point of the edge c and $\tilde{c}$ is just some edge in vertex $v \oplus c$.

The remaining freedom i defining the step operator is the choice of $\tilde{c}$ for every $\left| v, c \right\rangle$. On regular lattices there can be some simple rule for that as in the example of the walk on a line. In any other case we just make some choice allowed by the underlying graph while keeping the unitarity of S.

2.2 Percolated Quantum Walk

In our case we will use the percolation scheme to disrupt the underlying graph. In every step of the walk we use the original undirected graph $G(V, E)$ to generate a new graph $G_K(V, K)$ by removing (closing) some edges from $G(V, E)$. This new graph is called a percolation graph and is defined by the set (configuration) of remaining (open) edges $K \subset E$. In what we call a full percolation we just choose some probability $p \in (0, 1)$ and every edge is open with probability p and closed with probability $1 - p$ independently of all others. Therefore, any configuration $K \in 2^E$ is possible. In contrast to this full percolation, we will consider scenarios where we allow only some subset of 2^E (for example only configurations with just one open edge). That will be called a restricted percolation.

Let us now have some percolation graph $G_K(V, E_K)$. We need to modify the evolution operator U of the quantum walk so that it respects the structure of this new graph. There is a canonical way of how to define this step operator U_K once we have defined the operator U for the walk on $G(V, E)$. We modify the directed graph $G^{(d)}(V, E^{(d)})$ to produce a new directed graph $G_K^{(d)}(V, E_K^{(d)})$. We keep all the loops from $G^{(d)}(V, E^{(d)})$ the same and also all directed edges corresponding to edges that remain open. Let us now have an edge that is not in K and connects vertices A and B. Instead of directed edges from A to B and from B to A we introduce a loop in every of these two vertices. Note, that this change does not affect the Hilbert space and also both the in-degree and the out-degree of both vertices stays the same.

Now we need to modify the time evolution operator U_K of a quantum walk to respect the new graph $G_K^{(d)}(V, E_K^{(d)})$. The subspaces associated with vertices have not changed. Only the endpoints of some directed edges may be different. It means, that there is no
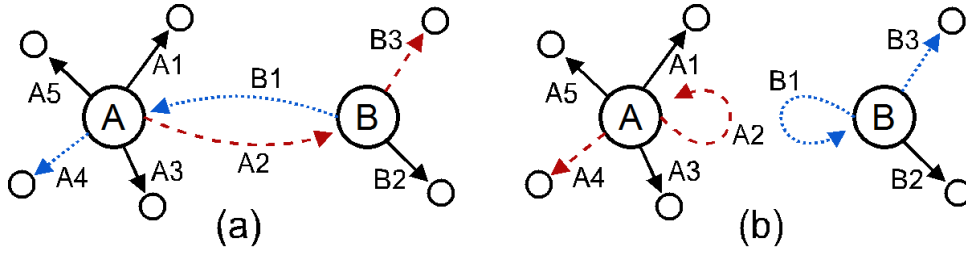
Figure 1: Visualisation of the step operator for an open (a) and closed (b) edge.

need for changing the coin operation C. Therefore, in a percolated quantum walk, the coin operation is independent of the choice of the percolation graph.

Unlike the coin operation, the step operator S needs to be modified to S_K according to the given configuration K. For loops and open edges, there is no difference. Let us again have two vertices A and B and an undirected edge $e \in E$ that is closed ($e \notin K$). Now it is advantageous to use the example in figure 1. The edge connecting vertices A and B has states $|A2\rangle$ and $|B1\rangle$ and the action of the step operator S when the edge is open is $S|A2\rangle = |B3\rangle$ and $S|B1\rangle = |A4\rangle$. For a closed edge one might want to let the walker stay in place, so $S|A2\rangle = |A2\rangle$ and $S|B1\rangle = |B1\rangle$, but then no other state is mapped to $|3B\rangle$ and there may also be different state mapped to $|2A\rangle$ so the resulting step operator S_K would not be a permutation.

For vertices A and B the resulting state after application of the step operator must remain in the vertex. The canonical choice is the mapping $S_K|A2\rangle = |A4\rangle$ and $S_K|B1\rangle = |B4\rangle$. In general, the end state for a walker that could not pass a closed edge must be the state that would otherwise (with the edge open) be the end state for a walker coming from the other direction.

2.3   Phase Shift

In previous definition of a percolated quantum walk we have left out the possible phase shift in the step operator. In general, for every base state (every directed edge) $|x_j\rangle$, there can be unique phase shift $e^{i\varphi_j}$, so that

$$S|x_j\rangle = e^{i\varphi_j}|x_{s(j)}\rangle. \tag{6}$$

Than if the edge containing $|x_j\rangle$ will be broken, there may be different phase shift:

$$S_K|x_j\rangle = e^{i\psi_j}|x_{k(j)}\rangle, \tag{7}$$

where k is the permutation map describing the action of the step operator S_K. We only allow the phase to depend on the edge determining $k(j)$ being open or closed. It can not depend on presence/absence of some other edges.

3 Finding Attractors

3.1 Percolated Quantum Walk as a Random Unitary Operation

Since percolation introduces a classical uncertainty to the evolution of the quantum walk, we use the description of the state by a density matrix. One step of the walk can be described as:

$$\rho(t+1) = \sum_{K \subset E} \pi_K U_K \rho(t) U_K^\dagger, \tag{8}$$

where $U_K = S_K C$ is the evolution operator corresponding to the configuration of the percolation graph K and π_K is the probability of occurrence of this configuration.

The asymptotic state (the limit for infinitely many steps) of the percolated quantum walk is than given as [1]:

$$\rho_{t \to \infty}(t) = \sum_{\lambda, i} \lambda^t \mathrm{tr}\left(\rho(0) X_{\lambda,i}^\dagger\right) X_{\lambda,i}, \tag{9}$$

where $X_{\lambda,i}$ so called attractors. Those are solutions of the equation

$$U_K X U_K^\dagger = \lambda X, \quad \text{for all } K \subset 2^E, \tag{10}$$

for some given λ fulfilling $|\lambda| = 1$. We can now use the procedure described in [2]. The decomposition $U_K = S_K C$ can be used to rewrite the equation (10) as

$$C X C^\dagger = \lambda S_K^\dagger X S_K. \tag{11}$$

Here we use the fact, that the coin operation is not affected by percolation of the graph and therefore the left-hand side of the equation is constant for all configurations. This allows us to solve it in two steps. Firs we choose one configuration K_0 and find the solution of the equation:

$$C X C^\dagger = \lambda S_{K_0}^\dagger X S_{K_0}. \tag{12}$$

A typical choice is the configuration, where all edges are closed, since in such case the equation can be solved locally in individual vertices. Nevertheless, any configuration from 2^E can be chosen in principle. Now we restrict our solution by what we will call the step condition:

$$S_K^\dagger X S_K = S_L^\dagger X S_L, \quad \text{for all } K, L \subset 2^E. \tag{13}$$

We end up with the set of attractors $\{X_{\lambda,i}\}$, where $|\lambda| = 1$ and i distinguishes different attractors for a given eigenvalue λ.

3.2 Step condition for general attractors

The step condition (13) can be investigated further. Let us use a general form of the step operator:

$$S_K = \sum_i \alpha_K(i) \left|x_{k(i)}\right\rangle \left\langle x_i\right|, S_K^\dagger = \sum_j \alpha_K^*(j) \left|x_j\right\rangle \left\langle x_{k(j)}\right|, \tag{14}$$

where $|x_i\rangle$ are base states corresponding to all directed edges of the graph $G^{(d)}$, k is the permutation map defining the operator S_K corresponding to the configuration K of the percolation graph, $\alpha_K(i)$ is the phase shift for the state $|x_i\rangle$ in the configuration K ($|\alpha_K(i)| = 1$) and the asterisk denotes a complex conjugate. We can decompose a general operator X in a similar way as $X = \sum_{s,t} X_t^s |x_s\rangle \langle x_t|$. Then the term of our interest will be

$$S_K^\dagger X S_K = \sum_{i,j} X_{k(j)}^{k(i)} \alpha_K(j)\alpha_K^*(i) |x_i\rangle \langle x_j|. \tag{15}$$

By comparing two step operators S_{K_1} and S_{K_2} given by permutation maps k and l respectively we obtain the condition

$$\sum_{i,j} X_{k(j)}^{k(i)} \alpha_K(j)\alpha_K^*(i) |x_i\rangle \langle x_j| = \sum_{i,j} X_{l(j)}^{l(i)} \alpha_L(j)\alpha_L^*(i) |x_i\rangle \langle x_j|. \tag{16}$$

We may now compare matrix elements one by one and by doing so we get

$$X_{k(j)}^{k(i)} \alpha_K(j)\alpha_K^*(i) = X_{l(j)}^{l(i)} \alpha_L(j)\alpha_L^*(i), \quad \text{for all } i, j, \tag{17}$$

which can also be written as

$$X_j^i = \frac{\alpha_K(k^{-1})(i)}{\alpha_L(k^{-1})(i)} \frac{\alpha_L(k^{-1})(j)}{\alpha_K(k^{-1})(j)} X_{lk^{-1}(j)}^{lk^{-1}(i)}, \quad \text{for all } i, j. \tag{18}$$

If we chose some state $|j\rangle$, then what is the state $|k^{-1}(j)\rangle$ depends on the configuration K. Nevertheless, there are only two options and both of them lie on one undirected edge. Let us have a look at figure 1. If we chose $|x_i\rangle = |A4\rangle$, then there are two possibilities. If in the configuration K the edge between vertices A and B is open, then $|x_{k^{-1}(i)}\rangle = |B1\rangle$. If that edge is closed, then $|x_{k^{-1}(i)}\rangle = |A2\rangle$. In either case the state $|x_{k^{-1}(i)}\rangle$ belongs to the undirected edge between A and B. Also the phases $\alpha_K(k^{-1}(j))$ and $\alpha_L(k^{-1}(j))$ are solely dependent on the edge between A and B being open/closed.

From now on, we assume that there are only two possible values of the phase shift for all edges: α for traversing an open edge and β for "reflection" on a closed edge.

For every pair of indices i, j there are two undirected edges (let us call them $e, f \in E$) determining the values of $lk^{-1}(i)$ and $lk^{-1}(j)$. If e is open or closed in both K and L, then $lk^{-1}(i) = i$ and the phases give $\frac{\alpha_K(k^{-1})(i)}{\alpha_L(k^{-1})(i)} = 1$ and analogously for the edge f and index j. If e is closed in K and open in L, then $lk^{-1}(i) \neq i$ and we will denote this index as $lk^{-1}(i) = \tilde{i}$. In general, $\tilde{i}$ is the state that the walker ends up in when traversing e in the opposite direction than the one resulting in i. For phases we have $\frac{\alpha_K(k^{-1})(i)}{\alpha_L(k^{-1})(i)} = \frac{\alpha}{\beta}$. Finally when e is closed in K and open in L there is just different phase: $\frac{\alpha_K(k^{-1})(i)}{\alpha_L(k^{-1})(i)} = \frac{\beta}{\alpha}$.

The most restrictive condition that can be obtained for an attractor matrix element is:

$$X_j^i = \frac{\alpha}{\beta} X_j^{\tilde{i}} = \frac{\beta}{\alpha} X_j^{\tilde{i}} = \frac{\beta}{\alpha} X_{\tilde{j}}^i = \frac{\alpha}{\beta} X_{\tilde{j}}^i = X_{\tilde{j}}^{\tilde{i}} = \frac{\alpha^2}{\beta^2} X_{\tilde{j}}^{\tilde{i}} = \frac{\alpha^2}{\beta^2} X_{\tilde{j}}^{\tilde{i}} = X_{\tilde{j}}^{\tilde{i}}. \tag{19}$$

This strongest condition does not hold if $k^{-1}(i)$ or $k^{-1}(j)$ belong to the loop in the original graph - the part containing $\tilde{i}$ or $\tilde{j}$ respectively is omitted allowing for more diverse attractors.
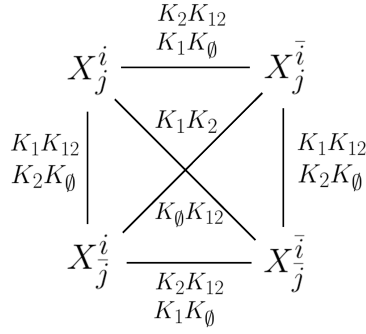
Figure 2: Relations between available configurations and matrix element equalities.

Another case with a weaker condition is when $e = f$ (that is either $i = j$ or $i = \tilde{j}$). In such case we cannot have conditions with an edge open and closed simultaneously. In this case the step condition reduces to:

$$X_j^i = X_{\tilde{j}}^{\tilde{i}}. \tag{20}$$

3.3   Restricted percolation

Let us now investigate what happens when we restrict the set of possible configurations of the percolation graph. First we note that the step condition is redundant - multiple pairs of configurations K and L give rise to the same condition. Now, our question is, what is the minimum set of allowed configurations that gives rise to the same overall step condition and therefore to the same asymptotic state.

Let us first solve the phase shifts. There is only one case when the step condition requires equality of the same matrix elements with only difference in phases. This difference arises from the order in which we make some edge open/closed. If it is open in K and closed in L we obtain different phase than in the case of $e \notin K$ and $e \in L$. It is obvious that we may interchange K and L arbitrarily and the only important fact is whether we have these two configurations at our disposal. Therefore, when concerning restricted percolation, we do not need to care about phases at all. Equivalence of conditions with phases is assured by equivalence of conditions for matrix elements on the level of states.

When leaving out the phases, the strongest step condition is:

$$X_j^i = X_j^{\tilde{i}} = X_{\tilde{j}}^i = X_{\tilde{j}}^{\tilde{i}}. \tag{21}$$

For given indices i, j, there are undirected edges e and f containing $k^{-1}(i)$ and $k^{-1}(j)$ respectively for any configuration K. Let us now use symbol $K_\emptyset$ for some configuration where both e and f are missing (closed). Further in K_e only e is present and f is missing, in K_f the edge f is present and e is not and finally in K_{ef} both edges are present. The figure 2 shows four matrix elements that can be connected by the step condition and these connections. For every connection, there are two pairs of configurations that give rise to the corresponding equality of matrix elements.

It is simple to check, that by removing any one of the configurations $K_\emptyset, K_e, K_f, K_{ef}$, all four matrix elements stay connected. On the other had, if any two configurations are removed, the step condition is weaken. This means that for every pair of distinct edges

we need any three of our four configurations to obtain the full step condition. Therefore, we have a sufficient condition for the restricted percolation to be equivalent to the full percolation.

3.3.1 Examples of equivalent restricted percolation schemes

As mentioned above, we may have restricted percolation where only one edge is present in every time step. Provided that the original graph has at least three edges, there are always configurations $K_\emptyset, K_e$ and K_f, so this scheme is equivalent.

Similarly to the previous case, if we only allow configurations with only one edge broken and all other present, we have configurations K_e, K_f and K_{ef} so this is again equivalent. (Once more we assume $|E| > 2$.)

One may also think of a sort of a site percolation, where vertices are broken. We may simulate this with our percolation when a broken vertex means broken all edges connected to it. Here again, there is no problem to have even all configurations $K_\emptyset, K_e, K_f, K_{ef}$ and also schemes wit just one vertex open/broken in every configuration will be equivalent. There is just one requirement on the underlying graph $G(V, E)$. It may not contain two vertices connected by more than one edge.

It is very important to note that adding any other configurations to an already equivalent scheme may not break the equivalence. This makes the model of a percolated quantum walk very suitable for simulation of real system where one can not rely on realisation of all configurations.

4 Percolation in Quantum Walks with Two Non-Interacting Distinguishable Walkers

Apart from the possibility of some non-separable initial states of the walk, the percolation brings another correlations - the two walkers walk the same graph. Therefore, the percolated walk with two walkers in not just a product of two one-walker quantum walks.

Even in the case of two walkers, the time evolution can be written in terms of the coin operator and the step operator with properties analogous to those for just one walker. We can again separate the search for attractors into two steps where we first solve the equation for one particular configuration and then apply the step condition. For the equivalence of the asymptotic state, the only thing of our concern will again be the step condition.

For two walkers we have just somewhat more involved step operator:

$$S_K = \sum_{i,j} \alpha_K(i)\alpha_K(j) \left| x_{k(i)} x_{k(j)} \right\rangle \left\langle x_i x_j \right|. \tag{22}$$

Comparison of two configuration leads to the step condition for matrix elements of the form:

$$X_{I,J}^{i,j} = \frac{\alpha_K(k^{-1}(i))\alpha_K(k^{-1}(j))}{\alpha_L(k^{-1}(i))\alpha_L(k^{-1}(j))} \frac{\alpha_L(k^{-1}(I))\alpha_L(k^{-1}(J))}{\alpha_K(k^{-1}(I))\alpha_K(k^{-1}(J))} X_{lk^{-1}(I),lk^{-1}(J)}^{lk^{-1}(i),lk^{-1}(j)}. \tag{23}$$

We are again interested in subsets of configuration leading to the same asymptotic state as the full percolation on walk with two walkers. We will not list all possible

equalities with phases. In fact, the phases again play no role for the same reason as in the one-walker case. There are fewer restrictions or the matrix elements here than there would be when applying the one-walker step condition on both walkers. Even in the full percolation, there can not be configurations with some edge e closed for one walker and simultaneously open for the other walker. Nevertheless, when concerning the edge configuration, we again only have to deal with pairs of edges an the equivalence condition is the same as for one walker.

In conclusion, for the restricted percolation of a quantum walk with two non-interacting distinguishable walkers to be equivalent with the full percolation (to have the same asymptotic state), there is the same sufficient condition on set of allowed configurations as in the one-walker case. Obviously, this holds also for any other finite number of walkers.

5   Conclusion

We have presented a sufficient condition for the set of allowed percolation graphs in percolated quantum walks that assure the same asymptotic behaviour of the walk as the full percolation. Also some examples of such sets of configurations were presented.

This result has two main applications. First, it shows that percolated quantum walks may be well utilised for simulation of real physical systems since by far not all configurations must be realised to give the same asymptotic behaviour. The second application is in experiments where it may be difficult or even impossible to realise all edge configurations. We have presented subsets with number of configurations linear in the number of edges contrasting with the exponentially growing number of all possible configurations.

References

[1] J. Novotny, G. Alber and I. Jex. *Asymptotic evolution of Random Unitary Operations.* Central Eur. J. Phys. **8** (2009), 1001–1014.

[2] B. Kollar, T. Kiss, J. Novotny and I. Jex. *Asymptotic dynamics of coined quantum walks on percolation graphs.* Phys. Rev. A **108** (2012).

Gibbs-like Asymptotic States of Quantum Markov Chains[*]

Jiří Maryška

2nd ročník PGS, email: `maryska.jiri@gmail.cz`
Katedra fyziky
Fakulta jaderná a fyzikálně inženýrská, ČVUT v Praze

školitelé:

Igor Jex, Katedra fyziky
Fakulta jaderná a fyzikálně inženýrská, ČVUT v Praze

Jaroslav Novotný, Katedra fyziky
Fakulta jaderná a fyzikálně inženýrská, ČVUT v Praze

Abstract. Quantum markov chains, i.e. iterated sequences of quantum operations, represent a convenient way of time-evolution description of open quantum systems. In recent years, quantum markov chains have shown great potential in many areas of quantum theory reaching from its very fundamentals to practical applications, i.e. random quantum walks. Recently, the asymptotic dynamics of a wide class of quantum markov chains on finite dimensional Hilbert space was studied. For this class, it was shown that the asymptotic dynamics is governed by so-called attractor space, which can be derived by solving a set of so-called attractor equations. The relations between elements of this attractor space (i.e. attractors) and the integrals of motions corresponding to the quantum markov chain were given. Here we show that the asymptotic states of such quantum markov chain can be rewritten in a form, which resembles a well known concept of a generalized Gibbs state. This so-called Gibbs-like states follow a principle, which can be regarded as a general- ization of maximal entropy principle.

Keywords: Quantum markov chain, asymptotic dynamics, integrals of motion, Gibbs states

Abstrakt. Kvantové markovovské řetízky, tj. iterované sekvence kvantových operací představují vhodný způsob popisu časového vývoje otevřených kvantových systémů. V posledních letech kvantové markovovské řetízky vykázaly velký potenciál v mnoha oblastech kvantové teorie s využitím jak při zkoumání fundamentálních principů, tak i praktických aplikací, např. náhodných kvantových procházek. Nedávno byla odvozena asymptotická dynamika široké třídy kvantových markovovských řetízků na konečnědimenzionálním Hilbertově prostoru. Bylo ukázáno, že tuto asymtptotickou dynamiku řídí tzv. atraktorový prostor, který lze nalézt řešením tzv. atraktorových rovnic. Byly nalezeny vztahy mezi elementy tohoto podprostoru (tj. atraktory) a integrály pohybu příslušící danému kvantovému markovskému řetízku. Cílem této práce je ukázat, že asymptotický stav takovýchto kvantových markovovských řetízků může být přepsán do tvaru, který připomíná dobře známé zobecněné Gibbsovy stavy. Tyto tzv. pseudo-Gibbsovy stavy se řídí principem, který lze považovat za zobecnění principu maximální entropie.

Klíčová slova: Kvantový markovovský řetíezk, asymptotická dynamika, Integrály pohybu, Gibbsovy stavy

---

1 Introduction

To obtain the analytic form of a time evolution of a quantum systems is one of the basic, yet most important tasks of quantum theory. Whereas the evolution of closed quantum system is easily solved thanks to Hermicity of the generator of time evolution, evolution of a general quantum system is a difficult task due to fact that the generator of time evolution needs not to be Hermitean, nor normal and thus the diagonalization of the generator in some orthonormal basis is not guaranteed.

Under the additional assumtion of the markovianity of the time evolution, one can derive so-called Master equation [1, 2], which describes the time evolution as a differential equation of first order, however appart from a few special cases, complete solutions are usually hard to find. Another approach utilizes properties of so-called completely positive maps (CP maps) [1, 2], which describe the most general change of a quantum state. The evolution is then described as a discrete sequence of CP maps, resulting in so-called quantum markov chain [3].

Motivated by results of equilibrium thermodynamics [4], one often assumes that the stationary state (i.e. the state which remains unchanged during time evolution) of a given system takes the form of so-called generalized Gibbs state [5], which maximalizes the von Neumann entropy with respect to given constraints represented by mean values of integrals of motion corresponding to system under investigation. As they fulfil relations analogous to classical Gibbs states, manipulation with generalized Gibbs states is often significantly easier than with general quantum state.

Here, we focus on the study of the asymptotic evolution (i.e. the limit $t \to \infty$) of a quantum markov chain in a finite-dimensional Hilbert space, which fulfils requirement of existence of so-called faithful invariant state. First, we summarize known results concerning asymptotic dynamics of a such quantum markov chain, with the stress putted on the subspace in which the asymptotics takes place - attractor space. We then proceed by derivation of the relations between elements of the attractor space and integrals of motion corresponding to the system under investigation. After reviewing the exponentiel map and its inverse - logarithm map, we show that stationary states corresponding to the quantum markov chain can be rewritten in a form which resembles the generalized Gibbs state. We then discuss the form of a entropy principle, which holds for this Gibbs-like states.

2 Attractor method for dynamics generated by quantum markov chain

The purpose of this section is to review important results concerning the asymptotic dynamics of a quantum markov chain. For more detailed analysis see [6]. A quantum markov chain is genereated by a CP map $\mathcal{P}$. Action of map $\mathcal{P}$ on an arbitrary element of the space of bounded operators on Hilbert space $\mathscr{H}$ (denoted by $\mathfrak{B}(\mathscr{H})$) can be written is Kraus representation as

$$\mathcal{P}(\cdot) = \sum_j A_j(\cdot)A_j^\dagger, \tag{1}$$

with $\{A_j\}_j \subset \mathfrak{B}(\mathscr{H})$. The adjoint map $\mathcal{P}^\dagger$ is also a CP map, which takes the Kraus form

$$\mathcal{P}^\dagger(\cdot) = \sum_j A_j^\dagger(\cdot)A_j. \qquad (2)$$

We distinguish several important classes of CP maps. First, we call a CP positive map $\mathcal{P}$ unital (subunital), if it fulfils the requirement $\mathcal{P}(I) = I$ ($\mathcal{P}(I) \leq I$). Next, $\mathcal{P}$ is called trace-preserving (trace-nonincreasing), if it meets $\mathcal{P}^\dagger(I) = I$ ($\mathcal{P}^\dagger(I) \leq I$). In the subsequent discussion, we will be interested in CP maps, which are trace-preserving. We will refer to these as to quantum operations. The dynamic of quantum markov chain is thus generated by quantum operation $\mathcal{P}$ is given by its repeated applications, i.e. starting from the initial state $\rho(0)$ the state after n application is given by

$$\omega(n) = \mathcal{P}^n(\omega(0)). \qquad (3)$$

By asymptotic evolution, we thus mean the limit $\lim_{n \to \infty} \omega(n)$. The stationary state of a quantum markov chain a quantum state ω_s, which fulfils the requirement $\mathcal{P}(\omega_s) = \omega_s$.

There always exists at least one stationary state corresponding to given quantum markov chain. Starting with an arbitrary state ω, we define state $\bar{\omega}$ as

$$\bar{\omega} = \lim_{n \to \infty} \frac{1}{n} \sum_{j=0}^{n-1} \mathcal{P}^j(\omega).$$

One can directly check that the equation $\mathcal{P}(\bar{\omega}) = \bar{\omega}$ holds. However, to be able to analytically describe the asymptotics of a quantum markov chain, we require the existence of so-called faithful invariant state [7] ρ. This state fulfils

(1) $\rho > 0$,
(2) $\mathcal{P}(\rho) = \rho$.

In the following text, the symbol ρ will be reserved for this faithful invariant state. This state is generally not unique - if there are two faithful invariant states, then the linearity of quantum operation $\mathcal{P}$ implies that any convex combination of these two states is also a faithful invariant state.

As was shown in [6], the asymptotic dynamics of a quantum markov chain is governed by attractor space $\mathrm{Atr}(\mathcal{P}) \subset \mathfrak{B}(\mathscr{H})$, which is defined as

$$\mathrm{Atr}(\mathcal{P}) = \bigoplus_{\lambda \in \sigma_1} \mathrm{Ker}\,(\mathcal{P} - \lambda I), \qquad (4)$$

with σ_1 being so-called attractor spectrum defined as

$$\sigma_1 = \{\lambda \in \sigma(\mathcal{P}) | |\lambda| = 1\}.$$

The elements of the attractor space are generally not density matrices, as any attractor (i.e. element of the attractor space) X corresponding to $\lambda \neq 1$ must fulfil $\mathrm{Tr}[X] = 0$. We are however always able to construct valid density matrix out of them. This is due to their algebraic structure, which we will discuss later.

Having constructed the attractor space with $\{X_{\lambda,1}, \ldots, X_{\lambda,d_\lambda}\}$ as the orthonormal basis of the subspace $\text{Ker}(\mathcal{P} - \lambda I)$, we can write the asymptotic state as

$$\rho(n \gg 1) = \sum_{\lambda \in \sigma_1, i=1}^{d_\lambda} \lambda^n \text{Tr}\left[\rho(0) X^{\lambda,i}\right] X_{\lambda,i}. \tag{5}$$

Here, $X^{\lambda,i}$ are operators dual to $X_{\lambda,i}$ (with respect to the Hilbert-Schmidt scalar product), i.e. they fulfil

$$\text{Tr}\left[X^{\lambda,i} X_{\mu,j}^\dagger\right] = \delta_{\lambda\mu}\delta_{ij}.$$

These dual vectors are nontrivial (i.e. they do not generally fulfil property $X^{\lambda,i} = X_{\lambda,i}$), except for the case of unital quantum operations. This is due to the fact that the kernels corresponding to different eigenvalues λ and μ are generally not orthogonal. However, they fulfil the relation

$$X^{\lambda,i} = \frac{1}{\text{Tr}\left[X_{\lambda,i}\rho^{-1}\right]} X_{\lambda,i}\rho^{-1},$$

with ρ being a faithful invariant state corresponding to $\mathcal{P}$. Simultaneously, operators $X_{\lambda,i}\rho^{-1}$ are attractors corresponding to map $\mathcal{P}^\dagger$. This means that there exist a simple relation between subspaces $\text{Atr}(\mathcal{P})$ and $\text{Atr}(\mathcal{P}^\dagger)$. There are several ways, how to write this relation:

$$X \in \text{Ker}(\mathcal{P} - \lambda I) \Leftrightarrow X\rho^{-1} \in \text{Ker}(\mathcal{P}^\dagger - \overline{\lambda}I),$$
$$\Leftrightarrow \rho^{-1}X \in \text{Ker}(\mathcal{P}^\dagger - \overline{\lambda}I),$$
$$\Leftrightarrow \rho^{-1/2}X\rho^{-1/2} \in \text{Ker}(\mathcal{P}^\dagger - \overline{\lambda}I).$$

The importance of quantum operation $\mathcal{P}^\dagger$ lies in its relation with integrals of motion corresponding to quantum operation $\mathcal{P}$. Integrals of motion are observables, which have constant mean value during time evolution. Operator $A \in \mathfrak{B}(\mathscr{H})$ is thus an integral of motion, if it meets requirements

(1) $A = A^\dagger,$
(2) $\text{Tr}\left[A\rho(n)\right] = \text{Tr}\left[A\rho(0)\right], \forall n.$

A simple calculation yields the following:

$$\text{Tr}\left[A\rho(n)\right] = \text{Tr}\left[A\mathcal{P}^n(\rho(0))\right] \text{Tr}\left[\mathcal{P}^{\dagger n}(A)\rho(0)\right] = \text{Tr}\left[A\rho(0)\right],$$

and thus $A = A^\dagger \in \mathfrak{B}(\mathscr{H})$ is an integral of motion, if $\mathcal{P}^\dagger(A) = A$, i.e. A is an attractor of $\mathcal{P}^\dagger$ corresponding to eigenvalue $\lambda = 1$. Quantum operation $\mathcal{P}^\dagger$ thus represents the Heisenberg picture of evolution. We can thus say that while the subspace $\text{Ker}(\mathcal{P} - I)$ contains all the stationary states corresponding to a given quantum markov chain, the subspace $\text{Ker}(\mathcal{P}^\dagger - I) \equiv \mathcal{I}(\mathcal{P})$ contains all the integrals of motion corresponding to a

given quantum markov chain. Furthermore, we can write the relation between these two subspaces as

$$\mathrm{Ker}(\mathcal{P} - I) = \rho^{\frac{1}{2}}\mathrm{Ker}(\mathcal{P}^\dagger - I)\rho^{\frac{1}{2}}, \tag{6}$$

with ρ being the faithful invariant state corresponding to $\mathcal{P}$. The obvious advantage of this relation is that it maps Hermitean operators to another Hermitean operators.

Next, we state some simple algebraic properties of important subspaces concerning maps $\mathcal{P}$ and $\mathcal{P}^\dagger$. More exactly, we are interested which of important subspaces form so-called C^*-algebras [8]. Generally, the subspaces $\mathrm{Atr}(\mathcal{P})$ and $\mathrm{Ker}(\mathcal{P}-I)$ are not C^*-algebras as they satisfy more complicated relations

(1) $\quad X_i \in \mathrm{Ker}(\mathcal{P} - \lambda_i I) \Rightarrow X_i^\dagger \in \mathrm{Ker}(\mathcal{P} - \overline{\lambda}_i I),$

(2) $\quad \rho^{-1}X_iX_j,\ X_i\rho^{-1}X_j,\ X_iX_j\rho^{-1} \in \mathrm{Ker}(\mathcal{P} - \lambda_i\lambda_j I).$

Only in case of unital $\mathcal{P}$ both $\mathrm{Atr}(\mathcal{P})$ and $\mathrm{Ker}(\mathcal{P} - I)$ form C^*-algebras. However, thanks to the fact that the map $\mathcal{P}$ is trace-preserving, the map $\mathcal{P}^\dagger$ is unital and $\rho \sim I$ is thus a faithful invariant state. Both subspaces $\mathrm{Atr}(\mathcal{P}^\dagger)$ and $\mathcal{I}(\mathcal{P})$ thus form C^*-algebras as they satisfy relations

(1) $\quad X_i \in \mathrm{Ker}(\mathcal{P}^\dagger - \lambda_i I) \Rightarrow X_i^\dagger \in \mathrm{Ker}(\mathcal{P}^\dagger - \overline{\lambda}_i I),$

(2) $\quad X_iX_j \in \mathrm{Ker}(\mathcal{P}^\dagger - \lambda_i\lambda_j I).$

Thanks to these properties, we can choose an orthonormal basis of $\mathcal{I}(\mathcal{P})$ as the set $\{I, Y_1, \ldots, Y_n\}$ with $Y_j^\dagger = Y_j$. An arbitrary integral of motion A corresponding to $\mathcal{P}$ can be thus written as

$$A = \alpha_0 I + \sum_j \alpha_j Y_j.$$

The fact that we are able to choose an orthonormal basis of the subspace $\mathcal{I}(\mathcal{P})$ made from integrals of motion and relations between subspaces $\mathrm{Ker}(\mathcal{P} - I)$ and $\mathcal{I}(\mathcal{P})$ enable us to write the asymptotic state in the Gibbs-like form.

3   Gibbs-like asymptotic states

Before rewriting the asypmototic state in the Gibbs-like form, we review basic facts about the exponentiel map and its inverse, the logarithm map acting on the $\mathfrak{B}(\mathscr{H})$ space. Exponentiel map is defined by its Taylor series - for any $A \in \mathfrak{B}(\mathscr{H})$ we have

$$\exp[A] := \sum_{n=0}^\infty \frac{A^n}{n!}.$$

If $A = A^\dagger$ and $\sigma(A) = \{\lambda_1, \ldots, \lambda_n\}$, then $\sigma(\exp[A]) = \{e^{\lambda_1}, \ldots, e^{\lambda_n}\}$. As a consequence, for any $A = A^\dagger$, $\exp[A]$ is a strictly positive operator, i.e. $\exp[A] > 0$. Thanks

to this property, density matrices are mapped again to density matrices, apart from normalization. Thus if σ represents a quantum state, operator $\tau = \frac{1}{\text{Tr}[\exp[\sigma]]} \exp[\sigma]$ represents a valid quantum state, which is strictly positive. The same holds for integrals of motion, i.e. if A is an integral of motion, then $\exp[A]$ is a strictly positive integral of motion. Furthermore, if we use relations between integrals of motion and stationary state, we can say that apart from normalization, operator

$$\tau = \rho^{\frac{1}{2}} \exp[A] \rho^{\frac{1}{2}} \tag{7}$$

represents a strictly positive stationary state. In the following, we will call state in the form (7) the Gibbs-like state. We ask, if for each stationary state there exists (in some sense) an integral of motion such that the stationary state can be written in the Gibbs-like form. To answer this question, let us study an inverse map. Logarithm map is defined by following requirement:

$$\log[B] = A \Leftrightarrow \exp[A] = B.$$

Generally, the logarithm of an operator is not uniquelly defined, however, for strictly positive A, $\log[A]$ is uniquelly defined.. The explicit form for $A > 0$ can be written again as Taylor series:

$$\log[A] = \log[I + (A - I)] = \sum_{n=0}^{\infty} \frac{(-1)^{n+1}}{n} (A - I)^n,$$

which converges for all such A.

Let us have a strictly positive stationary state ω. Operator τ_ω defined as

$$\tau_\omega = \rho^{-\frac{1}{2}} \omega \rho^{-\frac{1}{2}}$$

represents a strictly positive integral of motion. As the subspace $\mathcal{I}(\mathcal{P})$ forms a C^*-algebra, we must have

$$\log[\tau_\omega] = \sum_{n=0}^{\infty} \frac{(-1)^{n+1}}{n} (\tau_\omega - I)^n \in \mathcal{I}(\mathcal{P})$$

and consequently we can write

$$\omega = \rho^{\frac{1}{2}} \exp[\log[\tau_\omega]] \rho^{\frac{1}{2}} = \rho^{\frac{1}{2}} \exp\left[\alpha_0 I - \sum_j \alpha_j Y_j \right] \rho^{\frac{1}{2}} =$$

$$= \frac{1}{Z} \rho^{\frac{1}{2}} \exp\left[-\sum_j \alpha_j Y_j \right] \rho^{\frac{1}{2}},$$

with

$$Z = \text{Tr}\left[\exp\left[-\sum_j \alpha_j Y_j \right] \rho \right].$$

This means that every strictly positive stationary state can be written in a Gibbs-like form.

Let us now have a stationary state $\omega \geq 0$. We can define a one-parameter family of states $\omega(s)$ as

$$\omega(s) = \frac{1}{\text{Tr}[\omega + s\rho]}(\sigma + s\tau), \tag{8}$$

with τ an arbitrary faithful invariant state. One can easily see that there exists a certain neighbourhood of $s = 0$ such that $\omega(s) > 0$. We can thus write

$$\omega(s) = \frac{1}{Z(s)}\rho^{\frac{1}{2}}\exp\left[-\sum_j \alpha_j(s)Y_j\right]\rho^{\frac{1}{2}}.$$

By taking limit $s \to 0$, we obtain the result

$$\sigma = \lim_{s \to 0}\frac{1}{Z(s)}\rho^{\frac{1}{2}}\exp\left[-\sum_j \alpha_j(s)Y_j\right]\rho^{\frac{1}{2}}. \tag{9}$$

As $0 \in \sigma(\sigma)$, at least some of the parameters α_j must meet $|\lim_{s \to 0}\alpha_j(s)| = +\infty$. This is not ambiguous, as analogous states exist in classical physics, e.g. degenerate gas of fermions. However, the limit (9) is generally not unique for a given faithful invariant state ρ, as we have the freedom in choosing an arbitrary faithful invariant state τ in (8). Unlike generalized Gibbs-states, Gibbs-like states do not maximalize the von Neumann entropy under conditions given by mean values of integrals of motion (apart from case of unital map $\mathcal{P}$). Nevertheless, they follow a more general principle concerning so-called relative entropy [1]. Relative entropy of states ω_1 and ω_2 is defined as

$$S(\omega_1|\omega_2) = \text{Tr}\left[\omega_1 \log[\omega_1] - \omega_1 \log[\omega_2]\right].$$

It is straightforward to prove that given the faithful invariant state ρ Gibbs-like states ω minimalize the relative entropy $S(\omega|\rho)$. This principle reduces to the classical principle of maximal entropy in case $\rho \sim I$, i.e. for unital quantum operation $\mathcal{P}$ which is in consensus with a fact that for unital quantum operations, Gibbs-like states reduce to a generalized Gibbs states.

4 Conclusion

In previous section, we presented a method of solving asymptotic dynamics of a quantum markov chain, for which exists a special stationary state ρ, so-called faithful invariant state. We have demonstrated previously unknown relationship of the attractor space corresponding to quantum operation $\mathcal{P}$, which defines the quantum markov chain and its adjoint quantum operation $\mathcal{P}^\dagger$, which represents the Heisenberg picture of dynamics. By doing so, we have uncovered the relationship of integrals of motion and stationary states corresponding to given system.

In the second part, we have shown that every stationary state ω corresponding to a such quantum markov chain can be written in a Gibbs-like form as

$$\omega_{st} = \lim_{s \to 0} \frac{1}{Z(s)} \rho^{\frac{1}{2}} \exp\left[-\sum_j \alpha_j(s) Y_j\right] \rho^{\frac{1}{2}},$$

with

$$Z(s) = \mathrm{Tr}\left[\exp\left[-\sum_j \alpha_j(s) Y_j\right] \rho\right].$$

For strictly positive ω_{st}, functions $\alpha_j(s)$ are constatnts, in other cases at least some tend to infinity. The Gibbs-like form of a strictly positive stationary states is unique for given faithful invariant state ρ, this property is generally not present for other stationary states.

Furthermore, stationary states of considered quantum markov chains follow a principle, which can be regarded as a generalization of a maximal entropy principle. In future, obtained results can be completed by derivation of thermodynamic inequalities of quantum markov chain. Also, at the moment, the relationship of two different Gibbs-like forms of the same steady state is unclear. These questions will be focuse in a future work.

Literatura

[1] M. A. Nielsen, I. L. Chuang *Quantum Computation and Quantum Information*, Cambridge University Press, 2011

[2] B. Schumacher, M. D. Westmoreland *Quantum Processes, Systems and Information*, Cambridge University Press, 2010

[3] S. Gudder *Quantum Markov Chains*, Journal in Mathematical Physics, **49**, 10.1063, 2008

[4] R. Balian *From Microphysics to Macrophysics*, Springer Berlin Heidelberg, 2007.

[5] J. M. Hickey, S. Genway *Fluctuation Theorems and the Generalised Gibbs Ensemble in Integrable Systems*, Phys. Rev. E, **90** 022107, 2014

[6] J. Novotný, G. Alber, I.Jex *Asymptotic properties of quantum Markov chains*, J. Phys. A, **45**, 48, 2012.

[7] R.Alicki, K. Lendi *Quantum dynamical semigroups and applications*, Springer-Verlag Berlin Heidelberg, 2007.

[8] W. Arveson *An Invitation to C*-algebras*, Springer-Verlag, 1976

Variational Characterization of the Largest Eigenvalue of Compact Positively Homogeneous Operators[*]

Josef Navrátil

3rd year of PGS, email: `pepa.navratil.ez@volny.cz`
Department of Mathematics
Faculty of Nuclear Sciences and Physical Engineering, CTU in Prague

advisor: Milan Kučera, Department of Evolution Differential Equations
Institute of Mathematics, CAS

Abstract. Let $\mathcal{H}$ be a real Hilbert space, let $F : \mathcal{H} \to \mathcal{H}$ be a nonlinear, compact and positively homogeneous operator, i.e. $F(tu) = tF(u)$ for all $t \geq 0$, $u \in \mathcal{H}$. If there exists a function $\xi : \mathcal{H} \times \mathbb{R} \to \mathbb{R}$ satisfying

$$\lim_{t \to 0} \frac{\xi(h,t)}{t} = 0, \quad \text{for all} \ \ h \in \mathcal{H},$$

such that

$$\langle F(u + th), u + th \rangle - \langle F(u), u \rangle \leq 2t\langle F(u), h \rangle + \xi(h,t), \quad \text{for all } t \in \mathbb{R}, \ \ \text{for all } u, h \in \mathcal{H},$$

then the largest eigenvalue λ_0 of the positively homogeneous operator F can be characterized variationally in an analogy with a linear case, i.e.

$$\lambda_0 = \max_{u \in \mathcal{H}, u \neq 0} \frac{\langle F(u), u \rangle}{\|u\|^2}.$$

Let $S : \mathcal{H} \to \mathcal{H}$ be a compact linear operator. If the largest eigenvalue λ_1^S of S has odd multiplicity, then there exists τ_0 such that for any $\tau \in (0, \tau_0)$ and for any compact positively homogeneous operator F satisfying $\|F(u)\| \leq \tau\|u\|$ and $\langle F(u), u \rangle \geq 0$ for all $u \in \mathcal{H}$, there exists a bifurcation point $\lambda_b \in (\lambda_1^S - \tau, \lambda_0]$ of the equation

$$u \in \mathcal{H} : \quad \lambda u - Su + F(u) - N(u) = 0,$$

where $N : \mathcal{H} \to \mathcal{H}$ is a small compact nonlinear perturbation.

These general results are further applied to reaction-diffusion systems with unilateral terms of the type u^-.

Keywords: reaction-diffusion systems, Turing patterns, positively homogeneous operators, Neumann boundary condition, Dirichlet boundary condition

Abstrakt. Nechť $\mathcal{H}$ je reálný Hilbertův prostor, nechť $F : \mathcal{H} \to \mathcal{H}$ je nelineární, kompaktní a pozitivně homogenní operátor, tzn. $F(tu) = tF(u)$ pro všechna $t \geq 0$, $u \in \mathcal{H}$. Pokud existuje funkce $\xi : \mathcal{H} \times \mathbb{R} \to \mathbb{R}$ splňující

$$\lim_{t \to 0} \frac{\xi(h,t)}{t} = 0, \ \ \text{pro všechna } h \in \mathcal{H},$$

tak, že

$$\langle F(u+th), u+th \rangle - \langle F(u), u \rangle \le 2t\langle F(u), h \rangle + \xi(h,t), \quad \text{pro všechna } t \in \mathbb{R}, \text{ pro všechna } u, h \in \mathcal{H},$$

pak lze největší vlastní číslo λ_0 operátoru F charakterizovat variačně, tzn.

$$\lambda_0 = \max_{u \in \mathcal{H}, v \ne 0} \frac{\langle F(u), u \rangle}{\|u\|^2},$$

což je analogické vztahu pro lineární operátory.

Nechť $S : \mathcal{H} \to \mathcal{H}$ je kompaktní lineární operátor. Pokud největší vlastní číslo λ_1^S operátoru S má lichou násobnost, pak existuje $\tau_0 > 0$ tak, že pro každé $\tau \in (0, \tau_0)$ a pro každý nelineární, kompaktní a pozitivně homogenní operátor F, který splňuje předpoklady $\|F(u)\| \le \tau\|u\|$ a $\langle F(u), u \rangle \ge 0$ pro všechna $u \in \mathcal{H}$, existuje bifurkační bod $\lambda_b \in (\lambda_1^S - \tau, \lambda_0]$ rovnice

$$u \in \mathcal{H} : \quad \lambda u - Su + F(u) - N(u) = 0,$$

kde $N : \mathcal{H} \to \mathcal{H}$ je malá kompaktní nelineární porucha.

Tyto obecné výsledky jsou následně použity na systémy reakce-difúze s jednostrannými členy typu u^-.

Klíčová slova: systémy reakce-difúze, Turingovy vzory, pozitivně homogenní operátory, Neumannova okrajová podmínka, Dirichletova okrajová podmínka

This topic has been presented at VII. Symposium on Nonlinear Analysis in Toruń [1] and is a part of article [7], which is being prepared.

References

[1] Abstracts of SNA 2015 Toruń, [cit. 25.9.2015]
http://www-users.mat.umk.pl/~szwejk/program/KNAMiT/abstracts.php

[2] J. I. Baltaev, M. Kučera, M. Väth: A variational approach to bifurcation in reaction-diffusion systems with Signorini type boundary conditions, Appl. of Math., 2/2012, pg. 143-165

[3] Michael G Crandall, Paul H Rabinowitz: Bifurcation from simple eigenvalues; JOURNAL OF FUNCTIONAL ANALYSIS 8, 321-340 (1971)

[4] P. Drábek, J. Milota: Methods of Nonlinear Analysis: Applications to Differential Equations, Springer, 2013, ISBN: 978-3034803861

[5] L.C. Evans: Partial Differential Equations, Springer AMS, 2010, ISBN: 0821849743

[6] S. Fučík, A. Kufner: Nonlinear Differential Equations. Elsevier, Amsterdam-Oxford, New York, 1980

[7] M. Kučera, J. Navrátil: Reaction-diffusion systems with unilateral terms, in preparation

[8] J.D. Murray: Mathematical Biology II, Springer; 3rd edition, 2011

[9] A. Turing: A Chemical Base of Morphogenesis, Philosophical Transactions of the Royal Society of London, Series B, No.641, Vol. 237, 14 August 1952

Bound States in Waveguides with Complex Robin Boundary Conditions

Radek Novák

3rd year of PGS, email: `novakra9@fjfi.cvut.cz`
Department of Physics
Faculty of Nuclear Sciences and Physical Engineering, CTU in Prague

advisor: David Krejčiřík, Department of Theoretical Physics
Nuclear Physics Institute, CAS

Abstract. We consider the Laplacian in a tubular neighbourhood of a hyperplane subjected to non-self-adjoint $\mathcal{PT}$-symmetric Robin boundary conditions. Its spectrum is found to be purely essential and real for constant boundary conditions. The influence of the perturbation in the boundary conditions on the threshold of the essential spectrum is studied using the Birman-Schwinger principle. Our aim is to derive a sufficient condition for existence, uniqueness and reality of discrete eigenvalues. We show that discrete spectrum exists when the perturbation acts in the mean against the unperturbed boundary conditions and we are able to obtain the first term in its asymptotic expansion in the weak coupling regime.

Keywords: non-self-adjointness, waveguide, Robin boundary conditions, spectral analysis, essential spectrum, weak coupling, Birman-Schwinger principle

Abstrakt. Uvažujeme Laplacián ve válcovém okolí hyperroviny podrobený nesamosdruženým $\mathcal{PT}$-symetrickým Robinovým hraničním podmínkám. Jeho spektrum je nalezeno jakožto čistě esenciální a reálné pro konstantní hraniční podmínky. Vliv poruchy v hraničních podmínkách na práh esenciálního spektra studujeme použitím Birmanova-Schwingerova principu. Naším cílem je odvodit postačující podmínku pro existenci, jednoznačnost a reálnost diskrétních vlastních hodnot. Ukážeme, že diskrétní spektrum existuje, když porucha působí ve střední hodnotě proti neporušeným hraničním podmínkám, a jsme schopni získat první člen v jeho asymptotickém rozvoji v režimu slabé vazby.

Klíčová slova: nesamosdruženost, vlnovod, Robinovy hraniční podmínky, spektrální analýza, esenciální spektrum, slabá vazba, Birmanův-Schwingerův princip

This contribution is based on my paper accepted to journal Asymptotic Analysis.

Identification of Aliasing-Based Patterns in Re-Captured LCD Screens*

Adam Novozámský

5th year of PGS, email: `novozamsky@utia.cas.cz`
Department of Mathematics
Faculty of Nuclear Sciences and Physical Engineering, CTU in Prague

advisor: Stanislav Saic, Department of Image Processing
Institute of Information Theory and Automation, CAS

Abstract. This this paper we address the problem of identification of pictures and videos re-captured from LCD screens. We show that they often exhibit detectable periodic patterns that are caused by regular sampling grid of LCD screen and aliasing. We developed a method capable of detecting these patterns by using the theory of cyclostationarity. The term cyclostationarity refers to a special class of signals which exhibit periodicity in their statistics. Such signals have a frequency spectrum correlated with a shifted version of itself. Experimental results quantifying the performance of the developed method are also shown.

Keywords: image and video re-capturing, cyclostationary, aliasing, spectral analysis, CFA, image forensics

Abstrakt. V tomto článku řešíme problém identifikace přefocování LCD monitoru u obrazu a videa. Poukazujeme na periodické porušení, které je způsobeno pravidelným vzorkovacím rastrem u LCD obrazovky a aliasingem. Vyvinuli jsme metodu schopnou detekovat tyto vzory za pomoci teorie cyklostacionarity. Termín cyklostacionarita se odkazuje na speciální třídy signálů, jejichž pravděpodobnostní popis se periodicky opakuje. U těchto signálů koreluje frekvenční spektrum s posunutou verzí sebe sama. Experimentální výsledky kvantifikující úspěšnost vyvinuté metody jsou rovněž uvedeny.

Klíčová slova: přefocení obrazu a videa, cyklostacionarita, aliasing, spktrální analýza, CFA, forézní analýza obrazu

References

[1] B. Mahdian and S. Saic, "A bibliography on blind methods for identifying image forgery," Image Commun., vol. 25, no. 6, pp. 389–399, 2010.

[2] A. Popescu and H. Farid, "Exposing digital forgeries in color filter array interpolated images," IEEE Transactions on Signal Processing, vol. 53, no. 10, pp. 3948–3959, 2005. [Online]. Available: www.cs.dartmouth.edu/farid/publications/sp05a.html

[3] G. Sankar; V. Zhao; Yee-Hong Yang, "Feature based classification of computer graphics and real images," in Acoustics, Speech and Signal Processing, 2009. ICASSP 2009. IEEE International Conference on , vol., no., pp.1513-1516, 19-24 April 2009.

[4] W. Chen; Y.Q. Shi; X Guorong, "Identifying Computer Graphics using HSV Color Model and Statistical Moments of Characteristic Functions," in Multimedia and Expo, 2007 IEEE International Conference on , vol., no., pp.1123-1126, 2-5 July 2007.

[5] Z. Lin, J. He, X. Tang, and C.-K. Tang. 2009. Fast, automatic and fine-grained tampered JPEG image detection via DCT coefficient analysis. Pattern Recogn. 42, 11 (November 2009), 2492-2501.

[6] H. Huang; W. Guo; Y. Zhang, "Detection of Copy-Move Forgery in Digital Images Using SIFT Algorithm," in Computational Intelligence and Industrial Application, 2008. PACIIA '08. Pacific-Asia Workshop on , vol.2, no., pp.272-276, 19-20 Dec. 2008

[7] B. Mahdian and S. Saic, "Blind authentication using periodic properties of interpolation," IEEE Transactions on Information Forensics and Security, vol. 3, no. 3, pp. 529–538, September 2008.

[8] S. Prasad and K. R. Ramakrishnan, "On resampling detection and its application to image tampering," in Proceedings of the IEEE International Conference on Multimedia and Exposition, Toronto, Canada, 2006, pp. 1325–1328.

[9] H. Muammar and P. L. Dragotti, "An investigation into aliasing in images recaptured from an lcd monitor using a digital camera." in ICASSP. IEEE, 2013, pp. 2242–2246.

[10] X. Gao, B. Qiu, J. Shen, T.-T. Ng, and Y. Q. Shi, "A smart phone image database for single image recapture detection," in Proceedings of the 9th International Conference on Digital Watermarking, ser. IWDW'10. Berlin, Heidelberg: Springer-Verlag, 2011, pp. 90–104.

[11] T. Thongkamwitoon, H. Muammar, and P. L. Dragotti,"Robust image recapture detection using a k-svd learning approach to train dictionaries of edge profiles," In Proceeding, IEEE International Conference on Image Processing (ICIP), 2014.

[12] N. Kose and J.-L. Dugelay, "Classification of captured and recaptured images to detect photograph spoofing," in ICIEV 2012, IEEE/IAPR International Conference on Informatics, Electronics and Vision, 18-19 May 2012, Dhaka, Bangladesh, 2012.

[13] X. Gao, T.-T. Ng, B. Qiu, and S.-F. Chang, "Single-view recaptured image detection based on physics-based features." in ICME. IEEE, 2010, pp. 1469–1474.

[14] M. V. Scarzanella and P. L. Dragotti, "Modelling radial distortion chains for video recapture detection." in MMSP. IEEE, 2013, pp. 412–417.

[15] P. Bestagini, M. Visentini-Scarzanella, M. Tagliasacchi, P. Dragotti, and S. Tubaro, "Video recapture detection based on ghosting artifact analysis," in 2013 IEEE International Conference on Image Processing (ICIP), 2013.

[16] J. Li, Y. Wang, T. Tan, and A. K. Jain, "Live face detection based on the analysis of Fourier spectra," in In Biometric Technology for Human Identification, 2004, pp. 296–303.

[17] H. Cao and A. C. Kot, "Identification of recaptured photographs on lcd screens." in ICASSP. IEEE, 2010, pp. 1790–1793.

[18] J. Bai, T.-T. Ng, X. Gao, and Y.-Q. Shi, "Is physicsbased liveness detection truly possible with a single image?" in ISCAS. IEEE, 2010, pp. 3425–3428.

[19] J. C. Krumm and S. A. Shafer, "Sampled-grating and crossed-grating models of moire patterns from digital imaging," Optical Engineering, vol. 30, no. 2, pp. 195–206, 1991.

[20] C. Farrow, M. M. Shaw, H. Kim, P. Juhas, and S. Billinge, "The nyquist-shannon sampling theorem and the atomic pair distribution function," Physical Review B, vol. 84, 2011.

[21] S.-H. Lam and C.-W. Kok, "Demosaic: Color filter array interpolation for digital cameras," in PCM '01: Proceedings of the Second IEEE Pacific Rim Conference on Multimedia. London, UK: Springer-Verlag, 2001, pp. 1084–1089.

[22] W. A. Gardner, A. Napolitano, and L. Paura, "Cyclostationarity: Half a century of research," Signal Processing, vol. 86, no. 4, pp. 639–697, 2006.

[23] W. A. Gardner, "Spectral correlation of modulated signals: Part i–analog modulation," IEEE Transactions on Communications, vol. 35, no. 6, pp. 584–594, June 1987.

[24] ——, "The spectral correlation theory of cyclostationary time-series," Signal Process., vol. 11, no. 1, pp. 13-36, 1986.

[25] ——, "Exploitation of spectral redundancy in cyclostationary signals," IEEE Signal Processing Magazine, vol. 8, no. 2, pp. 14–36, April 1991.

Event Processing in the COMPASS DAQ

Josef Nový

4th year of PGS, email: `novyjos1@fjfi.cvut.cz`
Department of Software Engineering
Faculty of Nuclear Sciences and Physical Engineering, CTU in Prague

advisor: Tomáš Liška, Department of Software Engineering
Faculty of Nuclear Sciences and Physical Engineering, CTU in Prague

Abstract. This paper concentrate on description of data flow through both hardware and software parts of the data acquisition system (DAQ) of the COMPASS experiment at CERN. It also describes system of data quality control. Ability to recover from errors coming from frontend electronics and on possibility to easily identify origin of errors are important features of reliable DAQ, thus tests are implemented on all hardware layers and additional headers are added to data stream. These headers are later analyzed by software. System was deployed in the end of year 2014. Run was successful and event checks proved to be very useful part of DAQ. This paper is extension of paper [6] prepared for conference CSCAS2015.

Keywords: FPGA, Qt, data quality control

Abstrakt. Tento příspěvek popisuje cestu události skrze jak hardwarové tak i softwarové části nového systému pro sběr dat (DAQ) experimentu COMPASS v CERN využívajícího technologie FPGA k sestavování událostí. Také popisuje velmi důležitý systém kontroly dat. Schopnost vyrovnat se s chybami přicházejícími z elektroniky detektorů a možnost snadno identifikovat původ chyb je velmi důležitou součástí spolehlivého systému pro sběr dat, proto bylo nutné implementovat testy ve všech vrstvách hardwaru. Během testů se také přidávají nové identifikační hlavičky. Tyto hlavičky jsou později analyzovány softwarem. Celý systém byl nasazen koncem roku 2014. Sběr dat v tomto období byl úspěšný a systém testování událostí se ukázal jako velmi užitečná část DAQ. Tento příspěvek je rozšířením příspěvku [6] připraveného pro konferenci CSCAS2015.

Klíčová slova: FPGA, Qt, monitorování kvality

1 Introduction

This paper concentrate on description of data flow through both hardware and software parts of the data acquisition system (DAQ) of the COMPASS (Common muon and proton apparatus for structure and spectroscopy) experiment at CERN [10]. The COMPASS is a fixed target experiment situated at the SPS accelerator in the north area of the CERN laboratory in Geneva, Switzerland. Its goal is to study hadron structure and hadron spectroscopy with high intensity muon and hadron beams. Details about scientific program of the experiment can be found in [4] Data quality control and error control is important part of any modern DAQ. The COMPASS DAQ have many different pieces of equipment with different behavior during run which have to run in harsh environment, thus it was necessary to prepare robust data processing chain. Data checks on many levels of hardware and software were included to ensure this robustness. These checks

allows DAQ to recover from errors in detectors and also to identify more easily where the error appeared.

2 DAQ architecture

2.1 Hardware part

The DAQ of the COMPASS experiment consists of several layers. The frontend electronics that form the lowest layer continuously preprocess and digitize analogue data from the detectors. Data format vary based on detector in question. Many different kinds of frontend chips are used in COMPASS, thus it is very complicated to fully check data at this layer. There are approximately 300 000 detector channels; trigger rate can rise up to 45 kHz with 36 kB average event size. SPS accelerator operates in cycles that consist of two 4.8 s long period with beam (called spill) spread in time interval of 36-58.8 s (called supercycle) with minimum of 4.8 s period without beam between two spills. Data from multiple channels are readout and assembled by the concentrator modules called CATCH, GeSiCA, and GANDALF. The first standard header is added at this layer. Structure of this header is shown in Table 1. Similar header structure is also added by SMUX and TIGER modules [10], but without last word. The next layers use slightly different version of the header word meaning as is shown in Table 2.

meaning	mask
1. word	
event size	0x0000FFFF
source ID	0x03FF0000
event type	0x7C000000
error flag	0x80000000
2. word	
event number	0x000FFFFF
spill number	0x7FF00000
state	0x80000000
3. word	
status	0x000000FF
tcs error	0x0000FF00
error word	0x00FF0000
format	0xFF000000

Table 1: Format of header words used by CATCH, GeSiCA, and GANDALF

meaning	mask
1. word	
event size	0x0000FFFF
source ID	0x03FF0000
event type	0x7C000000
event size (the most significant bit)	0x80000000
2. word	
event number	0x000FFFFF
spill number	0x7FF00000
state	0x80000000
3. word	
status	0x000000FF
tcs error	0x0000FF00
error word	0x00FF0000
format	0xFF000000

Table 2: Format of header words used by DHC cards and spillbuffers

These modules receive signals from the time and trigger system; when the trigger signal arrives, the readout is performed and data are sent over optical connection S-Link to the following layer that is based on special FPGA DHC (Data Handling Card)
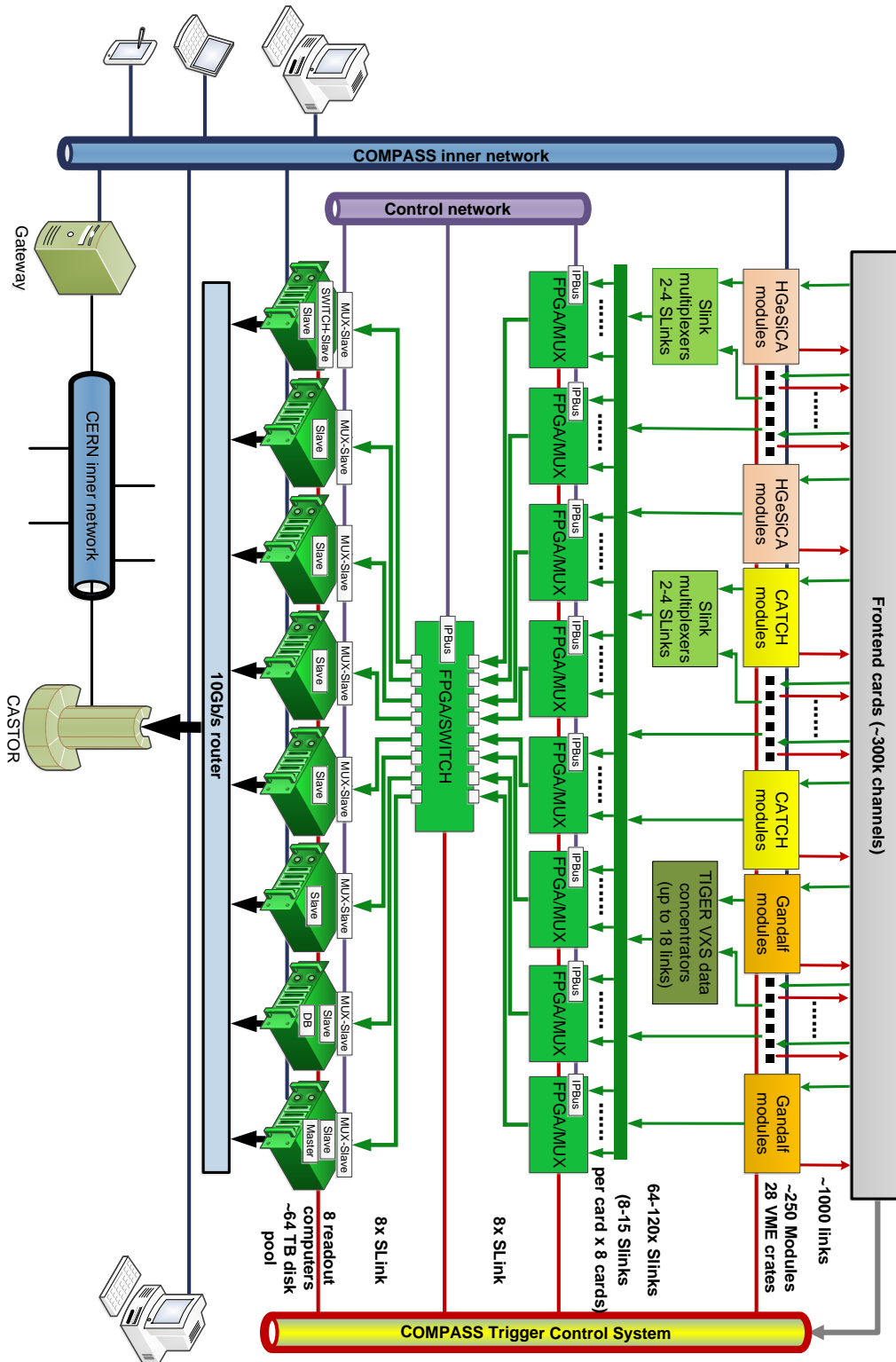
Figure 1: The new DAQ architecture

cards as shown in Figure 1. It is further divided into two layers and is responsible for building of complete events. This newly designed event building part allows usage of more compact control system. The hardware event builder performs online verification of data consistency. The last layer of the system consists of readout engine computers equipped with spillbuffer cards that readout assembled events and transfer them to the The CERN Advanced STORage (CASTOR) for long term storage.

2.2   Software part

The original DAQ system of the COMPASS was based the Data Acquisition and Test Environment (DATE) software (see [1]), originally developed for the ALICE experiment at CERN for control of the hardware, therefore many user programs expect that data files are in the DATE data format. Transformation of read out data to DATE data format is needed because of this limitation. Data quality monitoring and error control is also important part. The DAQ package of the COMPASS experiment composed of several processes; namely: Master, slaveReadout, slaveControl, GUI, messageBrowser, messageLogger. This paper focuses only on slaveReadout process responsible for processing of data stream. Details of other parts of DAQ software package can be found in [8, 7, 5, 2, 3].

3   Event processing in hardware

In the first step of the data acquisition process, data from detectors are prepared to the Slink format [11] and sent over optical fiber to DHC module with multiplexer firmware [8]. Module in this configuration contains up to 15 incoming links. Data from each link are verified. If an error is detected, data are discarded and artificial header with size of three words is generated. Otherwise header with correct size is generated and prepended in front of normal data. Some errors can be masked and payload is then kept. Both masked and unmasked errors are marked in appropriate bit of the added header. All links are then combined to one pack and one additional header with summary of sizes is prepended. Such data pack is sent to the following stage. This stage is represented with a single FPGA module with switch firmware [8]. The switch works very similarly to multiplexer from data handling point of view. However, it uses only 8 links instead of 15 as incoming. Remaining links are configured as outgoing and are connected to spillbuffer cards. Spillbuffer verifies data in the same way but adds only one specific header as it has only one connected link. This header has one additional word which contains precise timestamp of the event. Data from spillbuffers are retrieved by the readout program. Full diagram of the system is shown in Figure 2. The presented design is very flexible; additional layers can be easily added or removed as needed.

4   Event processing in software

Software processing is done in slaveReadout processes in several separate threads; namely: *main readout thread, circular buffer thread, processor thread, transformation threads, out-*
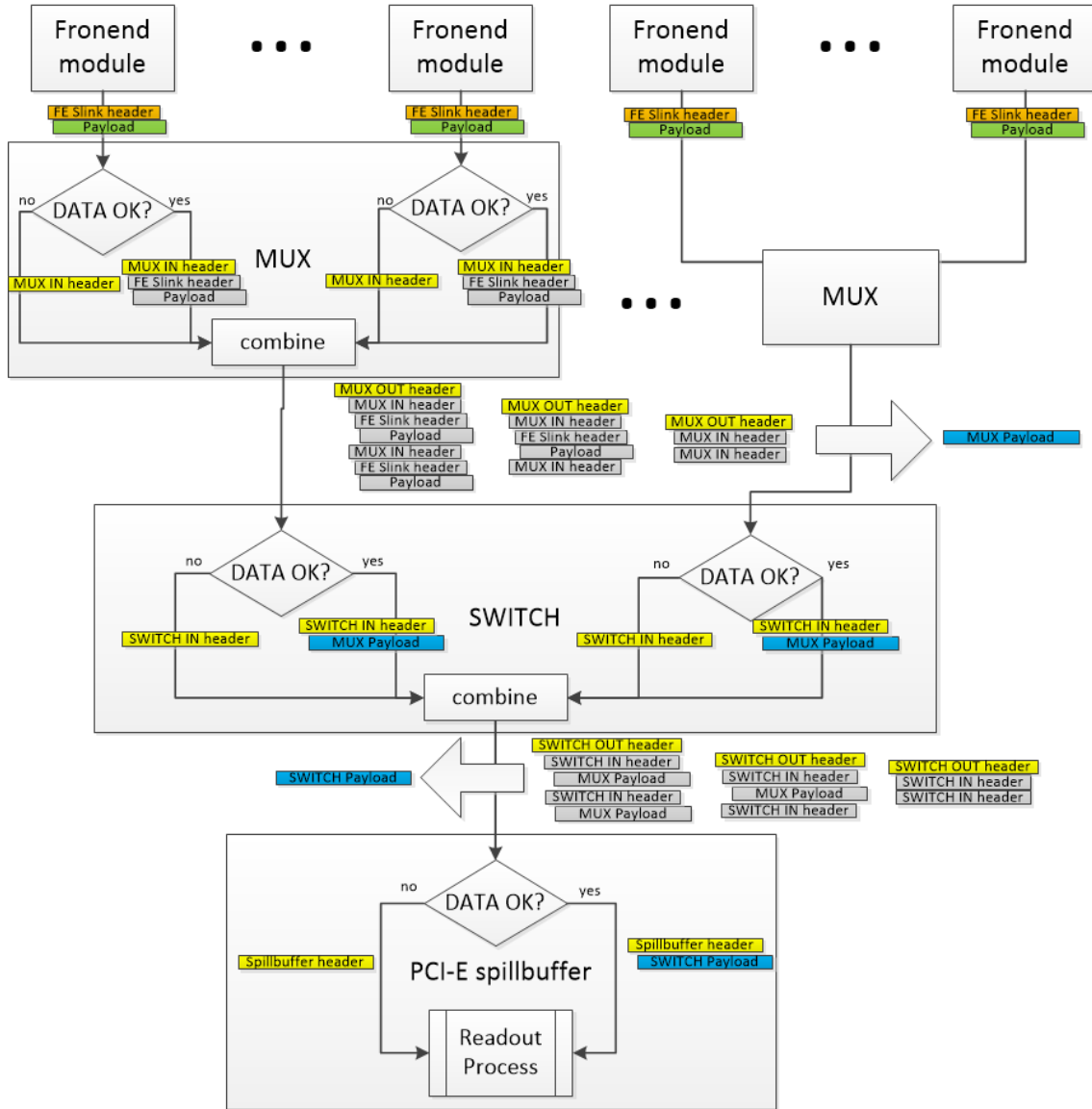
Figure 2: Event processing in hardware part

put threads, and *terminator thread*. Events are exchanged between threads by signal-slot mechanism (SSM) of the Qt framework [12]. Diagram of thread interactions is shown in Figure 3. To decrease the influence of overhead of the SSM on the overall performance of the system, we send several hundred events in one bunch. SlaveReadout processes have also *informator thread* used for communication with rest of the system [2].

4.1   Main readout thread

Main readout thread is the most time critical thread. It is responsible for reading of the events from spillbuffer through driver and for keeping of information about state of
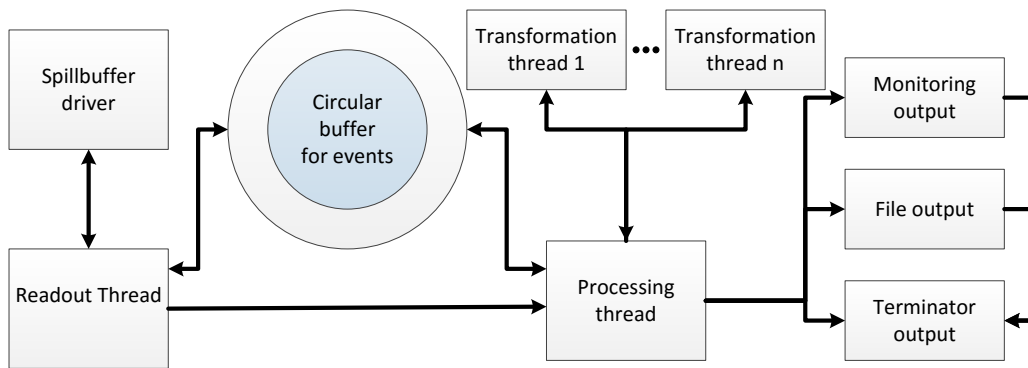
Figure 3: Event processing in software part

the process. The readout in this thread is done in following steps. In the first step, event from the memory of the spillbuffer is readout into the memory of readout engine computer. Memory for event is pre-allocated in super blocks of 512 MB. Memory pre-allocation is necessary to speed up the readout and decrease load on CPU as dynamic memory allocation with standard operator *new* can be slow. Influence of this scheme is quite significant as in original design the operator *new* could have been called even 90000 times per second. At first, the main readout thread requests the space required to store event from the memory manager object. If there is a free space in pre-allocated super block, the memory manager takes two blocks of 1024 kB from it and returns its address back to main thread. The first block is for raw event from driver and the second one is for event transformed into the DATE format. If there is no free space in actual super block memory, the manager allocates a new super block. Main thread prepares event object in the memory block to which the actual data are filled by driver. When preset number of events is readout, the message is formed and then it is sent to circular buffer thread for temporary storage. Main readout thread has highest priority.

4.2   Circular buffer thread

Circular buffer thread is support thread used for handling events until the processor thread declares readiness for new events and it is also used for monitoring of occupied memory. It is sleeping the most of the time and have no resource demanding function inside.

4.3   Processor thread

Processor thread has two parts in the first parts events are distributed to *transformation threads* and in the second part events are passed to outgoing threads. In the present DAQ version, a system for distribution of not transformed events to transformation threads is used. Processor thread continuously checking for available *transformation threads* and distributes events to them. Number of total processing threads can be change easily

before start of the system. Events are sent to zero to N output threads according to preselected options when the transformation is finished either one by one or in the whole blocks. All outputs are based on abstract class, thus it is relatively easy to add new ones. Main output represents file output which normally receives all events in blocks. Secondary outputs are used for monitoring and gets just fraction of events. This fraction is configurable and during normal physics run is in order of tenths of percent.

4.4   Transformation thread

Transformation thread is responsible for transformation of events into DATE data format. This transformation is very resource demanding as it has to process the entire tree of error checks in the structure of Figure 2, to analyze the additional headers, to remove them, to add header appropriate for the DATE data format, and also to decode specific parts of events for special information about run. Structure of event is compared to the structure described in the XML structure file. This file is generated by master process and is based on the active configuration stored in the database. Transformation process also generates error and warning messages about data quality based mainly, but not only on the additional headers. Transformation is not done on the place. The event in DATE format is build on new place in memory from pieces taken from raw event, together with newly created DATE headers. This system is more demanding on memory, but it is much faster.

4.5   Terminator output thread

Terminator output thread is special output thread. Its task is to monitor if all other outputs are finished with the event. This thread then decompose event when the event is marked as processed or when it is stacked in processing for too long.

5   Conclusion

Full DAQ was successfully deployed during run in the end of 2014 after 3 years of development. This system proved to be more flexible, scalable and resistant to errors of detectors than the original one. Many useful experiences were gathered which are invaluable for further improvements in monitoring of the system. More types of error and data checks were added before run 2015, but space for improvement still remains and many new features are planned. Speed of readout process proved to be more than sufficient as it is not the bottleneck of the system. Described system have also low peak and average load of processor. Peak load is around $60\,\%$ and average load is approximately $5\,\%$ on XEON $3.6\,\mathrm{GHz}$.

6   Acknowledgment

References

[1] T. Anticic, et al. (ALICE DAQ Project): *ALICE DAQ and ECS User's Guide* CERN, EDMS 616039, January 2006.

[2] J. Novy: *COMPASS DAQ - Basic Control System* Prague, 2012, Master thesis, Czech Technical University in Prague

[3] M. Bodlák: *COMPASS DAQ – Database Architecture and Support Utilities* ČVUT Fakulta jaderná a fyzikálně inženýrská, 2012

[4] G. K. Mallot, et al. (The COMPASS Collaboration): *COMPASS-II Proposal* CERN-SPSC-2010-014; SPSC-P-340, May 2010.

[5] J. Novy, et al.: *Developing Control and Monitoring Software for the Data Acquisition System of the COMPASS Experiment at CERN*. Acta polytechnica: Scientific Journal of the Czech Technical University in Prague. Prague, CTU, 2013, issue 4. Available at: `http://ctn.cvut.cz/ap/`

[6] J. Novy, et al.: *Events processing in the new DAQ of the COMPASS experiment* In: Communication systems and computing application science CSCAS2015, Jeju island, South Korea

[7] J. Novy, et al.: *FPGA based data acquisition system for COMPASS experiment*. Journal of Physics: Conference Series. 2014-06-11, vol. 513, issue 1, s. 012029-. DOI: 10.1088/1742-6596/513/1/012029.

[8] J. Novy, et al.: *New data acquisition system for the COMPASS experiment*. Journal of Instrumentation. 2013-02-01, vol. 8, issue 02, C02009-C02009. DOI: 10.1088/1748-0221/8/02/C02009.

[9] D. Levit, I. Konorov, et al.: *The COMPASS DAQ Upgrade* In: COMPASS collaboration meeting, Geneva,17-18 November 2011

[10] G. K. Mallot, et al. (The COMPASS Collaboration): *The COMPASS Experiment at CERN* In: Nucl. Instrum. and Phys. Res., A 577, 3 (2007) pp. 455-518.

[11] H. Fischer, et al., *The COMPASS Online Data Forma*, June 8, 2000. Reachable at: `http://hpfr02.physik.uni-freiburg.de/projects/compass/electronics/notes/dataformat-2000-8/format.html`

[12] *Qt framework documentation* [online]. [cit. 2015-09-25]. Reachable at: `http://doc.qt.io/qt-5/signalsandslots.html`

Využití UML v dolování znalostí z dat

Jiří Palek

3. ročník PGS, email: `jiri.palek@gmail.cz`
Katedra softwarového inženýrství
Fakulta jaderná a fyzikálně inženýrská, ČVUT v Praze

školitel: Jaromír Kukal, Katedra softwarového inženýrství
Fakulta jaderná a fyzikálně inženýrská, ČVUT v Praze

Abstract. Unified Modeling Language (UML) is generally use in information technology to deal with software projects. UML uses a wide variety of diagrams to handle different aspects of software projects. In this artical, activity and state diagrams are used to model a data mining projects.

Keywords: UML, data mining, state diagram, activity diagram

Abstrakt. Modelovací jazyk UML (Unified Modeling Language) se používá v oblasti informačních technologií k plánování a realizaci softwarových projektů. UML používá řadu diagramů, které zachycují různé aspekty softwarových projektů. V tomto příspěvku jsou použity diagram aktivit a stavový diagram k plánování projektů v oblasti dolování znalostí z dat.

Klíčová slova: UML, dolování znalostí z dat, stavový diagram, diagram aktivit

1 Úvod

Dolování znalostí z dat prodělalo od časů svého vzniku bouřlivý vývoj. Ve svých počátcích se jednalo o řešení nějaké reálné úlohy pomocí matematických modelů. Typickým příkladem je datová sada Iris a problém správné klasifikace kosatců podle šířky a délky okvětních a kališních listů, což je problém publikovaný R. A. Fisherem [4].

Ke konci dvacátého století, zejména s rozvojem informačních technologií, se situace dramaticky změnila. Výrazně narostly datové sady i množství matematických modelů, které jsou pro jejich řešení dostupné. Pro vyřešení úlohy je nyní třeba více odborníků z různých domén. Do popředí se tak dostala nutnost celý proces řešení efektivně řídit.

Z manažerského pohledu vznikla řada metodik, které danou poptávku vyřešila, jako jsou 5A, SEMMA, CRISP-DM [2], [3], [7]. Řízení a správa projektu z pohledu analytika ale příliš často řešena není, vyjma specializovaných nástrojů. Na druhou stranu se objevují přístupy, které využívají dobře propracované a rozšířené metodiky z jiných oblastí. V IT odvětví se k vývoji používá modelovací jazyk UML, který využívá diagramy pro modelování různých aspektů vývoje softwarového projektu. Existuje již několik článků, které se zabývají využitím UML pro dolování znalostí z dat [6], [8]. V tomto příspěvku bude využito diagramu aktivit modelovacího jazyku UML pro modelování procesu analýzy dat využívajícího klasické matematické modely a modely založené na jádrových funkcích. Dále pak stavového diagramu pro modelování reálného projektu na klasifikaci Alzheimerovy choroby.
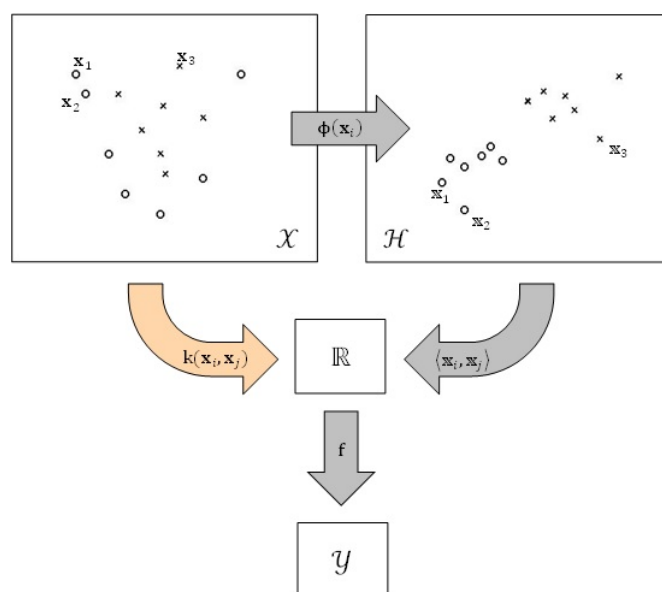
Obrázek 1: Využití jádrových funkcí k modelování.

2 Jádrový přístup k modelům

Jádrový přístup [10], [11] je moderní komplexní přístup k dolování znalostí z dat.

Mějme soubor pozorování a modelované vlastnosti $\{(\mathbf{x}_1, y_1), ..., (\mathbf{x}_n, y_n)\}$, kde $\mathbf{x}_i \in \mathcal{X}$ jsou pozorování, $y_i \in \mathcal{Y}$ je modelovaná vlastnost a $n \in \mathbb{N}$. Klasickým přístupem je následné využití vztahů mezi pozorováními v prostoru $\mathcal{X}$ a pomocí těchto vztahů modelovat požadovanou vlastnost $\mathcal{Y}$.

Myšlenka, kterou využívají jádrové funkce, je vložit mezi prostor $\mathcal{X}$ a $\mathcal{Y}$ další prostor; označme jej $\mathcal{H}$. Prostor $\mathcal{H}$ je zaveden jako Hilbertův prostor a obraz pozorování $\mathbf{x}_i$ v prostoru $\mathcal{H}$ dostaneme pomocí zobrazení Φ jako $\mathbb{x}_i = \Phi(\mathbf{x}_i)$. Takto získáme nový soubor pozorování $\{(\mathbb{x}_1, y_1), ..., (\mathbb{x}_n, y_n)\}$ v prostoru $\mathcal{H}$. Nyní, v prostoru $\mathcal{H}$, budeme skrze vzájemné vztahy mezi pozorování $\mathbb{x}_i$ modelovat prostor $\mathcal{Y}$. V kontextu teorie jádrových funkcí jsou vzájemné vztahy modelovány pomocí vzájemných vzdáleností vyjádřených pomocí skalárního součinu $\langle \mathbb{x}_i, \mathbb{x}_j \rangle$. Celý tento postup je znázorněn schematicky na obrázku 1 pomocí tmavé sekvence šipek.

Protože je prostor $\mathcal{H}$ volen buď jako vysokodimenzionální prostor, nebo dokonce spočetnědimenzionální prostor, je výše uvedený přístup technicky obtížně realizovatelný, v případě spočetnědimenzionálního prostoru dokonce nerealizovatelný. Tento zásadní nedostatek je odstraněn tím, že prostor $\mathcal{H}$ je konstruován tak, aby bylo možné skalární součin $\langle \mathbb{x}_i, \mathbb{x}_j \rangle$ počítat přímo z původních pozorování $\mathbf{x}_i$ pomocí tzv. jádrové funkce k jako $\mathrm{k}(\mathbf{x}_i, \mathbf{x}_j) = \langle \mathbb{x}_i, \mathbb{x}_j \rangle$. Tento postup je znázorněn na obrázku 1 pomocí světlé šipky. Vztahy mezi objekty můžeme shrnout následujícím způsobem

$$\mathrm{k}(\mathbf{x}_i, \mathbf{x}_j) = \langle \mathbb{x}_i, \mathbb{x}_j \rangle = \langle \Phi(\mathbf{x}_i), \Phi(\mathbf{x}_j) \rangle.$$

Přímým důsledkem předchozí formulace je skutečnost, že jednotlivé modely pro dolování dat založené na jádrových funkcích přebírají pozorování ve formě tzv. jádrové matice
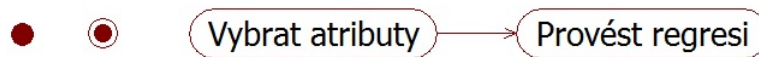
Obrázek 2: Základní komponenty diagramu aktivit. Zleva počátek, ukončení, dvě aktivity a přechod.

$\mathbb{K}$, která je definovaná následujícím způsobem

$$(\mathbb{K})_{ij} = \mathrm{k}(\mathbf{x}_i, \mathbf{x}_j), \forall i, j \in \{1, ..., n\}.$$

3 Modelovací jazyk UML

Modelovací jazyk UML (Unified Modeling Language) je nástroj sloužící hlavně k vývoji aplikací [5], [1]. Obsahuje řadu postupů, jak modelovat celý proces vývoje aplikací od požadavků, přes analýzu a návrh až po samotnou implementaci. To vše prostřednictvím názorných diagramů, které slouží k jasnému a jednoduchému popisu daných částí projektového cyklu.

Vzhledem k tomu, že nedílnou součástí dolování znalostí z dat je práce v oblasti IT, se využití UML v této oblasti přirozeně nabízí.

Pro potřeby modelování projektového cyklu byly vybrány diagram aktivit a stavový diagram.

3.1 Diagram aktivit

Diagram aktivit slouží v modelovacím jazyku UML jako nástroj pro modelování procesů. Proces se skládá z aktivit a přechodů mezi nimi. Diagramy aktivit jsou obdobou stavových diagramů (viz 3.2), kde stavy reprezentují vykonávání aktivit a ukončení aktivity vyvolává přechod. Diagramy aktivit se hojně připojují k případům užití, třídám, rozhraním, komponentám, uzlům, spolupracím, operacím a metodám. Diagramy aktivit slouží většinou k modelování manažerských procesů, díky čemuž se ukazují jako vhodné nástroje pro modelování samotné analýzy dat.

Akce se znázorňují jako obdélníky s oblými rohy (viz Obrázek 2) a popisem aktivity, kdy se v případě, že se jedná o prostou češtinu, používá sloveso nebo slovesná fráze.

Každý diagram aktivit se sestává z akcí, přechodů mezi nimi, které se značí šipkami, a dvou speciálních stavů; počátku a ukončení (viz Obrázek 2).

Jednotlivé přechody je možné vyhodnocovat a větvit na základě booleovských podmínek. Větvení se značí pomocí kosočtverce (viz Obrázek 3) a stejný symbol se využívá i pro sloučení.

Pomocí diagramu aktivit je možné modelovat i souběžné toky činností, kdy přechod se rozvětvuje do dvou nebo více souběžných toků, které se potom synchronizují pomocí spojení (viz Obrázek 3).

Další možnost přizpůsobení diagramu aktivit představují zóny, kdy jednotlivé činnosti sdružujeme podle potřeby do příbuzných oblastí. Zóny se obvykle využívají ke znázornění souběžných toků.

Obrázek 3: Diagram aktivit. Zleva logická podmínka a větvení.
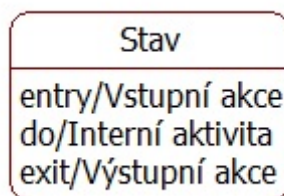
Obrázek 4: Stavový diagram - stav.

Využití diagramů aktivit pro dolování znalostí z dat je velmi přímočaré, protože dolování znalostí z dat je posloupnost operací, která se provádí na datech.

3.2   Stavový diagram

Stavový diagram je důležitým nástrojem pro modelování chování reaktivních systémů. Jak bylo zmíněno v části 3.1, diagramy aktivit jsou speciálním případem stavových diagramů.

V obecném smyslu se stavové diagramy používají k modelování životního cyklu jednoho reaktivního objektu. V kontextu dolování znalostí z dat by se dala za tento reaktivní objekt považovat data, která "reagují"na používané postupy, metody a modely a díky nim se mění.

Syntaxe je analogická jako u diagramu aktivit; opět máme počáteční a koncový stav, samotné stavy jsou obdélníky se zaoblenými rohy, přechody mezi stavy jsou modelovány šipkami, události jsou napsány nad přechody, které jsou díky nim vyvolány.

Stav je v daném konkrétním okamžiku určen hodnotami atributů daného objektu, relacemi s dalšími objekty a aktuálně vykonávanou aktivitou. Díky tomu je popis stavu komplexnější než popis aktivity. Obecná syntaxe stavu je na Obrázku 4. Další součásti jsou stejné, jako u diagramu aktivit v části 3.1.

4 Využití diagramů

V části 3 byly představeny dva diagramy, které budou nyní využity pro modelování procesu dolování znalostí z dat. V této části se omezíme jen na klasifikační úlohu.

4.1 Proces dolování znalostí z dat s využitím metod založených na jádrových funkcích

Klasický proces dolování znalostí z dat je znázorněn pomocí bílé série aktivit na Obrázku 5. Má poměrně pevnou strukturu, v rámci které se postupuje od nejjednodušších operací po ty nejkomplikovanější. Nejprve se provádí průzkumová analýza dat (EDA), na kterou navazuje výběr a transformace atributů. Další krok, deskriptivní modelování (DA), bývá v klasickém procesu nepovinné a používá se podle potřeby konkrétní analýzy. Následně jsou na vybrané datové sady použity jednotlivé klasifikátory. Těch se obvykle volí několik a v závěrečné fázi se vyhodnocují.

Jádrový přístup k analýze dat, který je na Obrázku 5 znázorněn pomocí černých aktivit, navazuje na úvodní průzkumovou analýzu dat a obvykle se využívá paralelně s klasickým. Vzájemná součinnost bývá použita například v případě analýzy hlavních komponent (PCA), kdy se na prvních několik komponent z jádrové varianty PCA použijí klasické klasifikátory.

Vyhodnocení všech klasifikátorů probíhá v závěrečném kroku společně jak pro klasické, tak pro jádrové klasifikátory.

Úvodní fáze dolování znalostí z dat, průzkumová analýza a výběr a transformace atributů v prostoru $\mathcal{X}$, představují obvykle většinu času celé analýzy a mají zcela zásadní vliv na kvalitu výsledků a úspěšnost projektu. Stejný vliv na výsledek má i reprodukující Hilbertův prostor $\mathcal{H}$ a proto by bylo vhodné podobně přistoupit i k jeho analýze. Vzhledem k vazbě obou prostorů $\mathcal{X}$ a $\mathcal{H}$ bylo navrženo upravené schéma procesu dolování znalostí z dat, které reflektuje tyto potřeby a které je znázorněno na Obrázku 6.

V rámci upraveného procesu na Obrázku 6 se nejprve provede analýza vstupního prostoru $\mathcal{X}$ pomocí průzkumové analýzy dat, výběru a transformace atributů a případně průzkumové analýzy dat. Výstupem je jeden nebo několik datových souborů, které slouží buď jako vstup do klasických klasifikátorů, nebo jako základ pro transformaci do prostoru $\mathcal{H}$. Následně se provede stejný proces v prostoru $\mathcal{H}$. Jeho cílem je vytvořit vhodné Hilbertovy prostory, což je z datového pohledu ekvivalentní vytvoření vhodných jádrových matic $\mathbb{K}$. Ty mohou sloužit buď jako vstup do jádrových klasifikátorů, nebo například jako podklad pro jádrovou PCA. V případě PCA je následně možné na vybrané komponenty použít klasické klasifikační modely.

4.2 Využití stavového diagramu

Modelování procesu dolování znalostí z dat pomocí diagramu aktivit je užitečné hlavně z manažerského pohledu, nebo v případě, kdy je třeba zdůraznit nuance v procesu, jako tomu bylo v části 4.1. Má však jeden základní nedostatek, neobsahuje informaci o datech. Pro dobré modelování procesu dolování znalostí z dat by bylo užitečné zároveň postihnout jak aktivity, tak data.
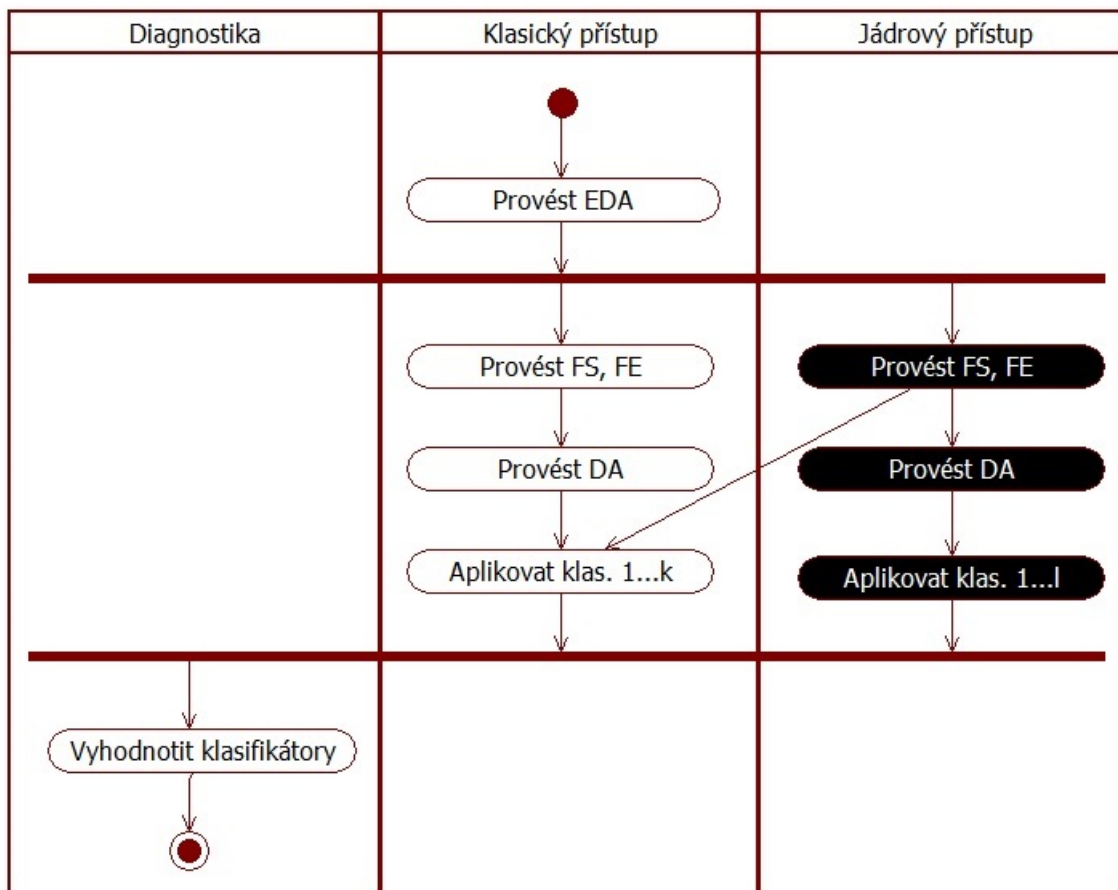
Obrázek 5: Klasické schéma dolování znalostí z dat s využitím diagramu aktivit. EDA - průzkumová analýza dat, FS, FE - výběr a transformace atributů, DA - deskriptivní analýza, klas. - klasifikátor.
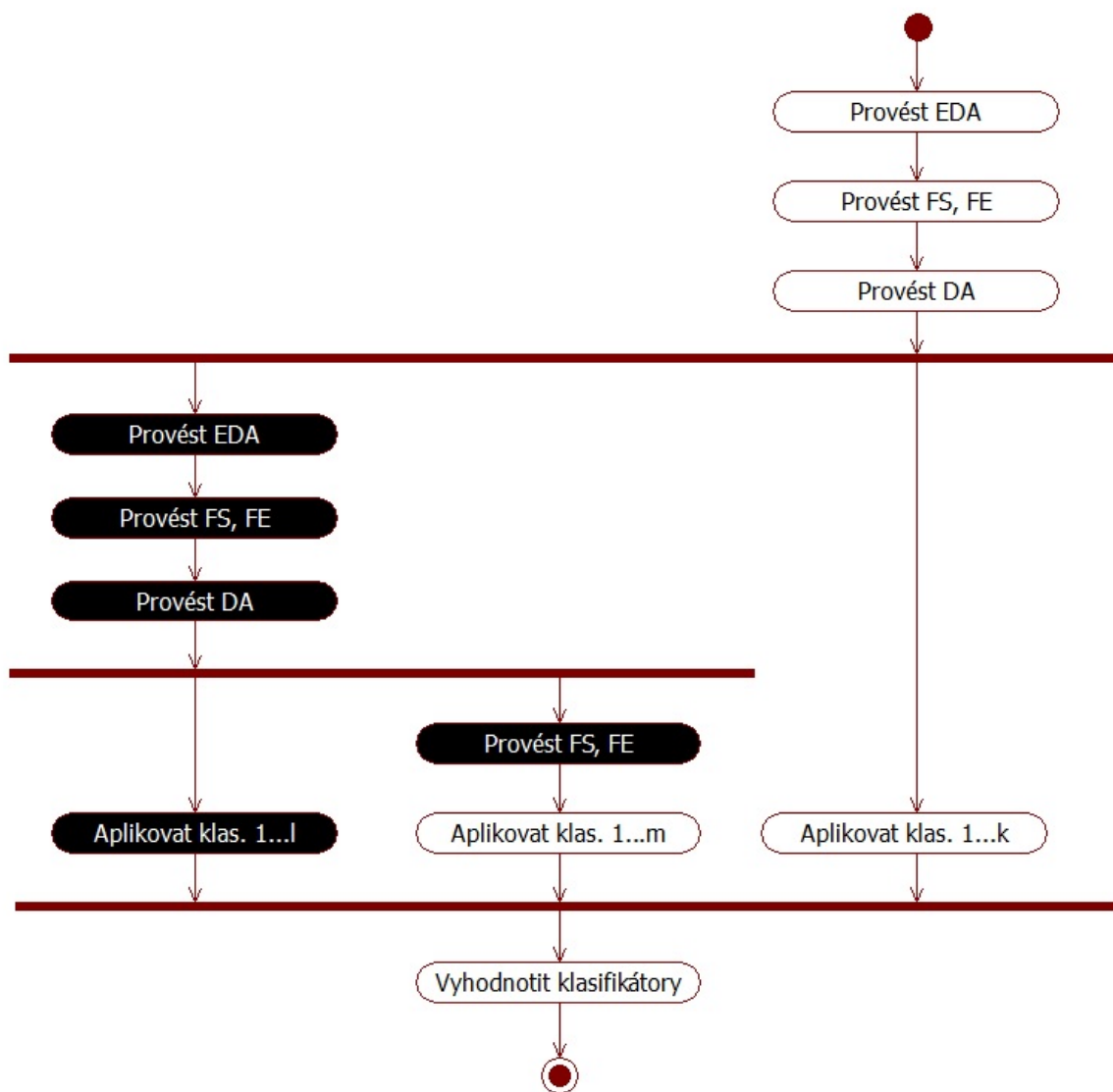
Obrázek 6: Upravené schéma dolování znalostí z dat s využitím diagramu aktivit. EDA - průzkumová analýza dat, FS, FE - výběr a transformace atributů, DA - deskriptivní analýza, klas. - klasifikátor.

Tento pohled na projekt umožňuje stavový diagram. Je určitě možné využít stavový diagram více způsoby. V navrženém schématu je ústředním bodem stav zpracování dat, v rámci kterého se prování určitá ucelená interní aktivita s daty. Výstupní akcí jsou následně upravená data.

Na Obrázku 7 je znázorněn stavový diagram pro klasifikaci Alzheimerovy choroby tak, jak byla provedena v [9]. Úvodní stav začíná načtením hrubých dat. Následně se data zpracují vyjmutím nepotřebných dat. Potom se data transformují do matic normy rozdílu pozorování a skalárního součinu, které slouží jako základ pro tvorbu prostorů $\mathcal{H}$. Vzhledem k náročnosti zpracování hrubých dat jsou data při opuštění tohoto stavu uložena.

V dalším stavu se data opět načtou a provede se jádrová PCA pro exponenciální, Gaussovské a polynomiální jádro. Pro exponenciální rodinu se použije vytvořená síť parametru σ, pro polynomiální jádro se zvolí stupeň jedna až deset. Data se v závěru uloží do příslušných proměnných.

V závěrečném stavu se provede kvadratická diskriminační analýza (QDA) na příslušná data. Vyzkouší se dvě až jedenáct komponent a vše se vyhodnotí s využitím leave-one-out křížové validace.

Samozřejmě úroveň detailu diagramu, toho, co je bráno jako stav, a jednotlivých akcí závisí na úloze a uvážení toho, kdo diagram tvoří. Diagram na Obrázku 7 rozčleňuje celou analýzu do tří stavů, uvádí přehled nejdůležitějších akcí, které byly ve stavech provedeny, a názvy hlavních proměnných.

Nespornou výhodou takového diagramu je možnost přehledně a úsporně vystihnout to nejdůležitější z projektu.

5 Závěr

UML je globálně rozšířený standard pro tvorbu softwarových projektů, který je založen na tvorbě různých diagramů. V tomto příspěvku byly vybrány dva diagramy, diagram aktivit a stavový diagram, a byly využiti pro modelování procesu dolování znalostí z dat.

Diagram aktivit byl použit pro formulaci procesu dolování znalostí z dat, v kterém jsou souběžně použity klasické i jádrové modely. Tento pohled na projekt je vhodný zejména při plánování činností.

Diagram aktivit však neobsahuje datovou stránku věci. Ta byla začleněna do projektu pomocí stavového diagramu, kde jednotlivé stavy byly použity jako stavy dat. V jednotlivých stavech se s daty pracuje pomocí akcí.

Výhodou využití diagramů je snadné vystižení průběhu projektu. Díky využití rozšířeného standardu UML v kontextu dolování znalostí z dat jsou navíc diagramy srozumitelné všem, kteří se s ním ve větší či menší míře již setkali.

Literatura

[1] J. Arlow and I. Neustadt. *UML a unifikovaný proces vývoje aplikací.* Computer Press, (2003).
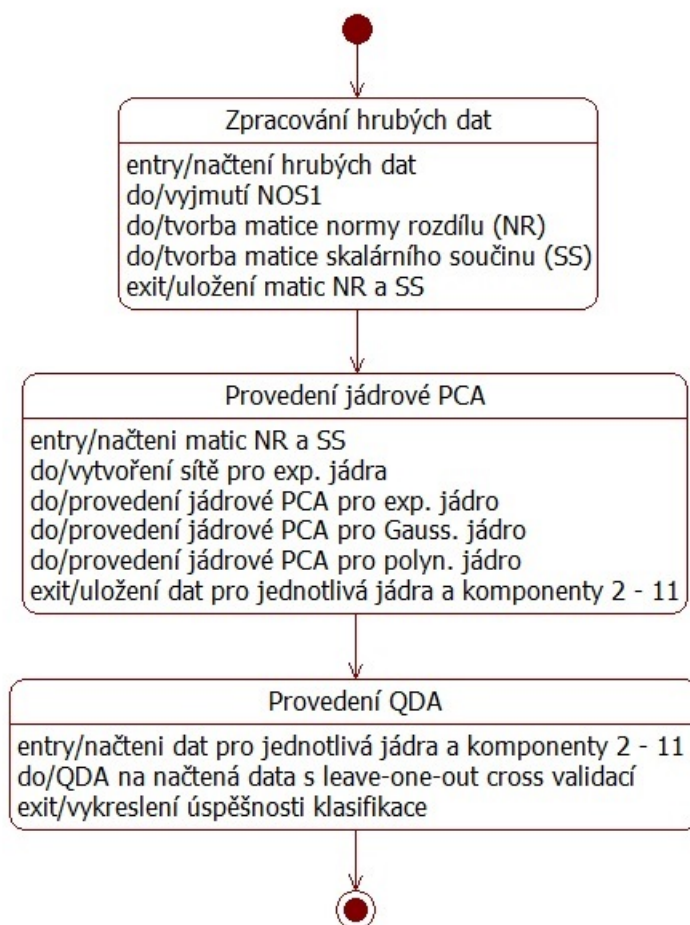
Obrázek 7: Stavový diagram pro klasifikaci Alzheimerovy choroby. QDA - kvadratická diskriminační analýza.

[2] A. I. R. L. Azevedo. *Kdd, semma and crisp-dm: a parallel overview.* In 'Proceedings of International Association for Development of the Information Society - IADIS', 182–185, (2008).

[3] P. Berka. *Dobỳvání znalostí z databází.* Academia, (2003).

[4] R. A. Fisher. *The use of multiple measurements in taxonomic problems.* Annals of eugenics **7** (1936), 179–188.

[5] H. Kanisová and M. Müller. *UML srozumitelně.* Computer Press, (2004).

[6] A. J. Knobbe, A. Siebes, H. Blockeel, and D. Van Der Wallen. *Multi-relational data mining, using uml for ilp.* In 'Principles of data mining and knowledge discovery', Springer (2000), 1–12.

[7] J. MacLennan, Z. Tang, and B. Crivat. *Data mining with Microsoft SQL server 2008.* John Wiley & Sons, (2011).

[8] Ó. Marbán and J. Segovia. *Extending uml for modeling data mining projects (dm-uml).* Journal of Information Technology & Software Engineering **3** (2013).

[9] J. Palek, J. Kukal, A. Bartos, R. Pichova, and H. Trojanova. *Kernel pca in alzheimer's disease diagnostics.* In 'MENDEL 2013', 349–352, (2013).

[10] B. Scholkopf and A. J. Smola. *Learning with kernels: support vector machines, regularization, optimization, and beyond.* MIT press, (2001).

[11] J. Shawe-Taylor and N. Cristianini. *Kernel methods for pattern analysis.* Cambridge university press, (2004).

Numerical Simulation of NAPL Vapor Transport above Porous Medium*

Ondřej Pártl

4th year of PGS, email: `partlond@fjfi.cvut.cz`
Department of Mathematics
Faculty of Nuclear Sciences and Physical Engineering, CTU in Prague

advisor: Michal Beneš, Department of Mathematics
Faculty of Nuclear Sciences and Physical Engineering, CTU in Prague

Abstract. In this contribution, we present a mathematical and numerical model for non-isothermal, compressible flow of a mixture of two ideal gases subject to a constant volume force. The mathematical model is based on balance equations for mass, momentum and energy combined with the ideal gas equation of state. The numerical model is based on the method of lines, where the spatial discretization is carried out by means of the control volume based finite element method, and for the time integration, the Runge-Kutta-Merson method is used. Finally, we present results of a numerical experiment that illustrate the ability of our numerical scheme.

Keywords: control volume based finite element method, multicomponent flow, compressible flow

Abstrakt. V tomto příspěvku prezentujeme matematický a numerický model neizotermálního, stlačitelného proudění směsi dvou ideálních plynů, na které působí konstantní objemová síla. Prezentovaný matematický model kombinuje zákony zachování hmoty, hybnosti a energie se stavovou rovnicí ideálního plynu. Numerický model je založen na metodě přímek, přičemž pro prostorovou diskretizaci je použita kombinace metody konečných prvků a metody konečných objemů a výsledný systém obyčejných diferenciálních rovnic řešen Mersonovou variantou Rungovy-Kuttovy metody. V závěru prezentujeme výsledky jednoho numerického experimentu, které ilustrují schopnosti našeho modelu.

Klíčová slova: metoda konečných prvků, vícekomponentní proudění, stlačitelné proudění

1 Introduction

Our research is focused on development of a numerical model for simulation of NAPL (Non-Aqueous Phase Liquids) vapor transport driven by air flow in porous medium and above its surface. The goal of this research is to put together a mathematical model based on balance equations for mass, momentum and energy for both types of flow, where the gases are considered to be ideal, and to implement a numerical solver in which these

flows are solved separately, and the information is passed between the flows via coupling conditions on the interface between the media.

The model we develop is similar to the one described in [6], but it differs in the following aspects:

1. Our model includes compressibility effects and gravity.

2. Our model is only singe-phase two-component.

Whereas the second item simplifies the model a lot, both the compressibility and gravity effects greatly complicate the numerical solution.

In this contribution, we present the part of our model that describes the free flow and we also present results of a numerical test that demonstrate the ability of our model.

2   Mathematical Model

According to the kinetic theory of gases summarized in [3], [4], [5], a mixture of two polyatomic ideal gases can be described by the following conservation laws:

- Conservation equation for the mass of the mixture

$$\frac{\partial \rho}{\partial t} + \nabla \cdot (\rho \boldsymbol{v}) = 0. \tag{1}$$

- Conservation equation for the mass of one of the gases (we choose the NAPL vapor)

$$\frac{\partial \rho_n}{\partial t} + \nabla \cdot [\rho_n (\boldsymbol{v} + \boldsymbol{V_n})] = 0. \tag{2}$$

- Conservation equation for the momentum of the mixture

$$\frac{\partial (\rho \boldsymbol{v})}{\partial t} + \nabla \cdot (\boldsymbol{P} + \rho \boldsymbol{v} \otimes \boldsymbol{v}) = \rho \boldsymbol{g}. \tag{3}$$

- Conservation equation for the energy of the mixture

$$\frac{\partial (\rho e)}{\partial t} + \nabla \cdot (\boldsymbol{Q} + \rho e \boldsymbol{v} + \boldsymbol{P} \cdot \boldsymbol{v}) = \rho \boldsymbol{g} \cdot \boldsymbol{v}. \tag{4}$$

In these equations, the quantities without subscripts refer to the whole mixture; the quantities related to the NAPL vapor and the second gas are denoted by the subscript n and g, respectively. The components of vectors and matrices are printed in the non-bold font, i.e. $\boldsymbol{v} = (v_1, v_2)^T$, where T denotes transposition. ρ [kg·m^{-3}] represents the density, t [s] the time, $\boldsymbol{v}$ [m·s^{-1}] the velocity, ρ_n [kg·m^{-3}] the density of the NAPL vapor, $\boldsymbol{V_n}$ [m·s^{-1}] the diffusion velocity of the NAPL vapor, $\boldsymbol{P}$ [Pa] the pressure tensor, $\boldsymbol{g}$ [m·s^{-2}]

the gravitational acceleration vector, e $[\text{m}^2 \cdot \text{s}^{-2}]$ the specific energy and $\boldsymbol{Q}$ $[\text{kg} \cdot \text{s}^{-3}]$ the heat flow vector. The fluxes $\boldsymbol{V}_i$, $\boldsymbol{P}$ and $\boldsymbol{Q}$ are defined as

$$\boldsymbol{V}_i = - \sum_{j \in \{n,g\}} D_{i,j} \left(\boldsymbol{d}_j + k_{Tj} \nabla \ln T \right), \quad i = g, n, \tag{5}$$

$$\boldsymbol{P} = p\boldsymbol{I} - 2\mu\boldsymbol{S}, \tag{6}$$

$$\boldsymbol{Q} = -\lambda \nabla T + p \sum_{i \in \{n,g\}} \left(k_{Ti} + \frac{\kappa}{\kappa - 1} \frac{p_i}{p} \right) \boldsymbol{V}_i, \tag{7}$$

where $\boldsymbol{d}_i$ $[\text{m}^{-1}]$ is the diffusion driving force defined by

$$\boldsymbol{d}_i = \nabla \left(\frac{p_i}{p} \right) + \left(\frac{p_i}{p} - \frac{\rho_i}{\rho} \right) \nabla \ln p, \tag{8}$$

where p_i [Pa] and ρ_i $[\text{kg} \cdot \text{m}^{-3}]$ are the partial pressure and density ($p = \sum_{i \in \{n,g\}} p_i$, $\rho = \sum_{i \in \{n,g\}} \rho_i$), respectively, and p [Pa] is the pressure. $D_{i,j}$ $[\text{m}^2 \cdot \text{s}^{-1}]$ is the multicomponent diffusion coefficient, $D_{i,j} = D_{j,i}$, $D_{i,i} = -\frac{\rho_j}{\rho_i} D_{j,i}$, if $\rho_i \neq 0$; otherwise, $D_{i,i}$ is not needed. k_{Ti} $[-]$ denote the thermal diffusion ratio, $k_{Tn} = -k_{Tg}$, μ $[\text{kg} \cdot \text{m}^{-1} \cdot \text{s}^{-1}]$ is the dynamic viscosity, $\boldsymbol{S}$ $[\text{s}^{-1}]$ the rate-of-shear tensor defined by

$$\boldsymbol{S}_{i,j} = \frac{1}{2} \left(\frac{\partial v_j}{\partial x_i} + \frac{\partial v_i}{\partial x_j} \right) - \frac{1}{3} \nabla \cdot \boldsymbol{v} \delta_{i,j}, \tag{9}$$

where x_i [m], $i = 1, 2$, are spatial coordinates, and $\delta_{i,j}$ is the Kronecker delta. λ $[\text{kg} \cdot \text{m} \cdot \text{K}^{-1} \cdot \text{s}^{-3}]$ denotes the thermal conductivity coefficient, T [K] the thermodynamic temperature, and $\kappa = \frac{c_p}{c_v}$ $[-]$ is the ratio of specific heats, where c_p $[\text{J} \cdot \text{kg}^{-1} \cdot \text{K}^{-1}]$ and c_V $[\text{J} \cdot \text{kg}^{-1} \cdot \text{K}^{-1}]$ denote the specific heat at constant pressure and volume, respectively. Moreover, it is useful to define the mass fraction of the species i in the mixture, X_i $[-]$, $X_i = \frac{\rho_i}{\rho}$.

The previous system is supplemented by the following formula relating the energy to the temperature

$$\rho e = c_V \rho T + \frac{1}{2} \rho \boldsymbol{v}^2 \tag{10}$$

and by the ideal gas equation of state

$$\rho = p \frac{\overline{M}}{RT}, \tag{11}$$

where R $[\text{J} \cdot \text{K}^{-1} \cdot \text{mol}^{-1}]$ is the gas constant, and $\overline{M}$ $[\text{kg} \cdot \text{mol}^{-1}]$ is the molar mass defined by

$$\overline{M} = \frac{\rho}{\sum_{i \in \{n,g\}} \frac{\rho_i}{M_i}}, \tag{12}$$

where M_i $[\text{kg} \cdot \text{mol}^{-1}]$ is the molar mass of the component i. Combining equations (10) and (11) with the Mayer relation $\overline{M}(c_p - c_V) = R$, we get the formula relating the energy to the pressure

$$p = (\kappa - 1) \left(\rho e - \frac{1}{2} \boldsymbol{v}^2 \rho \right). \tag{13}$$

Note that for $\rho_n = 0$, the governing equations reduce to the compressible Navier-Stokes equations.

The equations are solved in a rectangular domain $\Omega \subset \mathbb{R}^2$ and on a time interval $I = [t_{\mathrm{ini}}, t_{\mathrm{fin}}]$. The initial conditions are

$$\rho(t_{\mathrm{ini}}, \boldsymbol{x}) = \rho_{\mathrm{ini}}(\boldsymbol{x}), \ \ \boldsymbol{x} \in \overline{\Omega}, \tag{14}$$

$$\rho_n(t_{\mathrm{ini}}, \boldsymbol{x}) = \rho_{n,\mathrm{ini}}(\boldsymbol{x}), \ \ \boldsymbol{x} \in \overline{\Omega}, \tag{15}$$

$$T(t_{\mathrm{ini}}, \boldsymbol{x}) = T_{\mathrm{ini}}(\boldsymbol{x}), \ \ \boldsymbol{x} \in \overline{\Omega}, \tag{16}$$

$$\boldsymbol{v}(t_{\mathrm{ini}}, \boldsymbol{x}) = \boldsymbol{v}_{\mathrm{ini}}(\boldsymbol{x}), \ \ \boldsymbol{x} \in \overline{\Omega}. \tag{17}$$

As for the boundary conditions, there are many combinations of boundary conditions with which our system can be supplemented [1]. In this contribution, the mixture is assumed to flow in the horizontal direction from left to right, the gravitational force points in the vertical direction ($g_1 = 0$), and the following setup is considered (the division of the boundary is depicted in Figure 1a):

- Inflow

$$\rho|_{\mathrm{in}} = \rho_{\mathrm{in}}, \tag{18}$$

$$\rho_n|_{\mathrm{in}} = \rho_{n,\mathrm{in}}, \tag{19}$$

$$\boldsymbol{v}|_{\mathrm{in}} = \boldsymbol{v}_{\mathrm{in}}; \tag{20}$$

  the pressure p is extrapolated via the relation $\frac{\partial^2 p}{\partial x_1^2} = 0$ discretized by the second order central finite difference.

- Outflow

$$p|_{\mathrm{out}} = p_{\mathrm{out}}; \tag{21}$$

  the densities ρ and ρ_n and the velocity $\boldsymbol{v}$ are extrapolated via the same relation as the pressure on the inflow edge.

- Top and bottom edge

$$\boldsymbol{v}|_{\mathrm{top}} = \boldsymbol{v}_{\mathrm{top}}, \ \ \boldsymbol{v}|_{\mathrm{bot}} = \boldsymbol{v}_{\mathrm{bot}}, \tag{22}$$

  the density ρ_n is calculated from X_n, which is extrapolated linearly; the density ρ and the pressure p are extrapolated exponentially because by hydrostatic conditions at constant temperature, the pressure and density distribution is exponential.

3   Numerical Solution

The aforementioned mathematical problem is solved by means of the method of lines, where the spatial discretization is carried out by the control volume based finite element method [8]; for the time integration, the Runge-Kutta-Merson method [7] is employed.

(a) Boundary of Ω.

(b) Primary (solid line) and dual mesh (dashed line).
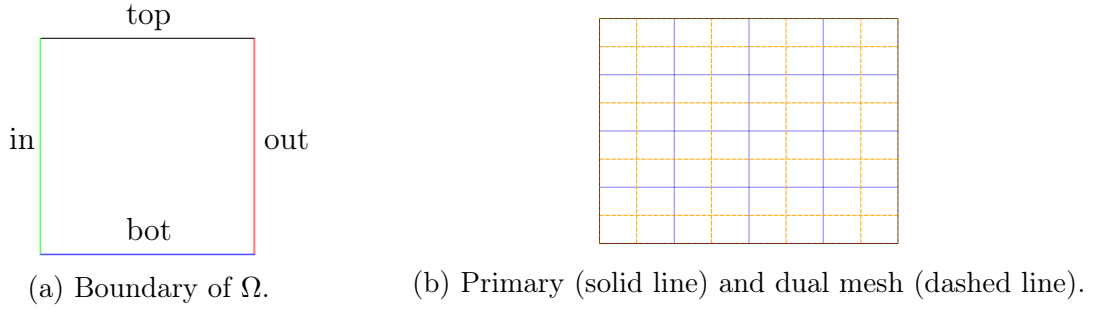
All of the unknown functions (the products ρv_i, $i = g, n$, and ρe are treated as a single variable) are approximated using the classical finite element space based on the bilinear elements [2], where the domain Ω is covered by a mesh $\mathcal{T} = \{T^e\}_{e=1}^{N_\mathcal{T}}$ of rectangles (see Figure 1b), where $N_\mathcal{T}$ is the number of rectangles in $\mathcal{T}$. Each vertex $\boldsymbol{x}_i$ of the mesh is associated with the basis function φ_i. Further, we use the node-centered dual mesh of finite volumes $\mathcal{V} = \{V_i\}_{i=1}^{N_\mathcal{V}}$, where $N_\mathcal{V}$ denotes the number of nodes in $\mathcal{T}$. This mesh will be described later on. Finally, the time interval I is divided by a strictly increasing sequence $(t_n)_{n=0}^{N_t}$, where $t_0 = t_{\mathrm{ini}}$ and $t_{N_t} = t_{\mathrm{fin}}$.

The following notation will be used throughout this text:

- $\mathcal{X} = \{\boldsymbol{x}_i\}_{i=1}^{N_\mathcal{V}}$ is the set of all vertices in the mesh $\mathcal{T}$;

- $\Lambda^e = \{i | \boldsymbol{x}_i \in T^e\}$;

- $\Lambda_i = \{j | (\exists T^e \in \mathcal{T})(\boldsymbol{x}_i \in \Lambda^e \wedge \boldsymbol{x}_j \in \Lambda^e)\} \setminus \{i\}$;

- $\Lambda_i^e = \Lambda^e \cap \Lambda_i$;

- $\Lambda_i^b = \Lambda_i \cap \{j | \boldsymbol{x}_j \in \partial\Omega\}$;

- $\Lambda_{i,j} = \{e | i \in \Lambda^e \wedge j \in \Lambda^e\}$;

- $\Lambda_i^n = \{e | \boldsymbol{x}_i \in \Lambda^e\}$;

- $\boldsymbol{x}_{i,j}$ is the midpoint of the line segment connecting the vertices $\boldsymbol{x}_i$ and $\boldsymbol{x}_j$;

- $\boldsymbol{x}_e$ is the circumcenter of T^e;

- $\Gamma_{i,j}^e$ is the line segment connecting the points $\boldsymbol{x}_e$ and $\boldsymbol{x}_{i,j}$;

- $\Gamma_{i,j}^b$ is the line segment connecting the boundary points $\boldsymbol{x}_i$ and $\boldsymbol{x}_{i,j}$;

- $\Gamma_i = \bigcup_{j \in \Lambda_i} \bigcup_{e \in \Lambda_{i,j}} \Gamma_{i,j}^e$;

- $\Gamma_i^b = \bigcup_{j \in \Lambda_i^b} \Gamma_{i,j}^b$ for $\boldsymbol{x}_i \in \partial\Omega$;

- $\boldsymbol{x}_{i,j}^e$ is the midpoint of $\Gamma_{i,j}^e$;

- $\boldsymbol{x}_{i,j}^b$ is the midpoint of $\Gamma_{i,j}^b$;

- $V_i^e = V_i \cap T^e$;

- $f(\boldsymbol{x}_i) = f_i$, $f(\boldsymbol{x}_{i,j}) = f_{i,j}$, $f(\boldsymbol{x}_{i,j}^e) = f_{i,j}^e$, $f(\boldsymbol{x}_{i,j}^b) = f_{i,j}^b$, $f(\boldsymbol{x}_e) = f_e$, where the time coordinate is omitted;

- $[\boldsymbol{f}]_k$ denotes the k-th component of the vector $\boldsymbol{f}$, when there are too many symbols in the definition of $\boldsymbol{f}$.

The preceding notation is used for scalar (f) as well as vector-valued ($\boldsymbol{f}$) functions.

The finite volume V_i associated with the node $\boldsymbol{x}_i$ is defined as the open set surrounded by the piecewise linear curve Γ_i (i.e., $\partial V_i = \Gamma_i$) for $\boldsymbol{x}_i \notin \partial\Omega$ and by the piecewise linear curve $\Gamma_i \cup \Gamma_i^b$ (i.e., $\partial V_i = \Gamma_i \cup \Gamma_i^b$) for $\boldsymbol{x}_i \in \partial\Omega$. The dual mesh of finite volumes is depicted in Figure 1b.

In our computations, the physical domain Ω is extended by one layer of dummy elements [1], and the aforementioned boundary conditions are prescribed at the corresponding dummy nodes. Therefore, equations (1)–(4) are solved in the whole of Ω.

The numerical scheme is derived by integrating equations (1)–(4) over a volume V_i, applying the Green formula and using the following approximation formulas:

- $\int_{V_i} f(\boldsymbol{x}) \, \mathrm{d}\boldsymbol{x} \doteq \sum_{e \in \Lambda_i^n} |V_i^e| \, f_i = |V_i| \, f_i$, where $|V_i^e|$ denotes the area of V_i^e.

- $\int_{V_i} (\nabla f)(\boldsymbol{x}) \, \mathrm{d}\boldsymbol{x} \doteq \sum_{e \in \Lambda_i^n} |V_i^e| \, (\nabla f)_e$.

- $\int_{\Gamma_i} \boldsymbol{f}(\boldsymbol{x}) \cdot \boldsymbol{n} \, \mathrm{d}\boldsymbol{x} \doteq \sum_{j \in \Lambda_i} \sum_{e \in \Lambda_{i,j}^e} |\Gamma_{i,j}^e| \, \boldsymbol{f}_{i,j}^e \cdot \boldsymbol{n}_{i,j}^e$, where $|\Gamma_{i,j}^e|$ denotes the length of the line segment $\Gamma_{i,j}^e$, and $\boldsymbol{n}_{i,j}^e$ is the unit outward normal with respect to $\Gamma_{i,j}^e$.

The previous procedure yields the system of ordinary differential equations for $k = n, g$ and $i = 1, 2, \ldots N_{\mathcal{V}}$ (the dummy nodes are used),

$$\sum_{e \in \Lambda_i^n} |V_i^e| \, \dot{\rho}_i + \sum_{j \in \Lambda_i} \sum_{e \in \Lambda_{i,j}} |\Gamma_{i,j}^e| \, \underline{\rho_{i,j}^e} \boldsymbol{v}_{i,j}^e \cdot \boldsymbol{n}_{i,j}^e = 0, \tag{23}$$

$$\sum_{e \in \Lambda_i^n} |V_i^e| \, \dot{\rho}_{n,i} + \sum_{j \in \Lambda_i} \sum_{e \in \Lambda_{i,j}} |\Gamma_{i,j}^e| \, \underline{\rho_{n,i,j}^e} \left(\boldsymbol{v}_{i,j}^e + \boldsymbol{V}_{n,i,j}^e \right) \cdot \boldsymbol{n}_{i,j}^e = 0, \tag{24}$$

$$\begin{aligned}
\sum_{e \in \Lambda_i^n} |V_i^e| \, (\dot{\rho v_k})_i &+ \sum_{e \in \Lambda_i^n} |V_i^e| \, [(\nabla p)_e]_k + \sum_{j \in \Lambda_i} \sum_{e \in \Lambda_{i,j}} |\Gamma_{i,j}^e| \, \left[(\boldsymbol{P} - p\boldsymbol{I})_{i,j}^e \cdot \boldsymbol{n}_{i,j}^e \right]_k \\
&+ \sum_{j \in \Lambda_i} \sum_{e \in \Lambda_{i,j}} |\Gamma_{i,j}^e| \, \underline{(\rho v_k)_{i,j}^e} \boldsymbol{v}_{i,j}^e \cdot \boldsymbol{n}_{i,j}^e = \sum_{e \in \Lambda_i^n} |V_i^e| \, \rho_i g_k,
\end{aligned} \tag{25}$$

$$\sum_{e \in \Lambda_i^n} |V_i^e| \, (\dot{\rho e})_i + \sum_{j \in \Lambda_i} \sum_{e \in \Lambda_{i,j}} |\Gamma_{i,j}^e| \, \left[(\boldsymbol{P} \cdot \boldsymbol{v})_{i,j}^e + \boldsymbol{Q}_{i,j}^e + \underline{(\rho e)_{i,j}^e} \boldsymbol{v}_{i,j}^e \right] \cdot \boldsymbol{n}_{i,j}^e = \sum_{e \in \Lambda_i^n} |V_i^e| \, \boldsymbol{g} \cdot (\rho \boldsymbol{v})_i, \tag{26}$$

where

$$\boldsymbol{V}^e_{n,i,j} = - \sum_{l\in\{n,g\}} D^e_{n,l,i,j} \left(\boldsymbol{d}^e_{l,i,j} + k^e_{T_l,i,j} \frac{\nabla T^e_{i,j}}{T^e_{i,j}} \right), \tag{27}$$

$$\boldsymbol{d}^e_{k,i,j} = \nabla \left(\frac{p_k}{p} \right)^e_{i,j} + \left(\frac{p^e_{k,i,j}}{p^e_{i,j}} - \frac{\rho^e_{k,i,j}}{\rho^e_{i,j}} \right) \frac{\nabla p^e_{i,j}}{p^e_{i,j}}, \tag{28}$$

$$\boldsymbol{P} = (p\boldsymbol{I} - 2\mu\boldsymbol{S})^e_{i,j}, \tag{29}$$

$$\boldsymbol{Q}^e_{i,j} = -\lambda \left(\nabla T\right)^e_{i,j} + p^e_{i,j} \sum_{l\in\{n,g\}} \left(k^e_{T_l,i,j} + \frac{\kappa}{\kappa-1} \left(\frac{p^e_{l,i,j}}{p^e_{i,j}} \right) \right) \boldsymbol{V}^e_{l,i,j}. \tag{30}$$

For stability reasons, the term $\int_{V_i} \nabla p$ is approximated as the volume integral in (25), and the underlined terms are modified by the full upwind formula

$$f^e_{i,j} = \begin{cases} f_{n,i}, & \boldsymbol{v}^e_{i,j} \cdot \boldsymbol{n}^e_{i,j} \geq 0 \\ f_{n,j}, & \boldsymbol{v}^e_{i,j} \cdot \boldsymbol{n}^e_{i,j} < 0 \end{cases}.$$

The terms ∇v_k and $\nabla \left(\frac{p_k}{p} \right)$ are calculated via

$$\nabla v_k = \nabla \left(\frac{(\rho v_k)}{\rho} \right) = \frac{\rho \nabla (\rho v_k) - (\rho v_k)\nabla\rho}{\rho^2}, \quad \nabla \left(\frac{p_k}{p} \right) = \frac{p\nabla p_k - p_k\nabla p}{p^2}.$$

4 Numerical Results

In this section, we present the results of the simulation of a traveling wave of NAPL vapor. The domain $\Omega = (0.0, 3.0) \times (-0.5, 0.5)$ is considered, where the units are [m], and there are 30 and 10 square elements in the vertical and horizontal direction, respectively. The same squares are used as the dummy elements. The time step of the Runge-Kutta-Merson method is bounded from above by $3.0 \cdot 10^{-4}$s. The initial ($t_{\mathrm{ini}} = 0.0$s) and boundary conditions are

$$\rho_{\mathrm{ini}}(\boldsymbol{x}) = p_{\mathrm{ref}} \frac{M_g g_2}{RT_{\mathrm{ref}}} \exp \left(\frac{M_g g_2}{RT_{\mathrm{ref}}} x_2 \right), \ \rho_{n,\mathrm{ini}}(\boldsymbol{x}) = 0, \ T_{\mathrm{ini}}(\boldsymbol{x}) = T_{\mathrm{ref}}, \ \boldsymbol{v}_{\mathrm{ini}}(\boldsymbol{x}) = \boldsymbol{v}_{\mathrm{ref}};$$

$$\rho_{\mathrm{in}}(\boldsymbol{x}) = p_{\mathrm{ref}} \frac{M_g g_2}{RT_{\mathrm{ref}}} \exp \left(\frac{M_g g_2}{RT_{\mathrm{ref}}} x_2 \right), \ \rho_{n,\mathrm{in}}(\boldsymbol{x}) = X_{n,\mathrm{ref}}\rho_{\mathrm{in}}(\boldsymbol{x}), \ \boldsymbol{v}_{\mathrm{in}}(\boldsymbol{x}) = \boldsymbol{v}_{\mathrm{ref}};$$

$$\boldsymbol{v}_{\mathrm{top}}(\boldsymbol{x}) = \boldsymbol{v}_{\mathrm{ref}}, \ \boldsymbol{v}_{\mathrm{bot}}(\boldsymbol{x}) = \boldsymbol{v}_{\mathrm{ref}};$$

$$p_{\mathrm{out}}(\boldsymbol{x}) = p_{\mathrm{ref}}.$$

Note that the initial density distribution is hydrostatic. The values of the physical constants are listed in Table 1. The coefficient k_{Tn} is defined by the formula $k_{Tn} = 0.35 X_n \overline{M} M_n^{-1}$, which is based on information in [3].

The numerical results are presented in Figures 2–3. We can see how the wave of non-zero mass fraction of NAPL vapor spreads towards the right edge. As we need to model only slow flows over very long time intervals in our application, the fact that the wavefront is smeared out should not pose any problems in our research.

parameter	value	unit
$D_{g,n}$	$-8.35 \cdot 10^{-5}$	$\mathrm{m}^2 \cdot \mathrm{s}^{-1}$
μ	$1.725 \cdot 10^{-5}$	$\mathrm{kg} \cdot \mathrm{m}^{-1} \cdot \mathrm{s}^{-1}$
λ	0.02428	$\mathrm{kg} \cdot \mathrm{m} \cdot \mathrm{K}^{-1} \cdot \mathrm{s}^{-3}$
κ	1.4	$-$
M_{g}	0.02896	$\mathrm{kg} \cdot \mathrm{mol}^{-1}$
M_{n}	0.13139	$\mathrm{kg} \cdot \mathrm{mol}^{-1}$
R	8.3144621	$\mathrm{J} \cdot \mathrm{K}^{-1} \cdot \mathrm{mol}^{-1}$

parameter	value	unit
g_1	0.0	$\mathrm{m} \cdot \mathrm{s}^{-2}$
g_2	-9.81	$\mathrm{m} \cdot \mathrm{s}^{-2}$
p_{ref}	101325	Pa
T_{ref}	295.15	K
$v_{\mathrm{ref},1}$	1.0	$\mathrm{m} \cdot \mathrm{s}^{-1}$
$v_{\mathrm{ref},2}$	0.0	$\mathrm{m} \cdot \mathrm{s}^{-1}$
$X_{n,\mathrm{ref}}$	0.01	$-$

Table 1: Values of constant physical parameters.
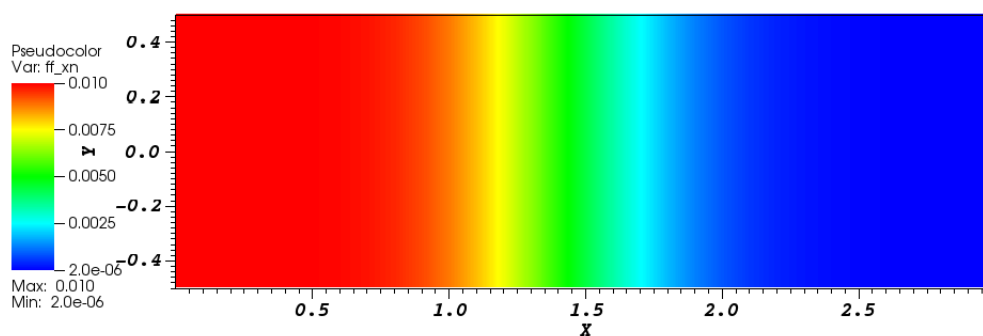
Figure 2: X_n at time $t = 1.5$s.
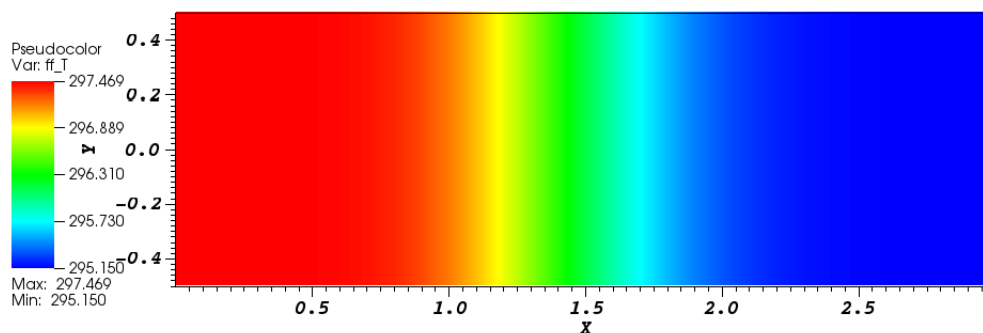
Figure 3: T at time $t = 1.5$s.

5 Conclusions

Our numerical scheme seems to solve the governing equations without producing non-physical oscillations in state variables. Therefore, it can be coupled with the numerical model for flow in porous medium.

References

[1] J. Blazek. *Computational Fluid Dynamics: Principles and Applications*. Elsevier Science, (2001).

[2] S. C. Brenner and L. R. Scott. *The Mathematical Theory of Finite Element Methods*. Springer, 3rd edition, (2008).

[3] S. Chapman and T. G. Cowling. *The Mathematical Theory of Non-Uniform Gases*. Cambridge University Press, 2nd edition, (1952).

[4] J. H. Ferziger and H. G. Kaper. *Mathematical Theory of Transport Processes in Gases*. North-Holland Publishing Company, 1st edition, (1972).

[5] V. Giovangigli. *Multicomponent Flow Modeling*. Birkhäuser Boston, 1st edition, (1999).

[6] K. Mosthaf, K. Baber, B. Flemisch, R. Helmig, A. Leijnse, I. Rybak, and B. Wohlmuth. *A coupling concept for two-phase compositional porous-medium and single-phase compositional free flow*. Water Resources Research **47** (2011).

[7] O. Pártl. *Computational studies of bacterial colony model*. American Journal of Computational Mathematics **3** (2013), 147–157.

[8] S. Patankar. *Numerical Heat Transfer and Fluid Flow*. Series in computational methods in mechanics and thermal sciences. Taylor & Francis, (1980).

Anisotropní škálování prostoru a času v Hořavově teorii gravitace

Filip Petrásek

2nd ročník PGS, email: `petrafil@fjfi.cvut.cz`
Katedra fyziky
Fakulta jaderná a fyzikálně inženýrská, ČVUT v Praze

školitel: Ladislav Hlavatý, Katedra fyziky
Fakulta jaderná a fyzikálně inženýrská, ČVUT v Praze

Abstract. The contribution involves a research part of further investigation into the Horava gravity. The ADM formalism of general relativity is introduced as a tool used in the framework of the Horava gravity, which may represent a modern-day candidate of renormalizable quantum gravity. The theory is essentially based on anisotropic scaling of space and time in the UV, resulting in relativistic invariance breaking.

Keywords: general relativity, ADM formalism, UV relativistic invariance breaking, renormalizability, Horava gravity, quantum gravity

Abstrakt. Tento příspěvek zahrnuje rešeršní část dalšího výzkumu v oblasti Hořavovy teorie gravitace. ADM formalismus obecné teorie relativity je zde uveden jako nástroj užívaný v rámci Hořavovy teorie gravitace, která by mohla představovat současného kandidáta renormalizovatelné kvantové teorie gravitace. Tato teorie v principu vychází z anisotropního škálování prostoru a času v UV oblasti s následným narušením relativistické invariance.

Klíčová slova: obecná teorie relativity, ADM formalismus, UV narušení relativistické invariance, renormalizovatelnost, Hořavova teorie gravitace, kvantová teorie gravitace

1 Úvod

Albert Einstein zrovnoprávnil prostorové souřadnice x^i a čas t, přičemž zavedl pojem prostoročasu $\mathcal{M}[x^\mu]$ jako 4-rozměrné hladké variety a položil tak základ obecné teorie relativity jako geometrické teorie gravitace invariantní vzhledem ke všem prostoročasovým difeomorfismům $\tilde{x}^\mu = \tilde{x}^\mu(x^\nu)$.

Nutnost řešit Cauchyho počáteční úlohu v obecné teorii relativity vedla R. Arnowitta, S. Desera a C. W. Misnera k zavedení ADM formalismu jako Hamiltonovského formalismu popisujícího $3 + 1$ rozštěpení prostoročasu $\mathcal{M}$ na prostorupodobné nadplochy $\Sigma(t)[x^i]$, které jsou číslovány časem t a pokryty souřadnicemi x^i. Prostoročas lze tímto způsobem rozvrstvit na tzv. foliace.

Ukazuje se [21], že obecná teorie relativity je v současné podobě v 3+1 dimenzích nerenormalizovatelnou teorií, neboť na úrovni Feynmanových diagramů vzrůstajícího smyčkového řádu vyžaduje přidávání stále dalších kontračlenů. Problémem také je, že gravitační vazbová konstanta G_N není bezrozměrná, $[G_N] = -2$ v jednotkách hmoty.

Vylepšené UV chování lze získat přidáním korekcí v podobě relativistických vyšších derivací metriky do lagrangiánu, viz. [8]. Modifikovaný propagátor pak sice nevykazuje

UV divergence, ale na druhou stranu zde vyvstanou jiné patologie ve smyslu duchových excitací, které narušují unitaritu v rámci poruchové teorie.

Petr Hořava v práci [9], [11] naznačil možnost renormalizovatelnosti gravitace v $3+1$ dimenzích pomocí postulování určité nerovnoprávnosti prostoru a času v UV oblasti, která je zavedena ve smyslu jejich anisotropního škálování na krátkých vzdálenostech, přičemž na velkých vzdálenostech by se jejich rovnoprávnost zachovala jako odraz efektivní platnosti obecné teorie relativity. Jedná se tedy o narušení relativistické invariance v UV oblasti a jejímu přirozenému vynoření v IR oblasti. Tento mechanismus má úzký vztah k polním teoriím fyziky kondenzovaných látek a má základ již v popisu tzv. Lifshitzova skaláru. Hořavova teorie gravitace v podstatě odpovídá podobnému mechanismu, který je nicméně aplikován jako nerelativistická limita ADM rozkladu obecné teorie relativity. Skutečnost, že narušením relativistické invariance lze docílit tzv. power-counting renormalizovatelnosti teorie gravitace, byla podpořena v práci [20].

2 ADM rozklad obecné teorie relativity

Řešení Cauchyho počáteční úlohy v obecné teorii relativity představuje hledání časového vývoje počáteční 3-dimenzionální hladké variety. Pokud x^μ jsou souřadnice v hledaném prostoročasu, speciálně $x^0 = t$, pak $t = 0$ určuje počáteční varietu Σ jako jeho prostorovou nadplochu. Obecně $\Sigma(t)$ označuje prostorupodobné řezy (tzv. foliace) odpovídající $t > 0$, přičemž se standardně předpokládá, že každým bodem výsledného prostoročasu bude procházet právě jeden takovýto řez.[1]

2.1 Funkce lapse N, vektor shift N^i a geometrie nadploch h_{ij}

Časupodobnou do budoucna orientovanou jednotkovou normálu n_μ k prostorupodobné nadploše $\Sigma(t)$ a tečné pole k liniím času t^μ lze definovat[2] jako

$$n_\mu = -N \frac{\partial \hat{t}}{\partial x^\mu}, \quad n_\mu n^\mu = -1, \quad t^\mu = \frac{\partial \hat{x}^\mu}{\partial t}.$$

Vektorové pole t^μ udává časový postup $\Sigma(t) \to \Sigma(t + \Delta t)$, přičemž bodům různých nadploch Σ ležících na stejné integrální křivce tohoto pole se přiřazují stejné prostorové souřadnice x^i. Pole t^μ lze rozložit do normálové a tečné složky vzhledem k nadploše Σ jako

$$t^\mu = N n^\mu + N^\mu,$$

kde N je funkce lapse a N^μ je vektor shift definované jako

$$N = -n_\mu t^\mu, \quad N^\mu = h^\mu_\nu t^\nu, \quad h^\mu_\nu = \delta^\mu_\nu + n^\mu n_\nu,$$

kde h^μ_ν je projektor na nadplochu Σ.[3]

---

[1] Prostoročasy, které lze takto rozvrstvit na Cauchyho nadplochy, se nazývají globálně hyperbolické. Cauchyho nadplocha je varieta, v jejíž minulosti ani budoucnosti neexistují singularity.

[2] V principu se jedná o zavedení diferenciální 1-formy n_μ, která v tzv. adaptovaných souřadnicích (t, x^i) má tvar $n_\mu = (-N, 0, 0, 0)$, a následný přechod do obecných souřadnic x^μ jako $t = \hat{t}(x^\mu)$, $x^i = \hat{x}^i(x^\mu)$.

[3] Vektorové pole t^μ není nutně úměrné n^μ, tedy kolmé k Σ, neboť v adaptovaných souřadnicích (t, x^i) platí $t^\mu = \delta^\mu_0$, zatímco $n^\mu = -Ng^{\mu 0}$. V rámci stacionárních axiálně symetrických prostoročasů je tedy $t^\mu = Nn^\mu$, $N^\mu = 0$ pouze v případě statické metriky $g^{i0} = 0$.

ADM rozklad prostoročasové metriky $g_{\mu\nu}$ v adaptovaných souřadnicích (t, x^i) je pak určen jako

$$ds^2 = -N^2 dt^2 + h_{ij}(N^i dt + dx^i)(N^j dt + dx^j),$$

resp. jako

$$g_{\mu\nu} = -n_\mu n_\nu + h_{\mu\nu} = \begin{pmatrix} -N^2 + N_i N^i & N_j \\ N_i & h_{ij} \end{pmatrix}, \tag{1}$$

$$g^{\mu\nu} = -n^\mu n^\nu + h^{\mu\nu} = \begin{pmatrix} -\frac{1}{N^2} & \frac{N^j}{N^2} \\ \frac{N^i}{N^2} & -\frac{N^i N^i}{N^2} + h^{ij} \end{pmatrix},$$

přičemž v adaptovaných souřadnicích (t, x^i) platí

$$t^\mu = \delta_0^\mu, \quad t_\mu = \left(-N^2 + N_i N^i, N_i\right), \quad n_\mu = -N\delta_\mu^0, \quad n^\mu = \frac{1}{N}\left(1, -N^i\right),$$

$$N^\mu = (0, N^i), \quad g_{\mu j} = h_{\mu j}, \quad h_j^\mu = \delta_j^\mu, \quad h^{0\mu} = 0, \quad h_0^0 = 0, \quad h_{ik}h^{kj} = \delta_i^j.$$

Prostoročasová metrika $g_{\mu\nu}$ tedy indukuje prostorovou metriku $h_{\mu\nu}$ na nadploše Σ.

2.2 Tenzor vnější křivosti

Uvažovaný 3+1 pohled je výhodný, pokud v prostoročasu existuje nějaká privilegovaná foliace na prostorupodobné nadplochy $\Sigma(t)$. Pak vektorové pole t^μ představuje tok času a nadplochy $\Sigma(t)$ prostorovou geometrii v daném okamžiku. Ve smyslu řešení Cauchyho počáteční úlohy je nicméně smysluplnější považovat nadplochy $\Sigma(t)$ za identifikované prostřednictvím toku vektorového pole t^μ a uvažovat vývoj prostorové geometrie h_{ij} na určité nadploše Σ. Dynamickou proměnnou úlohy je pak vnitřní geometrie $h_{ij}(t)$ této nadplochy. Dále je ovšem nutné sledovat vývoj její časové derivace, která ale nepředstavuje tenzorovou veličinu. Ukazuje se, že vhodnou tenzorovou veličinou žádaného významu je ve skutečnosti Lieova derivace prostorové metriky ve směru normály n^μ.

Touto veličinou je symetrický tenzor vnější křivosti, který lze vyjádřit jako

$$K_{\mu\nu} = h_\mu^\alpha h_\nu^\beta \nabla_\beta^{(4)} n_\alpha = h_\nu^\beta \nabla_\beta^{(4)} n_\mu = \nabla_\nu^{(4)} n_\mu + a_\mu n_\nu = \frac{1}{2}\mathcal{L}_n h_{\mu\nu} = \frac{1}{2N}\left(\mathcal{L}_t h_{\mu\nu} - \mathcal{L}_N h_{\mu\nu}\right),$$

kde $a_\mu = n^\rho \nabla_\rho^{(4)} n_\mu$, přičemž $\nabla_\mu^{(4)}$ je 4D kovariantní derivace odpovídající Riemannově konexi metriky $g_{\mu\nu}$.

Ve smyslu 3D kovariantní derivace ∇_μ na nadploše Σ odpovídající Riemannově konexi metriky $h_{\mu\nu}$ a definované pomocí projektoru h_ν^μ na tenzorová pole $T^{\mu\cdots}{}_{\alpha\cdots}$ působící pouze[4] na tečných a kotečných prostorech nadplochy Σ jako

$$\nabla_\rho T^{\mu\cdots}{}_{\alpha\cdots} = h_\nu^\mu \ldots h_\alpha^\beta \ldots h_\rho^\sigma \nabla_\sigma^{(4)} T^{\nu\cdots}{}_{\beta\cdots}$$

lze tenzor vnější křivosti zapsat ve tvaru

$$K_{\mu\nu} = \frac{1}{2N}\left(\dot{h}_{\mu\nu} - \nabla_\mu N_\nu - \nabla_\nu N_\mu\right), \tag{2}$$

kde $\dot{h}_{\mu\nu}$ je časová derivace prostorové metriky $h_{\mu\nu}$.

---

[4]Tenzorová pole řádu (m, n) splňující pro každé $i \in \hat{m}$, $j \in \hat{n}$ vztahy $n^{\alpha_i} T^{\mu_1\cdots}{}_{\alpha_1\cdots} = n_{\mu_j} T^{\mu_1\cdots}{}_{\alpha_1\cdots} = 0$.

2.3   Einstein-Hilbertova akce v ADM rozkladu

Einstein-Hilbertova akce obecné teorie relativity má tvar

$$S_{EH} = \frac{1}{16\pi G_N} \int d^4x \sqrt{-g} \left(R^{(4)} - 2\Lambda \right),$$

kde $g = \det(g_{\mu\nu})$, $R^{(4)}$ je 4D skalární prostoročasová křivost a Λ je kosmologická konstanta.

V rámci ADM rozkladu lze Einstein-Hilbertovu akci vyjádřit jako

$$S_{EH} = \frac{1}{16\pi G_N} \int d^4x \sqrt{h} \, N \left(K_{\mu\nu} K^{\mu\nu} - K^2 + R - 2\Lambda \right), \tag{3}$$

kde $h = \det(h_{ij})$, R je 3D skalární křivost nadplochy Σ a $K = h^{\mu\nu} K_{\mu\nu} = K_\mu^\mu$.

V adaptovaných souřadnicích (t, x^i) nicméně platí

$$\nabla_i N_j = \nabla_i^{(4)} N_j, \quad K_\mu^0 = 0, \quad K^{0\mu} = 0, \quad K = K_i^i$$

a akci (3) lze přepsat jako

$$S_{EH} = \frac{1}{16\pi G_N} \int d^4x \sqrt{h} \, N \left(K_{ij} K^{ij} - K^2 + R - 2\Lambda \right), \tag{4}$$

přičemž prostorová část tenzoru vnější křivosti (2) je dána jako

$$K_{ij} = \frac{1}{2N} \left(\dot{h}_{ij} - \nabla_i N_j - \nabla_j N_i \right). \tag{5}$$

3   Hořavova teorie gravitace

3.1   Anisotropní škálování

Nerovnoprávnost prostoru a času lze interpretovat ve smyslu zkoumání teorie vzhledem ke speciálně zvolenému difeomorfismu v podobě anisotropního škálování prostoročasu, které je charakterizováno dynamickým kritickým exponentem $z \in \mathbb{N}_0$ jako

$$x^i \to b x^i, \quad t \to b^z t. \tag{6}$$

Modely kompatibilní s anisotropním škálováním (6) jsou běžné v polních teoriích kondenzovaných hmot. Přehled teorií gravitace s řadou hodnot z v různých prostoročasových dimenzích $D + 1$ lze nalézt v [9], [11]. Případ teorie Yang-Millsova kalibračního pole s hodnotou $z = 2$ byl diskutován v [10].

V rámci anisotropního škálování (6) lze pro složky obecně i netenzorové veličiny[5] $T^{\mu\cdots}_{\alpha\cdots}(t, x^i)$ zavést její škálovací dimenzi jako

$$\left[T^{\mu\cdots}_{\alpha\cdots}(t, x^i) \right]_z = \log_b \left(\frac{T^{\mu\cdots}_{\alpha\cdots}(t, x^i)}{T^{\mu\cdots}_{\alpha\cdots}(b^z t, b x^i)} \right). \tag{7}$$

---

[5]Uvažujeme pouze takové veličiny, pro které má výraz (7) smysl, tj. veličiny, které jsou kompatibilní s anisotropním škálováním (6).

Škálovací dimenze dané veličiny není obecně invariantní vzhledem k prostoročasovým difeomorfismům. Z tohoto důvodu je nutné výraz (7) chápat pouze ve smyslu jistého referenčního systému (t, x^i), který odpovídá řešení uvažované teorie popisující UV pevný bod volného pole s vlastnostmi anisotropního škálování danými pomocí (6). Škálovací dimenze všech objektů se tedy dále vztahují k tomuto referenčnímu systému.[6]

Podle vztahu (7) lze určit škálovací dimenze prostorových souřadnic a času jako

$$[\,x^i\,]_z = -1, \quad [\,t\,]_z = -z. \tag{8}$$

Z obecného zavedení prostoročasové metriky $g_{\mu\nu}$, diferenciálního elementu intervalu

$$ds^2 = g_{\mu\nu} dx^\mu dx^\nu$$

a požadavku

$$[\,s\,]_z = [\,x^i\,]_z = [\,x^0\,]_z = -1$$

podle (8) a vztahu $g_{\mu\rho} g^{\rho\nu} = \delta_\mu^\nu$ platí

$$[\,g_{\mu\nu}\,]_z = [\,g^{\mu\nu}\,]_z = 0.$$

V rámci standardního zavedení souřadnice x^0 užívaného v obecné teorii relativity ve tvaru

$$x^0 = c\,t$$

platí, že

$$[\,c\,]_z = z - 1. \tag{9}$$

Povaha škálovaní rychlosti světla (9) naznačuje, že pro $z \neq 1$ není c absolutní konstantou nezávislou na souřadnicích (t, x^i) v rámci teorie, která by byla kompatibilní s anisotropním škálováním (6), a tedy se v takovém případě jedná o striktně nerelativistickou teorii.[7]

Lze ukázat (viz. [20]), že k tzv. power-counting renormalizovatelnosti teorie gravitace v $3 + 1$ dimenzích kompatibilní s anisotropním škálováním (6) je potřeba, aby dynamický kritický exponent dosahoval hodnoty alespoň $z = 3$ v UV oblasti, tj. na krátkých vzdálenostech. Taková striktně nerelativistická teorie byla představena právě v práci [11].

3.2 Kalibrační grupa symetrií

ADM rozklad obecné teorie relativity je popsán prostoročasovou metrikou (1), která při relativistickém chování rychlosti světla

$$c = konst. \neq 1$$

je parametrizována jako

$$g_{\mu\nu} = \begin{pmatrix} -N^2 + \frac{N_i N^i}{c^2} & \frac{N_j}{c} \\ \frac{N_i}{c} & h_{ij} \end{pmatrix}, \tag{10}$$

---

[6]Ve zvoleném referenčním systému (t, x^i) jsou tedy prostoročasová tensorová pole s anisotropním škálování (6) kompatibilní.

[7]Pro konstantní skalár K nezávislý na souřadnicích (t, x^i) je $[\,K\,]_z = 0$ pro libovolné $z \in \mathbb{N}_0$.

kde prostorová metrika h_{ij} představuje dynamická pole, přičemž lapse N, resp. shift N_i jsou kalibrační pole zodpovědná za Hamiltonovskou, resp. hybnostní vazbu v obecné teorii relativity.

Obecná teorie relativity je invariantní vzhledem ke spojité grupě prostoročasových difeomorfismů $\tilde{x}^\mu = \tilde{x}^\mu(x^\nu)$, které lze chápat jako infinitesimální transformace souřadnic s příslušnými generujícími vektorovými poli ve tvaru

$$\delta x^\mu = \xi^\mu(x^\nu).$$

Infinitesimální transformace složek prostoročasové metriky $g^4_{\mu\nu}$ jsou dány Lieovou derivací podél generujícího vektorového pole ξ^μ jako

$$\delta g_{\mu\nu} = \mathcal{L}_\xi g_{\mu\nu} = \xi^\kappa \partial_\kappa g_{\mu\nu} + g_{\kappa\nu} \partial_\mu \xi^\kappa + g_{\mu\kappa} \partial_\nu \xi^\kappa.$$

Vzhledem k ADM parametrizaci (10) a standardnímu zavedení časové souřadnice t jako

$$x^\mu = \left(c\,t, x^i \right), \quad \partial_\mu = \left(\frac{1}{c}\,\partial_t, \partial_i \right), \quad \xi^\mu = \left(c\,f, \xi^i \right)$$

lze infinitesimální transformace dynamických a kalibračních polí zapsat jako

$$\delta h_{ij} = f\dot{h}_{ij} + \xi^k \partial_k h_{ij} + N_j \partial_i f + h_{kj} \partial_i \xi^k + N_i \partial_j f + h_{ik} \partial_j \xi^k,$$

$$\delta N_i = f\dot{N}_i + \xi^j \partial_j N_i + c^2 \left(-N^2 + \frac{N_i N^i}{c^2} \right) \partial_i f + N_j \partial_i \xi^j + N_i \dot{f} + h_{ij} \dot{\xi}^j, \qquad (11)$$

$$\delta N = \xi^j \partial_j N + N\dot{f} + f\dot{N} + \mathcal{O}\left(\frac{1}{c^2} \right).$$

Plánované narušení relativistické invariance v UV oblasti vynucuje nepřítomnost singulárních členů ve výrazech (11) při provádění nerelativistické limity $c \to \infty$. Za tímto účelem je tedy třeba požadovat dodatečnou podmínku

$$\partial_i f = 0,$$

která omezuje obecné difeomorfismy na prostoročasové difeomorfismy prostoru a časové reparametrizace času s generátory infinitesimálních transformací ve tvaru

$$\delta x^i = \xi^i(t, x^j), \quad \delta t = f(t). \qquad (12)$$

S ohledem na (12) mají infinitesimální transformace (11) při nerelativistické limitě tvar

$$\delta h_{ij} = f\dot{h}_{ij} + \xi^k \partial_k h_{ij} + h_{kj} \partial_i \xi^k + h_{ik} \partial_j \xi^k,$$
$$\delta N_i = f\dot{N}_i + \xi^j \partial_j N_i + N_j \partial_i \xi^j + N_i \dot{f} + h_{ij} \dot{\xi}^j, \qquad (13)$$
$$\delta N = \xi^j \partial_j N + N\dot{f} + f\dot{N}.$$

Tvar generátorů infinitesimálních transformací (12) naznačuje, že grupa symetrií budované teorie nebude tvořena všemi prostoročasovými difeomorfismy, jak je tomu v případě obecné teorie relativity, ale pouze určitou její podgrupou

$$\mathrm{Diff}_\mathcal{F}(\mathcal{M}) \subset \mathrm{Diff}(\mathcal{M})$$

obsahující pouze foliaci zachovávající difeomorfismy

$$\tilde{x}^i = \tilde{x}^i(t, x^j), \quad \tilde{t} = \tilde{t}(t),$$

přičemž $\mathcal{F}$ označuje foliaci kodimenze 1, která odpovídá omezenému tvaru generátorů infinitesimálních transformací (12). Z hlediska topologie se pak předpokládá, že prostoročasová foliace je dána jako

$$\mathcal{M} = \mathbb{R} \times \Sigma,$$

tj. všechny listy foliace jsou topologicky ekvivalentní fixní nadploše Σ. Poznamenejme, že požadavkem menší grupy kalibračních symetrií získá budovaná teorie větší volnost, než je tomu v případě obecné teorie relativity.

3.3   Akce Hořavovy teorie gravitace

3.3.1   Obecný tvar

Za účelem tzv. power-counting renormalizovatelnosti je akce Hořavovy teorie gravitace

$$S_H = S_{\mathcal{K}} - S_{\mathcal{V}}$$

konstruována na základě následujících kritérií:

(i)   Kinetická část akce $S_{\mathcal{K}}$ je kvadratická v $\dot{h}_{ij}$.

(ii)   Potenciálová část akce $S_{\mathcal{V}}$ nezávisí na $\dot{h}_{ij}$, $\dot{N}_i$ ani $\dot{N}$.

(iii) S_H je invariantní vzhledem ke kalibrační grupě $\mathrm{Diff}_{\mathcal{F}}(\mathcal{M})$.

(iv) S_H je kompatibilní s anisotropním škálováním (6) pro dynamický kritický exponent $z \in \mathbb{N}_0$, přičemž $[\, S_H \,]_z = 0$ pro libovolné $z \in \mathbb{N}_0$.

(iv)   V UV oblasti teorie přechází do $z = 3$.

(v)   V IR oblasti teorie přechází do $z = 1$, přičemž S_H je pouze určitou modifikací Einstein-Hilbertovy akce (4).

Podle kritérií (i) - (iii) má akce Hořavovy teorie gravitace obecný tvar

$$S_H = \frac{2}{\kappa^2} \int dt d^3 x \sqrt{h} \, N \left(K_{ij} K^{ij} - \lambda K^2 - \mathcal{V} \right), \tag{14}$$

kde $K = h^{ij} K_{ij}$, přičemž K_{ij} je tensor vnější křivosti (5) odpovídající preferované časové foliaci $\mathcal{F}$ a potenciální člen $\mathcal{V}$ je funkce prostorové metriky h_{ij}, jejích prostorových derivací a také vektoru $a_i = \partial_i \ln N$.

V referenčním systému UV pevného bodu volného pole jsou dle kritéria (iv) škálovací dimenze příslušných veličin pro $z \in \mathbb{N}_0$ vzhledem k (10) určeny jako

$$[\, h_{ij} \,]_z = 0, \quad [\, N \,]_z = 0, \quad [\, N_i \,]_z = z - 1, \quad [\, K_{ij} \,]_z = z, \quad [\, \mathcal{V} \,]_z = 2z.$$

Koeficienty κ, λ jsou vazbové konstanty, které zůstávají neurčeny kalibrační grupou $\mathrm{Diff}_{\mathcal{F}}(\mathcal{M})$, se škálovacími dimenzemi

$$[\,\kappa\,]_z = \frac{z-3}{2}, \quad [\,\lambda\,]_z = 0.$$

Potenciální člen $\mathcal{V}$ lze podle [2] vyjádřit jako obecný invariant vzhledem ke kalibrační grupě $\mathrm{Diff}_{\mathcal{F}}(\mathcal{M})$ sestavený z objektů h_{ij}, R_{ij}, ∇_i a a_i ve tvaru[8]

$$\mathcal{V} = w^2 \mathcal{V}_6 + \eta^2 \mathcal{V}_4 + \mu^2 \mathcal{V}_2,$$

kde $\mathcal{V}_n$ označuje člen n-tého řádu v prostorových derivacích metriky h_{ij}, resp. vektoru a_i, přičemž w, η a μ jsou vazbové konstanty se škálovacími dimenzemi

$$[\,w\,]_z = z-3, \quad [\,\eta\,]_z = z-2, \quad [\,\mu\,]_z = z-1.$$

Poznamenejme, že tato teorie obsahuje propagující se 2-spinový i 0-spinový graviton a v IR oblasti se redukuje na skalár-tenzorovou teorii gravitace s narušenou relativistickou invariancí, viz. [2].

3.3.2   Akce minimální teorie

Na základě kritéria (iv) a (v) lze podle [12], [13] potenciálový člen akce Hořavovy teorie gravitace v rámci tzv. minimální teorie[9] zapsat ve tvaru

$$\mathcal{V} = w^2 \mathcal{V}^{\mathrm{UV}} + \ldots + \mu^2 \mathcal{V}^{\mathrm{IR}},$$

kde

$$\mathcal{V}^{\mathrm{UV}} = \mathcal{V}_6 = C_{ij}C^{ij}, \quad [\,C_{ij}\,]_z = 3,$$
$$\mathcal{V}^{\mathrm{IR}} = \mathcal{V}_2 = -(R - 2\Lambda), \quad [\,R\,]_z = [\,\Lambda\,]_z = 2,$$

přičemž C^{ij} je Cotton-Yorkův tenzor[10] definovaný jako

$$C^{ij} = \frac{\varepsilon^{ikl}}{\sqrt{h}} \nabla_k \left(R_l{}^j - \frac{1}{4} R\, \delta_l{}^j \right),$$

R je 3D skalární křivost nadplochy Σ, Λ je kosmologická konstanta a symbol $\ldots$ reprezentuje členy řádu n v prostorových derivacích metriky h_{ij}, kde $2 < n < 6$.

Chování potenciálu $\mathcal{V}$ a tedy i celé teorie gravitace lze charakterizovat hodnotami vazbových konstant κ, λ, w a μ v UV oblasti jako

$$z = 3, \quad w \not\approx 0, \quad [\,\kappa\,]_3 = 0, \quad [\,w\,]_3 = 0, \quad [\,\mu\,]_3 = 2,$$

resp. v IR oblasti jako

$$z = 1, \quad \kappa^2 \approx 32\pi c\, G_N, \quad \lambda \approx 1, \quad \mu^2 \approx 1, \quad [\,\kappa\,]_1 = -1, \quad [\,w\,]_3 = -2, \quad [\,\mu\,]_1 = 0.$$

---

[8]Tento tvar odpovídá dodatečnému požadavku ve smyslu vynechání členů lichého řádu v prostorových derivací metriky narušujících paritu.

[9]Minimální teorie se zabývá pouze členy $\mathcal{V}$ dominující v UV, resp. v IR oblasti, tj. členy řádu 6, resp. řádu 2 v prostorových derivacích metriky h_{ij}, kde nejvyšší řád je určen tzv. Cotton-Yorkovým tenzorem v rámci tzv. podmínky detailní rovnováhy a tzv. podmínky projektibility $N = N(t)$.

[10]Cotton-Yorkův tenzor je unikátní tenzor obsahující 3. prostorové derivace metriky h_{ij}, který navíc disponuje vlastnostmi $C^{ij} = C^{ji}$, $h_{ij}C^{ij} = 0$, $\nabla_i C^{ij} = 0$. Tento tenzor také nahrazuje Weylův tenzor ve 3 dimenzích na úrovni testování konformní plochosti Riemannovy metriky h_{ij}, tj. vlastnosti $C^{ij} = 0$. Tento tenzor lze odvodit ve smyslu podmínky detailní rovnováhy z gravitačního Chern-Simonsova členu.

4 Závěr a další výzkum

V rámci Hořavovy teorie gravitace se v některých případech za účelem zjednodušení možného tvaru potenciálového členu $\mathcal{V}$ požadují 2 dodatečné podmínky, resp. jejich různé kombinace. Jedná se o podmínku projektivity ve tvaru

$$N = N(t), \tag{15}$$

resp. o podmínku detailní rovnováhy ve tvaru[11]

$$\mathcal{V} = \frac{1}{h} \frac{\delta W}{\delta h_{ij}} \mathcal{G}_{ijkl} \frac{\delta W}{\delta h_{kl}}, \tag{16}$$

tj. omezení ve smyslu, že potenciální člen $\mathcal{V}$ lze odvodit ze superpotenciálu $W[h_{ij}]$, přičemž $\mathcal{G}_{ijkl}$ je inverze De Wittovy metriky G^{ijkl}.[12]

Akce původní Hořavovy teorie gravitace [11] i akce minimální teorie [12], [13] jsou také odvozeny s uvažováním obou dodatečných podmínek. Tyto teorie ale disponují řadou patologií, např. členy narušující paritu, resp. problém disperzní relace a power-counting renormalizovatelnosti skalárního módu, resp. znaménko a hodnota holé kosmologické konstanty [1], [15], resp. IR chování skalárního módu gravitonu při nepřijatelně nízkých energiích [3], [4]. Některé zmíněné problémy lze vyřešit narušením podmínky detailní rovnováhy [14], [15], [16].

V současnosti je však na vzestupu především neprojektivní verze Hořavovy teorie gravitace s podmínkou detailní rovnováhy [17], [18], [19], kde se zkoumají nové možnosti superpotenciálů z hlediska vektoru $a_i = \partial_i \ln N$, který v projektivní verzi vůbec nevystupuje. Dále lze upřít pozornost na potřebné snížení počtu nezávislých vazbových konstant v celkové akci nebo na problém energie vakua. Zkoumat lze také power-counting renormalizovatelnost vzhledem ke členům se smíšenými derivacemi [5], [6]. A v neposlední řadě zůstává nadále otevřenou otázkou renormalizovatelnost nad rámec power-counting argumentů [7].

Literatura

[1] C. Appignani, R. Casadio, S. Shankaranarayanan *The Cosmological Constant and Horava-Lifshitz Gravity.* JCAP **1004** (2010) 006. arXiv:0907.3121v2 [hep-th]

[2] D. Blas, O. Pujol, S. Sibiryakov. *A healthy extension of Horava gravity.* Phys. Rev. Lett. **104** (2010) 181302. arXiv:0909.3525v1 [hep-th]

[3] D. Blas, O. Pujol, S. Sibiryakov. *On the Extra Mode and Inconsistency of Horava Gravity.* JHEP **029** (2009) 0910. arXiv:0906.3046v2 [hep-th]

[4] Ch. Charmousis, G. Niz, A. Padilla, P. M. Saffin *Strong coupling in Horava gravity.* JHEP **0908** (2009) 070. arXiv:0905.2579v2 [hep-th]

---

[11]Tento tvar je kromě jiného motivován jednak lepšími renormalizačními vlastnostmi a jednak faktem, že kinetický člen akce S_H lze rovněž zapsat pomocí tzv. De Wittovy metriky jako $\mathcal{K} = K_{ij} G^{ijkl} K_{ij}$.

[12]De Wittova metrika má tvar $G^{ijkl} = \frac{1}{2} \left(h^{ik} h^{jl} + h^{il} h^{jk} \right) - \lambda h^{ij} h^{kl}$, přičemž její inverze je definována jako $\mathcal{G}_{ijmn} G^{mnkl} = \delta^{(k}_{(i} \delta^{l)}_{j)} = \frac{1}{2} \left(\delta^k_i \delta^l_j + \delta^k_j \delta^l_i \right)$, což vede na $\mathcal{G}_{ijkl} = \frac{1}{2} \left(h_{ik} h_{jl} + h_{il} h_{jk} \right) - \frac{\lambda}{3\lambda - 1} h_{ij} h_{kl}$.

[5] M. Colombo, A. E. Gumrukcuoglu, T. P. Sotiriou. *Horava gravity with mixed derivative terms.* Phys. Rev. D **91** (2015) 044021. arXiv:1410.6360v1 [hep-th]

[6] M. Colombo, A. E. Gumrukcuoglu, T. P. Sotiriou. *Horava Gravity with Mixed Derivative Terms: Power-Counting Renormalizability with Lower-Order Dispersions.* arXiv:1503.07544v2 [hep-th]

[7] G. D'Odorico, F. Saueressig, M. Schutten. *Asymptotic freedom in Horava-Lifshitz gravity.* Phys. Rev. Lett. **113** (2014) 171101. arXiv:1406.4366v1 [hep-th]

[8] E. S. Fradkin, A. A. Tseytlin. *Conformal Supergravity.* Phys. Rept. **119** (1985) 233.

[9] P. Hořava. *Membranes at Quantum Criticality.* JHEP **0903** (2009) 020. arXiv:0812.4287v3 [hep-th]

[10] P. Hořava. *Quantum Criticality and Yang-Mills Gauge Theory.* Phys. Lett. B **694** (2010) 172. arXiv:0811.2217v1 [hep-th]

[11] P. Hořava. *Quantum Gravity at a Lifshitz Point.* Phys. Rev. D **79** (2009) 084008. arXiv:0901.3775v2 [hep-th]

[12] P. Hořava. *Spectral Dimension of the Universe in Quantum Gravity at a Lifshitz Point.* Phys. Rev. Lett. **102** (2009) 161301. arXiv:0902.3657v2 [hep-th]

[13] P. Hořava, Ch. M. Melby-Thompson. *General Covariance in Quantum Gravity at a Lifshitz Point.* Phys. Rev. D **82** (2010) 064027. arXiv:1007.2410v2 [hep-th]

[14] K. Koyama, F. Arroja. *Pathological behaviour of the scalar graviton in Horava-Lifshitz gravity.* JHEP **1003** (2010) 061. arXiv:0910.1998v3 [hep-th]

[15] T. P. Sotiriou, M. Visser, S. Weinfurtner. *Phenomenologically viable Lorentz-violating quantum gravity.* Phys. Rev. Lett. **102** (2009) 251601. arXiv:0904.4464v3 [hep-th]

[16] T. P. Sotiriou, M. Visser, S. Weinfurtner. *Quantum gravity without Lorentz invariance.* JHEP **0910** (2009) 033. arXiv:0905.2798v3 [hep-th]

[17] D. Vernieri. *On power-counting renormalizability of Horava gravity with detailed balance.* Phys. Rev. D **91** (2015) 124029. arXiv:1502.06607v2 [hep-th]

[18] D. Vernieri, T. P. Sotiriou. *Horava-Lifshitz gravity with detailed balance.* J. Phys. Conf. Ser. **453** (2013) 012022. arXiv:1212.4402v1 [hep-th]

[19] D. Vernieri, T. P. Sotiriou. *Horava-Lifshitz gravity: detailed balance revisited.* Phys. Rev. D **85** (2012) 064003. arXiv:1112.3385v2 [hep-th]

[20] M. Visser. *Lorentz Symmetry Breaking as a Quantum Field Theory Regulator.* Phys. Rev. D **80** (2009) 025011. arXiv:0902.0590v3 [hep-th]

[21] S. Weinberg. *Ultraviolet Divergences in Quantum Theories of Gravitation.* General Relativity. An Einstein Centenary Survey. Cambridge University Press. (1980).

Zobecněný výpočet fázové rovnováhy vícesložkových směsí při daném objemu, teplotě a složení[*]

Tereza Petříková

3rd ročník PGS, email: jindrter@fjfi.cvut.cz
Katedra matematiky
Fakulta jaderná a fyzikálně inženýrská, ČVUT v Praze

školitel: Jiří Mikyška, Katedra matematiky
Fakulta jaderná a fyzikálně inženýrská, ČVUT v Praze

Abstract. Studying multiphase equilibrium of multicomponent mixtures and development of robust and effcient algorithms for its computation play important roles in large-scale compositional hydrocarbon reservoir simulations. While there was a main focus on two-phase compositional modelling in the past, nowadays, there is an increasing interest in three and generally multiphase compositional models which is motivated by CO_2 sequestration [1], processes related to CO_2 or steam enhanced oil recovery [2] or asphaltene precipitation from bitumens [3, 4].

Injecting a pure component (e.g. CO_2) into a reservoir, it may dissolve in the reservoir fluid or it can mix and the mixture can split into two or more phases. Let us consider a closed system of total volume V containing a multicomponent mixture with mole numbers $N_1, \ldots, N_n$ at temperature T. To find out whether the system is under given conditions in single-phase or splits into two phases, the single-phase stability at constant volume, temperature, and moles (the so-called VT-stability) is solved. In case of phase-splitting, the two-phase split calculation at constant volume, temperature, and moles (the so-called VT-flash) is performed to establish amounts and compositions of both phases, and consequently the equilibrium pressure of the system is calculated from the equation of state. In the previous work [5, 6, 7], these problems were formulated for two-phase systems and algorithms were proposed and tested on a number of examples. In [9], the results were partially extended to three phases for $CO_2 - H_2O$ system and the performance of the algorithm was shown on several examples of two- and three-phase equilibrium calculations of $CO_2 - H_2O$ mixtures under geologic carbon storage conditions.

The contribution deals with the investigation of multi-phase equilibrium of multicomponent mixtures at constant volume, temperature and moles. In [7] we have proposed a numerical algorithm for constant-volume two-phase split calculation which is based on the constrained minimization of the total Helmholtz energy of the mixture. The algorithm uses the Newton-Raphson method with line-search and the modified Cholesky decomposition of the Hessian matrix to produce a sequence of states with decreasing values of the total Helmholtz free energy. Fast convergence towards the exact solution is ensured due to the Newton-Raphson method. To initialize the algorithm, the results of the constant-volume stability algorithm, which has been developed in [6], are used. Now we extend the method and propose a general strategy for N-phase equilibrium computation at constant volume, temperature, and moles, where $N \in \mathbb{N}$ is the number of phases. As the number of phases is not necessarily known a-priori, the proposed strategy

---

is based on the repeated constant-volume stability testing and the constant-volume phase-split calculation until a stable N-phase state is found. The performance of the algorithm has been tested on many examples of two-, three- and even four-phase equilibrium calculations of multi-component mixtures under various conditions. The mixture behavior is described using either the Peng-Robinson equation of state [10] or the Cubic-Plus-Association equation of state [11].

Abstrakt. Zkoumání výpočtu vícefázové rovnováhy vícesložkových směsí a vývoj robustních a efektivních algoritmů jejich výpočtu hraje důležitou roli v kompozičních simulacích ropných rezervoárů. Zatímco v minulosti byl zájem soustředěn na dvoufázové kompoziční modelování, v dnešní době je rostoucí zájem o tří- a obecně vícefázové kompoziční modely, což je motivováno např. CO_2 sekvestrací [1], procesy spojenými se zvyšováním výtěžnosti ropných rezervoárů pomocí CO_2 nebo páry [2] nebo modelováním srážení asfaltenů z bitumenu (živice) [3, 4].

Při injektování čisté komponenty (např. CO_2) do rezervoáru může docházet buď k jejímu rozpuštění v kapalině nacházející se v rezervoáru nebo k jejich smíchání a následnému rozdělení směsi do dvou nebo více fází. Uvažujeme-li uzavřený systém obsahující vícesložkovou směs s látkovými množstvími $N_1, \ldots, N_n$ o celkovém objemu V při teplotě T, nachází se tento systém za daných podmínek buď stabilně v jedné fázi nebo je nestabilní a dojde k jeho rozdělení do dvou nebo více fází; jedná se o problém jednofázové stability při konstantním objemu, teplotě a složení (tzv. VT-stabilita). V případě rozdělení do dvou fází určíme objemy a složení obou fází, a následně vypočítáme rovnovážný tlak systému ze stavové rovnice; jedná se o problém výpočtu dvoufázové rovnováhy při konstantním objemu, teplotě a složení (tzv. VT-flash). V předchozí práci [5, 6, 7] byly tyto problémy formulovány pro systémy ve dvoufázových stavech a příslušné výpočetní algoritmy byly navrženy a testovány na řadě příkladů. V [9] byly výsledky částečně rozšířeny do třech fází pro směs $CO_2 - H_2O$ a navržený algoritmus byl testován na příkladech výpočtu dvou- a třífázové rovnováhy za běžných sekvestračních podmínek.

Článek pojednává o vyšetřování vícefázové rovnováhy vícesložkových směsí při konstantním objemu, teplotě a složení. V [7] byl navržen numerický algoritmus pro výpočet dvoufázové rovnováhy za konstantního objemu, teploty a složení založený na minimalizaci celkové Helmholtzovy volné energie směsi při zachování podmínek na bilanci hmoty a objemu. Algoritmus je zde založen na Newtonově-Raphsonově minimalizační metodě s použitím metody line-search a modifikovaného Choleskyho rozkladu matice Hessiánu, čímž je vytvořena posloupnost stavů s klesajícími hodnotami celkové Helmholtzovy volné energie. Rychlá konvergence k přesnému řešení je zajišťena použitím Newtonovy-Raphsonovy metody. K inicializaci algoritmu pro VT-flash se využívají výsledky algoritmu pro testování stability, který byl navžen v [6]. Nyní tuto metodu rozšíříme a navrhneme obecnou strategii pro výpočet N-fázové rovnováhy při konstantním objemu, teplotě a složení, kde $N \in \mathrm{N}$ je počet fází. Vzhledem k tomu, že počet fází není nutně znám předem, navržená strategie je založena na opakovaném testování stability a výpočtu fázové rovnováhy při konstantním objemu, teplotě a složení, dokud není nalezen stabilní N-fázový stav. Navržený algoritmus byl testován na mnoha příkladech výpočtu dvou-, tří- a dokonce čtyřfázové rovnováhy vícesložkových směsí při různých podmínkách. Chování směsi je popsáno buď pomocí Pengovy-Robinsonovy stavové rovnice [10] nebo kubické stavové rovnice s asociačním členem [11].

Klíčová slova: fázová rovnováha při konstantním objemu, minimalizace Helmholtzovy volné energie, Newtonova-Raphsonova metoda, modifikovaná Choleskyho dekompozice.

Tato práce byla prezentována na konferenci Interpore 2015 v Padově, Itálie (17.–22.5.2015) a celý článek [8] byl publikován v impaktovaném časopise Fluid Phase Equilibria.

Literatura

[1] A. M.M. Leal, M. J. Blunt, T. C. LaForce, *A Robust and Efficient Numerical Method for Multiphase Equilibrium Calculations: Application to* CO_2-*brine-rock Systems at High Temperatures, Pressures and Salinities*. Advances in Water Resources, **62** (2013), 409–430.

[2] V. Alvarado, E. Manrique *Enhanced Oil Recovery: An Update Review*. Energies **3** (2010), 1529–1575.

[3] Z. Li, A. Firoozabadi, *Modeling Asphaltene Precipitation by n-Alkanes from Heavy Oils and Bitumens Using Cubic-Plus-Association Equation of State*. Energy & Fuels, **24** (2010), 1106–1113.

[4] Z. Li, A. Firoozabadi, *Cubic-Plus-Association Equation of State for Asphaltene Precipitation in Live Oils*. Energy & Fuels, **24** (2010), 2956–2963.

[5] A. Firoozabadi, J. Mikyška. *A New Thermodynamic Function for Phase-Splitting at Constant Temperature, Moles, and Volume*. AIChE Journal **57(7)** (2011), 1897–1904.

[6] A. Firoozabadi, J. Mikyška. *Investigation of Mixture Stability at Given Volume, Temperature, and Number of Moles*. Fluid Phase Equilibria **321** (2012), 1–9.

[7] T. Jindrová, J. Mikyška. *Fast and Robust Algorithm for Calculation of Two-Phase Equilibria at Given Volume, Temperature, and Moles*. Fluid Phase Equilibria **353** (2013), 101–114.

[8] T. Jindrová, J. Mikyška. *General Algorithm for Multiphase Equilibria Calculation at Given Volume, Temperature, and Moles*. Fluid Phase Equilibria **393** (2015), 7–25.

[9] T. Jindrová, J. Mikyška. *Phase Equilibria Calculation of* $CO_2 - H_2O$ *System at Given Volume, Temperature, and Moles in* CO_2 *Sequestration*. IAENG International Journal of Applied Mathematics **45(3)** (2015), 183–192

[10] D.Y. Peng, D.B. Robinson. *A New Two-Constant Equation of State*. Industrial & Engineering Chemistry Fundamentals **15(1)** (1976), 59–64.

[11] A. Firoozabadi, Z. Li. *Cubic-Plus-Association Equation of State for Water-Containing Mixtures: Is "Cross Association" Necessary?*. AIChE Journal **55(7)** (2009), 1803–1813.

[12] A. Firoozabadi. *Thermodynamics of Hydrocarbon Reservoirs*, McGraw-Hill, New York, 1999.

Comparing SVM, Gaussian Process and Random Forest Surrogate Models for the CMA-ES*

Zbyněk Pitra†

2nd year of PGS, email: `z.pitra@gmail.com`
Department of Mathematics
Faculty of Nuclear Sciences and Physical Engineering, CTU in Prague

advisor: Martin Holeňa, Department of Nonlinear Dynamics & Complex Systems
Institute of Computer Science, CAS

Abstract. In practical optimization tasks, it is more and more frequent that the objective function is black-box which means that it cannot be described mathematically. Such functions can be evaluated only empirically, usually through some costly or time-consuming measurement, numerical simulation or experimental testing. Therefore, an important direction of research is the approximation of these objective functions with a suitable regression model, also called surrogate model of the objective functions. In [2] we combined two surrogate models for continuous black-box optimization, Gaussian processes [8] and random forests [3], with the state-of-the-art evolutionary algorithm CMA-ES [4]. Results on the BBOB testing set showing that fitness function evaluations can be saved especially in the initial phase of the algoritm were published in [1]. In [7] we evaluate two different approaches to the continuous black-box optimization which both integrates surrogate models with CMA-ES. The first Ranking SVM surrogate model estimates the ordering of the sampled points as the CMA-ES utilizes only the ranking of the fitness values [6]. However, we show that continuous Gaussian processes model provides in the early states of the optimization comparable results. Comparison in [5] shows the speed-up of two methods based on Gaussian processes, Model Guided Sampling Optimization and Gaussian processes as a surrogate model for CMA-ES, to CMA-ES with no surrogate model.

Keywords: benchmarking, black-box optimization, surrogate model, Gaussian process, random forest

Abstrakt. Při řešení optimalizačních úloh z praxe je stále častější, že cílová funkce je tzv. black-box funkcí, což znamená, že pro ni nelze najít správné matematické vyjádření. Hodnoty takovéto funkce lze získat pouze empiricky, obvykle pomocí finančně a časově náročných měření, numerických simulací nebo experimentálního testování. Z tohoto důvodu jsou aproximace těchto cílových funkcí s vhodným regresním modelem, někdy nazývaným náhradním modelem cílové funkce, velice důležitým směrem výzkumu. V článku [2] jsme zkombinovali dva náhradní modely určené pro spojitou black-box optimalizaci, gaussovské procesy [8] a náhodné lesy [3], s v současnosti nejlepším evolučním algoritmem CMA-ES [4]. Výsledky testování na balíčku testovacích funkcí BBOB ukazují, že počet vyhodnocení fitness funkce lze snížit zejména v počátečních fázi

algoritmu, což bylo publikováno v [1]. V [7] využíváme dva různé přístupy ke spojité black-box optimalizaci, z nichž oba používají náhradní modely v kombinaci s algoritmem CMA-ES. První náhradní model nazývaný Ranking SVM odhaduje pořadí bodů, jelikož pořadí funkčních hodnot bodů CMA-ES využívá [6]. My však ukazujeme, že spojitý model s gaussovskými procesy poskytuje v počátečních fázích optimalizace lepší výsledky. Článek [5] porovnává urychlení dvou metod založených na gaussovských procesech, algoritmus Model Guided Sampling Optimization a gaussovské procesy jako náhradní model pro CMA-ES, s algoritmem CMA-ES bez náhradního modelu.

Klíčová slova: benchmarking, black-box optimalizace, náhradní modelování, gaussovské procesy, náhodné lesy

References

[1] L. Bajer, Z. Pitra, and M. Holeňa. *Benchmarking Gaussian processes and random forests surrogate models on the BBOB noiseless testbed.* In 'Proceedings of the 17th GECCO Conference Companion', Madrid, (July 2015). ACM, New York.

[2] L. Bajer, Z. Pitra, and M. Holeňa. *Investigation of Gaussian processes and random forests as surrogate models for evolutionary black-box optimization.* In 'Proceedings of the 17th GECCO Conference Companion', Madrid, (July 2015). ACM, New York.

[3] L. Breiman. *Classification and regression trees.* Chapman & Hall/CRC, (1984).

[4] N. Hansen. *The CMA evolution strategy: A comparing review.* In 'Towards a New Evolutionary Computation', J. A. Lozano, P. Larrañaga, I. Inza, and E. Bengoetxea, (eds.), number 192 in Studies in Fuzziness and Soft Computing, Springer Berlin Heidelberg (January 2006), 75–102.

[5] A. Kudinov, L. Bajer, Z. Pitra, and M. Holeňa. *Investigation of Gaussian Processes in the Context of Black-Box Evolutionary Optimization.* In 'ITAT 2015: Information Technologies - Applications and Theory', J. Yaghob, (ed.), volume 1422 of *CEUR Workshop Proceedings*, 159–166. CreateSpace Independent Publishing Platform, (2015).

[6] I. Loshchilov, M. Schoenauer, and M. Sebag. *BI-population CMA-ES Algorithms with Surrogate Models and Line Searches.* In 'Genetic and Evolutionary Computation Conference (GECCO Companion)', 1177–1184. ACM Press, (July 2013).

[7] Z. Pitra, L. Bajer, and M. Holeňa. *Comparing SVM, Gaussian Process and Random Forest Surrogate Models for the CMA-ES.* In 'ITAT 2015: Information Technologies - Applications and Theory', 186–193, North Charleston, USA, (2015). CreateSpace Independent Publishing Platform.

[8] C. E. Rasmussen and C. K. I. Williams. *Gaussian Processes for Machine Learning.* Adaptative computation and machine learning series. MIT Press, (2006).

Bayesian Network Models for Adaptive Testing[*]

Martin Plajner

2nd year of PGS, email: `martin.plajner@fjfi.cvut.cz`
Department of Software Engineering
Faculty of Nuclear Sciences and Physical Engineering, CTU in Prague

advisor: Jiří Vomlel, Department of Decision Making Theory
Institute of Information Theory and Automation, CAS

Abstract. Computerized adaptive testing (CAT) [6, 1] is an interesting and promising approach to testing human abilities. CAT aims at creating shorter tests taking less time without sacrificing their reliability. There is a promising possibility of applications in the field of knowledge tests [7, 8]. Tests are computer administered and use a model of tested subjects to make their decisions. In our research we model students by Bayesian networks [2, 3, 4].

We collected data from paper tests solved by grammar school students. Tests focused on mathematical knowledge in the domain of functions. Students were asked to solve different mathematical problems including graph drawing and reading, computing points on the graph, root finding, description of function shape and other function properties. 281 students participated in testing.

We propose 14 different models to serve as a student model. Each model is a Bayesian network created with different settings. Each network consists of at least one skill node which describes abilities of the modeled student. Skill nodes are parents of question nodes which serve as data inputs of the model. Question nodes are used for estimations of consequent answers. Some models operate with additional information collected during the test administration (such as age, gender, grades,...).

Models described above were used in a simulated adaptive test with our data set. The procedure of adaptive testing is formed by the following steps: (1) the next question to be asked is selected, (2) the question is asked and a result is obtained, (3) the result is inserted into the network as evidence, (4) the network is updated based on this new evidence, (5) answers are estimated. This procedure is repeated. One of the most interesting part is the selection of the next question. In our approach we select questions by the maximization of information gain. This information gain is measured as the reduction of the Shannon entropy of skill variables' marginal probabilities.

We have found out that most of the proposed models are making reasonable decisions. The mean success rate of estimation of answers was over 75% during the whole process. An interesting and important finding is that the additional information given to the model (i.e. gender, age, grades, etc. of the student) is not very important for the quality of the model. These factors make a difference only during the initial questions. After a few answers the influence of additional information diminish and models without this information are behaving similarly to those containing it.

In the following work we would like to further explore some of the tested models, namely those with multivalued skill variables. We plan to compare proposed models also with other psychometric models such as item response theory [1].

Keywords: adaptive testing, Bayesian network

Abstrakt. Počítačové adaptivní testování znalostí (Computerized Adaptive Testing - CAT [6, 1]) je slibný přístup k testování lidských schopností. Adaptivní test je vytvářen výběrem otázek v průb2hu testování tak, aby výsledný test byl kratší. Test tak zabere méně času a výběr otázek z banky otázek je nastaven tak, aby nedošlo k velkým ztrátám informace. Možnosti aplikace takovýchto testů jsou značné [7, 8]. Test je řízen počítačem a využívá model studenta. V našem přístupu je tento model realizován pomocí bayesovské sítě [2, 3, 4].

Nejprve jsme zajistili data pro náš výzkum pomocí papírových testů. Testování se účastnili studenti středních škol. Testy byly zaměřeny na matematické úlohy v oblasti funkcí (črtání grafu a čtení z grafu, hledání kořenů, výpočty bodů funkcí, atd). Testování se zúčastnilo celkem 281 studentů.

V našem návrhu je 14 různých modelů, které mohou sloužit jako model studenta. Každý z modelů je bayesovská síť vytvořená s různými nastaveními. V každé síti je alespoň jeden dovednostní uzel, který zachycuje schopnosti studenta. Dovednostní uzly jsou pak rodiči uzlů otázek. Uzly otázek slouží jako datové vstupy modelu a současně jsou využívány pro odhady odpovědí. Některé z modelů používají ke své práci dodatečné informace (věk, pohlaví, známky studenta). Tyto informace byly také získány během testování.

Výše popsané modely jsme využili k simulovanému adaptivnímu testu. Procedura testu je následující: 1) vybereme otázku, která má být položena, 2) otázku položíme a získáme odpověď, 3) vložíme odpověď do sítě jakožto novou evidenci, 4) síť aktualizujeme s touto novou evidencí, 5) odhadneme odpovědi na otázky. Jedna ze zajímavých částí procesu je výběr další otázky. V našem případě jsme se rozhodli použít princip založený na informačním zisku. Tento informační zisk je vypočten jako úbytek Shannonovi entropie marginálních pravděpodobností dovednostních uzlů.

Zjistili jsme, že námi navrhované modely poskytují rozumná rozhodnutí a odhady. Průměrná úspěšnost modelů se pohybovala nad hranicí 75% během celého procesu testování. Zajímavým zjištěním je, že dodatečná informace (věk, pohlaví, známky) nehraje pro model významnou roli. Vliv těchto informací je znatelný pouze při prvních položených otázkách. Poté již vliv odpovědí převáží a modely, které tyto informace neobsahují, se chovají velice podobně těm, které je obsahují.

V budoucnosti bychom se chtěli blíže zaměřit na některé z modelů představených v této práci. Především se jedná o modely s více-stavovými dovednostními uzly. Také plánujeme provést srovnání s dalšími psychometrickými modely, jako je IRT [1].

Klíčová slova: adaptivní testování, bayesovská síť

This work was presented at 12th Bayesian Modelling Application Workshop held on 16.7.2015 in Amsterdam as a part of UAI conference [5].

References

[1] R. G. Almond and R. J. Mislevy. *Graphical Models and Computerized Adaptive Testing.* Applied Psychological Measurement **23** (1999), 223–237.

[2] U. B. Kjærulff and A. L. Madsen. *Bayesian Networks and Influence Diagrams.* Springer, (2008).

[3] E. Millán, M. Trella, J. Pérez-de-la Cruz, and R. Conejo. *Using Bayesian networks in computerized adaptive tests.* In 'Computers and Education in the 21st Century', M. Ortega and J. Bravo, (eds.), Springer (2000), 217–228.

[4] E. Millán, T. Loboda, and J. L. Pérez-de-la Cruz. *Bayesian networks for student model engineering.* Computers & Education **55** (December 2010), 1663–1683.

[5] M. Plajner and J. Vomlel. Bayesian network models for adaptive testing. In 'Proceedings of 12th Annual Bayesian Modelling Applications Workshop', Amsterdam, Netherlands, (July 2015).

[6] W. J. van der Linden and C. A. Glas. *Computerized Adaptive Testing: Theory and Practice.* Springer, (2000).

[7] J. Vomlel. *Bayesian networks in educational testing.* International Journal of Uncertainty, Fuzziness and Knowledge-Based Systems **12** (2004), 83–100.

[8] D. J. Weiss and G. G. Kingsbury. *Application of Computerized Adaptive Testing to Educational Problems.* Journal of Educational Measurement **21** (1984), 361–375.

Molecular Simulations of the Vapor–Liquid Phase Interfaces of Pure Water Modeled with the SPC/E and the TIP4P/2005 Molecular Models

Barbora Planková

4th year of PGS, email: `barbora.plankova@gmail.com`
Department of Mathematics
Faculty of Nuclear Sciences and Physical Engineering, CTU in Prague

advisor: Jan Hrubý, Department of Thermodynamics
Institute of Thermomechanics, CAS

Abstract. In our previous study [Planková et al., EPJ Web. Conf. **92**, 02071 (2015)], several molecular simulations of vapor-liquid phase interfaces for pure water were performed using the DL_POLY Classic software. The TIP4P/2005 molecular model was successfully used for the modeling of the density profile and the thickness of phase interfaces together with the temperature dependence of the surface tension. In the current study, the extended simple point charge (SPC/E) model for water was employed along with the TIP4P/2005 for the investigation of vapor-liquid phase interfaces over a wide temperature range from 250 K to 600 K. Results of the new simulations are in a good agreement with most of the literature data. TIP4P/2005 provides better results for the saturated liquid density with its maximum close to 275 K, while SPC/E predicts slightly better saturated vapor density. Both models give qualitatively correct representation for the surface tension of water.

This text is a short version of the one that will be presented at Experimental fluid mechanics 2015 in Prague (17.– 0.11.2015). Whole text will be subsequently published in The European Physical Journal.

Keywords: Molecular dynamics, TIP4P/2005, SPC/E, surface tension

Abstrakt. V předchozí práci [Planková et al., EPJ Web. Conf. **92**, 02071 (2015)] jsme provedli několik molekulárních simulací fázových rozhraní kapalina-pára pro čistou vodu s použitím softwaru DL_POLY Classic. Model TIP4P/2005 byl úspěšně použit pro modelování profilu hustoty a tloušťky fázového rozhraní spolu s teplotní závislostí povrchového napětí. V této studii jsme použili rozšířený model simple point charge (SPC/E) pro vodu a TIP4P/2005 ke zkoumání fázových rozhraní kapalina-pára pro širokou škálu teplot od 250 K do 600 K. Výsledky nových simulací jsou v dobrém souladu s většinou dat z literatury. TIP4P/2005 dává lepší výsledky pro hustotu syté páry se svým maximem v 275 K, zatímco SPC/E predikuje trochu lepší hodnoty syté páry. Oba dva modely dávají kvalitativně správné hodnoty povrchového napětí.

Tento text je krátkou verzí práce, která bude prezentována na konferenci Experimental fluid mechanics 2015 v Praze (17.–20.11.2015). Celý text následně publikován v žurnálu The European Physical Journal.

Klíčová slova: Molekulární dynamika, TIP4P/2005, SPC/E, povrchové napětí

1   Introduction

Molecular simulations (MS) represent a computational technique that allows to study a large variety of physical and chemical processes on the molecular scale. MS works particularly well for fluid systems as the liquid phase and the gas phase can be treated simultaneously. The only difference between the phases is given by the local density.

There are two different methods of MS, the molecular dynamics (MD) and Monte Carlo. MD solves a simple Newton equation of motion for every atom in discretized time-steps while Monte Carlo uses the probability nature of the statistical mechanics.

One of the most important substances investigated using the approaches of MS is water. Water is essential in daily life, industry, and biological and natural processes. However, it has a typical non-standard behavior and many anomalies, which are still hard to model theoretically. The non-trivial phenomena are caused especially by its polar character and by the formation of hydrogen bonds.

In this study, we continue MD simulations of water [8] focused on the investigation of properties at the vapor–liquid phase interface. A series of MS was performed with both the SPC/E and TIP4P/2005 models in order to evaluate the density profiles, the thicknesses of the phase interface, and the surface tensions. A "slab" geometry with water molecules was simulated at various temperatures from the triple point of water to the temperatures close to the critical point. The conditions and settings of MS were inspired by the works of Vega and Miguel [13] and Sakamaki *et al.* [9]. All simulations were performed using DL_POLY Classic 1.9 [12, 10] running on a cluster with 4×2 Intel(R) Xeon(R) CPU E5645 (12 cores effectively for each CPU) @ 2.53GHz CPUs. New results were compared to both MS from the literature and the experimental data.

2   Water models

Despite the fact that water molecule is flexible and polarizable, simple rigid models are used regularly in many MS. Therefore, systems with large numbers of molecules can be modeled for a longer times. The most widespread simple models belong to the SPC and TIPXP families. An extended modification of the simple bond charge, i.e. the SPC/E model by Berendsen *et al.* [4], including empirical corrections to the polarization energy is very successful and reproduces vapor–liquid data very well. The most widely used TIPXP model is the TIP4P/2005 which was proposed by Vega and Abascal [1] in 2005. They tried to combine the good phase diagram of TIP4P with target properties of SPC/E improving the melting point.

In the present study, the two models TIP4P/2005 and SPC/E are employed to investigate vapor–liquid interfacial properties of water. Both the TIP4P/2005 and SPC/E models consider the Lennard–Jones interactions only between the oxygen atoms, because hydrogen atoms have a negligible mass compared to oxygen. The electrostatic interaction occurs between the hydrogen atoms and oxygen atom in the SPC/E model and between hydrogen atoms and the massless atom Q with the negative charge in the TIP4P/2005 model, respectively. A schematic representation of the SPC/E and TIP4P/2005 molecular models is shown in figure 1.
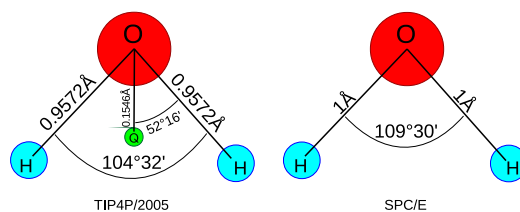
Figure 1: Schematic representation of the SPC/E and TIP4P/2005 molecular models for water.

3   Simulation methods

A series of MD simulations was performed with the NVT ensemble, i.e. for a constant number of molecules, a constant total volume of the system, and a constant temperature. The ensemble consisted of 1372 molecules, which is considerably more than in other studies, e.g., both Vega and Miguel [13] and Sakamaki *et al.* [9] considered 1024 molecules. The simulations were carried out in two steps. At first, a cubic box consisting only of liquid phase was simulated for 50 ps with 1 ps equilibration time. After a homogeneous liquid phase was formed in the cubic box, the z-size of the simulation box was symmetrically expanded by a factor of 3. As a result, the liquid phase forms a slab in the centre of the simulation box and the expanded empty volumes on each side of the slab allow subsequent formation of the vapor phase. The slab configuration was simulated for 10 ns in all cases. A constant time step of 2 fs was considered in all simulations.

In both simulations (in the cubic box and in the slab geometry), the periodic boundary conditions were imposed on all walls of the simulation box.

The MD simulations do not fix the temperature implicitly, therefore a thermostat is needed to correct kinetic energies of the molecules and thus regulate the temperature of the system. For this purpose, we used the Nosé–Hoover thermostat with the relaxation constant of 100 fs. The Verlet velocity integrator was used. The cutoffs of the Lennard–Jones interactions and the van der Waals forces were set to 14.5 Å. The direct Ewald method with an automatic parameter optimization constant set to 10^{-5} was used for electrostatic interactions.

4   Results

A series of 15 simulations at various temperatures spaced by 25 K was performed for each of the two water models. One simulation of the slab geometry running on 22 CPU cores took on average 48 hours in the case of the SPC/E model and 62 hours in the case of the TIP4P/2005 model. The difference in the computational time is caused by the additional massless atom Q that needed to be included in the TIP4P/2005 model.

The density profile $\rho(z)$ at a given temperature was computed as an average from the histograms of positions of water molecules in the z-direction calculated at each time step. Properties of the phase interface can, according to Chapela *et al.* [5], be determined from the correlation of the averaged density profile by a hyperbolic tangent function given in

the following manner

$$\rho(z) = \frac{\rho_{\mathrm{L}} + \rho_{\mathrm{V}}}{2} - \frac{\rho_{\mathrm{L}} - \rho_{\mathrm{V}}}{2} \tanh\left(\frac{z - z_0}{d}\right). \tag{1}$$

In equation (1), z marks the coordinate perpendicular to the phase interface, $\rho(z)$ denotes the density in Å^{-3} and z_0, d, ρ_{L}, and ρ_{V} are adjustable parameters. z_0 is the position of the Gibbs dividing surface of the interface, d is a parameter of the phase interface thickness, ρ_{L} denotes the saturated liquid density, and ρ_{V} is the saturated vapor density. We note that Chapela *et al.* [5] used the term $2(z - z_0)/d$ in the hyperbolic tangent, while the subsequent studies, e.g., [2, 13, 9], considered only $(z - z_0)/d$. To assure compatibility with other MS studies of water, we decided to use the later definition in equation (1) as well.

Figure 2 shows the saturated liquid and vapor densities obtained with the SPC/E model compared to other MS and to experimental data. The experimental data are represented by predictions of the reference equation of state IAPWS-95 [14] obtained from the TREND package [11]. The new simulations are in good agreement with other studies [2, 13, 9]. The saturated vapor density ρ_{V} obtained with the SPC/E model is in a quite good agreement with the IAPWS-95 equation of state, while the saturated liquid density ρ_{L} shows a clear deviation. The SPC/E liquid density is lower by 0.6% and 5.3% than the experimental data at temperatures 250 K and 500 K, respectively. We note that the difference becomes less pronounced when comparing the densities related to the reduced temperature $T_{\mathrm{r}} = T/T_{\mathrm{c}}$.

The melting point temperature of both water models considered in this work is below the real triple point of water 273.16 K. The triple point values are 213 K for the SPC/E model and 249 K for the TIP4P/2005 model [9]. Consequently, the vapor–liquid equilibrium could be calculated down to 250 K for both models.
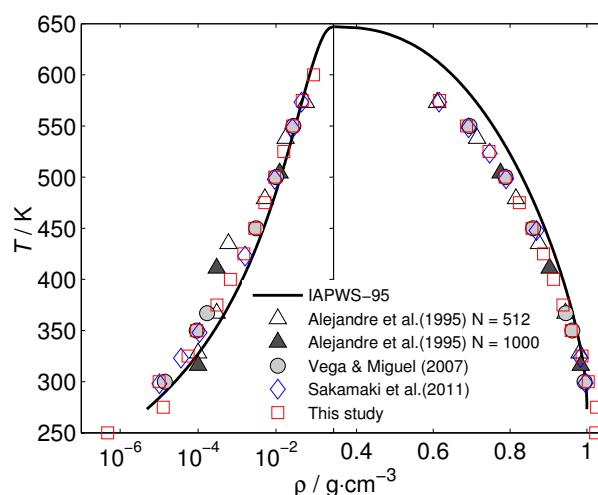

Figure 2: Saturated liquid and vapor densities for water obtained from MS with the SPC/E water model. Comparison of results from this study with the literature data [2, 13, 9] and the reference equation of state IAPWS-95 [14].

The densities for the TIP4P/2005 model are shown in figure 3. The saturated liquid density obtained with TIP4P/2005 lies closer to IAPWS-95 than the SPC/E model data (see figures 2 and 3). The TIP4P/2005 liquid density is lower only by 0.2% and 1.9% than the experimental data at temperatures 250 K and 500 K, respectively. Moreover, the TIP4P/2005 model provides relatively good representation of the maximum in the density of liquid water at 277 K. The maximum of approximately 0.999 g/cm^3 lies close to 275 K in our simulations. The saturated vapor density obtained with TIP4P/2005 is slightly worse than in the case of SPC/E.
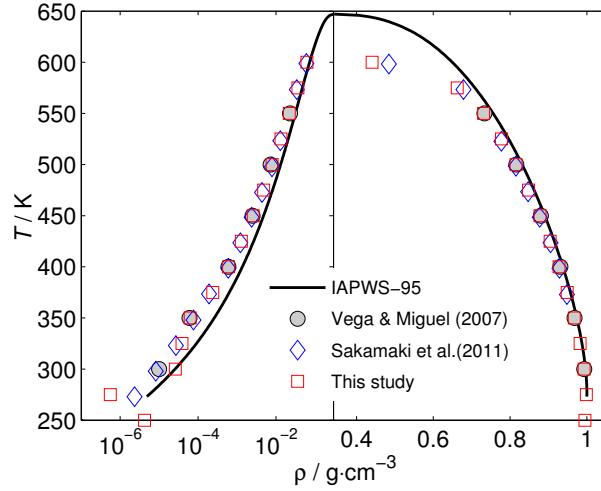

Figure 3: Saturated liquid and vapor densities for water obtained from MS with the TIP4P/2005 water model. Comparison of results from this study with the literature data [13, 9] and the reference equation of state IAPWS-95 [14].

The surface tension was computed in a conventional way as a sum of the pressure tensor (or initial) term γ_{pt} and the tail correction to the long-range Lennard–Jones interactions γ_{tail} that corrects the cutoff truncation error,

$$\gamma = \gamma_{\text{pt}} + \gamma_{\text{tail}}. \tag{2}$$

The pressure tensor term can be determined in the following manner

$$\gamma_{\text{pt}} = \frac{L_{\text{z}}}{2} \left(P_{\text{zz}} - \frac{P_{\text{xx}} + P_{\text{yy}}}{2} \right), \tag{3}$$

where L_{z} denotes the box size in z direction, P_{ii} is the ii-th diagonal component of the pressure tensor. The tail correction γ_{tail} is given by

$$\begin{aligned} \gamma_{\text{tail}} &= 12\pi\epsilon\sigma^6(\rho_{\text{L}} - \rho_{\text{V}})^2 \\ &\times \int_0^1 \int_{r_{\text{c}}}^{\infty} \coth\left(\frac{rs}{d}\right) \frac{3s^3 - s}{r^3} \mathrm{d}r\mathrm{d}s, \end{aligned} \tag{4}$$

where ϵ and σ are the Lennard–Jones parameters for oxygen atom, r_{c} is the cutoff for the Lennard–Jones potential and ρ_{L} and ρ_{V} are the bulk densities determined from equation (1).
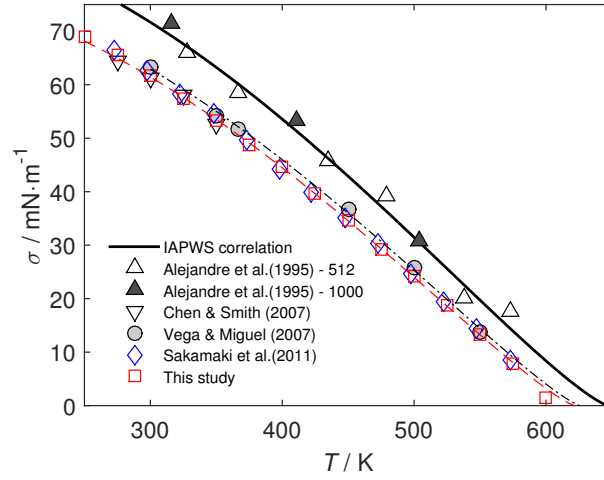
Figure 4: Surface tension of water obtained from MS with the SPC/E water model. Comparison of results from this study with the literature data [2, 6, 13, 9] and the IAPWS standard [7]. Dash-and-dotted black line and dashed red line are results of relation (5).

The results for the surface tension obtained with the SPC/E model are shown in figure 4. The new simulations are in a very good agreement with the previous studies by Chen and Smith [6], Vega and Miguel [13], and Sakamaki *et al.* [9]. The surface tension predicted in 1995 by Alejandre *et al.* [2] is much higher compared to other MS studies and lies remarkably close to the experimental data represented by the IAPWS standard for the surface tension of ordinary water [7]. Moreover, the data by Alejandre *et al.* [2] show relatively large scatter compared to other studies. Alejandre *et al.* [2] performed rather short simulations with 250 ps equilibration time and subsequent production runs of 250 ps and 125 ps for samples with 512 and 1000 molecules, respectively. The time step was set to 2.5 fs, i.e. a similar value as in other simulations. However, the overall simulation time between 375 and 500 ps seems to be insufficient in order to obtain correct and reproducible results. For example, Vega and Miguel [13] stated that a minimum time for the surface tension simulations is above 0.5 ns. They performed their simulations for 1.5 to 2.0 ns, which is still at least five times less than in the case of Sakamaki *et al.* [9] and this study. Chen and Smith [6] concluded that a minimum time for an accurate surface tension simulations is around 2 to 5 ns. T

The TIP4P/2005 model gives a better prediction for the surface tension of water compared to the SPC/E model. The difference between the models can be seen from the deviations of the SPC/E and TIP4P/2005 results from the black line representing the IAPWS standard [7] in figures 4 and 5. The new results for TIP4P/2005 are in good agreement with our previous simulations [8] and the results by Vega and Miguel [13] and Sakamaki *et al.* [9].

The surface tension data shown in figures 4 and 5 were correlated by the following equation

$$\gamma(T) = B \left(1 - T/T_\mathrm{c}\right)^{11/9} \left[1 - b\left(1 - T/T_\mathrm{c}\right)\right], \qquad (5)$$
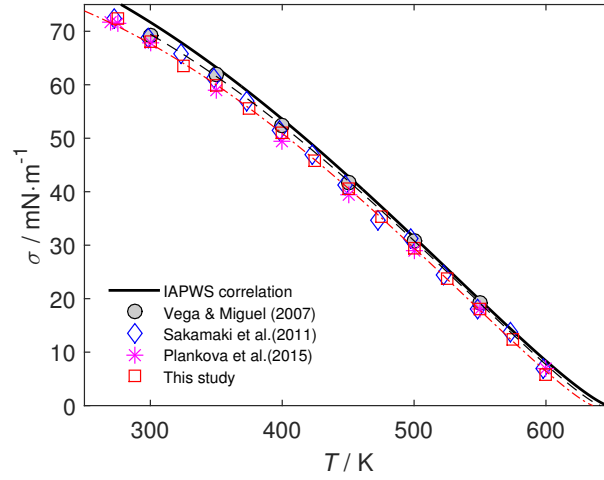
Figure 5: Surface tension of water obtained from MS with the TIP4P/2005 water model. Comparison of results from this study with the literature data [8, 13, 9] and the IAPWS standard [7]. Dash-and-dotted black line and dashed red line are results of correlation (5).

Table 1: Influence of the number of molecules N in the simulation with the SPC/E model at a constant temperature 350 K on the following results: ρ_L liquid density, ρ_V vapor density, t 10–90 interface thickness, γ surface tension.

Property / N	500	864	1372	2048
ρ_L (g/cm^3)	0.954	0.957	0.959	0.960
$\rho_\mathrm{V} \cdot 10^5$ (g/cm^3)	9.85	10.41	9.11	11.54
t (Å)	3.879	4.256	4.332	4.550
γ (mN/m)	53.38	53.71	53.35	53.65

where B and b are adjustable parameters and T_c is the critical temperature of the molecular model. We continue using this equation for comparison purposes. We note that Eq. (5) is of the same form as the IAPWS standard [7], except for the exponent, whose IAPWS value 1.256 is closer to the current estimate 1.260 of the universal critical exponent [3].

Table 1 contains results for the saturated liquid and vapor densities, the thickness of the phase interface, and the surface tension. The liquid density slightly increases in a larger ensemble. The vapor density and the surface tension show small fluctuations with no obvious dependency on the number of simulated molecules. The only significant influence of the ensemble size can be seen for the 10–90 thickness of the phase interface t, which continuously increases approximately by 17% with increasing the number of molecules from 500 to 2048.

5   Conclusions

Properties of the vapor–liquid phase interfaces of pure water were studied using the approaches of MD. Two commonly used molecular models of water, SPC/E and TIP4P/2005, were used to model the density profiles and the surface tensions of water at temperatures ranging from 250 K to 600 K. Results of our new simulations are in good agreement with most of the previous MS studies. Both models were found to provide relatively good results for the vapor-liquid phase equilibria and the densities of water at temperatures up to 500 K. At higher temperatures, both models start to deviate from the experimental data as they underpredict the critical point of water. SPC/E gives slightly better reproduction of the vapor density while TIP4P/2005 is more accurate on the liquid side. The TIP4P/2005 model gives higher values for the surface tension lying closer to the experimental data correlated by IAPWS [7] than the SPC/E model.

On the basis of the previous studies by Vega and Miguel [13] and Sakamaki *et al.* [9] and our new results we conclude that the TIP4P/2005 molecular model is convenient for modelling the interfacial properties and surface tension of pure water in the temperature range from 250 K to 550 K, although a fully quantitative prediction cannot be expected of these relatively simple models.

References

[1] J. L. Abascal and C. Vega. *A general purpose model for the condensed phases of water: Tip4p/2005.* J. Chem. Phys. **123** (2005), 234505.

[2] J. Alejandre, D. J. Tildesley, and G. A. Chapela. *Molecular dynamics simulation of the orthobaric densities and surface tension of water.* J. Chem. Phys. **102** (1995), 4574.

[3] M. A. Anisimov and C. E. Bertrand. *Thermodynamics of fluids at meso and nano scales.* In 'Applied Thermodynamics of Fluids', The Royal Society of Chemistry (2010).

[4] H. Berendsen, J. Grigera, and T. Straatsma. *The missing term in effective pair potentials.* J. Phys. Chem. **91** (1987), 6269–6271.

[5] G. Chapela, G. Saville, S. Thomson, and J. Rowlinson. *Computer simulation of a gas–liquid surface.* J. Chem. Soc. Faraday Trans. II (1977), 1133 – 1144.

[6] F. Chen and P. E. Smith. *Simulated surface tensions of common water models.* J. Chem. Phys. **126** (2007), 221101.

[7] International Association for the Properties of Water and Steam. *IAPWS Revised Release on the Surface Tension of Ordinary Water Substance,* (2014). URL: `http://www.iapws.org/`.

[8] B. Planková, V. Vinš, J. Hrubý, M. Duška, T. Němec, and D. Celný. *Molecular simulation of water vapor–liquid phase interfaces using tip4p/2005 model.* EPJ Web. Conf. **92** (2015), 02071.

[9] R. Sakamaki, A. K. Sum, T. Narumi, and K. Yasuoka. *Molecular dynamics simulations of vapor/liquid coexistence using the nonpolarizable water models.* J. Chem. Phys. **134** (2011).

[10] W. Smith, T. Forester, and I.T.Todorov. *The DL_ POLY Classic User Manual.* Daresbury Laboratory, United Kingdom, (2012).

[11] R. Span, T. Eckermann, S. Herrig, S. Hielscher, A. Jäger, and M. Thol. TREND. thermodynamic reference and engineering data 2.0. Technical report, TREND. Thermodynamic Reference and Engineering Data 2.0, Lehrstuhl fuer Thermodynamik, Ruhr-Universitaet Bochum, (2015).

[12] I. Todorov, W. Smith, K. Trachenko, and M. Dove. *Dl_ poly_ 3: new dimensions in molecular dynamics simulations via massive parallelism.* J. Mater. Chem. **16** (2006), 1911–1918.

[13] C. Vega and E. De Miguel. *Surface tension of the most popular models of water by using the test-area simulation method.* J. Chem. Phys. **126** (2007), 154707.

[14] W. Wagner and A. Pruss. *The iapws formulation 1995 for the thermodynamic properties of ordinary water substance for general and scientific use.* J. Phys. Chem. Ref. Data **31** (2002), 387 − 535.

The Data Acquisition System for COMPASS Experiment*

Ondřej Šubrt

1st year of PGS, email: `subrton2@fjfi.cvut.cz`
Department of Software Engineering
Faculty of Nuclear Sciences and Physical Engineering, CTU in Prague

advisor: Tomáš Liška, Department of Software Engineering
Faculty of Nuclear Sciences and Physical Engineering, CTU in Prague

Abstract. This paper discusses the current status of the new data acquisition system (DAQ) of the COMPASS experiment at CERN. In the original DAQ, the event building is performed by software deployed on switched computer network. The new system replaces the event building network with a custom FPGA-based hardware. The new DAQ software is based on state machines and C++ with usage of the Qt framework, the DIM library, and the IPBus library. The detail description of the new DAQ from hardware, software and process point of view is presented. Moreover, several improvements for future development are introduced, namely, load balancing across multiple transformation threads and crosspoint switch.

Keywords: data acquisition, FPGA, load balancing, crosspoint switch

Abstrakt. Tento článek popisuje současný stav nového systému pro sběr dat na experimentu COMPASS. V původním systému pro sběr dat bylo sestavování událostí zajištěno na softwarové úrovni na síťově propojených počítačích. Tento přístup byl nahrazen hardwarovým sestavováním událostí a využívá nejmodernějších FPGA technologií. Nový systém sběru dat je postaven na stavových automatech, jazyce C++ s použitím Qt frameworku, knihoven DIM a IPBus. Podrobný popis systému pro sběr dat je prezentován z hardwarového, softwarového a procesního pohledu. Kromě toho je představeno několik vylepšení pro budoucí vývoj a sice vyvažování zátěže mezi více transformačními vlákny a koncept crosspoint switche.

Klíčová slova: sběr dat, FPGA, vyvažování zátěže, crosspoint switch

1 Introduction

This paper presents current status and proposed improvements for future development of the hardware and software part of a new data acquisition system (DAQ), based on the Field Programmable Gate Array (FPGA) technology [3], for the COMPASS (COmmon Muon Proton Apparatus for Structure and Spectroscopy) experiment at CERN [1].

Development of the new DAQ software and hardware was started to improve reliability and speed of system. Main idea of the hardware upgrade is to use FPGA technology for event building purposes and consequently reducing number of used computers to only eight. Reliable, flexible and cost-effective hardware event-building can be prepared today thanks to improvements in FPGA technology. The new software has to cope with

---

challenges linked to control of such new hardware event-building network and has to allow users to operate whole system efficiently.

This paper is organized as follows. Section 2 provides information about experiment COMPASS in a deeper way. In Section 3, the overview of current status of the DAQ is described and its segments are discussed in detail. Proposed improvements for future development of the DAQ are presented in Section 4. Section 5 concludes the paper.

2   Experiment COMPASS

The purpose of the COMPASS experiment is the study of nucleon spin structure and hadron spectroscopy [7, 1]. The experiment, which utilizes a polarized target and is situated at the Super Proton Synchrotron (SPS) at North Area, see Figure 1, at CERN in Geneva, Switzerland, was approved conditionally in 1997 and commissioned in 2001. In 2002, the experiment started operating. It's main mission is to study the structure and the spectroscopy of hadrons using high intensity muon and hadron beams. The unique CERN SPS M2 beam line is used as a source of these particles, serving the beam with energy within the range of 50 GeV and 280 GeV. Particle identification is carried out employing a Ring-imaging Cherenkov (RICH) detector, two electro-magnetic calorimeters, two hadron calorimeters and two muon filters.

Over the span of eight years from 2002 to 2009, data-taking had been taking place with the exception of year 2005, in which an accelerator upgrade was realized. The beams used during these years were primarily muon beams and partially hadron beams. As the apparatus of the experiment had been proven to be very versatile, an extension of the COMPASS program has been approved in 2010 by the CERN research board, prolonging its lifespan by seven years and shifting the focus of the experiment to tests of chiral perturbation theory, study of the Drell-Yan process and research in field of Generalised Parton Distributions [7, 1].

During the previous years, it had a usual data rate of approximately 1500 MB/s during approximately 10 seconds on-spill with the off-spill time between 30 and 50 seconds, depending on SPS super cycle. The original DAQ of the experimentm was built during years 1999-2001. The Data Acquisition and Test Environment (DATE) software, originally developed for the ALICE at CERN, was used to control DAQ and event building in old system. Both software package and usage of FPGA-based cards have been widely studied and as the result a design of the new DAQ was prepared.

3   Overview of current status of the DAQ

New DAQ replaces the old one, however, some parts do not change. The article is not aimed at comparison of new and old one. In following section, the current status of the new DAQ is discussed from hardware, software and process point of view.
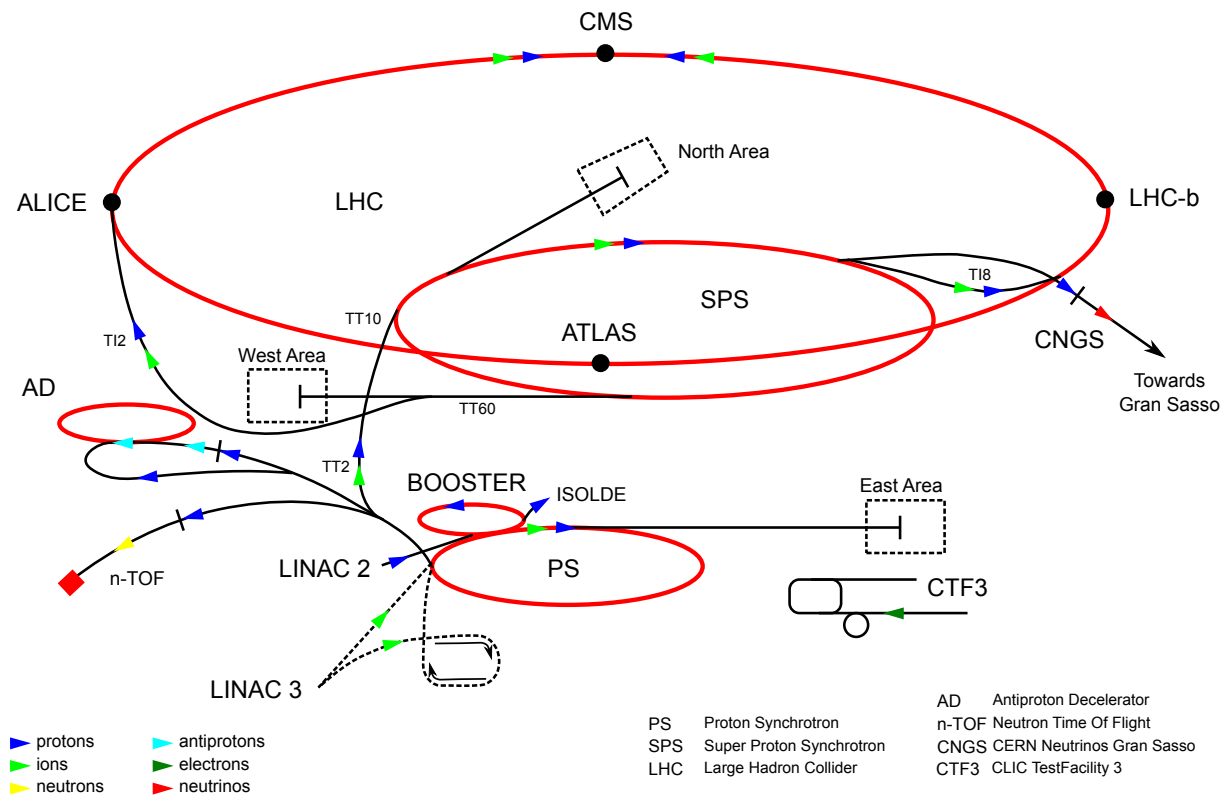
Figure 1: COMPASS location within the CERN accelerator complex [4]

3.1 Hardware structure of the DAQ

The COMPASS DAQ is currently undergoing a major hardware and complete software replacement, the first part of which was finished in 2014, and the second part of which is planned to be completed in 2016. As can be seen in Figure 2, the new DAQ can be divided into five basic layers, the first one being frontend cards which process analog data from the detectors and convert them to digital form. The front-end cards are connected to HGeSiCA, CATCH and Gandalf modules which make up the second layer [9, 6, 8]. The second layer handles the first level of multiplexing (consolidating multiple data streams into a single stream). The data from some of the HGeSiCA and CATCH modules go through SLink multiplexers and the data from Gandalf modules through TIGER VXS data concentrators, creating a sublayer. SLink multiplexers and TIGER VXS data concentrators are used for multiplexing.

Using SLinks, this sublayer is connected to the third layer, which comprises eight FPGA cards which are referred to as Data Handling Cards (DHC) within this context. The third layer handles another level of multiplexing. SLinks are also used to connect the third layer to the fourth layer, which is made up of a single DHC with switch firmware – this layer handles event building. The fifth layer, again utilizing SLinks for connection to the previous layer, consists of readout computers which run the DAQ software. These computers are collectively referred to as the readout engine. The connection of an SLink and the memory of a readout computer is handled by a Spillbuffer – a PCI Express card with an FPGA chip and 2GB RAM, which is also partially used for buffering. The

acquired data which are to be stored are then sent directly to the CERN CASTOR facility [5].
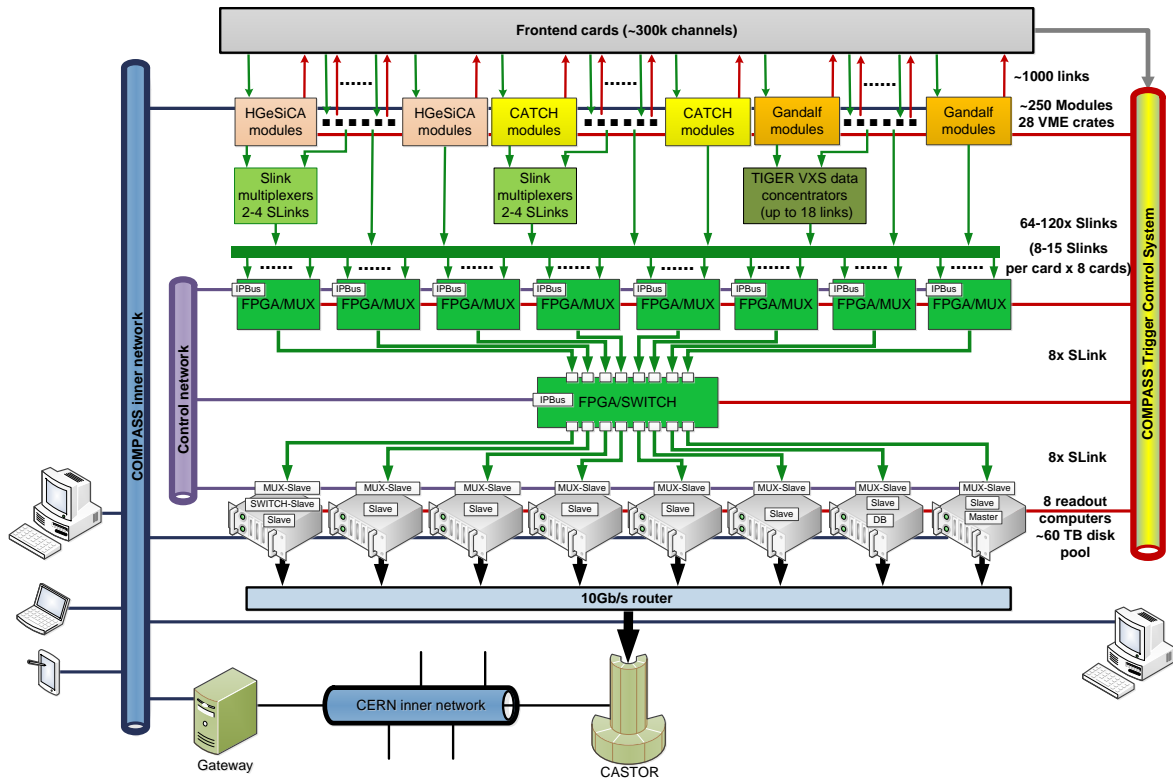

Figure 2: COMPASS DAQ topology as used in the run 2015 [4]

3.2   Software structure of the DAQ

The DAQ software is deployed on the readout engine, the individual computers of which run the Scientific Linux CERN 6 (SLC6) operating system [10]. The software is based on C++ and uses the Qt Framework not only for its GUI, but also for its threading. Furthermore, Qt data types and a variety of non-GUI classes are also used in the software. The Qt version used in the DAQ software is 5.2.1. Python and Bash script also find use in the DAQ, their scripts being particularly useful for starting processes remotely using SSH. Finally, XML is used to describe the hardware configuration of the DAQ in so-called XML structure files and the IPBus configuration in so-called XML connection files and address files.

Six main functions are provided by the DAQ software: configuration of the hardware, monitoring of the data taking process, remote control of the hardware, data flow control, logging of information and errors and log browsing [4].

The DAQ software also includes a connection to an SQL database. The database is used to store, among others: configuration information of the DAQ's hardware, information logs and error logs. The events read out from the detectors by the DAQ are stored in the DATE format, which is the format used in the DATE (Data Acquisition and Test

Environment) software. The DATE software is the data acquisition software that was originally developed for the ALICE experiment and a modified version of which was being used in the COMPASS DAQ before the overhaul [2].
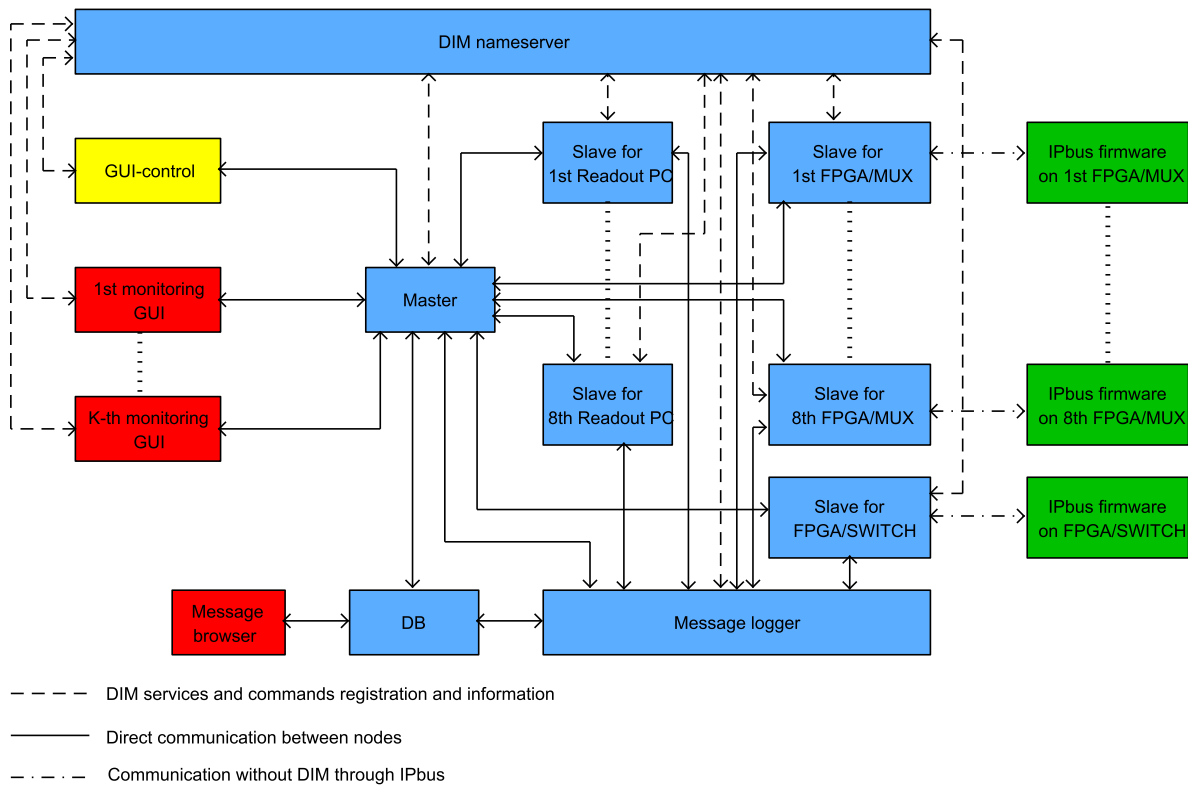
3.3 Processes of the DAQ

Figure 3: The communication diagram of the DAQ [4]

The software comprises the following processes: Master, Slave Control, Slave Readout, RunControl GUI, MessageLogger and MessageBrowser.

The Master is a vital process for the DAQ – using DIM, it mediates communication between the RunControl GUI and the slave processes as well as the communication between the slave processes and the configuration database. It also plays a major role in the DAQ's error handling.

The purpose of the Slave Control process is to configure and monitor the FPGA cards – it is the only process which communicates with the FPGA cards directly. All communication with the FPGA cards is carried out using IPbus.

The Slave Readout is a very resource-demanding process responsible for readout of data from connected devices, as well as its processing and subsequent storage. It comprises a large number of threads.

The RunControl GUI, which can run in two different modes, is the means of user interaction with the DAQ. The first mode, Run Control, provides the user with complete control over the DAQ as well as information concerning the current run and status of the

hardware. Only one instance of this mode can run at a time. The second mode, Monitoring, retains the information and status providing capabilities, but does not provide the user with any direct control over the DAQ. There is no practical limit to how many instances of this mode can run at a time.

The MessageLogger is a process which receives status and error messages from all parts of the DAQ and stores them in the database.

The MessageBrowser is a GUI tool used for visualization of these messages [3].

A diagram showing communication between individual processes of the DAQ can be found in Figure 3. The meaning of the colors is as follows:

- Blue: Processes vital for data acquisition

- Red: Optional monitoring tools

- Yellow: Main control GUI

- Green: Firmware interface

4   Proposed improvements in the DAQ

New DAQ was built and prepared in 2014. Nevertheless, many ways how to improve it have already risen. Some of them – namely load balancing across multiple transformation threads and the crosspoint switch – are mentioned in following section. The work on DAQ is never ending process including improvement in reliability, efficiency and amount of execution time.

4.1   Load balancing across multiple transformation threads

The Readout Slave has several responsibilities. Besides the readout of data from connected devices and their storage, it has a crucial responsibility for data processing as well. Events have to be transformed and stored in DATE format. Nowadays, the data processing run in ten parallel threads. Each thread processes only one event at once. Ten events are assigned to ten threads at once, it waits until the last thread finishes its work and then next ten events are assigned to those ten threads again and so forth. This approach has one crucial drawback. Some threads are very often inactive and without any work. For instance, nine threads must wait until the tenth one finishes its work.

To overcome this deficiency, the new approach concerning load balancing and entire utilization of ten threads is proposed. In Figure 4, load balancing across multiple transformation threads is stated. In this proposal, each thread processes only one event at once and immediately starts to process the next event after finishing its work on the previous one. The subroutine *AssignThread* is located on the right. In this subroutine, the loop iterates the events in *BlockOfEvents* starting at position *index*. The event is assigned to first free thread. If no free thread is available, the current *index* of event is returned.

The flowchart on the left represents loop iterating the events in *BlockOfEvents*. It is necessary to keep the same order of events *BlockOfEvents* for monitoring and storage. For this reason, the loop has to wait until the transformation of current event is prepared, however, the performance of load balancing is not affected by the waiting of this loop.
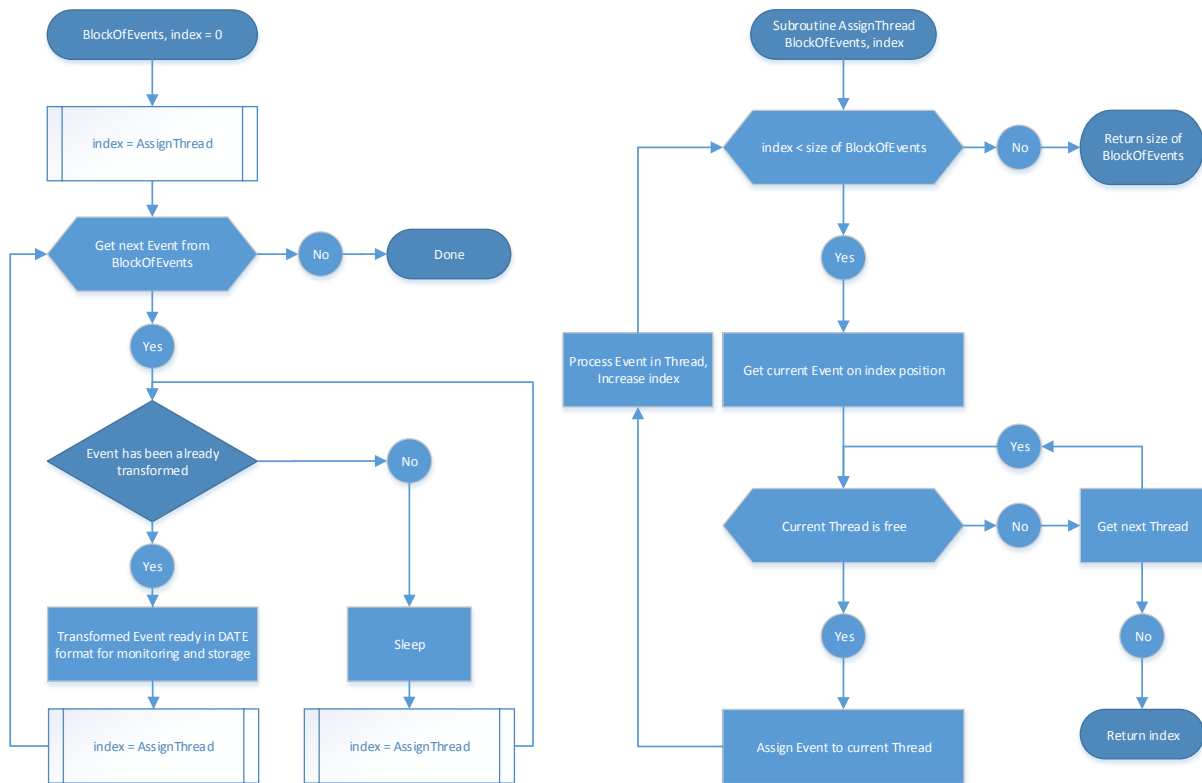
Figure 4: Load balancing across multiple transformation threads

4.2 The crosspoint switch

In 2015, it is planned to wire all point-to-point high speed links via a fully programmable crosspoint switch. The crosspoint switch will therefore provide a fully customizable DAQ network topology between front-end electronics, the event building hardware, and the online computers. The adaptability of the system topology allows to compensate for hardware failure in the event builder by activating spare resources replacing broken or malfunctioning modules. Algorithms shall identify hardware failure and synchronously reconfigure the DAQ topology to substitute the broken module by a spare one without human intervention.

In this way, the fully programmable crosspoint switch contributes substantially to an improved system reliability since every broken FPGA module of the event builder as well as the online computers can be exchanged on-the-fly and data loss is reduced. In Figure 5, proposed DAQ topology including the crosspoint switch is given.

The hardware is still not prepared and thus the final design is not exactly known. It is assumed that the crosspoint switch will have 144 incoming SLinks and 144 outgoing SLinks. The board will contain two chips connected together through data bus with 20 lines and one FPGA card controlling both of them by control bus.

Initially, 120 SLinks was leading to eight FPGA cards from frontend cards. In this proposal, these 120 Slinks are connected directly to crosspoint switch and the chips handle 60 SLinks each. The crosspoint switch has 120 outgoing SLinks to 8 Multiplexer FPGA cards, 8 outgoing SLinks to DHC-Switch FPGA card and 8 outgoing SLinks to 8 readout

computers. It also consists of 8 incoming SLinks from 8 Multiplexer FPGA cards and 8 SLinks from DHC-Switch FPGA card. In sum, it uses 136 incoming SLinks from 144 and 136 outgoing SLinks from 144.

It is challenging to ensure the communication between Multiplexer FPGA cards and DHC-Switch FPGA card through 20 lines between chips, since Multiplexer and Switch do not have to be connected to the same chip and have to use data bus between chips. The next challenge will be to ensure manually reconnection in GUI of incoming and outgoing SLinks in crosspoint switch without stopping the run. The proposal even contains the automatic reconnection without stopping the run based on finding the best path between incoming and outgoing SLinks.
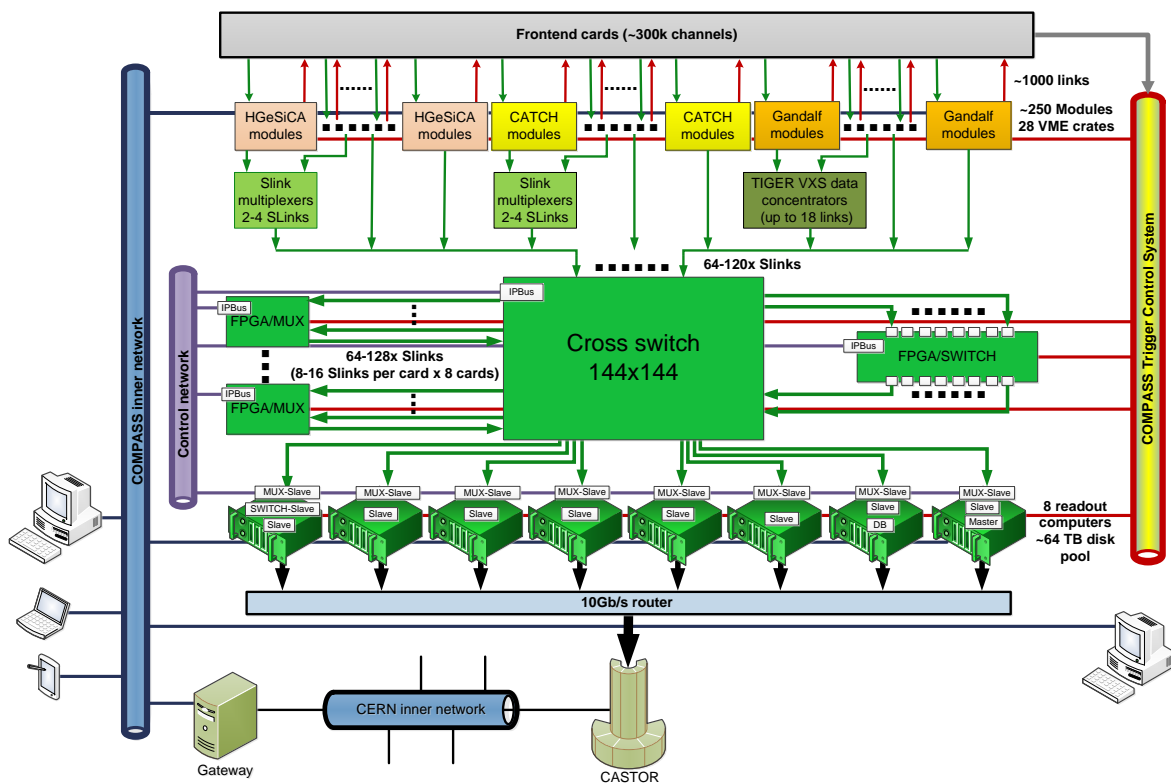

Figure 5: Proposed DAQ topology including the crosspoint switch

5 Conclusion

Design of the DAQ has been prepared with respect to demands and restrictions which were extracted from the initial studies of the present DAQ of the COMPASS experiment at CERN and discussion among collaboration of the experiment. All processes were implemented in the C++ language using the Qt library. PHP, MySQL, javascript, bashscript and python were chosen as languages for support function and web interface. The first full version of software package has been tested and used during preparation for winter 2014 data taking. The stable version of the new DAQ is currently taking data

from the COMPASS experiment.

Load balancing across multiple transformation threads is designed to assign event to free thread as soon as possible. The improved transformation process becomes more effective and reduces the execution time. The concept of crosspoint switch brings the improvement of system reliability, the exchanging of broken computers on-the-fly and the reduction of data loss. The crosspoint switch is the most challenging part from communication, stability and optimization point of view. These improvements are considered for future development and will be implemented and tested very soon.

References

[1] V. Y. Alexakhin et al. *COMPASS-II Proposal.* The COMPASS Collaboration, (May 2010). CERN-SPSC-2010-014; SPSC-P-340.

[2] T. Anticic et al. *ALICE DAQ and ECS Users Guide.* CERN, ALICE internal note, ALICE-INT-2005-015, (2005).

[3] M. Bodlak et al. *FPGA based data acquisition system for COMPASS experiment.* Journal of Physics: Conference Series . 2014-06-11, vol. 513, issue 1, s. 012029-. DOI: 10.1088/1742-6596/513/1/012029.

[4] J. Novy. *Processing of large quantity of data from the COMPASS experiment.* PhD thesis, Faculty of Nuclear Sciences and Physical Engineering, Czech Technical University, (September 2015). Written dissertation preparation – in preparation for release.

[5] CASTOR - CERN Advanced Storage manager [online]. `http://castor.web.cern.ch`. Accessed 2015-09-09.

[6] Electronic developments for COMPASS at Freiburg [online]. `http://hpfr02.physik.uni-freiburg.de/projects/compass/electronics/catch.html`. Accessed 2015-09-09.

[7] COMPASS: COmmon Muon Proton Apparatus for Structure and Spectroscopy [online]. `http://wwwcompass.cern.ch`. Accessed 2015-09-09.

[8] The GANDALF Module [online]. `http://wwwhad.physik.unifreiburg.de/gandalf/pages/hardware/the-gandalf-module.php?lang=EN`. Accessed 2015-09-09.

[9] iMUX/HGESICA module [online]. `http://wwwcompass.cern.ch/twiki/pub/Detectors/FrontEndElectronics/imux_manual.pdf`. Accessed 2015-09-09.

[10] Linux at CERN [online]. `http://linux.web.cern.ch/linux/scientific6/`. Accessed 2015-09-09.

Number Fields Generated by Pisot Units[*]

Tomáš Vávra

4th year of PGS, email: `t.vavra@seznam.cz`
Department of Mathematics
Faculty of Nuclear Sciences and Physical Engineering, CTU in Prague

advisors:

Zuzana Masáková, Department of Mathematics
Faculty of Nuclear Sciences and Physical Engineering, CTU in Prague

Petr Kůrka, Center for Theoretical Study, Charles University in Prague

Abstract. This contribution is devoted to the study of number fields that can be generated by Pisot units. A Pisot number is a real algebraic integer $\alpha > 1$, i.e. a zero of $x^n + a_1 x^{n-1} + \cdots + a_{n-1} a_n \in \mathbb{Z}[x]$, whose conjugates α_i satisfy $|\alpha_1| < 1$. It has been shown by R. Salem in 1963 that for any real number field K there is a Pisot number α such that $K = \mathbb{Q}(\alpha)$. In 2013, Q. Chen and J. Zhuang showed that this Pisot generator can be found in polynomial time given that the integral basis of K is known. It has been also known that any real number field can be generated by a Pisot unit, i.e. a Pisot number that is invertible in the ring of algebraic integers, see for example [1]. However, no explicit algorithm for determining such a generator was known so far. Utilizing an integer programming methods for an integer lattice problem, we provide an algorithm for finding the Pisot unit generator of the minimal magnitude. For complex fields, we use the notion of complex Pisot units, an analogy to Pisot numbers where only one complex pair of conjugates is allowed to lie outside the unit circle. For all complex fields with the exception of CM fields without a nontrivial root of unity, we are able to adjust the algorithm to find the Pisot unit generator of minimal absolute value. In case of CM fields containing a complex unit, but not a nontrivial root of unity, one can still find a complex Pisot unit generator, but not of minimal absolute value. The remaining case is a complex field without any complex unit. Clearly, in this case the field cannot be generated by a unit. A characterization of such fields, however, still remains an open problem.

Keywords: number fields, pisot units, cm fields, units

Abstrakt. Tento příspěvek se věnuje studiu číselných těles generovaných Pisotovými jednotkami. Pisotovo číslo je reálné algebraické celé číslo $\alpha > 1$, tzn. kořen $x^n + a_1 x^{n-1} + \cdots + a_{n-1} a_n \in \mathbb{Z}[x]$, jehož sdružené kořeny α_i splňují $|\alpha_i| < 1$. V roce 1963 ukázal R. Salem, že pro každé reálné těleso K existuje Pisotovo číslo α takové, že $K = \mathbb{Q}(\alpha)$. V roce 2013 ukázali Q. Chen and J. Zhuang, že pokud je známa integrální báze K, pak je možné tento generátor najít v polynomiálním čase. Je také známo, že jako generátor lze brát Pisotovu jednotku, tj. Pisotovo číslo, které je invertibilní v okruhu algebraických celých čísel, viz [1]. Nicméně, dosud nebyl znám algoritmus k najítí takového generátoru. Využitím algoritmu celočíselného programování na problém v celočíselné mřížce budeme schopni najít generující Pisotovy jednotku minimální velikosti. Pro komplexní tělesa uvažujeme komplexní Pisotova čísla, analogii Pisotových čísel. Pro komplexní Pisotova čísla pouze jeden pár sdružených kořenů může ležet vně jednotkové kružnice. Náš algoritmus je možno upravit na případ komplexních těles a jeho výstupem je, s

---

výjimkou CM těles bez netriviálního kořenu jedničky, generující komplexní Pisotova jednotka minimální absolutní hodnoty. V případě, že CM těleso obsahuje komplexní jednotku, ale ne netriviální kořen jedničky, potom stále můžeme najít generující Pisotovu jednotku, ale již ne minimální absolutní hodnoty. Zbývající případ je, kdy CM těleso neobsahuje komplexní jednotku. V takovém případě samozřejmě nemůže být těleso generováno jednotkou. Klasifikace, kdy nastává tento případ, však zatím není známa.

Klíčová slova: číselná tělesa, pisotovy jednotky, cm tělesa, jednotky

The results have been presented at the 29th Journées Arithmétiques conference in Debrecen and are being prepared to be submitted.

References

[1] M.-J. Bertin, A. Decomps-Guilloux, M. Grandet-Hugot, M. Pathiaux-Delefosse, and J.-P. Schreiber. *Pisot and Salem numbers.* Birkhäuser Verlag, Basel, 1992. With a preface by David W. Boyd.

[2] Q. Cheng, J. Zhuang. *On certain computations of Pisot numbers.* Inform. Process. Lett., 113(8):271–275, 2013.

[3] R. Salem. *Algebraic numbers and Fourier analysis.* Heath mathematical monographs. Heath, 1963.

Local-time Representation of Path Integrals

Václav Zatloukal

5th year of PGS, email: `zatlovac@fjfi.cvut.cz`
Department of Physics
Faculty of Nuclear Sciences and Physical Engineering, CTU in Prague

advisor: Petr Jizba, Department of Physics
Faculty of Nuclear Sciences and Physical Engineering, CTU in Prague

Abstract. We derive a local-time path-integral representation for a generic one-dimensional time-independent quantum-mechanical system. In particular, we show how to rephrase the matrix elements of the Bloch density matrix as a path integral over x-dependent local-time profiles. The latter quantify the time that the sample paths $x(t)$ in the Feynman path integral spend in the vicinity of an arbitrary point x. Generalization of the local-time representation that includes arbitrary functionals of the local time is also provided. We argue that the results obtained represent a powerful alternative to the traditional Feynman–Kac formula, particularly in the high and low temperature regimes. To illustrate this point, we apply our local-time representation to analyze the asymptotic behavior of the Bloch density matrix at low temperatures. Further salient issues, such as a connections with the Sturm–Liouville theory and the Rayleigh–Ritz variational principle are also discussed.

The path integral (PI) has been used in quantum physics since the revolutionary work of Feynman [1], although the basic observation goes back to Dirac [2] who appreciated the rôle of the Lagrangian in short-time evolution of the wave function, and even suggested the time-slicing procedure for finite, i.e., non-infinitesimal, time lags. Since then the PI approach yielded invaluable insights into the structure of quantum theory and provided a viable alternative to the traditional operator-formalism-based canonical quantization. During the second half of the 20th century, the PI became a standard tool in quantum field theory and statistical physics, often providing the easiest route to derivation of perturbative expansions and serving as an excellent framework for (both numerical and analytical) non-perturbative analysis [3].

Feynman PI has its counterpart in pure mathematics, namely, in the theory of continuous-time stochastic processes. There the concept of integration over a space of continuous functions (so-called fluctuating paths or sample paths) had been introduced by Wiener [4] already in 1920's in order to represent and quantify the Brownian motion. Interestingly enough, this so-called Wiener integral (or integral with respect to Wiener measure) was formulated 2 years before the discovery of the Schrödinger equation and 25 years before Feynman's PI formulation of quantum mechanics.

The *local time* for a Brownian particle has been of interest to physicists and mathematicians since the seminal work of Paul Lévy in 1930's [6]. In its essence, the local time characterizes the time that a sample trajectory $x(t)$ of a given stochastic process spends in the vicinity of an arbitrary point X. This in turn defines a sample trajectory L^X of a new stochastic process. A rich theory has been developed for local-time processes that stem from diffusion processes (see, e.g., Ref. [7] and citations therein). We should particularly highlight the Ray–Knight theorem which states that the local time of the Wiener process can be expressed in terms of the squared Bessel process. In contrast to mathematics, the concept of the local time is not uniquely settled in physics literature. Various authors define essentially the same quantity under different names (local time, occupation time, sojourn time, etc.), and with different applications in mind.

The aim of this paper is to derive a local-time PI representation of the Bloch density matrix, i.e., the matrix elements $\langle x_b | e^{-\beta \hat{H}} | x_a \rangle$ of the Gibbs operator. This can serve not only as a viable alternative to the commonly used Feynman–Kac representation but also as a powerful tool for extracting both large and small temperature behavior. Furthermore, by analytically continuing the result back to the real time via the inverse Wick rotation, $\beta \to it/\hbar$, one obtains the local-time PI representation of quantum-mechanical transition amplitudes, i.e., matrix elements of the evolution operator $e^{-it\hat{H}/\hbar}$. Apart from the general theoretical outline, our primary focus here will be on the low-temperature behavior which is technically more challenging than the large-temperature regime. This is because the low-temperature regime is controlled by paths with a large local time near the global minimum of the potential. In our formulation, we uncover an interesting connection between a low-temperature PI expansion and the Rayleigh–Ritz variational principle. On the contrary, the high-temperature regime of the Boltzmann density function $\rho(x, x, \beta)$ is dominated by paths that spend a sizable amount of time in the vicinity of the point x. In fact, the large-temperature expansion was already treated in some detail in our previous paper [8].

The action in our local-time PI is identified as the action of a radial harmonic oscillator, which indeed coincide with the squared Bessel stochastic process. Relation to the Sturm–Liouville theory is also highlighted, at arbitrary temperatures, and a local-time analog of the Feynman–Matthews–Salam formula is presented and employed to compute the one-point distribution of the local time. Last but not least, we also wish to promote the concept of the local time which is not yet sufficiently well known among the path-integral practitioners.

Keywords: path integral, local times, Ray–Knight theorem, Rayleigh-Ritz variational principle

Full article is currently under journal review, and it is available at `http://arxiv.org/abs/1506.00888`.

References

[1] R.P. Feynman, Rev. Mod. Phys. **20**, 367 (1948).

[2] P.A.M. Dirac, Physikalische Zeitschrift der Sowjetunion **3**, 64 (1933).

[3] H. Kleinert, *Path Integrals in Quantum Mechanics, Statistics, Polymer Physics, and Financial Markets*, 5th edition, (World Scientific, London, 2009).

[4] N. Wiener, J. Math. & Phys. **2**, 132 (1923).

[5] M. Kac, Trans. Am. Math. Soc. **65**, 1 (1949).

[6] P. Lévy, Compositio Mathematica **7**, 283 (1939).

[7] M. Marcus and J. Rosen, *Markov Processes, Gaussian Processes, and Local Times*, 1st edition, (Cambridge University Press, Cambridge, 2006).

[8] P. Jizba and V. Zatloukal, Phys. Rev. E **89**, 012135 (2014).